Enlightening the Dark Universe Through Light Particles

A thesis submitted in partial fulfilment of

the requirements for the degree of

Doctor of Philosophy

by

Tanmay Kumar Poddar

(Roll No. 17330036)

Under the supervision of

Prof. Srubabati Goswami

Professor

Theoretical Physics Division

Physical Research Laboratory, Ahmedabad, India.

DISCIPLINE OF PHYSICS

INDIAN INSTITUTE OF TECHNOLOGY GANDHINAGAR

2022

Dedicated to

My Beloved Family

Declaration

I declare that this written submission represents my ideas in my own words and where others' ideas or words have been included, I have adequately cited and referenced the original sources. I also declare that I have adhered to all principles of academic honesty and integrity and have not misrepresented, fabricated, or falsified any idea/data/fact/source in my submission. I understand that any violation of the above will lead to disciplinary action by the Institute and can also evoke penal action from the sources which have thus not been properly cited or from whom proper permission has not been taken when needed.

Signature

Name: Tanmay Kumar Poddar

(Roll No: 17330036)

Date:

CERTIFICATE

It is certified that the work contained in the thesis titled **“ Enlightening the Dark Universe Through Light Particles ”** by Mr. Tanmay Kumar Poddar (Roll No. 17330036), has been carried out under my supervision and that this work has not been submitted elsewhere for a degree.

Prof. Srubabati Goswami
Theoretical Physics Division,
Physical Research Laboratory,
Ahmedabad, India.

(Thesis Supervisor)

Date:

Acknowledgements

First and foremost, I would like to convey my profound gratitude and sincere thanks to my supervisor Prof. Srubabati Goswami for her continuous support, advice, and patience during my Ph.D. Her immense knowledge and expertise in academics have always inspired me to continue my research in high energy physics. I have learnt the time management skill and maintain a balance between academic and non-academic life from her. I am also thankful to her for giving me the freedom to do research in astroparticle physics as well. This thesis would not have been possible without her continuous support, encouragement, and motivation.

Besides my supervisor, I am very much grateful to one of my Doctoral Studies Committee (DSC) members, Prof. Subhendra Mohanty for his invaluable guidance, support, motivation, and collaboration during my Ph.D. life. I have learnt a lot from him during these five years. He was always there to listen to my personal and professional problems and I could not have imagined a humble, and simpler person than him. I have also learnt from him to stay calm in solving any type of problem in life.

I would also like to sincerely thank my other DSC members, Prof. Partha Konar, and Prof. Dibyendu Chakraborty for their insightful comments, suggestions, and discussions during my DSC seminars which always helped me to be on the right track of my Ph.D. I am also grateful to the other faculty members of the Theoretical Physics Division, Prof. Hiranmaya Mishra, Prof. Jitesh Bhatt, Prof. Namit Mahajan, Dr. Ketan Patel, Prof. Navinder Singh, Prof. Anjan Joshipura, Prof. Raghavan Rangarajan (now at Ahmedabad University), and Prof. Dilip Angom from whom I have learnt a lot through personal level discussions and also during several seminars and conferences. I would like to say thanks to all the faculty members who taught me during the Ph.D.course work.

I am very much grateful for the wonderful collaborations with Dr. Soumya Jana, Dr. Arindam Das, Dr. Vishnudath K.N., and Dr. K.N. Deepthi. I am also thankful to my seniors in the theory division, Dr. Kaustav Chakraborty, Dr. Priyank Parashari, Dr. Bhavesh Chauhan, Dr. Bharti Kindra, Dr. Arvind Kumar Mishra, Dr. Richa Arya, Dr. Aman Abhishek, Dr. Balbeer Singh, Dr. Samiran Roy, Dr. Sukannya Bhattacharya, Dr. Nimmala Narendra, Dr. Abhass Kumar, Dr. Abhijit Kumar Saha, Dr. Tripurari Srivastava, Dr. Ayon Patra, Dr. V.S. Prasannaa, Dr. Golam Sarwar, Dr. Debashis Saha, Dr. Rinku Maji, and Dr. V. Suryanarayana Mummidi with whom I have had fruitful and stimulating academic discussions.

I would like to express my special thanks of gratitude to all the staff members of the theory division, administration, library, computer centre, canteen, dispensary, workshop for their assistance and support. I would also like to acknowledge the academic and administrative staff members of PRL Ahmedabad, and IIT Gandhinagar for their help in registration and other paper works throughout my Ph.D.

I had a great time at PRL Navrangpura hostel and spent quality time with my friends and colleagues. I would like to mention Prithish, Ramanuj, and Sovan who were always there especially in my difficult times. I would also like to thank my friends and peers, Sarika, Anshika, Vishal, Satyajit, Hrushikesh, Rituparna, Ankit, Shivani, Alka, Milan, Tanu, Atif, Pravin, *Deepak, Sudipta, Sushant, Amit, Suraj, Sumeet, Komal, Gourav, Siddhartha, Arijit, Devaprasad, Bijoy, Jiban, Swagatika, Kimi, Ajayeta, Gurucharan, Sourabh, Chandrima, and Yogesh. Please forgive if I have missed someone and I am thankful to all of you. I am also grateful to Supriya and Debashish for the partial proofreading of my thesis. I am indebted to Akanksha for her immense care, encouragement, motivation, and support during my Ph.D.*

Last, but not least, I would like to pay my deepest gratitude to my parents and my sister for their unconditional love, support, and blessings throughout my life.

Tanmay Kumar Poddar

Abstract

The Standard Model (SM) of particle physics and Einstein's theory of General Relativity (GR) are the two most important theories that can explain the four fundamental forces governing the interactions between the particles in nature. Since, gravitational interaction is not quantized, it cannot be accomodated in the SM of particle physics that deals with strong, electromagnetic, and weak interactions. The classical GR theory explains the gravitational interaction between massive objects very well. In fact, these two theories can explain a wide range of observational and experimental results with a high level of accuracy. However, there are theoretical, and experimental motivations for studying physics Beyond Standard Model (BSM) of particle physics and physics beyond Einstein's GR theory. The most prominent BSM signatures are the existence of dark matter, neutrino mass, matter-antimatter asymmetry etc. There are motivations to go beyond Einstein's GR theory as well to explain phenomena such as the massive gravity theory, fifth force, singularity problem, dark energy etc.

In this thesis, we have studied light particles such as axions (spin-0), light gauge bosons (spin-1), massive gravitons (spin-2), and sterile neutrinos (spin-$1/2$) to explore the unknown dark sector of the universe such as dark matter, neutrino mass, massive gravity, and fifth force. We obtain bounds on the properties of these particles through orbital period loss of compact binary systems (Neutron Star-Neutron Star (NS-NS), Neutron Star-White Dwarf (NS-WD)), gravitational light bending, Shapiro time delay, perihelion precession test, and neutrino experiments.

If a compact star such as NS or WD is immersed in a low mass axionic potential then it can develop a long range axion hair outside of the compact star. Here, we have considered several compact binary systems like NS-NS and NS-WD and calculated the inverse of their orbital time period which is $\sim 10^{-19}$ eV or less. This mass range is in the ballpark of Fuzzy Dark Matter (FDM) which includes Axion Like Particles (ALPs). The orbital period loss of the compact binary systems is mainly due to the gravitational wave radiation. The orbital period can also decay due to the radiation of ultralight ALPs if its mass is smaller than the orbital frequency of the binary system. We consider four compact binary systems such as PSR J0348+0432, PSR J1738+0333, PSR J0737-3039, and PSR B1913+16. Comparing with the experimental data, we obtain bounds

on the axion decay constant $f_a \lesssim \mathcal{O}(10^{11}\ \mathrm{GeV})$ with axion mass $m_a \lesssim \mathcal{O}(10^{-19}\ \mathrm{eV})$. The result suggests that if ALPs are FDM, then they do not couple with quarks. If the NS is a pulsar, it can also emit electromagnetic radiation. The long range axion hair from a pulsar can change the polarization of the electromagnetic radiation which is called the birefringent effect. We calculate the birefringent angle due to the interaction of long range axions with the electromagnetic radiation as 0.42°. This value is within the accuracy of measuring the linear polarization angle of pulsar light. This value holds for the axions of mass $m_a < 10^{-11}$ eV which is constrained by the radius of the pulsar and axion decay constant $f_a \lesssim \mathcal{O}(10^{17}\ \mathrm{GeV})$ which is constrained by the requirement that the axions are sourced by pulsars. Like NS, WD, pulsars, the celestial objects like earth and Sun can also mediate long range axion hair outside of these massive bodies. The range of the axion mediated Yukawa type fifth force is constrained by the distance between earth and Sun which sets the upper bound on the axion mass $m_a \lesssim 10^{-18}$ eV. The contribution of axionic Yukawa potential is within the experimental uncertainties in the measurement of light bending and Shapiro time delay. We have calculated the amount of light bending and Shapiro time delay due to the axion emission and by comparing with the experimental data, we obtain bounds on axion decay constant. The Shapiro delay puts the stronger bound on axion decay constant as $f_a \lesssim 9.85\times 10^6$ GeV. The result also implies if ALPs are FDM, then they do not couple with quarks.

We have also attempted to probe gauged $U(1)_{L_i-L_j}$ scenario from orbital period loss of compact binary systems and perihelion precession of planets. Due to large chemical potential of degenerate electrons, the NS contains lots of muons and hence the compact binary systems can mediate gauged $U(1)_{L_\mu-L_\tau}$ force. The vector gauge bosons of $U(1)_{L_\mu-L_\tau}$ type can radiate from the binary systems and its contribution is within the experimental uncertainty in the measurement of orbital period loss of the compact binary systems. The mass of the gauge boson is constrained by the orbital frequency of the binary system and for the radiation of gauge bosons, the mass is restricted by $M_{Z'} < 10^{-19}$ eV. Comparing with the experimental data, we obtain a bound on $U(1)_{L_\mu-L_\tau}$ gauge coupling as $g < \mathcal{O}(10^{-20})$. Presence of electrons in the Sun and Planets is also responsible for the mediation of long range Yukawa $U(1)_{L_e-L_{\mu,\tau}}$ type of gauge force between the planets and the Sun. The mass of the $U(1)_{L_e-L_{\mu,\tau}}$ gauge boson is constrained by the distance between the Sun and the planets that puts the stronger bound on the gauge boson mass as $M_{Z'} < 10^{-19}$ eV. The contribution of $U(1)_{L_e-L_{\mu,\tau}}$ gauge bosons is within the experimental uncertainty in the measurement of the perihelion precession of planets. We calculate the perihelion precession of planets due to the mediation of $U(1)_{L_e-L_{\mu,\tau}}$ gauge bosons and by comparing with the experimental data, we obtained a bound on $U(1)_{L_e-L_{\mu,\tau}}$ gauge coupling as $g \lesssim \mathcal{O}(10^{-25})$. We find that the planet Mars puts the stronger bound on coupling.

Next, we have calculated the energy loss due to massless graviton radiation in Einstein's GR theory for a single graviton vertex process using Feynman diagram techniques. This gives the same result as one obtains from the quadrupole formula. Following the same technique, we have calculated the energy loss due to massive graviton radiaiton for several massive gravity theories such as Fierz-Pauli (FP) theory, Dvali-Gabadadze-Porrati (DGP) theory, and modified Fierz-Pauli theory. Theories of massive graviton has a peculiarity that at zero graviton mass limit, the massive graviton propagator does not go to the massless graviton propagator. This is called vanDAM-Veltman-Zakharov (vDVZ) discontinuity. We study the vDVZ discontinuity in these massive gravity theories. We also obtain bounds on the graviton mass in these massive theories from the binary pulsar timing.

Lastly, we analyze the effect of sterile neutrino on the effective Majorana mass ($m_{\beta\beta}$) governing neutrino-less double beta decay ($0\nu\beta\beta$) for Dark Large Mixing Angle (DLMA) solution. The later arises in presence of neutrino non standard interaction and admits a solution for the solar mixing angle $\theta_{12} > 45°$. We have checked that the MSW resonance in the sun can take place in the DLMA parameter space in the 3+1 scenario. Next, we investigate how the values of the solar mixing angle θ_{12} corresponding to the DLMA region alter the predictions of $m_{\beta\beta}$ by including a sterile neutrino in the analysis. We also compare our results with three generation cases for both standard large mixing angle (LMA) and DLMA. Additionally, we evaluate the discovery sensitivity of the future ^{136}Xe experiments in this context.

Keywords: Dark matter, Neutrino mass, Gravitational waves, Modified gravity, Fuzzy dark matter, Axions, ultralight Gauge bosons, Graviton, Sterile neutrino, neutrinoless double beta decay.

Contents

List of Figures

Chapter 1

Introduction

The proding curiosity to fully comprehend the universe has been prevailing since historic times. Several observations and experiments have confirmed the existence of four fundamental forces in nature. These are the gravitational force that acts between any two massive particles in the universe, the electromagnetic force which combines electricity and magnetism in the same framework, the weak nuclear force, which is responsible for β decay and the strong nuclear force, which is responsible for the nucleons to bind together. The fundamental forces of interactions are mediated by the exchange of particles which are called the gauge bosons. The gravitational interaction is mediated by spin-2 gauge boson, called graviton, the elctromagnetic interaction is mediated by spin-1 gauge boson which is called photon, the weak nuclear force is carried by spin-1 $W^{\pm}, Z^{0}$ gauge bosons and the strong nuclear force is carried by spin-1 gluons. Except for the graviton, all the other gauge bosons have been experimentally confirmed.

The standard model (SM) of particle physics is a very successful theory that explains the strong, electromagnetic, and weak interactions between particles. However, the gravitational interaction cannot be explained by SM. The prescription which can explain the gravitational interaction is Einstein's general relativity (GR) theory. It relates the curvature of the spacetime with the matter-energy density. Einstein's GR theory is a massless spin-2 graviton theory and there are lots of observations that validate Einstein's GR theory with great accuracy. Despite the tremendous success of SM in particle physics and GR theory, there are observations and experiments that motivate one to look beyond the standard picture. Also, the gravitational observations provide excellent appreciative checks to several particle physics models. Therefore, combined results of particle physics and gravity can serve as a unique probe to understand the physics beyond SM and Einstein's gravity.

In this introductory chapter, we first briefly discuss the standard model of particle physics and its shortcomings in Section 1.1. Next, we discuss Einstein's GR theory and its shortcomings in Section 1.2. After that, we give a brief introduction to the neutrino mass, neutrino oscillation, non-standard interaction, and neutrinoless double beta decay in Section 1.3. In Sections 1.4 and 1.5 we discuss salient features of the dark matter (DM) and the massive gravity theory respectively. We also explain the fifth force in Section 1.6. Finally, we discuss the thesis overview in Section 1.7.

1.1 The Standard Model and Its Shortcomings

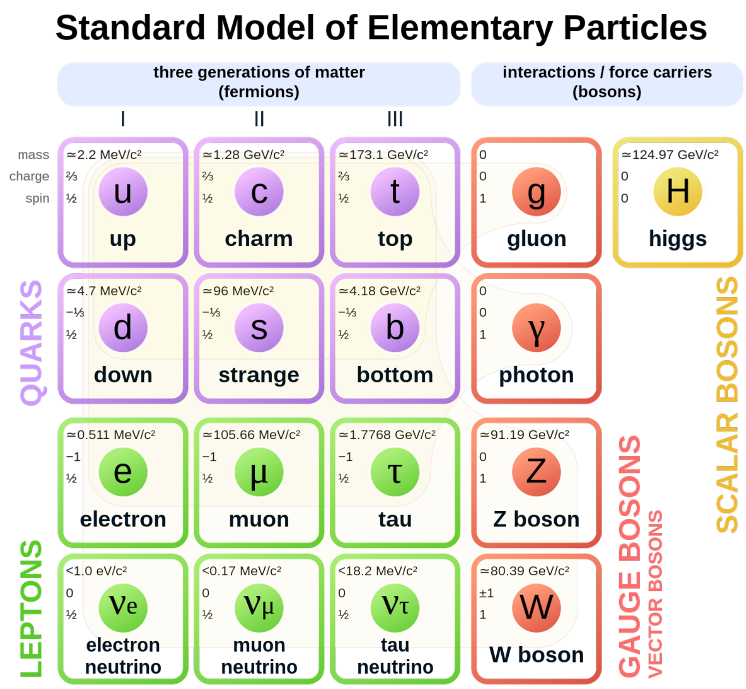

Figure 1.1: Standard Model of particle physics https://en.wikipedia.org/wiki/Standard_Model.

The SM of particle physics is a local gauge theory that is based on the symmetry group $SU(3)_c \times SU(2)_L \times U(1)_Y$, where c stands for a color quantum number, L

stands for left-handed fermions, transforming as a doublet under $SU(2)$, and Y stands for the hypercharge. Each generator of the gauge group corresponds to a gauge boson which acts as the mediator of the respective fundamental force. Figure 1.1 denotes the building block of the SM. The matter particles consist of quarks and leptons and each of them contains three generations. The fourth column denotes the gauge bosons of the three fundamental interactions. The last column stands for Higgs that gives mass to the matter particles except neutrino. The charge, mass, and spin of all those particles are given in the figure. The SM gauge group breaks into $SU(3)_c \times U(1)_Q$ (Q denotes the electromagnetic charge), when the Higgs boson gets the non-zero vacuum expectation value and the fermions, gauge bosons, and Higgs boson become massive. The photon, gluons, and neutrinos remain massless in SM. The discovery of the Higgs boson at the LHC in 2012 [1, 2] was considered the last missing piece in the SM theory. However, still, there are experimental evidences and theoretical motivations to look beyond the SM. In SM, neutrinos are massless, however, neutrino oscillation experiments have confirmed that neutrinos have mass. Also, the present energy density of the universe contains about 5% of visible matter, and the rest about 95% is unknown to us. Among the 95%, about 27% is dark matter (DM) and the remaining is dark energy [3]. Fig.1.2 illustrates the energy density of the universe contributed by visible matter, DM, and dark energy. Baryon asymmetry in the universe is another experimental motivation that require physics beyond the SM. There are other theoretical motivations for studying beyond standard model (BSM) physics such as gauge unification, hierarchy problem, presence of a large number of free parameters in SM, etc. Therefore, widening our perspective beyond SM theory is a necessity. This is done in two ways- either by enhancing just the particle content and/or extending the model by additional symmetry operations.

1.2 Einstein's General Theory of Relativity and Its Shortcomings

Einstein's GR theory is a theory of gravity that explains gravity is not a force but a mere geometry of spacetime. It connects the curvature of spacetime with matter and

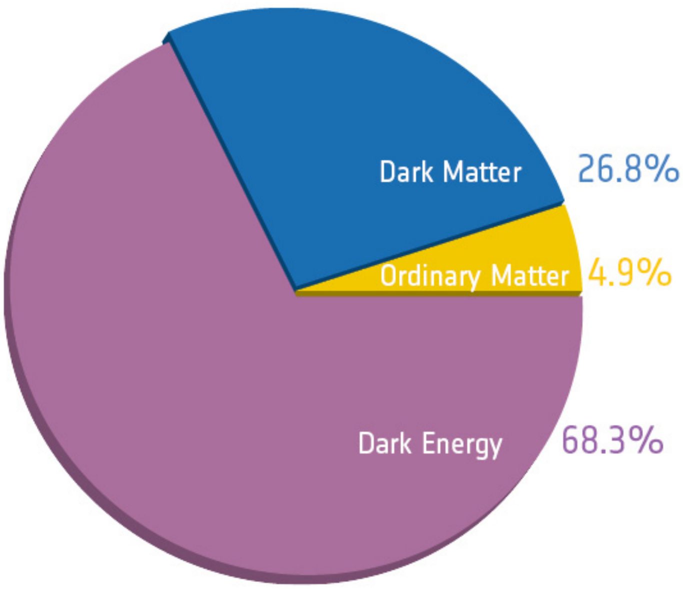

Figure 1.2: Energy density of the universe. https://nataliebhogg.com/research/.

radiation. Newton's theory of gravitational force cannot explain several observations like the orbital period loss of binary systems, perihelion precession of planet Mercury, the bending of light due to the presence of a massive object, the Shapiro time delay, etc. All these can be well explained by Einstein's GR theory. Also, the recent gravitational wave events such as GW150914 [4], and GW170817 [5] observed by LIGO and Virgo detectors validate Einstein's GR theory with great accuracy. However, there are theoretical and observational motivations such as singularity problem, dark matter, dark energy, etc. for which one can look beyond Einstein's GR theory. Also, the orbital period loss of the binary systems due to the GW radiation measured by pulsar timing arrays (PTAs) matches Einstein's GR theory with an uncertainty of $< 1\%$ [6, 7]. The perihelion precession measurements of Mercury planet by the MESSENGER mission [8, 9] match the GR result, however, it has $\mathcal{O}(10^{-3})$ uncertainty in the measurement. There are other tests of Einstein's GR theory like gravitational light bending, Shapiro time delay, etc. whose precision measurements by different observations open up a new way to study physics beyond the standard GR theory. Another motivation for studying beyond Einstein's theory is to realize a quantized version of gravity which helps to construct a mathematical framework to unify all four fundamental forces of nature. To resolve these shortcomings, one need to extend the standard GR theory. Such extensions include adding some new fields or the nonlinear terms, going to the higher dimensions etc.

In this thesis, we will try to encounter some of these shortcomings in particle physics and gravity sectors and enlighten the universe beyond the standard picture. We also highlight how the gravity sector can put complementary bounds on BSM physics. In the following, we discuss some of the beyond standard picture phenomena such as neutrino mass, dark matter, massive gravity theory, and fifth force in more detail.

1.3 Neutrino mass and Oscillation

Neutrino is an elementary spin-1/2 particle that does not carry any electric charge and belongs to the lepton family which obeys Fermi-Dirac statistics. In SM, neutrinos are massless. There are three flavors of neutrinos in SM corresponding to the charged leptons e^-, μ^-, and τ^-. These are called electron neutrino (ν_e), muon neutrino (ν_μ), and tau neutrino (ν_τ) respectively. They have also their anti-particles. Neutrinos are only taken part in weak interaction. Experiments by Wu [10] confirm that parity is violated in the weak interaction. The experiment by Goldhaber et al. [11] confirms that SM neutrinos are entirely left-handed.

However, several solar, atmospheric, reactor, and accelerator neutrino experiments [12–31] have confirmed that neutrinos oscillate among their flavor eigenstates. This phenomenon is called neutrino oscillation where the neutrino flavor eigenstates can be expressed as a linear superposition of the mass eigenstates (propagating eigenstates, where the Hamiltonian of the neutrino evolution equation is diagonalized) as

$$|\nu_l>=\sum_{\alpha=1}^{3}U_{l\alpha}|\nu_\alpha> \tag{1.1}$$

where $l=e,\mu,\tau$ denote the flavor eigenstates and $\alpha=1,2,3$ denote the mass eigenstates. The 3×3 unitary matrix U is called the Pontecorvo-Maki-Nakagawa-Sakata ($\mathrm{U}_{\mathrm{PMNS}}$) matrix which transforms the flavor eigenstates into mass eigenstates. Since the neutrino is electrically neutral, it can be its own antiparticle. In that case the neutrino is called a Majorana neutrino, otherwise, it is called a Dirac neutrino. If the neutrino is a Dirac particle, then $\mathrm{U_{PMNS}}$ contains three mixing angles and one Dirac CP (charge conjugation-parity) phase and if the neutrino is a Majorana particle, then $\mathrm{U_{PMNS}}$ contains three mixing angles, two Majorana phases, and one Dirac CP phase. One can parametrize the $\mathrm{U_{PMNS}}$ matrix as

$$\mathrm{U_{PMNS}} = \begin{bmatrix} c_{12}c_{13} & s_{12}c_{13} & s_{13}e^{-i\delta} \\ -c_{23}s_{12} - s_{23}s_{13}c_{12}e^{i\delta} & c_{23}c_{12} - s_{23}s_{13}s_{12}e^{i\delta} & s_{23}c_{13} \\ s_{23}s_{12} - c_{23}s_{13}c_{12}e^{i\delta} & -s_{23}c_{12} - c_{23}s_{13}s_{12}e^{i\delta} & c_{23}c_{13} \end{bmatrix} \mathrm{P}, \tag{1.2}$$

where $c_{ij} = \cos\theta_{ij}$, $s_{ij} = \sin\theta_{ij}$, and $P = \mathrm{diag}(1, \mathrm{e}^{\mathrm{i}\beta_2}, \mathrm{e}^{\mathrm{i}(\beta_3+\delta)})$ contains the Majorana phases. The Dirac CP phase is denoted by δ and the Majorana CP phases are β_2 and β_3. In vacuum, we can write the flavour transition probability as

$$\begin{aligned} P_{\nu_l\to\nu_m} = \delta_{lm} - 4\sum_{l>m} \mathrm{Re}(\mathrm{U^*_{l\alpha}U_{m\alpha}U_{l\beta}U^*_{m\beta}}) \sin^2\left(\frac{\Delta \mathrm{m}^2_{\alpha\beta}\mathrm{L}}{4\mathrm{E}}\right) \\ +2\sum_{l>m} \mathrm{Im}(\mathrm{U^*_{l\alpha}U_{m\alpha}U_{l\beta}U^*_{m\beta}}) \sin^2\left(\frac{\Delta \mathrm{m}^2_{\alpha\beta}\mathrm{L}}{2\mathrm{E}}\right), \end{aligned} \tag{1.3}$$

where L denotes the distance between the source and the detector and E denotes the energy of the neutrino. The oscillation probability is sensitive to $\Delta m^2_{\alpha\beta}$ and the mixing angles characterizing the $\mathrm{U_{PMNS}}$ matrix. The standard three generation picture of neutrino oscillation is well established and the oscillation parameters are being measured with increased precision. Such high precision experiments can also help in probing signatures of physics beyond SM, such as- neutrino mass ordering, sterile neutrino, non-standard interaction, CPT violation, long range forces, neutrino decay, etc. Apart from the above, there are other unknown issues in neutrino physics, such as the nature of neutrino: Dirac/Majorana, mechanism of neutrino mass generation, absolute neutrino mass, etc. In the following, we have discussed some of the signatures beyond the standard picture which would be relevant for this thesis.

1.3.1 Neutrino mass ordering

The oscillation probability of flavor transition changes due to charge current (ν_e) and neutral current $(\nu_e, \nu_\mu, \nu_\tau)$ interactions of neutrinos with the matter. This is called Mikhaev-Smirnov-Wolfenstein (MSW) effect. The matter effect of the solar neutrino oscillation confirms that $\Delta m^2_{21} > 0$. However, the mass squared difference (Δm^2_{31}

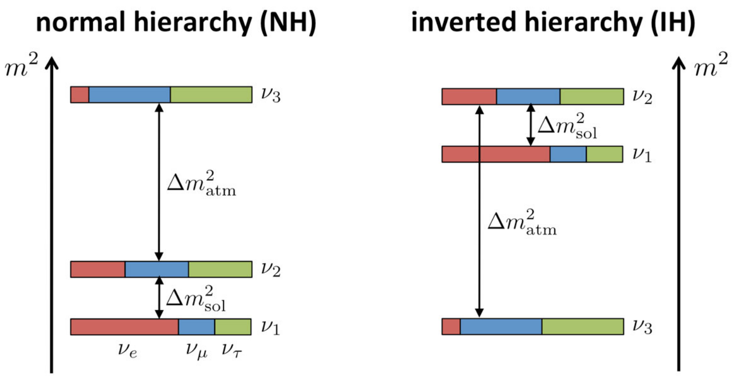

Figure 1.3: Neutrino mass ordering: Normal Hierarchy and Inverted Hierarchy https://neutrinos.fnal.gov/mysteries/mass-ordering/.

or Δm^2_{32}) observed by the atmospheric neutrino oscillation experiments are still unknown. This implies that there can be two possible hierarchies of the light neutrino mass eigenstates (Fig.1.3). They are normal hierarchy (NH) where,

$$m_1 < m_2 < m_3, \qquad \Delta m^2_{21} > 0, \qquad \Delta m^2_{31} > 0,$$
$$m_2 = \sqrt{m_1^2 + \Delta m^2_{21}}, \qquad m_3 = \sqrt{m_1^2 + \Delta m^2_{31}}, \tag{1.4}$$

and inverted hierarchy (IH) where,

$$m_3 < m_1 < m_2, \qquad \Delta m^2_{21} > 0, \qquad \Delta m^2_{32} < 0,$$
$$m_2 = \sqrt{m_3^2 + \Delta m^2_{23}}, \qquad m_1 = \sqrt{m_3^2 + \Delta m^2_{23} - \Delta m^2_{21}}. \tag{1.5}$$

The 3σ ranges of all the oscillation parameters are given in Chapter 5.

1.3.2 Non-Standard Interaction (NSI) of neutrinos and DLMA solution

The neutral current non-standard interaction (NSI) Lagrangian for neutrinos in matter is [32]

$$\mathcal{L}_{NSI} = -2\sqrt{2}G_F \epsilon^{fP}_{\alpha\beta}(\bar{\nu_\alpha}\gamma^\mu \nu_\beta)(\bar{f}\gamma_\mu P f), \tag{1.6}$$

where $P = L, R$ denotes the projection operator, f denotes the fermion, and $\epsilon^{fP}_{\alpha\beta}$ denotes the NSI parameters which characterizes the deviation of neutrino interaction from the standard picture. The neutral current NSI parameters affect the propagation of neutrinos through vector coupling with the matter. It is also well known that in the presence of non-standard interactions (NSI), solar neutrino data admits a new solution for $\theta_{12} > 45°$, known as the dark large mixing angle (DLMA) solution [32–34]. This is nearly a degenerate solution with $\Delta m^2_{21} \simeq 7.5 \times 10^{-5}$ eV^2 and $\sin^2\theta_{12} \simeq 0.7$. The DLMA parameter space was shown to be severely constrained by neutrino-nucleus scattering data from the COHERENT experiment [35]. However, the bound depends on the mass of the light mediator [36]. Thus if neutrinos have non-standard interactions (NSI) [34, 37], then there is a degeneracy in the solar neutrino solution corresponding to the solar mixing angle $> 45°$. This solution is called the dark large mixing angle (DLMA) solution.

1.3.3 Neutrinoless double beta decay $(0\nu\beta\beta)$

The transition probability for the neutrino oscillation does not tell anything about the nature of the neutrino, i.e; whether it is a Dirac particle or Majorana particle. Also, the oscillation experiments are insensitive to the absolute neutrino mass. The β decay experiments put bounds on the absolute neutrino mass [38–41], however, the stronger bound on the sum of the neutrino mass is obtained from cosmology which gives $\sum m_\nu < 0.12$ eV [3]. The nature of neutrinos is still unknown, i.e; whether it is a Dirac particle or Majorana particle. The neutrinoless double beta decay $(0\nu\beta\beta)$ is a direct experimental probe of this. It is a very rare process $(X^A_Z \rightarrow X^A_{Z+2} + 2e^-)$, where the lepton number is violated by two units which establish the Majorana nature of the neutrino [42, 43]. The rate of $(0\nu\beta\beta)$ process is given by

$$\frac{\Gamma_{0\nu\beta\beta}}{\ln 2} = G^{0\nu(Q,Z)}|M_\nu|^2\frac{|m_{\beta\beta}|^2}{m_e^2}, \tag{1.7}$$

where the phase space factor is denoted by $G^{0\nu}$. Z denotes the atomic number of the isotope, and $Q = M_i - M_f - 2m_e$. $M_{i,f}$ denote the mass of the initial and final nuclei and m_e denotes the mass of the electron. M_ν denotes the nuclear matrix element, and the effective Majorana mass is denoted by $m_{\beta\beta} = |\sum U^2_{ei}m_i|$. So, $0\nu\beta\beta$ is also sensitive to the absolute neutrino mass through the effective Majorana mass. The best limit of the half-life of $0\nu\beta\beta$ is obtained from the KamLAND-Zen experiment using

^{136}Xe and the lower bound of the half-life is $T_{1/2} > 1.07 \times 10^{26}$ years [44] which gives a bound on the effective Majorana mass as

$$m_{\beta\beta} \leq 0.061 - 0.165 \text{ eV}, \tag{1.8}$$

where the range corresponds to the uncertainty in the nuclear matrix elements.

1.4 Dark Matter

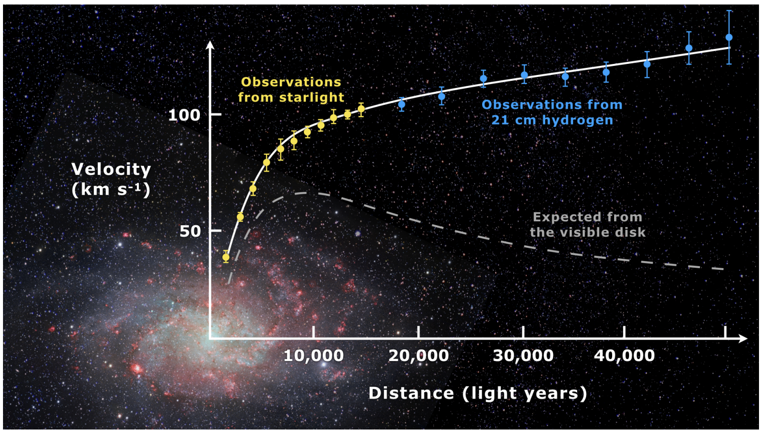

Figure 1.4: Galactic rotation curve of Messier 33 spiral galaxy. https://en.wikipedia.org/wiki/Galaxy_rotation_curve.

There is far more non-luminous matter in the universe than visible matter. This non-luminous matter is called dark matter which only has gravitational interaction. The existence of DM was first predicted by Fritz Zwicky in 1933 from the observation of the Coma cluster. Zwicky estimated the mass of the Coma cluster based on the motion of galaxies and compared it to an estimate based on the brightness and number of galaxies. He obtained 400 times more mass than that of visible matter. This is called the missing mass problem. Later in 1970, Vera Rubin observed several galaxies and plotted the rotation curve. The observation suggested that most of the mass of the galaxy is in the central hub and the stars are in the hand of the spiral galaxy. The stars can rotate around the central hub similar to the planets rotating around the Sun in the solar system. The centripetal force of the stars is balanced by the gravitational force for the rotation of the star which demands that the velocity of the star should decrease with distance. In practice, the velocity remains constant with distance after a certain galactic scale [45, 46]. This is called the galactic rotation curve which is shown in Fig.1.4. The mismatch between the expectation and observation implies that there is more non-luminous matter in the galaxy than luminous matter, and their distribution is more like a halo over the visible galaxy. Most of the DM in the universe is now non-relativistic and they are called cold dark matter (CDM). The velocity distribution of DM is Maxwellian. It was also observed by the Chandra X-ray observatory in 2006 through gravitational lensing that when two giant clusters were collided then there were more matter present than luminous matter. The luminous matter after collisions were diffused and were stuck together and heated up while the non-luminous matter was almost collisionless and surrounded the visible baryonic matter. In Fig.1.5

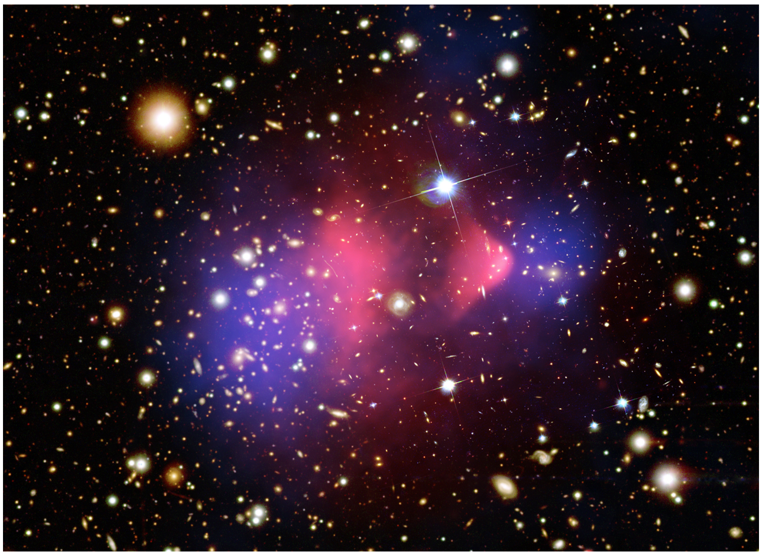

Figure 1.5: Bullet cluster observation `https://www.esa.int/ESA_Multimedia/Images/2007/07/The_Bullet_Cluster2`.

we have shown the X-ray map for the Bullet cluster from Chandra Observatory [47]. The red region corresponds to the luminous matter and the blue region corresponds to the non-luminous (dark) matter which has been confirmed from gravitational lensing. These observations are the evidence of DM at the galactic scale. At the cosmological scale, the evidence of DM can be explained by the temperature anisotropies in the cosmic microwave background radiation (the last scattering surface from which photons decouple from the thermal plasma when the temperature of the universe is about $3000\ \mathrm{K}$), angular power spectrum, and the large scale structure of the universe. Planck satellite estimates the energy budget of the universe as $\Omega_b = 0.0490 \pm 0.0003$,

$\Omega_{CDM} = 0.2607 \pm 0.002$, $\Omega_\Lambda = 0.6889 \pm 0.056$ at 68% C.L within the standard model of cosmology (also called the ΛCDM model) [3]. Here, b, CDM, and Λ denote the baryonic matter, Cold Dark Matter, and the dark energy respectively. A DM particle should be massive since it has only gravitational interaction. It does not interact with light and is hence non-luminous. The DM should be non-relativistic or cold to form structures in the universe and it should also be stable. The DM mass range can vary from a very few eV to several GeV. One of the promising candidates of DM is the weakly interacting massive particle (WIMP) which is theorized in supersymmetry (SUSY) theory [48]. There are many experiments that are trying to look for DM. Several direct detection experiments like CDMS [49], LUX [50], XENON [51], etc. where the DM can scatter with the SM particles and can produce signals in the detectors. There are other indirect detection experiments like PAMELA [52], Fermi-LAT [53], AMS-02 [54], etc. where the DM particles annihilate to produce SM particles, and collider experiments where SM particles collide to produce DM. None of the experiments have given any evidence for the existence of WIMP DM which put stringent constraints on DM mass > 1 GeV [50, 51, 55]. In Fig.1.6, we have shown the bounds of the WIMP-nucleon scattering cross section from direct detection experiments [56]. However, to evade the direct detection bounds, one can explore parameter spaces of

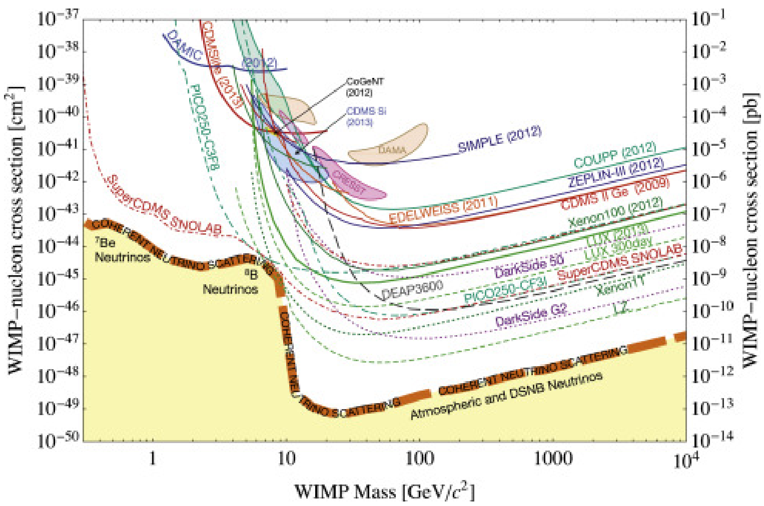

Figure 1.6: Bounds on WIMP nucleon scattering cross section from direct detection experiments.

DM candidates other than WIMPs and can construct alternative DM models such as feebly interacting massive particles (FIMPs) [57], strongly interacting massive particles (SIMPs) [58], fuzzy dark matter (FDM) [59], etc., where particles such as sterile neutrino [60], axions or axion like particles [61–63], ultralight particles [64–66] etc., can be the possible dark matter candidates [67]. Some compact objects like primordial black holes [68–70] can also be a candidate for dark matter. So far we have discussed the particle nature of DM. In the following, we discuss the alternative prescription of DM-modified gravity.

1.4.1 Gravity as a Dark Matter

It is still an open question whether the DM has a particle nature or it is a modification of gravity in the outer part of the galaxy. The alternative to the DM particle theory is the Modified Newtonian Dynamics (MOND) which is one of the modified gravity theories that alters Newton's law at the outer regions of the galaxy to explain the galactic rotation curve. The idea was first proposed by Mordehai Milgrom in 1983 [71]. Newton's law is well tested in the solar system or earth, however, in the outer part of the galaxy, where the acceleration is less, there can be a modification of Newton's law. This theory is an alternative to DM because it can fit the rotation curve very well, better than the DM model. According to Milgrom's law of MOND theory, either the gravitational force experienced by a star in the outer part of the galaxy is proportional to the square of its centripetal acceleration or Newton's second law of motion is proportional to the square of the acceleration in the low acceleration region. However, large scale observations like CMB, structure formation, etc. cannot be explained by MOND theory. The bullet cluster experiment strongly supports the particle nature of DM. A recent study has found some galaxies which consist of only baryonic matter and lack DM [72]. If MOND is a valid universal theory then it should be true for all the galaxies at all scales where we have a flat rotation curve. But observation of baryonic galaxies and hence a falling rotation curve strongly disfavors MOND theory. On the other hand, it is possible that some galaxies do not have DM because they gravitationally scatter off from the galaxy. However, there are theories that are trying to solve the large scale observations by modifying the MOND theory.

1.4.2 Small Scale Structure, Problems, and solutions

Another motivation for studying non-WIMP dark matter candidates is explaining the small scale structure problems [73, 74]. The evolution and present state of the universe can be well explained by the standard model of cosmology (ΛCDM) where the large scale structure ($\gtrsim 1$ Mpc) observations are fitted nicely. However, some of the small scale structure ($\sim$ galactic scale) problems like core-cusp problems, missing satellite problems, and too big to fail problems cannot be explained by this model [75].

At the galactic scale (below 1 kpc), observations predict a core like structure with a constant density however, the CDM simulations predict a cuspy nature of the DM density profile. This is called the core-cusp problem [76]. In Fig.1.7, it has been ob-

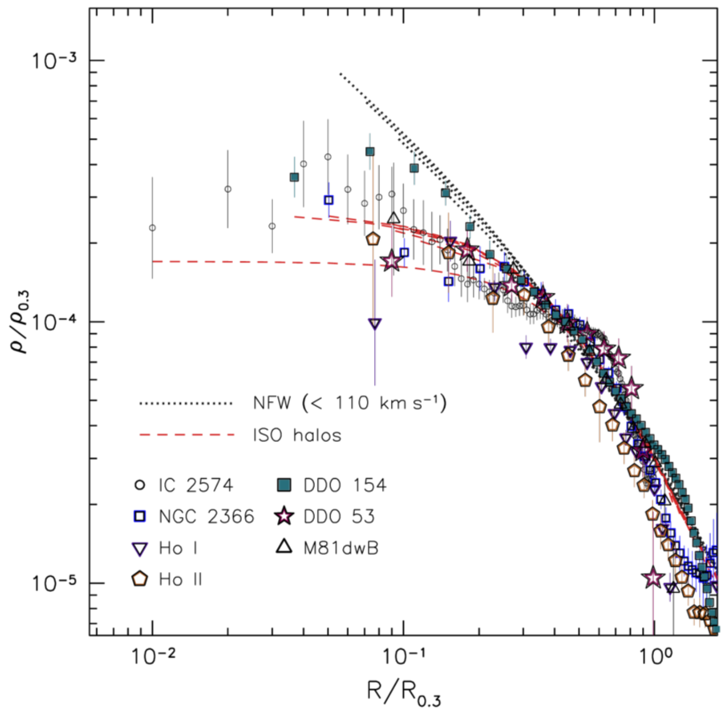

Figure 1.7: The core-cusp problem from the dwarf galaxy survey [76].

served from the dwarf galaxy survey that within one-third kiloparsec of the galaxy has a constant density core instead of a cuspy profile as predicted from CDM simulations. One solution to this problem is the baryonic feedback which can erase the cuspy density and results in central core structure in the inner part of the galaxy. The SIDM [77] or the FDM [59] models can also resolve these problems.

It was predicted from the CDM simulations that there are too many satellite galaxies with masses large enough to allow for galaxy formation ($> 10^7$ $\mathrm{M}_\odot$) than that observed in our Milky Way galaxy with masses as low as $300\ \mathrm{M}_\odot$ within $300\ \mathrm{kpc}$ [78]. This is called the missing satellite problem. As the galaxy can form due to the infall of the baryonic matter in the DM potential well, one solution to the missing satellite problem could be that the galaxy formation becomes extremely inefficient as the halo mass drops and the DM halos have failed to form galaxies. However, recent studies from the Sloan Digital Sky Survey (SDSS) with a corrected detection efficiency count an equal number of satellite galaxies that are predicted from the CDM simulations [79].

Another small scale structure problem is that the local universe contains fewer galaxies with large central densities (10^{10} $\mathrm{M}_\odot$) than expected from the CDM simulations [78]. The DM subhalos are too massive to have failed to form stars. This is called the too-big-to-fail problem. Possible solutions for this problem are alternative DM models like the Warm Dark Matter (WDM) model [80], Self Interacting Dark Matter (SIDM) model [77], and the FDM model. In the following, we particularly discuss the FDM model in some detail.

1.4.3 Fuzzy Dark Matter

Fuzzy dark matter (FDM) is one of the alternative DM models that can solve both the small scale structure problems of the universe and evade the direct detection bounds. In this thesis, we obtain bounds from several observations and experiments on axions and ultralight gauge bosons that are promising candidates of FDM. The very small mass ($10^{-21} - 10^{-22}\ \mathrm{eV}$) of the FDM candidate makes its de-Broglie wavelength of the size ($\sim 1\ \mathrm{kpc}$) of the dwarf galaxy. The ultralight axion like particles (ALPs) that arise due to string compactification [81] (detailed studies of axions and ALPs are discussed in Chapter 2) can be good candidates for FDM. The ALP DM which can erase the problems at small scale can be treated as a DM fluid. We can write the action for the ALP field (ϕ) as

$$S = \int d^4x\sqrt{-g}\Big[\frac{1}{2}g^{\mu\nu}\partial_\mu\phi\partial_\nu\phi - \frac{1}{2}m^2\phi^2\Big], \tag{1.9}$$

where $g_{\mu\nu}$ denotes the Friedman-Robertson-Walker (FRW) metric, and the last term is the mass term for the axion field. Solving the action, we will get the equation of motion

$$\ddot{\phi} + 3H\dot{\phi} - \frac{\nabla^2\phi}{a^2} + m^2\phi = 0, \tag{1.10}$$

where a denotes the scale factor, and H denotes the Hubble parameter of the axion field which at late time redshifts like a cold DM. The number density of such bosonic particles is very large and lots of such particles can stay in the same state. Hence, we can treat those particles as classical fields. Also one can calculate the matter power

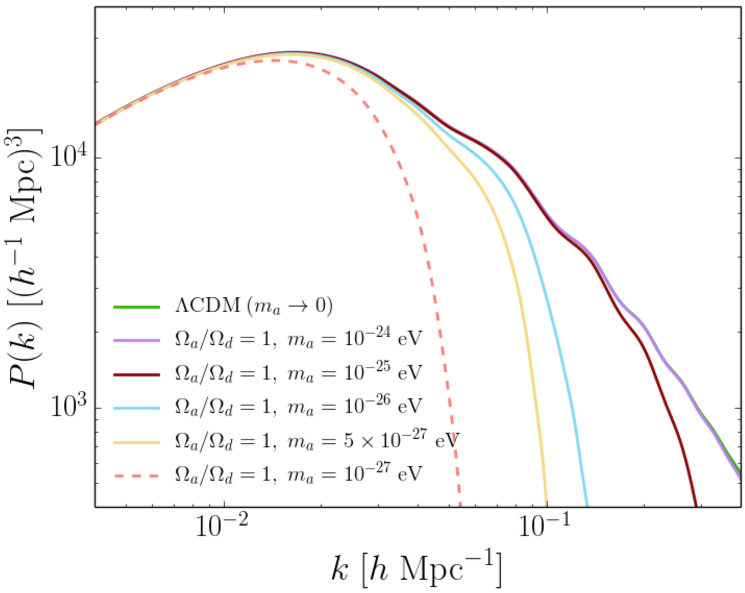

Figure 1.8: Variation of matter power spectrum with length scale for different ultra-light axion mass [82]. Ω_a denotes the axion relic density, Ω_d denotes the total dark matter density, and m_a denotes the axion mass.

spectrum for FDM particles and it has been observed that the power at the small length scale is suppressed as we decrease the FDM mass which is shown in Fig.1.8 [82]. It has also been checked that FDM with a lower mass satisfies the core-cusp problem in a better way which is shown in Fig. 1.9 [83]. However, there is a strong constraint on FDM mass $(m > 10^{-21}\ \mathrm{eV})$ from Lyman-α forest [84]. In Chapters 2 and 3 we have discussed the FDM model in more detail.

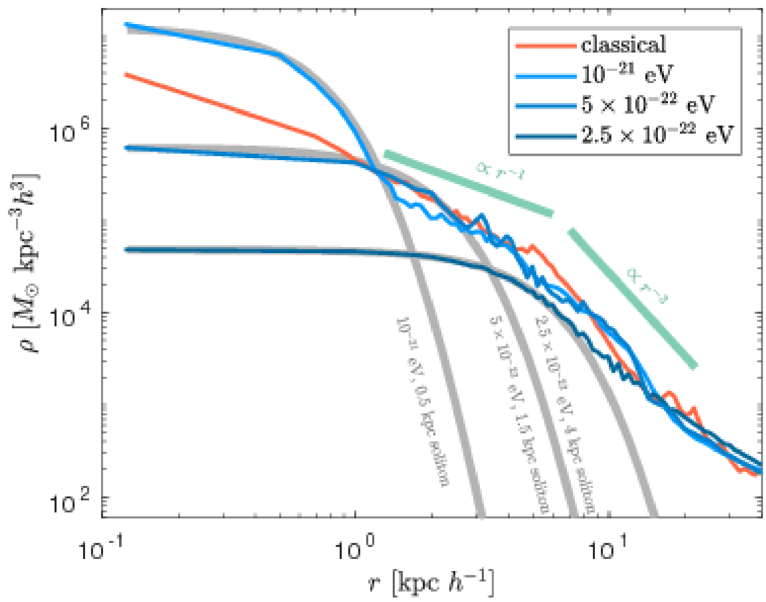

Figure 1.9: Dark matter density profile with radius [83] .

1.5 Massive Gravity Theory

The massive gravity theory is a modification of Einstein's GR theory where the mediator of the gravitational interaction, i.e; the spin-2 graviton takes a non zero mass. Einstein's GR theory which connects the curvature of spacetime with matter and radiation field contains two constants, the universal gravitational constant G and the cosmological constant Λ which is responsible for the accelerated expansion of the universe and is associated with the dark energy. It was earlier believed, that the sum of the zero point energy at every space time point results in the vacuum energy density. However, there is a strong disagreement $(60-120$ orders of magnitude) between the observed value of the vacuum energy density Λ and the theoretical large value of the quantum mechanical zero point energy. This is called the cosmological constant problem or vacuum catastrophe [85]. One of the motivations of studying massive gravity theories (such as bigravity theory) is that it gives natural solution to the cosmological constant problem and it does not require any dark energy for the accelerated expansion of the universe. Another motivation is to find an alternative to DM. Since, DM only has gravitational interaction, and since, we do not have any evidence of particle DM candidate till now, it is believed that modified gravity can explain the observations where DM is needed to explain those phenomena.

The graviton can be realized as the perturbations $(\kappa h_{\mu\nu})$ in the flat Minkowski spacetime background and we can use the linearized theory of Einstein's gravity in the limit $\kappa h_{\mu\nu} \ll 1$, where $\kappa = \sqrt{32\pi G}$. However, nonlinearities in GR come into play at different length scales. If we have a massive object of mass M then we can use the linearized gravity theory for the distance $r > R_s$, where R_s is the Schwarzschild radius. For Sun, the Schwarzschild radius is $3\,\mathrm{km}$ and Einstein's linear equation is applicable in the entire solar system. In the length scale $R_{\text{Planck}} < r < R_s$, classical non-linearities appear, where $R_{\text{Planck}} \sim 10^{-35}$ m is called the Planck scale. In this region, we can still ignore the quantum corrections. This region corresponds to the near black hole region. If $r < R_{\text{Planck}}$, then quantum corrections become important which corresponds to the region near the singularity. There exists another limit $r > r_V$ where perturbative theory is still valid, where r_V is called the Vainshtein radius (the minimum radius above which the linear approximation is valid). Physicists have started to construct massive theories of gravity since the twentieth century. A brief overview of massive gravity theories are discussed in [86] and in the references therein. The first massive gravity theory was proposed by Fierz and Pauli (FP) by considering massive graviton propagating in a flat spacetime [87]. However, this theory faced a serious problem because of the existence of pathological ghosts. There is another problem with building massive gravity theory which is popularly known as van-Dam-Veltman-Zakharov (vDVZ) discontinuity. The massive theory can go to the massless theory in the zero graviton mass limit in the action level, however, we cannot derive the massless theory from the massive theory in the zero graviton mass limit at the propagator level. This is simply because the massless graviton has two states of polarization whereas the massive graviton has five states of polarization. Basically, the scalar degree of freedom of the massive theory contributes to the vDVZ discontinuity. There were many models that were derived over the years to eliminate such loopholes which are Dvali Gabadadze Porrati (DGP) theory [88] which is a five dimensional theory, modified Fierz-Pauli theory where the ghosts cancel the scalar degrees of freedom etc. However, these theories either simultaneously do not solve the appearance of ghosts and vDVZ discontinuity, or there are certain assumptions. The work by Claudia deRham, Gabadadze and Tolley in 2010 can solve all of these problems in four and higher dimensions. This model is popularly called the dRGT model [89]. Other models of massive gravity theories like bimetric gravity [90] has its own importance in solving the cosmological constant problem. The speed of graviton in the massive gravity theories should be less than that of light. Different experiments have put bounds on the mass of graviton. GW170104 event puts the upper bound on graviton mass as 7.7×10^{-23} eV [91]. In Chapter 4, we have elaborately discussed the FP theory, DGP theory, and modified FP theory. We have also put bounds on the mass of the graviton in these massive gravity theories from the orbital period loss of binary systems.

1.6 Fifth Force

In nature, there are four observed fundamental forces or interactions, gravity, electromagnetic force, strong nuclear force, and weak nuclear force. However, there are theories and experiments which suggest a new kind of force coined as the fifth force. The first indication of the fifth force was in 1986 from the reanalysis of the Eötvös experiment of measuring accelaration of different composition of the earth [92]. Later other experiments have also suggested hints for the fifth force. However, till now there is no direct evidence of a fifth force. Recently in 2015, the ATOMKI group has claimed an existence of a new particle $X17$ which is a light boson of mass $17\ \mathrm{MeV}$ due to nuclear transition which can mediate a short range fifth force [93]. In 2021, Fermilab has also suggested the existence of a new force while measuring the muon $g-2$ [94]. The fifth force can be mediated by ultra-light scalar, or vector particles and it has a Yukawa behaviour. The deviation from the Newtonian inverse square law of force in any experiment suggests evidence for the presence of a fifth force. The fifth force is characterized by two parameters, its strength and its range. The strength of the fifth force is similar to or less than the gravitational force otherwise we would realize the force till now. The range of this new force can be as small as in millimetre scale or less or can be as large as the cosmological scale. The interesting feature of the fifth force is that it can interact with the dark sector viz, DM and dark energy. It is also believed that the missing mass problem of the universe is due to some fifth force. Also, the accelerated expansion of the universe could be due to the quintessence dark energy which can be a fifth force. Due to these several implications, physicists are now trying to hunt for this fifth force. There are several types of fifth forces, like long range, short range, composition dependent, composition independent. Another type of fifth force that can arise in extra-dimensional Kaluza-Klein theory, string theory, supergravity theory has a Yukawa behaviour. In Chapters 2 and 3 we have elaborately discussed the search for the long range fifth force from orbital period loss of binary systems, perihelion precession of planets, gravitational light bending, and Shapiro time delay which is mediated by either ultra-light axions or ultra-light gauge bosons.

1.7 Thesis Overview

In this thesis, we have considered axion (spin-0), light gauge boson (spin-1), massive graviton (spin- 2), and sterile neutrino (spin-$1/2$) and constrain the dark sector using these light particles. We have considered several laboratory and astrophysical observations, and experiments that can measure the orbital period loss of compact binary systems, perihelion precession of planets, birefringence effect, gravitational light bending, Shapiro time delay, and several neutrinoless double beta decay experiments. From such measurements, we obtain bounds on these light particles. Some of the bounds that we have discussed in this thesis are combined analyses from both gravity and particle physics sectors that are the complementary checks of several particle physics models. In the following, we summarize the content of each chapter.

- In Chapter 2, we have considered several compact binary systems like neutron star-neutron star (NS-NS) and neutron star-white dwarf (NS-WD) binary systems. The inverse of the orbital time period of these compact bianries is $\sim 10^{-19}$ eV or less. This mass range is in the ballpark of Fuzzy Dark Matter (FDM). It is observed that the orbital period decreases with time mainly due to the gravitational wave radiation. There is less than one per cent uncertainty in the measurement of orbital period loss of these binary systems. If the axion like particles (ALPs) have couplings with nucleons then the dipole radiation of ALPs can contribute to the orbital period loss within the experimental uncertainty. Comparing with the observational data, we obtain constraints on mass and couplings of ALPs. We find that these values do not satisfy the constraints coming from relic density, if ALPs are FDM. Thus we conclude that if ALPs are FDM then they do not couple with quarks.

If the NS is a pulsar, it can also emit electromagnetic radiation. The long range axion hair from pulsar can change the polarization of the electromagnetic radiation. This is called the birefringent effect. We have calculated the birefringent angle due to the interaction of long range axions with the electromagnetic radiation. Comparing with the experimental results, we obtain bounds on the axion parameters.

We have also discussed if celestial objects like the earth and the Sun contain lots of axions, their emission can contribute to the measurement of light bending and Shapiro time delay within the experimental uncertainty. We have calculated the amount of light bending and Shapiro time delay due to the axion emission and by comparing with the experimental data, we obtain bounds on axion mass and axion decay constant. The result also disfavors ALPs as FDM. The Shapiro time delay puts a stronger bound on the axion parameters than the gravitational light bending and orbital period loss.

- In Chapter 3, we obtain bounds for several particle physics models from the astronomical observations. we have attempted to probe gauged $L_\mu - L_\tau$ scenario from orbital period loss of binary systems. The NS contains lots of muons and hence, the binary systems can mediate gauged $L_\mu - L_\tau$ force. The vector gauge bosons of $L_\mu - L_\tau$ type can radiate from the binary systems and contribute to the orbital period loss within the experimental uncertainty. Comparing with the experimental data, we obtain a bound on $L_\mu - L_\tau$ gauge coupling. The mass of the gauge boson is constrained from the orbital frequency of the binary systems.

  We have also seen, due to the presence of electrons in the Sun and planets, long range $L_e - L_{\mu,\tau}$ type of gauge force can mediate between the planets and the Sun. The mediation of $L_e - L_{\mu,\tau}$ gauge bosons can contribute to the measurement of the perihelion precession of planets within the experimental uncertainty. We calculate the perihelion precession of planets due to the mediation of $L_e - L_{\mu,\tau}$

gauge bosons and by comparing with the experimental data, we obtained a bound on $L_e - L_{\mu,\tau}$ gauge coupling. The planet Mars puts the stronger bound on coupling.

- In Chapter 4, we have developed massive graviton theories from Feynman diagram techniques. we study the vanDAM-Veltman-Zakharov (vDVZ) discontinuity in Fierz-Pauli theory, Dvali-Gabadadze-Porrati theory, and modified Fierz-Pauli theory, and the presence of vDVZ discontinuity can be realized from the orbital period loss of compact binary systems. We have calculated the energy loss due to the massive graviton radiation in these three massive graviton theories. We also put bounds on the graviton mass in those theories from the binary pulsar timing.

- In Chapter 5, we have analyzed the effect of the Dark Large Mixing Angle (DLMA) solution on the effective Majorana mass $(m_{\beta\beta})$ governing neutrinoless double beta decay $(0\nu\beta\beta)$ in presence of a sterile neutrino. We consider the $3+1$ picture and check that the Mikheyev-Smirnov-Wolfenstein (MSW) resonance in the Sun can take place in the DLMA parameter space in this scenario. We have also investigated how the values of the solar mixing angle θ_{12} corresponding to the LMA and DLMA solutions alter the prediction of $m_{\beta\beta}$ in presence of a sterile neutrino. We also evaluate the discovery sensitivity of the future ^{136}Xe experiment in this context.

- Finally, in Chapter 6, we have summarized our conclusions and discussed the implications of the results obtained in this thesis.

Chapter 2

Axion (Spin 0): Dark Matter, Long Range Force, Precision tests of Einstein's General Relativity Theory, and its Searches

2.1 Introduction

Axion was first introduced to solve the strong CP problem [95–98]. The theory of strong interaction is governed by Quantum Chromodynamics (QCD) and we can write the QCD Lagrangian

$$\mathcal{L} = -\frac{1}{4}G^a_{\mu\nu}G^{a\mu\nu} + \sum_{i=1}^{n}[\bar{q}_i i\not{D} q_i - (m_i\bar{q}_i q_i + h.c)] + \theta\frac{g_s^2}{32\pi^2}G^a_{\mu\nu}\tilde{G}^{a\mu\nu}, \tag{2.1}$$

where the dual of the gluon field strength tensor is,

$$\tilde{G}^{\mu\nu} = \frac{1}{2}\epsilon^{\mu\nu\gamma\delta}G_{\gamma\delta}, \tag{2.2}$$

where $\epsilon^{\mu\nu\gamma\delta}$ denotes the four dimensional Levi-Civita symbol. The last term in the QCD Lagrangian violates the discrete symmetries P, T, and CP. Since all the quark masses are non-zero, the θ term in the Lagrangian must be present. The QCD depends on θ through some combination of parameters, $\bar{\theta} = \theta + \arg(\det(\mathcal{M}))$, where $\mathcal{M}$ is the quark mass matrix [99]. The most stringent probe of the strong CP violation is the electric dipole moment of the neutron. The neutron electric dipole moment (EDM) depends on $\bar{\theta}$ and from chiral perturbation theory, we can obtain the neutron EDM as $d_n \simeq 10^{-16}\bar{\theta}$ e.cm. However, the current experimental constraint on the neutron EDM is $d_n < 10^{-26}$ e.cm, which implies $\bar{\theta} \lesssim 10^{-10}$ [100]. The smallness of $\bar{\theta}$ is called the strong CP problem.

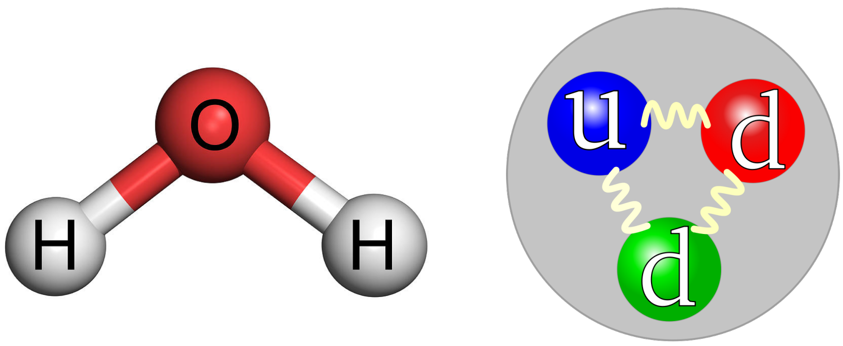

(a) Water molecule (b) Neutron

Figure 2.1: (a)Structure of a water molecule (https://www.sciencephoto.com/media/9556/view/water-molecule). (b) Quark content of neutron (http://www.sci-news.com/physics/article00400.html).

The dipole moment ($d = \sum_i q_i r_i$) is defined as the sum of the product of charges (q_i) and distances (r_i) of individual particles of a system. For example, the water molecule (H_2O) consists of two hydrogen atoms and one oxygen atom Fig.2.1(a). The size of an atom or molecule is roughly 10^{-8}cm. Hence, one can estimate the dipole moment of the water molecule as $d_{H_2O} = \sum_i q_i r_i \sim 10^{-8}$ e.cm which matches with the current experimental data [101]. Similarly, we can try to measure the dipole moment of the neutron classically. A neutron consists of three quarks, two down quarks and one up quark Fig.2.1(b). The up quark has the charge $+\frac{2}{3}e$ and the down quark has the charge $-\frac{1}{3}e$. The nuclear size is $\sim 10^{-13}$ cm. Hence, one can estimate the dipole moment of the neutron as $d_n \sim 10^{-13}\sqrt{1-\cos\theta}$ e.cm [102], where θ is the angle between the up and the down quark. The dipole moment of the neutron can be calculated from the Larmor precession. Neutrons with all spins pointing in the same direction can be placed in electric and magnetic fields where the electric and magnetic fields are parallel to each other. After some time, some of the neutrons will rotate along the direction of the field and the number can be calculated from the Larmor precessional frequency $f_1 \propto |\mu B + dE|$. In the next round, one can flip the direction of the magnetic field so that the electric and magnetic fields become antiparallel to each other. In this setup, the Larmor precessional frequency of the neutron becomes $f_2 \propto |\mu B - dE|$. Taking the difference between f_1 and f_2, one can calculate the dipole moment of the neutron. The recent best measured value of neutron electric dipole moment is $d_n < 10^{-26}$ e.cm [103–105] which implies $\theta < 10^{-13}$. Classically, the extremely small value of θ implies that all the three quarks are in a straight line. This is called the strong CP problem. There are two symmetry operations that can set the neutron electric dipole moment to zero. These are the parity (P) and the charge conjugation times parity (CP) symmetry or the time reversal symmetry (T) (CPT is good symmetry of nature). The P symmetry transforms $\vec{x} \to -\vec{x}$. Suppose the spin (s) and the dipole moment (d) of a neutron are parallel to each other. Under P operation, $s \to s$ and $d \to -d$. Hence, after the P operation, s and d are antiparallel to each other. Since, under P, the neutron will not loss its identity, so one way to make them equal is that $d = 0$ if parity is a good symmetry of nature. Similarly, under CP/T operation, the dipole moment remains the same whereas the spin vector flips its sign. From the same argument, $d = 0$ if CP is a good symmetry of nature. However, CP and P symmetries are badly broken in nature (P symmetry is badly broken by the weak interactions and CP symmetry is badly broken due to the CP violating phase ($\sim \pi/3$) in the Cabibbo-Kobayashi-Maskawa (CKM) matrix) and we cannot have zero dipole moment solution of the neutron from the symmetry solution. Another solution is if all the quark masses vanish which is not possible in SM. Hence, the remaining solution is the axion which can solve the strong CP problem. To solve this, Peccei and Quinn, in 1977 [95], came up with an idea that $\bar{\theta}$ is not just a parameter but it is a dynamical field driven to zero by its own classical potential. They postulated a global $U_{PQ}(1)$ quasi symmetry which is a symmetry at the classical level but explicitly broken by the non perturbative QCD effects which produces the θ term, and spontaneously broken at a scale f_a. Thus, the pseudo-Nambu-Goldstone bosons appear and these are known as

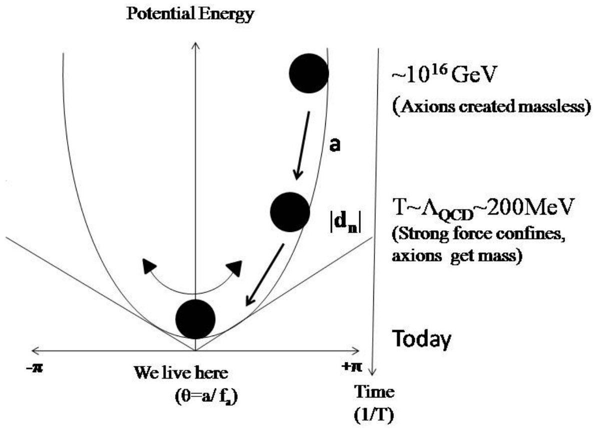

Figure 2.2: Variation of the axion potential and dipole moment with $\theta = \dfrac{a}{f_a}$

the axions. The strong force generates the generic axion potential as

$$V(a) \approx \frac{1}{2}\Lambda_{QCD}^4\Big[1 - \cos\Big(\frac{a}{f_a}\Big)\Big]. \tag{2.3}$$

The second derivative of Eq.2.3 yields the axion mass $m_a \sim \dfrac{\Lambda_{QCD}^2}{f_a} = \dfrac{m_\pi f_\pi}{f_a}$. Hence, $m_a = 5.7 \times 10^{-12}$ eV$\Big(\dfrac{10^{18}\ \text{GeV}}{\text{f}_\text{a}}\Big)$, where m_π is the pion mass and f_π is the pion decay constant. So if we need axion decay constant less than the Planck scale (M_{pl}) then the mass of the axion is $m_a \gtrsim 10^{-12}$ eV [106]. In Fig.2.2, we have shown the variation of the axion potential and the neutron dipole moment with $\theta = \dfrac{a}{f_a}$. The θ can take values from $-\pi$ to $+\pi$. At the very early universe ($\sim 10^{16}$ GeV), the axions are created massless due to global $U(1)_{PQ}$ symmetry breaking. As the universe expands, the temperature drops and at $T \sim \Lambda_{QCD}$, the strong force confines and the axion get mass due to non perturbative QCD effects. As the axions become massive, it rolls down to the bottom of the potential and subsequently today the dipole moment of the neutron becomes zero.

Also, there are other pseudo scalar particles that are not the actual QCD axions, but these particles have many similar properties to the QCD axions. These are called axion like particles (ALPs). For ALPs, the mass and decay constant are independent of each other. These ALPs are motivated by the string theory [81]. The interaction of

ALPs with the standard model particles is governed by the Lagrangian [107]

$$\mathcal{L} = \frac{1}{2}\partial_\mu a \partial^\mu a - \frac{\alpha_s}{8\pi} g_{ag} \frac{a}{f_a} G_a^{\mu\nu} \tilde{G}^a_{\mu\nu} - \frac{\alpha}{8\pi} g_{a\gamma} \frac{a}{f_a} F^{\mu\nu} \tilde{F}_{\mu\nu} + \frac{1}{2}\frac{1}{f_a} g_{af} \partial_\mu a \bar{f} \gamma^\mu \gamma_5 f, \quad (2.4)$$

where g's are the coupling constants which depend on the model. The first term is the dynamical term of ALPs. The second, third, and last terms denote the coupling of ALPs with the gluons, photons, and fermion fields respectively. ALPs couple with the SM particles very weakly because the couplings are suppressed by $\frac{1}{f_a}$, where f_a is called the axion decay constant and for ALPs, it generally takes larger value.

The axions or ALPs can also couple with the nucleons or quarks through the electric and magnetic dipole moment operators described by the terms $g_{EDM} a \bar{N} \sigma_{\mu\nu} \gamma_5 N F^{\mu\nu}$ and $g_{MDM} a \bar{N} \sigma_{\mu\nu} N F^{\mu\nu}$ respectively.

ALPs are pseudo-Nambu Goldstone bosons which have a spin-dependent coupling with nucleons so that, in an unpolarized macroscopic body, there is no net long range field for ALPs outside the body. However, if the ALPs also have a CP violating coupling, then they can mediate long range forces even in unpolarized bodies [108, 109].

Besides solving the strong CP problem, the axion can be a good candidate of dark matter. Explaining the nature of dark matter and dark energy is a major unsolved problem in modern cosmology. An interesting dark matter model is the fuzzy dark matter (FDM)[59, 64]. The FDM is axion like particles (ALPs) with mass$(10^{-21}\ \mathrm{eV} - 10^{-22}\ \mathrm{eV})$ such that the associated de Broglie wavelength is comparable to the size of the dwarf galaxy $(\sim 2\ \mathrm{kpc})$. Axions and ALPs can be possible dark matter candidates [61] or can be dynamical dark energy [110]. Axions can also form clouds around black hole or neutron star from superradiance instabilities and change the mass and spin of the star [111, 112]. Cold FDM can be produced by an initial vacuum misalignment and, to have the correct relic dark matter density, the axion decay constant should be $f_a \sim 10^{17}$ GeV [64]. This ultra light FDM can solve the small scale structure problems of the universe [61, 113–115].

In the beginning of the universe, we can write the action of the dynamical axion field as

$$S = \int d^4x \sqrt{-g}\mathcal{L} = \int d^4x \sqrt{-g}\Big[\frac{1}{2}\partial_\mu a \partial^\mu a - V\Big(\frac{a}{f_a}\Big)\Big], \quad (2.5)$$

where $g = \det(g_{\mu\nu})$ is the determinant of the metric and the axion field evolves with a periodic potential

$$V\left(\frac{a}{f_a}\right) = m_a^2 f_a^2 \left[1 - \cos\left(\frac{a}{f_a}\right)\right]. \tag{2.6}$$

Using Eq.(2.6), we can solve the action Eq.(2.5) to obtain the equation of motion of the axion field in Friedman-Robertson-Walker (FRW) spacetime in Fourier space as

$$\ddot{a_k} + 3H\dot{a_k} + \frac{k^2}{R^2}a_k + m_a^2 a_k = 0, \tag{2.7}$$

where H is the Hubble parameter, $R(t)$ is the scale factor in FRW spacetime. In Fourier space, all the modes decouple and for non relativistic or zero modes, we can omit the third term in Eq.(2.7). Hence, the axionic field has a damped harmonic oscillatory solution. If $H \gtrsim m_a$, then the axion field takes a constant value $a_0 = \theta_0 f_a$ which fixes the initial misalignment angle θ_0. After that, the axion starts oscillating with a frequency $\sim m_a$. The oscillation starts at $H \sim m_a$ and the energy density of the axion field is damped as $\frac{1}{R^3}$. Hence, at the late time the axion field varies as $a \propto T^{\frac{3}{2}} \cos(m_a t)$, where $T = \frac{1}{R}$ is the temperature of the universe at that epoch and the axion field energy density redshifts like a cold dark matter. If $T_{\rm osc}$ is the temperature at which the oscillation starts and $H \sim m_a$ then [64]

$$\frac{T_{\rm osc}^2}{M_{pl}} = m_a, \tag{2.8}$$

where $M_{pl} = 2.435 \times 10^{18}$ GeV is the Planck mass. At this oscillation temperature $T_{\rm osc}$, the radiation energy density is of order $T_{\rm osc}^4$ and the matter energy density is of order $m_a^2 a_0^2$. With the expansion of the universe, the ratio of the energy densities of dark matter and radiation increases as $\frac{1}{T}(\propto R)$ and at $T' \sim 1$ eV, the two energy densities are supposed to be equal and the universe becomes matter dominated. Hence,

$$\frac{m_a^2 a_0^2 T_{\rm osc}}{T_{\rm osc}^4 T'} \sim 1. \tag{2.9}$$

Using Eq.(2.8) in Eq.(2.9), we obtain the initial axion field as

$$a_0 \sim \frac{M_{pl}^{\frac{3}{4}} T'^{\frac{1}{2}}}{m_a^{\frac{1}{4}}} \sim 0.5 \times 10^{17} \text{ GeV}, \tag{2.10}$$

with $m_a = 10^{-22}$eV. Hence, the axionic FDM relic density (normalized by the critical density) becomes

$$\Omega_{FDM} h^2 \sim 0.12 \left(\frac{a_0}{10^{17} \text{ GeV}}\right)^2 \left(\frac{m_a}{10^{-22} \text{ eV}}\right)^{\frac{1}{2}}. \tag{2.11}$$

For ALPs of mass $m_a = 10^{-22}$ eV, the oscillation temperature becomes $T_{\rm osc} \sim 500$ eV (using Eq.(2.8)). The temperature is after nucleosynthesis which is roughly at 1MeV. So at this temperature, the radiation is the dominant one and the axion energy density is the subdominant one oscillating in the background. This axion oscillation starts dominating at $T_{\rm osc} \sim 500$ eV. Hence, this type of dark matter is a late appearance of dark matter and at this temperature, the coherent oscillation of dark matter starts. The initial misalignment angle can take values from $-\pi$ to $+\pi$. The coupling of ALPs with matter is proportional to $\frac{1}{f_a}$. Hence, large values of f_a correspond to the weaker coupling of axions with the matter. Any value of f_a other than 10^{17} GeV requires fine tuning of θ_0 which can take values $-\pi < \theta_0 < \pi$.

The axion field can oscillate with time as $a(t) \sim \frac{\sqrt{2\rho_{DM}}}{m_a}\sin(m_a t)$, where ρ_{DM} is the dark matter energy density. Axion can also form topological defects like cosmic strings and domain walls [116–118]. They can also behave as dark radiation [119–124].

Strong dipolar magnetic field induces **E**.**B** density outside a pulsar which can also be a source of pseudoscalar axion and can rotate the polarization vector of the electromagnetic radiation [125]. There can also be a galactic axion dark matter background which can rotate the polarization of the pulsar light [126]. The ALP dark matter background also rotates the CMB modes which constrain the mass of the axion and axion photon coupling constant [127]. There is also a study where photon can change its polarization when it passes through neutrino gas [128]. Axions can also be probed from superradiance phenomena in a polarimetric measurement for a black hole [129, 130]. Constraints on the rotation of the polarization angle can also be obtained from the protoplanetary disk polarimetry [131], the active galactic nuclei [132], and quasar polarization [133].

There is no direct evidence of axions in the universe. However, there are lots of experimental and astrophysical bounds on axion parameters. There are some ongoing searches for solar axions which correspond to $f_a \sim 10^7$ GeV having sub-eV masses [134, 135]. If solar axions were there, then from the supernova 1987A result we obtain $f_a \gtrsim 10^9$ GeV. Axions with $f_a \lesssim 10^8$ GeV provide the component of hot dark matter[136–138]. Large value of f_a is allowed in the anthropic axion window and can be studied by isocurvature fluctuations [139]. The laboratory bounds for the axions are discussed in [140–147]. The cosmological bounds for the cold axions are produced by the vacuum realignment mechanism are discussed in[148, 149]. The bounds on axion mass and decay constant are discussed in [150–152], if cold axions are produced by the decay of axion strings.

There are a few experiments like ABRACADABRA [153, 154], CASPEr [155–158], GNOME [159–161] which are looking for axions using magnetometers [162]. Storage rings can also be used for the detection of axions [163]. Constraints on axion mediated force from torsion pendulum experiment is discussed in [164].

This chapter is organized as follows. In Section2.2, we discuss the constraints on ultralight axions from indirect evidence of gravitational waves by calculating the orbital period loss of compact binary systems due to the quadrupole radiation of gravitational waves and the Larmor radiation of axions. This is based on [62]. In Section2.3, we discuss the constraints on ultralight axions from birefringence effect of pulsars by calculating the birefringent angle due to the interaction of axions with photons which is based on the work discussed in [165]. In Section2.4 we discuss the constraints on ultralight axions from gravitational light bending and Shapiro time delay by calculating the light bending and time delay in presence of axion field which is based on [63]. Finally, in Section 2.5, we conclude the chapter with the important results.

2.2 Constraints on Ultralight Axions from the Indirect Evidence of Gravitational Waves

It has been observed by Hulse and Taylor that the orbital period loss of the compact binary system (consists of one pulsar and one neutron star) decreases over a long period of time which is the indirect evidence of gravitational waves emission. The pulsar can behave as an atomic clock and the radio antennas on the earth can collect the signal emitted from the Hulse-Taylor (HT) binary system at regular intervals. Fig.2.3(a) denotes the pictorial representation of Hulse Taylor binary system and the orbital period loss diagram is shown in Fig.2.3(b).

If there is no gravitational wave emission then the orbital period of the binary

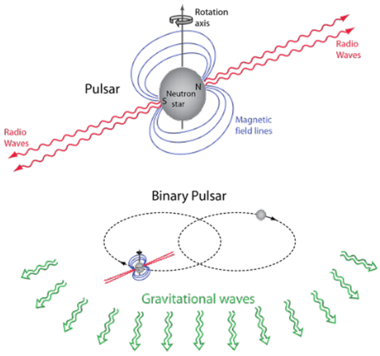

(a) Hulse Taylor binary system

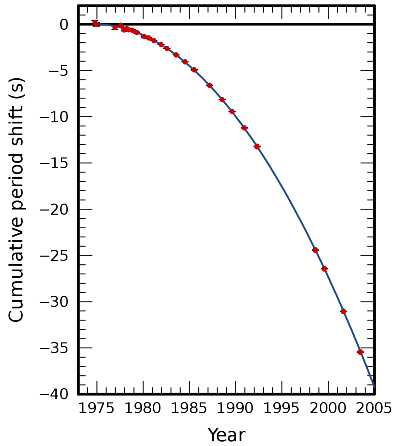

(b) orbital period loss

Figure 2.3: (a)Hulse-Taylor binary system consists of one neutron star and one pulsar (http://hyperphysics.phy-astr.gsu.edu/hbase/Astro/pulsrel.html). (b) Orbital period loss of the HT binary system. The straight line parallel to time axis defines that there is no GW emission or orbital period loss (https://en.wikipedia.org/wiki/Hulse-Taylor_binary).

system would remain constant. However, experimentally it was found that the orbital period decays over a large period of time and for this discovery, Hulse and Taylor won the Noble prize (1993). Although the first direct evidence of gravitational wave was confirmed from the event GW150914 (2015) which was a merger event of two stellar mass black holes. The quadrupole formula for the gravitational wave radiation is

$$P = \frac{G}{5}\left(\frac{d^3Q_{ij}}{dt^3}\frac{d^3Q_{ij}}{dt^3} - \frac{1}{3}\frac{d^3Q_{ii}}{dt^3}\frac{d^3Q_{jj}}{dt^3}\right), \tag{2.12}$$

where P stands for emitted power for the GW radiation, G denotes the Newton's universal gravitational constant, and Q_{ij} stands for the quadrupole moment of the GW radiation field. In 1963, Peters and Mathews calculated the energy loss for arbitrary eccentric Keplerian orbit as

$$\frac{dE}{dt} = \frac{32G}{5}\Omega^6\left(\frac{m_1m_2}{m_1+m_2}\right)^2 a^4(1-e^2)^{-7/2}\left(1+\frac{73}{24}e^2+\frac{37}{96}e^4\right), \tag{2.13}$$

where m_1 and m_2 denote the masses of the two stars in the binary system, Ω is the orbital frequency, and a denotes the semi major axis of the elliptic orbit with e as the eccentricity. The orbital period loss is related with the energy loss as

$$\dot{P}_b = 6\pi G^{-\frac{3}{2}}(m_1 m_2)^{-1}(m_1+m_2)^{-\frac{1}{2}}a^{\frac{5}{2}}\left(\frac{dE}{dt}\right). \tag{2.14}$$

The orbital period loss for the HT binary system from general relativistic (GR) calculation is $\dot{P}_{b\mathrm{GR}} = -2.4025 \times 10^{-12}\ \mathrm{s\,s^{-1}}$ whereas $\dot{P}_{b\mathrm{observed}} = -2.4225 \times 10^{-12}\mathrm{s\,s^{-1}}$ [6, 166]. The observed orbital period loss value matches quite well with the GR predicted value. This is an indirect evidence of GW. However, there is less than 1% uncertainty in the measurement. The orbital period of the HT binary system is ~ 8 h and the corresponding frequency is 10^{-19} eV which is in the ballpark of fuzzy dark matter. Hence, particles with this small mass or even less can emit from the binary systems and contribute to the orbital period loss within the experimental uncertainty limit.

It has been pointed out recently [167] that if a compact star is immersed in an axionic potential (which will take place if the ALPs are FDM candidates), a long range field is developed outside the star.

The ALPs can be sourced by compact binary systems such as neutron star-neutron star (NS-NS), neutron star-white dwarf (NS-WD), and can have very small mass ($< 10^{-19}$ eV). They can be possible candidates of FDM. The FDM density arises from a coherent oscillation of an axionic field in free space. If such axionic FDM particles have a coupling with nucleons, then the compact objects (NS, WD) immersed in the dark matter potential develop a long range axionic hair. When such compact stars are in a binary orbit, they can lose the orbital period by radiating the axion hair in addition to the gravitational wave[167, 168].

2.2.1 The Long Range Axion Profile

Effective Potential of Axion in Vacuum

The interaction of axion with other standard model particles below the Peccei Quinn (PQ) and electroweak (EW) symmetry breaking scales is governed by the Lagrangian [106]

$$\mathcal{L} = \frac{1}{2}\partial_\mu a \partial^\mu a + \frac{a}{f_a}\frac{\alpha_s}{8\pi}G_{\mu\nu}\tilde{G}^{\mu\nu} + \frac{1}{4}a g^0_{a\gamma\gamma}F_{\mu\nu}\tilde{F}^{\mu\nu} + \frac{\partial_\mu a}{2f_a}j^\mu_{a,0}, \tag{2.15}$$

where the kinetic term of the axion field is denoted by the first term, the coupling of axion with the gluon field is denoted by the second term, the third term denotes the axion field couples with the photon field and the last term denotes the derivative coupling of axion field with the quark field q through an axial vector current $j^{\mu}_{a,0} = g^0_q \bar{q}\gamma^{\mu}\gamma_5 q$. The axion photon coupling is defined as $g^0_{a\gamma\gamma} = \frac{\alpha}{2\pi f_a}\frac{E}{N}$, where α is the electromagnetic fine structure constant, E/N is the ratio of the electromagnetic to the color anomaly. Note, the coupling of axion with the other standard model fields are inversely proportional to f_a.

We can give a chiral rotation to the quark field $q \to e^{i\gamma_5 \frac{a}{f_a} Q_a} q$ so that derivative coupling disappears from the quark mass term, where $q = (u, d)$, and $\mathrm{trQ_a} = 1$. Hence Eq. (2.15) becomes

$$\mathcal{L} = \frac{1}{2}\partial_{\mu}a\partial^{\mu}a + \frac{1}{4}a g_{a\gamma\gamma}F_{\mu\nu}\tilde{F}^{\mu\nu} + \frac{\partial_{\mu}a}{2f_a}j^{\mu}_a - \bar{q}_L M_a q_R + \mathrm{h.c.} \tag{2.16}$$

The new axion photon coupling constant becomes

$$g_{a\gamma\gamma} = \frac{\alpha}{2\pi f_a}\Big[\frac{E}{N} - 6\mathrm{tr}(\mathrm{Q_a Q^2})\Big], \tag{2.17}$$

and the axial current density is

$$j^{\mu}_a = j^{\mu}_{a,0} - \bar{q}\gamma^{\mu}\gamma_5 Q_a q. \tag{2.18}$$

The quark mass matrix in the new mass basis becomes

$$M_a = e^{i\frac{a}{f_a}Q_a} M_q e^{i\frac{a}{f_a}Q_a}, \tag{2.19}$$

where $M_q = \begin{bmatrix} m_u & 0 \\ 0 & m_d \end{bmatrix}$, and $Q = \begin{bmatrix} \frac{2}{3} & 0 \\ 0 & -\frac{1}{3} \end{bmatrix}$, m_u and m_d are the masses of the up and down quarks respectively.

Such chiral transformation of the quark field helps to move all the non derivative coupling into the two lightest quarks. Hence, we can integrate out all the other quarks and can work in the two flavour effective theory. M_a contains non derivative couplings on the axions. So in the chiral expansion at the leading order, all the non derivative couplings of axions is contained in the pion mass term of the Lagrangian

$$\mathcal{L}_{\pi} \supset 2B_0\frac{f_{\pi}^2}{4} < UM_a^{\dagger} + M_a U^{\dagger} >, \tag{2.20}$$

where

$$U = e^{\frac{i\Pi}{f_\pi}}, \quad \Pi = \begin{bmatrix} \pi^0 & \sqrt{2}\pi^+ \\ \sqrt{2}\pi^- & -\pi^0 \end{bmatrix}. \tag{2.21}$$

Here f_π is the pion decay constant and, B_0 is related to the chiral condensate. To derive the effective axion potential to the leading order, we only consider the neutral pion sector. Choosing Q_a proportional to the identity matrix, we can write

$$V(a,\pi^0) = -B_0 f_\pi^2 \Big[m_u \cos\left(\frac{\pi^0}{f_a} - \frac{a}{2f_a}\right) + m_d \cos\left(\frac{\pi^0}{f_a} + \frac{a}{2f_a}\right)\Big], \tag{2.22}$$

or,

$$V(a,\pi^0) = -m_\pi^2 f_\pi^2 \sqrt{1 - \frac{4m_u m_d}{(m_u+m_d)^2}\sin^2\left(\frac{a}{2f_a}\right)} \cos\left(\frac{\pi^0}{f_\pi} - \phi_a\right), \tag{2.23}$$

where

$$\tan\phi_a = \frac{m_u - m_d}{m_u + m_d}\tan\left(\frac{a}{2f_a}\right), \tag{2.24}$$

where m_π is the pion mass. On the vacuum, the neutral pion gets a vev and trivially be integrated out. Hence, the effective axion potential becomes

$$V \approx -m_\pi^2 f_\pi^2 \sqrt{1 - \frac{4m_u m_d}{(m_u+m_d)^2}\sin^2\left(\frac{a}{2f_a}\right)}. \tag{2.25}$$

The minimum of the potential is at $< a >= 0$ *i.e;* $\bar{\theta} = 0$ and solves the strong CP problem. The second derivative of the potential gives the axion mass

$$m_a^2 = \frac{m_u m_d}{(m_u+m_d)^2}\frac{m_\pi^2 f_\pi^2}{f_a^2}. \tag{2.26}$$

We want to probe the axions whose mass is lighter than that obtained from Eq. (2.25) by a factor of $\sqrt{\epsilon}$ and we consider the parameter space $\epsilon \lesssim 0.1$. For these axions, the potential becomes

$$V \approx -\epsilon m_\pi^2 f_\pi^2 \sqrt{1 - \frac{4m_u m_d}{(m_u+m_d)^2}\sin^2\left(\frac{a}{2f_a}\right)}, \tag{2.27}$$

and consequently in the $m_u = m_d$ limit, the mass of the axion becomes

$$m_a = \frac{m_\pi f_\pi}{2f_a}\sqrt{\epsilon}. \tag{2.28}$$

Effective axion potential at finite density

We are considering the astrophysical and celestial objects like neutron stars, white dwarfs, pulsars, and planets which are made of non relativistic matter mostly like neutrons and protons. The axion potential comes from the quark mass term. From Feynman-Hellmann theorem, one can develop the quark condensate in the medium. If $H(\lambda)$ denotes a Hermitian operator which depends on a real parameter λ and operates on a normalized eigenvector $|\psi(\lambda)>$ with eigenvalue $E(\lambda)$ then [169]

$$H(\lambda)|\psi(\lambda)>=E(\lambda)|\psi(\lambda)>. \tag{2.29}$$

Hence, from Feynman-Hellmann theorem, we can write

$$<\psi(\lambda)|\frac{d}{d\lambda}H(\lambda)|\psi(\lambda)>=\frac{d}{d\lambda}<\psi(\lambda)|H(\lambda)|\psi(\lambda)>. \tag{2.30}$$

The chiral symmetry is explicitly broken by the quark mass term which is governed by the Hamiltonian

$$\mathcal{H}_{mass}=m_u\bar{u}u+m_d\bar{d}d+m_s\bar{s}s+...,\tag{2.31}$$

where m_u, m_d, and m_s denote the quark mass terms correspond to the quark fields u, d, and s respectively. The dots denote the similar contributions from the heavier quarks. We can write Eq. (2.31) as

$$\mathcal{H}_{mass}=2m_q\bar{q}q-\frac{1}{2}\delta m_q(\bar{u}u-\bar{d}d)+m_s\bar{s}s+...,\tag{2.32}$$

where we define $\bar{q}q=\frac{1}{2}(\bar{u}u+\bar{d}d)$, $m_q=\frac{1}{2}(m_u+m_d)$ and $\delta m_q=m_d-m_u$. Putting $H\rightarrow\int d^3x\mathcal{H}_{QCD}$ and $\lambda\rightarrow m_q$ in the Feynman-Hellmann theorem, we obtain

$$2<\psi(m_q)|\int d^3x\bar{q}q|\psi(m_q)>=\frac{d}{dm_q}<\psi(m_q)|\int d^3x\mathcal{H}_{QCD}|\psi(m_q)>. \tag{2.33}$$

Multiplying both sides by m_q, we obtain from Eq. (2.33)

$$2m_q<\psi(m_q)|\int d^3x\bar{q}q|\psi(m_q)>=m_q\frac{d}{dm_q}<\psi(m_q)|\int d^3x\mathcal{H}_{QCD}|\psi(m_q)>. \tag{2.34}$$

Here, we neglect the isospin breaking terms, though it is not necessary.

Consider two cases, $|\psi(m_q)>=|n_N>$ and $|\psi(m_q)>=|0>$ in Eq. (2.34). $|n_N>$ denotes the ground state with nucleon density n_N and $|0>$ denotes the vacuum state.

Taking the differences of this two cases, we obtain

$$2m_q(<\bar{q}q>_{n_N} - <\bar{q}q>_0) = m_q \frac{d\xi}{dm_q}. \tag{2.35}$$

The nuclear matter energy density ξ is given by

$$\xi = M_N n_N + \delta\xi, \tag{2.36}$$

where $\delta\xi$ contributes to the energy density from nucleon kinetic energy and nucleon nucleon interaction. The quark condensate at low density can be expressed by nucleon σ term, σ_N which is defined as

$$\sigma_N = 2m_q \int d^3x(< N|\bar{q}q|N > - < 0|\bar{q}q|0 >). \tag{2.37}$$

From Eq. (2.34) we obtain

$$\sigma_N = m_q \frac{dM_N}{dm_q}. \tag{2.38}$$

Combining Eq. (2.35), Eq. (2.36) and Eq. (2.38) we obtain

$$2m_q(<\bar{q}q>_{n_N} - <\bar{q}q>_0) = \sigma_N n_N + ... \tag{2.39}$$

From Gell-Mann-Oakes-Renner relation, we can write

$$2m_q <\bar{q}q>_0 = -m_\pi^2 f_\pi^2. \tag{2.40}$$

In the effective two flavour theory, we define the effective up and down quark mass as

$$m_{u,d}^{eff} = m_{u,d}\Big[1 - \frac{\sum \sigma_N^{u,d} n_N}{m_\pi^2 f_\pi^2} \frac{m_u + m_d}{m_{u,d}}\Big]. \tag{2.41}$$

From Eq. (2.25), in $m_u = m_d$ limit, the effective axion potential at finite density becomes

$$V = -m_\pi^2 f_\pi^2 \Big\{ \Big(\epsilon - \frac{\sigma_N n_N}{m_\pi^2 f_\pi^2}\Big) \Big| \cos\Big(\frac{a}{2f_a}\Big)\Big| + \mathcal{O}\Big(\Big(\frac{\sigma_N n_N}{m_\pi^2 f_\pi^2}\Big)^2\Big)\Big\}. \tag{2.42}$$

2.2.2 The Axion Profile for an Isolated Neutron Star/White Dwarf

It has been pointed out in [167] that, if we consider ALPs which couple to nucleons, then compact stars such as neutron stars and white dwarfs can be the source of long range axionic force. The reason for this long range force is as follows. In the vacuum, the potential for the ALPs is Eq.(2.27) and the mass of the ALP is Eq. (2.28) .

Inside a compact star, the quark masses are corrected by the nucleon density and the potential inside the star is Eq.2.42. We have chosen the nucleon σ term as $\sigma_N \sim 59\mathrm{MeV}$ from lattice simulation [170] and we consider the parameter space where $\epsilon \leq 0.1$[167]. The tachyonic mass of the ALPs is the square root of the second derivative of the potential Eq. (2.42) at $a = 0$. Inside of the neutron star, $\sigma_N n_N / m_\pi^2 f_\pi^2$ is not equal to zero and $m_T \gtrsim m_a$. Thus the magnitude of the tachyonic mass of the ALPs inside the compact star becomes

$$m_T = \frac{m_\pi f_\pi}{2 f_a} \sqrt{\frac{\sigma_N n_N}{m_\pi^2 f_\pi^2} - \epsilon}, \qquad r < r_{NS}, \tag{2.43}$$

where r_{NS} is the radius of the compact star. The sign change of the axion potential at high nucleon density allows axions to be sourced by compact stars. Inside of the compact star, the axion field is tachyonic and resides on one of the local maxima of the axion potential as shown in Fig.2.4(a). Inside the compact star, the axion field takes a constant value $a = 4\pi f_a$. Now we compare the gradient energy f_a^2/r^2 required to move the axion from its unstable solution with the gain in potential energy $m_\pi^2 f_\pi^2 \left(\epsilon - \frac{\sigma_N n_N}{m_\pi^2 f_\pi^2}\right)$ by putting $a = 4\pi f_a$ in the expression of the effective axion potential Eq. (2.42). When the gain in potential energy is greater than the gradient energy then the axion field rolls down asymptotically to $a = 0$ at $r \to \infty$. Hence,

$$m_\pi^2 f_\pi^2 \left(\epsilon - \frac{\sigma_N n_N}{m_\pi^2 f_\pi^2}\right) > \frac{f_a^2}{r_c^2},$$

The ALPs can be sourced by compact objects if its size is larger than the critical size given by [167]

$$r_c \gtrsim \frac{1}{m_T}. \tag{2.44}$$

For a typical neutron star and white dwarf, the condition Eq. (2.44) is satisfied. By matching the axionic field solution inside and outside of the compact star, we get the long range behaviour of the axionic field. The axionic potential has degenerate vacua and this degeneracy can be weakly broken by higher dimensional operators suppressed by the Planck scale [171]. The degeneracy can also be broken by a finite density effect like the presence of a NS and WD. At the very high nuclear density, the axionic potential changes its sign which allows the ALPs to be sourced by the compact stars. Due to the very small size of the nuclei, it cannot be the source of the ALPs and long range axion fields arise only in large sized objects like NS and WD. Using Eq. (2.28) in Eq. (2.43) we can write the tachyonic mass as

$$m_T^2 = \sigma_N n_N / 4 f_a^2 - m_a^2 \tag{2.45}$$

Putting values of all the parameters and $m_a \sim 10^{-19}$ eV, we get the upper bound of the axion decay constant (using Eq. (2.44)) as $f_a \lesssim 2.636 \times 10^{17}$ GeV. Axions can never be sourced by neutron star if f_a is greater than this upper bound. Similarly, the white dwarf cannot be the source of axions if $f_a \gtrsim 9.95 \times 10^{14}$ GeV.

Compact stars with large nucleon number density can significantly affect the axion potential. The second derivative of the potential Eq. (2.42) with respect to the field value is

$$\frac{\partial^2 V}{\partial a^2} = m_\pi^2 f_\pi^2 \Big\{ \Big(\epsilon - \frac{\sigma_N n_N}{m_\pi^2 f_\pi^2} \Big) \frac{1}{4 f_a^2} \cos\Big(\frac{a}{2 f_a} \Big) + \mathcal{O}\Big(\Big(\frac{\sigma_N n_N}{m_\pi^2 f_\pi^2} \Big)^2 \Big) \Big\}. \tag{2.46}$$

Outside of the compact star, $\sigma_N = 0$ which implies that

$$\frac{\partial^2 V}{\partial a^2} = m_\pi^2 f_\pi^2 \Big\{ \epsilon \frac{1}{4 f_a^2} \cos\Big(\frac{a}{2 f_a} \Big) + \mathcal{O}\Big(\Big(\frac{\sigma_N n_N}{m_\pi^2 f_\pi^2} \Big)^2 \Big) \Big\}. \tag{2.47}$$

Therefore, outside of the compact star ($r > r_{NS}$), the potential attains minima ($\frac{\partial^2 V}{\partial a^2} > 0$) corresponding to the field values $a = 0, \pm 4\pi f_a, ...$ and maxima ($\frac{\partial^2 V}{\partial a^2} < 0$) corresponding to the field values $a = \pm 2\pi f_a, \pm 6\pi f_a ...$ etc.

Inside of the compact star ($r < r_{NS}$), $\sigma_N \neq 0$ and $\frac{\sigma_N n_N}{m_\pi^2 f_\pi^2} > \epsilon$. Therefore, inside of the compact star, the potential has maxima at $a = 0, \pm 4\pi f_a, ...$ and minima at the field values $a = \pm 2\pi f_a, \pm 6\pi f_a ...$ etc.

The axionic field becomes tachyonic inside of a compact star and resides on one of the local maxima of the axionic potential and, outside of the star, the axionic field rolls down to the nearest local minimum and stabilizes about it. The axionic field asymptotically reaches zero value $a = 0$ at infinity. Therefore, throughout the interior of the compact star the axionic field assumes a constant value $a = 4\pi f_a$, the nearest local maximum.

For an isolated compact star of constant density the equation of motion for the axionic field is [167]

$$\nabla^\mu \nabla_\mu \Big(\frac{\theta}{2} \Big) = \begin{cases} -m_T^2 \sin\Big(\frac{\theta}{2} \Big) \operatorname{sgn}\{\cos\Big(\frac{\theta}{2} \Big)\} & (r < r_{NS}), \\ m_a^2 \sin\Big(\frac{\theta}{2} \Big) \operatorname{sgn}\{\cos\Big(\frac{\theta}{2} \Big)\} & (r > r_{NS}), \end{cases} \tag{2.48}$$

where $\theta = a/f_a$. The sgn function is required to take care of the absolute value $|\cos(\theta/2)|$ in the potential. Note that the equation of motion for the axionic field inside the compact star is satisfied by the field value $a = 4\pi f_a$.

Assuming the exterior spacetime geometry due to the compact star to be Schwarzschild, the axionic field equation Eq. (2.48) becomes (see Appendix A.1)

$$\left(1 - \frac{2GM}{r}\right)\frac{d^2a}{dr^2} + \frac{2}{r}\left(1 - \frac{GM}{r}\right)\frac{da}{dr} = m_a^2 a, \tag{2.49}$$

where M denotes the compact star mass, and we use the approximation $\sin(\theta/2) \approx \theta/2$ for small θ.

At a large distance ($r >> 2GM$) from the compact star, the axionic field Eq. (2.49) becomes

$$\frac{d^2a}{dr^2} + \frac{2}{r}\frac{da}{dr} = m_a^2 a. \tag{2.50}$$

Assuming $a = \xi(r)/r$, the above equation reduces to $\xi'' - m_a^2\xi = 0$ (where prime denotes derivative with respect to r). This has the solution $\xi = C_1 e^{m_a r} + C_2 e^{-m_a r}$. Since $a \to 0$ in the limit $r \to \infty$, $C_1 = 0$. Thus, a behaves as $a \sim q_{eff} e^{-m_a r}/r$, where we rename the integration constant C_2 as q_{eff}. Further, for sufficiently light mass ($m_a << 1/D << 1/r_{NS}$) where D is the distance between the stars in a binary system), the scalar field has a long range behaviour with an effective charge q_{eff}. For scalar Larmor radiation, the orbital frequency (ω) of the binary pulsar should be greater than the mass of the particle that is radiated (i.e. $\omega > m_a$). This translates the mass spectrum of radiated ALPs for a typical neutron star- neutron star (NS-NS) or a neutron star- white dwarf (NS-WD) binary system into $m_a \lesssim 10^{-19}$ eV. Also, the axion Compton wavelength should be much larger than the binary distance in order to use the massless limit in the computation of scalar radiation and effective charge, i.e. $m_a^{-1} >> D$. The critical value of axion mass required for the scalar radiation and the binary distance for four compact binary systems are given in Table 2.1 which is consistent with the assumption of $m_a \lesssim 10^{-19}$ eV. Consequently, the axion Compton wavelength (inverse of axion mass) is larger than the binary distance and, hence, the size of the star (size of NS is 10^{20} GeV^{-1} and size of WD is 10^{23} GeV^{-1}).

To identify the effective charge q_{eff}, we exploit the continuity of the axion field across the surface of the compact star. Therefore, we solve Eq. (2.49) in the massless

Table 2.1: Summary of the axion Compton wavelength (m_a^{-1}) and binary distance D for all the four compact binaries. All relevant parameters for the numerical calculation are given in section 2.2.4.

Binary system	Critical value of m_a^{-1} (GeV^{-1})	binary separation D (GeV^{-1})
PSR J0348+0432	2.14×10^{27}	4.64×10^{24}
PSR J0737-3039	2.08×10^{27}	4.83×10^{24}
PSR J1738+0333	7.41×10^{27}	9.65×10^{24}
PSR B1913+16	6.76×10^{27}	1.08×10^{25}

limit ($m_a\to0$), i.e.

$$\left(1-\frac{2GM}{r}\right)\frac{d^2a}{dr^2}+\frac{2}{r}\left(1-\frac{GM}{r}\right)\frac{da}{dr}=0. \tag{2.51}$$

Integrating Eq. (2.51) we get $a'=-C_3/r^2(1-2GM/r)$ and further integration yields $a=-\dfrac{C_3}{2GM}\ln\left(1-2GM/r\right)+C_4$, where C_3 and C_4 are integration constants. For $r>>2GM$ limit, $a\to q_{eff}/r$ and, therefore, $C_3=q_{eff}$ and $C_4=0$. Therefore, we get the axionic field profile outside the compact star

$$a=-\frac{q_{eff}}{2GM}\ln\left(1-\frac{2GM}{r}\right). \tag{2.52}$$

The behaviour of the axionic potential as a function of the distance are illustrated in Fig.2.4(b). The nature of the axionic field as we go from inside to the outside of a compact star is also shown in Fig.2.4(c). Variation of the effective charge to mass ratio of a compact star is shown in Fig.2.4(d) as a function of the mass to radius ratio for different decay constants. At the surface of the compact star, $a(r_{NS})=4\pi f_a$. Thus we identify

$$q_{eff}=-\frac{8\pi GMf_a}{\ln\left(1-\frac{2GM}{r_{NS}}\right)}. \tag{2.53}$$

If $\dfrac{GM}{r_{NS}}<<1$, $q_{eff}\sim4\pi f_a r_{NS}$ [167]. However, for a typical neutron star ($M=1.4M_\odot$ and $r_{NS}=10$ km) the above correction is not negligible. For white dwarf the effect is negligible. The charges can be both positive as well as negative depending on the sign of the axionic field values at the surface of the compact star. If q_1 and q_2 are the charges of two compact stars, then if $q_1q_2>0$ the two stars attract each other and,

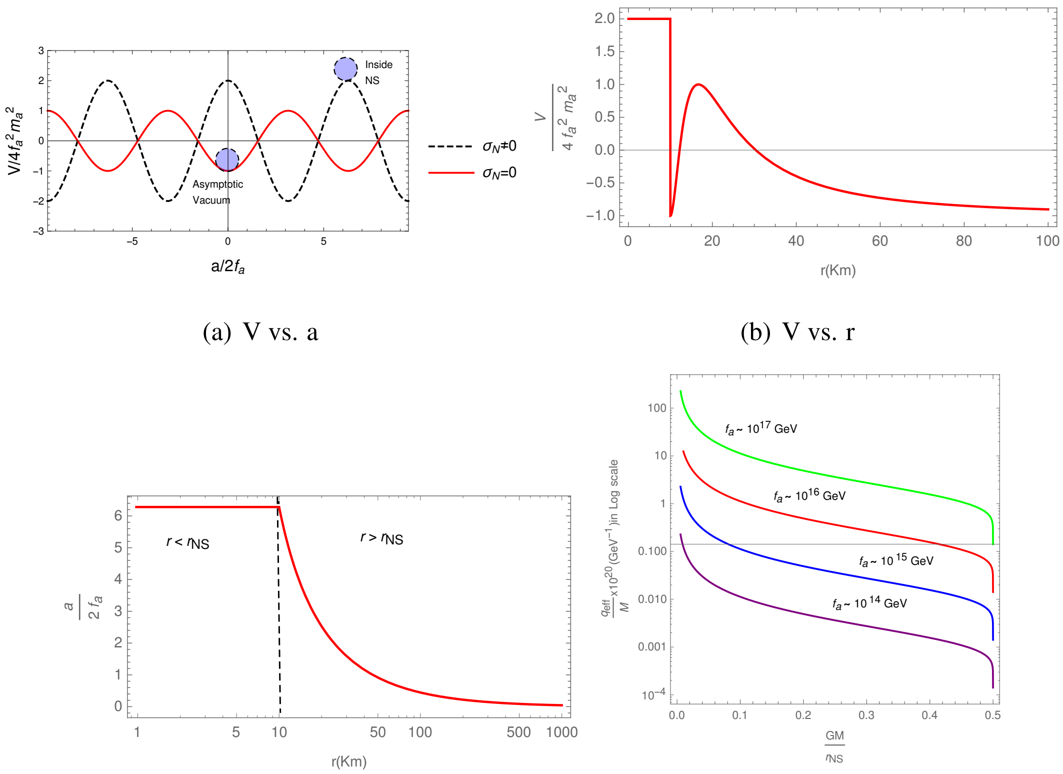

(a) V vs. a

(b) V vs. r

(c) a vs. r

(d) $\frac{q_{\text{eff}}}{M}$ vs. $\frac{GM}{r_{\text{NS}}}$

Figure 2.4: (a) plot of the axionic potential V as the function of the axionic field. We assume $m_T^2/m_a^2 = 2$. The black dashed line corresponds to $\sigma_N \neq 0$ (i.e; inside the compact star) and the red solid line corresponds to $\sigma_N = 0$. Note that the axionic field evolves from the local maximum $a = 4\pi f_a$ inside a compact star to nearest local minimum $a = 0$ outside the compact star. (b) The plot of V as the function of r inside and outside of the neutron star. Note that there is discontinuity in $V(r)$ at $r = r_{NS}$ due to sign change in the potential. (c) plot of the axionic field a as the function of r. We assume neutron star as the example of the compact object in the plots. The typical mass and radius of a neutron star are $M = 1.4M_\odot$ and $r_{NS} = 10$ km respectively. (d) The variation of effective charge to mass ratio of the neutron star with the ratio of mass to radius for different values of axion decay constant. We can also obtain similar type of profiles for white dwarfs as well.

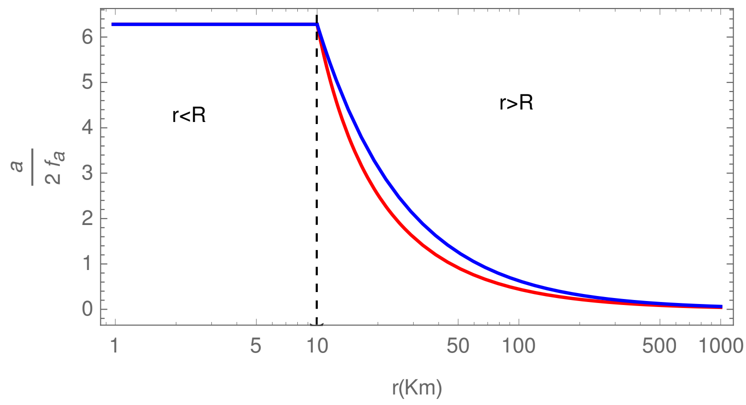

(a) a vs. r

Figure 2.5: plot of the axion field a as the function of r. The blue curve stands for the axion field $a \sim q_{eff}/r$ and the red curve stands for the axion field $a \sim -q_{eff}/2GM \ln(1-2GM/r)$ outside of the neutron star. For blue curve, the effective axion charge is $q_{eff} = 4\pi f_a r_{NS}$ and for the red curve q_{eff} is given by Eq.(2.53).

if $q_1 q_2 < 0$, then they repel each other [167]. For neutron star, the new effective axion charge Eq. (2.53) is smaller than $4\pi f_a r_{NS}$ by 21.46%. The effect of the new axion charge is illustrated in Fig. 2.5(a) where the plot of the axion profile inside and outside of a neutron star is shown.

2.2.3 Axionic fifth force and the scalar radiation for the compact binaries

Such a long range axionic field mediates a "fifth" force (in addition to the Newtonian gravitational force) between the stars of a binary system (NS-NS or NS-WD),

$$F_5 = \frac{q_1 q_2}{4\pi D^2}, \tag{2.54}$$

where $q_{1,2}$ are effective charges of the stars in the binary system. Due to the presence of this scalar mediated fifth force the Kepler's law is modified by [172]

$$\omega^2 = \frac{G(m_1+m_2)}{D^3}(1+\alpha), \tag{2.55}$$

where $\alpha = \dfrac{q_1 q_2}{4\pi G m_1 m_2}$ is the ratio of the scalar mediated fifth force to the gravitational force, and $\mu = m_1 m_2/(m_1+m_2)$ is the reduced mass of the binary system. There are constraints on the fifth force from either scalar-tensor theories of gravity [172–174] or the dark matter components [174–176]. In this section, we show that the constraint on α from time period loss by scalar radiation is more stringent than the measured change in orbital period Eq. (2.55) due to fifth force.

The orbital period of the binary star system decays with time because of the energy loss primarily due to the gravitational quadrupole radiation and about one per cent due to ultra light scalar or pseudoscalar Larmor radiation. The total power radiated for such quasi-periodic motion of a binary system is

$$\frac{dE}{dt} = -\frac{32}{5}G\mu^2 D^4\omega^6(1-e^2)^{-\frac{7}{2}}\left(1+\frac{73}{24}e^2+\frac{37}{96}e^4\right) - \frac{\omega^4 p^2}{24\pi}\frac{(1+e^2/2)}{(1-e^2)^{\frac{5}{2}}}, \tag{2.56}$$

where e is the eccentricity of the elliptic orbit and E is the total energy of the binary system. The gravitational quadrupole radiation formula [168, 175] is given by the first term in the right hand side of Eq.2.56 and the second term is the massless scalar dipole radiation formula [7, 167, 168]. There is the radiation of the ALPs if the orbital frequency is greater than the mass of the ALPs. The dipole moment in the centre of mass frame of the binary system can be written as

$$p = q_1 r_1 - q_2 r_2 = q_1\frac{\mu D}{m_1} - q_2\frac{\mu D}{m_2}, \tag{2.57}$$

or,

$$p = 8\pi G f_a \mu D\left[\frac{1}{\ln\left(1-\frac{2Gm_2}{r_{NS}}\right)} - \frac{1}{\ln\left(1-\frac{2Gm_1}{r_{NS}}\right)}\right], \tag{2.58}$$

where $r_{1,2}$ are the radial distances of the stars in the binary system from the centre of mass along the semi-major axis. For nonzero scalar radiation, the charge-to-mass ratio (q/m) should be different for two stars. Thus for the companion star in a binary system with an equal effective charge, there should be some mass difference between the two stars. The decay of the orbital time period is given by[168, 177]

$$\dot{P}_b = 6\pi G^{-\frac{3}{2}}(1+\alpha)^{-\frac{3}{2}}(m_1 m_2)^{-1}(m_1+m_2)^{-\frac{1}{2}}D^{\frac{5}{2}}\left(\frac{dE}{dt}\right), \tag{2.59}$$

where $P_b = 2\pi/\omega$ (see Appendix A.2). NS-NS binaries (with different mass components) as well as NS-WD binaries are the sources for the scalar Larmor radiation and also for the axion mediated fifth force. On the other hand, NS-BH systems can be the source of scalar radiation but there is no long range fifth force in between, as the scalar charges for the black holes (BH) are zero[178].

In the next section, we consider four compact binaries and put constraints on f_a.

2.2.4 Constraints on axion parameters of different compact binaries

PSR J0348+0432

This binary system is consist of a neutron star and a low mass white dwarf companion. The orbital period of the quasi-periodic binary motion is $P_b = 2.46$ h. The mass of the neutron star in this binary system is $M_p = 2.01 M_\odot$ and the mass of the white dwarf is $M_{WD} = 0.172 M_\odot$. The radius of the white dwarf is $r_{WD} = 0.065 R_\odot$ and we assume the radius of the neutron star $r_{NS} = 10$ km. We compute the semi-major axis of the orbit using Kepler's law Eq. (2.55). The observed decay of the orbital period is $\dot{P}_b = 0.273 \times 10^{-12}\ \mathrm{s\,s^{-1}}$[179]. This is primarily due to gravitational quadrupole radiation from the binary NS-WD system. The contribution from the radiation of some scalar or pseudoscalar particles must be within the excess of the decay of the orbital period, i.e. $\dot{P}_{b(scalar)} \leqslant |\dot{P}_{b(observed)} - \dot{P}_{b(gw)}|$. If ALPs are emitted as scalar Larmor radiation, then we can find the upper bound on the axion decay constant. Using Eqs. (2.55),(2.56), (2.58) and (2.59) and taking the ALPs as massless, we obtain an upper bound on the axion decay constant as, $f_a \lesssim 1.66 \times 10^{11}$ GeV. The ratio of the axionic fifth force and the Newtonian gravitational force between the stars in this system comes out to be $\alpha \lesssim 5.73 \times 10^{-10}$.

PSR J0737-3039

It is a double neutron star binary system whose average orbital period is $P_b = 2.4$ h. Its observed orbital period decays at a rate $\dot{P}_b = 1.252 \times 10^{-12}\ \mathrm{s\,s^{-1}}$. The pulsars have masses $M_1 = 1.338 M_\odot$ and $M_2 = 1.250 M_\odot$. The eccentricity of the orbit is $e = 0.088$[180]. Using Eqs. (2.55), (2.56), (2.58), and (2.59) we obtain the upper bound on the axion decay constant as $f_a \lesssim 9.76 \times 10^{16}$ GeV. Besides the axion radiation, axion mediated fifth force arises in this binary system. We obtain the value of $\alpha \lesssim$

9.21×10^{-3} .

PSR J1738+0333

This pulsar-white dwarf binary system has an average orbital period $P_b = 8.5$ h and the orbit has a very low eccentricity $e < 3.4 \times 10^{-7}$. The mass of the pulsar is $M_p = 1.46 M_\odot$ and the mass of the white dwarf is $M_{WD} = 0.181 M_\odot$. The radius of the white dwarf is $r_{WD} = 0.037 R_\odot$. The rate of the intrinsic orbital period decay is $\dot{P}_b = 25.9 \times 10^{-15} \mathrm{s\,s}^{-1}$[181]. Using this system, we obtain the upper bound on the axion decay constant as $f_a \lesssim 2.03 \times 10^{11}$ GeV. The value of α comes out to be $\lesssim 8.59 \times 10^{-10}$.

PSR B1913+16: Hulse Taylor binary pulsar

The observed orbital period of the Hulse Taylor binary decays at the rate of $\dot{P}_b = 2.40 \times 10^{-12}$ s s^{-1}. The masses of the stars in this binary system are $m_1 = 1.42 M_\odot$ and $m_2 = 1.4 M_\odot$[168]. The eccentricity of the orbit is $e = 0.617127$ and the average orbital frequency is $\omega = 0.2251 \times 10^{-3}$ s^{-1}. For this system, we obtain the upper bound on the decay constant as $f_a \lesssim 2.12 \times 10^{17}$ GeV. We obtain the value of α for this system $\lesssim 3.4 \times 10^{-2}$. Note that the binary orbit of this system is highly eccentric. As a result, the contributions of the eccentricity factors in the radiation formula Eq. (2.56) are important. For the GW radiation, the eccentricity factor is 11.85 and, for the scalar radiation, it is 3.94.

In Table 2.2, we have obtained the upper bound of the axion decay constant and the relative strength of axion mediated force for the four compact binaries [62].

Table 2.2: Summary of the upper bounds on the axion decay constant f_a of ALPs radiated from compact binaries. For all the binaries we assume $m_a < 10^{-19}$ eV.

Compact binary system	f_a (GeV)	α
PSR J0348+0432	$\lesssim 1.66 \times 10^{11}$	$\lesssim 5.73 \times 10^{-10}$
PSR J0737-3039	$\lesssim 9.76 \times 10^{16}$	$\lesssim 9.21 \times 10^{-3}$
PSR J1738+0333	$\lesssim 2.03 \times 10^{11}$	$\lesssim 8.59 \times 10^{-10}$
PSR B1913+16	$\lesssim 2.12 \times 10^{17}$	$\lesssim 3.4 \times 10^{-2}$

2.2.5 Implication for the axionic Fuzzy dark matter (FDM)

we have discussed that ultralight axions or ALPs can be possible candidates of FDM whose mass is $\mathcal{O}(10^{-21}\ \mathrm{eV} - 10^{-22}\ \mathrm{eV})$, the axion decay constant $f_a \sim 10^{17}$ GeV, and has a de Broglie wavelength of order kpc scale.

For the NS-WD binaries PSR J0348+0432 and PSR J1738+0333, the bound on the axion decay constant ($f_a \lesssim \mathcal{O}(10^{11}\ \mathrm{GeV})$) is well below the GUT scale and this gives the stronger bound. The mass of the axions is $m_a \lesssim 10^{-19}$ eV. This implies that if the ultra-light ALPs has to be FDM then they do not couple with quarks as it will not satisfy the FDM relic density (Eq.(2.11)).

2.3 Constraints on Ultralight Axions from Birefringence Effect

As described in Section.2.2.2 for NS and WD, the pulsars can also behave as a source of axions due to the sign change in the axion potential from the coupling to gluons at large densities. The coherent oscillation of the axion potential in free space produces the axionic density. Similar to the NS and WD, the pulsars immersed in the axionic potential also develop a long-range axion hair due to the coupling of axions with nucleons. Since, the dipole axis is not aligned along the spin axis, the pulsar can also emit electromagnetic radiation. As the dipole axis precesses around the spin axis, there is a synchrotron radiation along the magnetic poles appears as the pulsed signal in a cone swept out by the radio beam. When the electromagnetic radiaiton from the pulsar passes through the long range axion hair emitted from the same pulsar then the axion hair rotates the polarization of the electromagnetic radiation and produces birefringence. A typical pulsar of mass $M = 1.4M_\odot$ and radius $R = 10$ km can be a source of axions if Eq. (2.44) is satisfied which gives the upper bound on the axion decay constant, $f_a \lesssim 4.41 \times 10^{17}$ GeV. The radius of the pulsar $(10\ \mathrm{km})$ constrains the mass of the axion that results $m_a < 10^{-11}$ eV.

In the Schwarzschild spacetime background and in the non zero axion mass limit, we cannot analytically solve the Klein-Gordon equation for a massive Yukawa axion field

$$\nabla^{\mu}\nabla_{\mu}a = m_a^2 a. \tag{2.60}$$

To solve Eq. (2.60), we expand the axion field in a perturbative way where the perturbation parameter is GM/R and the leading order term is the long range Yukawa term. Suppose the axion field is

$$a(r) = a_0(r) + \frac{GM}{R}a_1(r) + \mathcal{O}\Big(\frac{GM}{R}\Big)^2, \tag{2.61}$$

where $a_0(r) = q_a \dfrac{e^{-m_a r}}{r}$ is the leading order Yukawa term. Hence, the axion field solution becomes

$$a(r) = \frac{q_a e^{-m_a r}}{r}\Big[1+\frac{GM}{r}\{1-m_a r\ln(m_a r)+m_a r e^{2m_a r}E_i(-2m_a r)\}\Big]+\mathcal{O}\Big(\Big(\frac{GM}{R}\Big)^2\Big), \tag{2.62}$$

where Ei is the exponential integral function. From the continuity of axion field at the surface of the pulsar, we obtain the effective axion charge

$$q_a = 4\pi f_a R e^{m_a R}\Big[1+\frac{GM}{R}\{1-m_a R\ln(m_a R)+m_a R e^{2m_a R}E_i(-2m_a R)\}\Big]^{-1} + \mathcal{O}\Big(\Big(\frac{GM}{R}\Big)^{-2}\Big). \tag{2.63}$$

In the limit $GM/R \ll 1$ and $m_a \to 0$, we obtain $q_a \sim 4\pi f_a R$ [167].

Therefore, outside of the pulsar, the axion field solution becomes

$$a = \frac{q_a e^{-m_a r}}{r}\Big[1+\frac{GM}{r}\{1-m_a r\ln(m_a r)+m_a r e^{2m_a r}E_i(-2m_a r)\}\Big]+\mathcal{O}\Big(\Big(\frac{GM}{R}\Big)^2\Big), \quad r > R, \tag{2.64}$$

whereas inside of the pulsar, the solution becomes

$$a = 4\pi f_a, \; r < R. \tag{2.65}$$

We assume that the spacetime metric outside the pulsar is Schwarzchild because, for a typical pulsar ($M = 1.4M_{\odot}, R = 10\,\mathrm{km}$), GM/R is not very much small. The plot of axion field and axion potential inside and outside of a pulsar and the variation of axion charge with axion mass is shown in Fig.2.4.

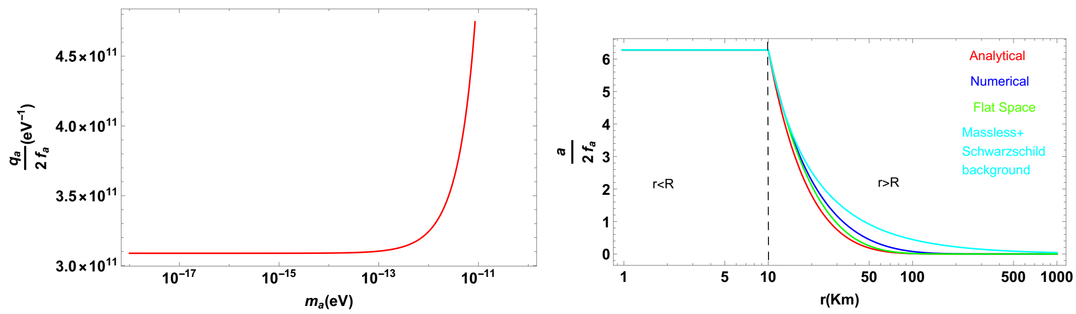

(a) q vs. m_a (b) a vs. r

Figure 2.6: (a)Variation of axion charge with mass. (b)Variation of the axion field as a function of distance obtained numerically and analytically and for different spacetimes.

In Fig.2.6(a), we obtain a variation of axion charge with mass. We also obtain the axion field as a function of distance both numerically and analytically for different spacetimes, shown in Fig.2.6(b). The red curve denotes the axion field by solving Eq. (2.64) analytically. The blue curve denotes its numerical solution. The green curve denotes the axion field profile in a flat spacetime for non zero axion mass. The cyan curve denotes the axion profile for the massless axion in the Schwarzschild background.

The spacetime outside of a pulsar is described by the approximate form of the Kerr metric,

$$ds^2 = \left(1-\frac{2GM}{r}\right)dt^2-\left(1-\frac{2GM}{r}\right)^{-1}dr^2-r^2(d\theta^2+\sin^2\theta d\phi^2)-\frac{4GMj}{r}\sin^2\theta d\phi dt. \tag{2.66}$$

Where j is the angular momentum per unit mass and this approximation is valid as long as $j \ll GM$. For a typical pulsar $j = 10^{-6}$ km, $GM = 1.5$ km, and we can neglect the last term. Hence, in this limit, the metric outside of the pulsar effectively becomes Schwarzschild [125].

2.3.1 Photon propagation through an axionic hair: Birefringence

When a linearly polarized pulsar light passes through a long range axionic hair which is originated from the same pulsar then due to their dispersion relations the left and the right circular polarization modes will attain opposite corrections. This effect is called birefringence.

The Lagrangian which describes the interaction between the axion couples with two photons is

$$\mathcal{L} = \frac{1}{2}(\partial_\mu a)(\partial^\mu a) - \frac{1}{4}F^{\mu\nu}F_{\mu\nu} - \frac{1}{4}g_{a\gamma\gamma}aF_{\mu\nu}\tilde{F}^{\mu\nu}. \tag{2.67}$$

Here $g_{a\gamma\gamma}$ is given as

$$g_{a\gamma\gamma} = \frac{c\alpha_{em}}{2\pi f_a}, \tag{2.68}$$

where c is a model dependent parameter of order unity and α_{em} is the electromagnetic fine structure constant. The modified Maxwell's field equations in presence of axion coupling become [125]

$$\nabla.\mathbf{E} = -g_{a\gamma\gamma}(\nabla a).\mathbf{B}, \tag{2.69}$$

$$\nabla \times \mathbf{B} - \frac{\partial \mathbf{E}}{\partial t} = g_{a\gamma\gamma}\Big[(\nabla a) \times \mathbf{E} + \mathbf{B}\frac{\partial a}{\partial t}\Big], \tag{2.70}$$

$$\nabla.\mathbf{B} = 0, \tag{2.71}$$

$$\nabla \times \mathbf{E} + \frac{\partial \mathbf{B}}{\partial t} = 0, \tag{2.72}$$

where $\mathbf{E}$ and $\mathbf{B}$ are the electric and magnetic field vectors of the electromagnetic radiation. Since, the long range Yukawa type axion field has only r dependence, the second term in the r.h.s of Eq. (2.70) is zero. Taking curl of Eq. (2.70) and using Eq. (2.71) and Eq. (2.72), we obtain

$$\nabla_\mu \nabla^\mu \mathbf{B} = -g_{a\gamma\gamma}(\nabla a) \times \frac{\partial \mathbf{B}}{\partial t}. \tag{2.73}$$

Suppose this magnetic field has a harmonic variation and we can write

$$B(x,t) = \mathcal{B}e^{i\phi(x,t)}, \tag{2.74}$$

where $\mathcal{B}$ is the magnitude of the magnetic field of electromagnetic radiation and ϕ is the phase. A linearly polarized wave is an equal admixture of right and left circularly polarized waves. So we can write the transverse magnetic field as

$$\mathcal{B}_\pm = \mathcal{B}_i \pm i\mathcal{B}_j, \tag{2.75}$$

where $\mathcal{B}_i$ and $\mathcal{B}_j$ are the components of $\mathcal{B}$ along $\hat{e}_i$ and $\hat{e}_j$ orthogonal to $\hat{r}$. In the Fourier space we can write Eq. (2.73) as

$$k_\mu k^\mu \mathcal{B} = ig_{a\gamma\gamma}(\nabla a \times \omega\mathcal{B}), \tag{2.76}$$

where $k^\mu = (\omega, \mathbf{k})$ is the photon four momentum. Eq. (2.76) decouples for the two circularly polarized modes and we obtain

$$k_\mu k^\mu \mathcal{B}_\pm \mp g_{a\gamma\gamma}(\partial_r a)\omega \mathcal{B}_\pm = 0. \tag{2.77}$$

Hence, the dispersion relation for the two circularly polarized modes due to different phase velocities propagating radially from the poles of the pulsar is [125]

$$\omega^2 \Big(1 - \frac{2GM}{r}\Big)^{-1} - k_r^2 \Big(1 - \frac{2GM}{r}\Big) = \pm g_{a\gamma\gamma}(\partial_r a)\omega. \tag{2.78}$$

Therefore, we can write the propagation vector from Eq. (2.78) as

$$k_r = \omega \Big(1 - \frac{2GM}{r}\Big)^{-1} \mp \frac{g_{a\gamma\gamma}}{2}(\partial_r a). \tag{2.79}$$

So the phase shift between the left and the right circularly polarized modes is

$$\Delta\phi = \int_R^\infty (k_r^+ - k_r^-) dr. \tag{2.80}$$

Using Eq. (2.79) we can rewrite the phase shift as

$$\Delta\phi = g_{a\gamma\gamma}[a(\infty) - a(R)]. \tag{2.81}$$

The axion field has a long range behaviour outside of the pulsar. Using Eq. (2.64), Eq. (2.68), and Eq. (2.81) we can write the phase difference as

$$\Delta\phi = -\frac{c\alpha_{em}}{2\pi f_a}\frac{q_a e^{-m_a R}}{R}\Big[1 + \frac{GM}{R}\{1 - m_a R \ln(m_a R) + m_a R e^{2m_a R} E_i(-2m_a R)\}\Big], \tag{2.82}$$

where the axion field goes to zero at infinity. A Positive sign of phase shift implies anti clockwise rotation and a negative sign of phase shift implies clockwise rotation by looking down the light path.

The observed birefringent angle which is the angle of rotation of the linear polarization $(\Delta\theta)$ is half the phase shift $\Delta\phi$ between the two circular polarization modes. Using Eqs. (2.63), and Eqs. (2.82) we obtain

$$\Delta\theta = -c\alpha_{em}, \tag{2.83}$$

where, c is a model dependent parameter of $\mathcal{O}(1)$ (exact value of c depends on the ratio of the electromagnetic and the color factor anomaly E/N, which depends on

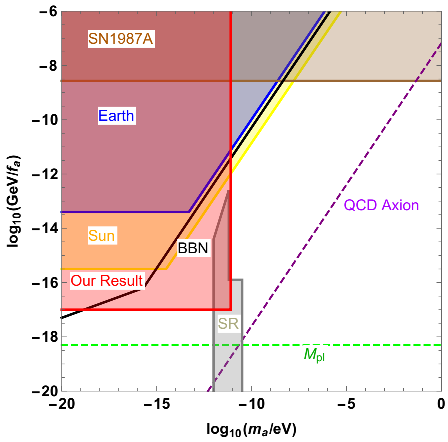

Figure 2.7: The brown shaded region is excluded by SN1987A, the blue shaded region is excluded by direct measurement of the earth, and the yellow shaded region is excluded by direct measurement of Sun. The grey shaded region is excluded by black-hole superradiance measurements. The green dotted line denotes the reduced Planck scale. The black continuous line denotes the constraints from BBN if axion is the dark matter. The violet dotted line corresponds to QCD axions. Our result of the birefringent angle can probe the red shaded region.

what model we are choosing) and $\alpha_{em} = 1/137$. Hence we obtain the birefringent angle

$$\Delta\theta = 7.299 \times 10^{-3}\ \text{radian} = 0.42^{\circ}. \tag{2.84}$$

Any systematic deviation ($\leq 1.0^{\circ}$ [126, 131, 182]) in the linear polarization angle can be due to the long range axion hair. The External magnetic field can also give rise to such type of rotation of the polarization vector which is called the Faraday effect. The primary difference between the optical rotation by long range axion hair and the Faraday effect is that for the Faraday effect the birefringent angle is proportional to λ^2, where λ is the wavelength of the electromagnetic wave and for our case i.e; the optical rotation by axion field, the birefringent angle is independent of λ. The existing constraints ([183, 184], [185]) on axion parameters and the region in which our result is valid are shown in Fig.2.7 [165].

2.4 Constraints on Ultralight Axions from Gravitational Light Bending and Shapiro Time Delay

If celestial bodies like Sun, Earth etc., are immersed in a low mass axionic FDM potential and if the axions have coupling with nucleons then the coherent oscillation of the axionic field results in a long range axion hair outside of those objects similar to the neutron stars, white dwarfs, and pulsars. The long range Yukawa type of axionic potential between the Sun and Earth changes the effective gravitational potential and affects the measurement of bending of light and Shapiro time delay.

The bending of light or the gravitational lensing [186, 187] is one of the tests of Einstein's general theory of relativity (GR) along with the perihelion precession of Mercury planet and the gravitational redshift [188]. When a light ray from a distant star passes through a massive object like Sun then the speed of light decreases due to the presence of increasing gravitational potential. In other words, massive objects with higher gravity distort the spacetime geometry and bend the light. In 1915, Einstein became the first person to calculate the amount of bending of light near the Sun which is $1.75\ \mathrm{arcsec}$ based on equivalence principle. This value agrees well with the experiment to an uncertainty of $\sim 10^{-4}\ \mathrm{arcsec}$ [189]. Another test of Einstein's GR theory is the Shapiro time delay which was predicted by Irwin Shapiro in 1964 [190, 191]. When a radar signal is sent from Earth to Venus and it reflects back from Venus to Earth, then the time taken for the round trip is delayed by the presence of strong gravitational potential near the Sun. The calculated amount of time delay is $2 \times 10^{-4}\ \mathrm{sec}$ which agrees well with the experiment to an uncertainty of $\sim 10^{-5}\ \mathrm{sec}$ [192]. Gravitational waves, high energy neutrinos etc., also have this Shapiro time delay from which one can constrain the violation of the weak equivalence principle [193, 194].

The Earth and Sun which can be the sources of axions, mediate a long range Yukawa type of potential and result in an axionic fifth force between those massive objects. This long range Yukawa potential affects the effective gravitational potential between Earth and Sun and contribute to the bending of light and Shapiro time delay within the experimental uncertainty.

The parameters that we have chosen in our following analysis are: the radius of the

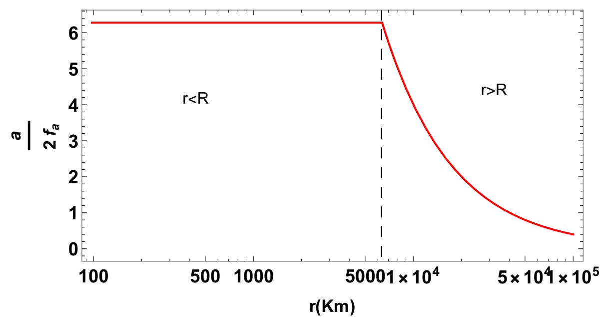

Figure 2.8: Variation of the axion field with distance for earth

Sun $R_\odot \sim r_0 \sim b = 6.96 \times 10^{10}$ cm $= 3.52 \times 10^{24}$ GeV^{-1}, the radius of the Earth $R_\oplus = 6.38 \times 10^8$ cm $= 3.22 \times 10^{22}$ GeV^{-1}, the distance between Earth and Sun is $D = r_e = 1.49 \times 10^{13}$ cm $= 7.52 \times 10^{26}$ GeV^{-1}, the distance between Sun and Venus is $r_v = 1.08 \times 10^{13}$ cm $= 5.47 \times 10^{26}$ GeV^{-1}, the mass of Sun $M = M_\odot = 10^{57}$ GeV, the mass of Earth $M_p = M_\oplus = 3.35 \times 10^{51}$ GeV, $G = 10^{-38}$ GeV^{-2}.

2.4.1 Celestial objects as the sources of ALPs

A celestial object like Earth or Sun can be the source of axions if its size is greater than the critical size which is given by Eq.(2.44). Using the values of $\sigma_N = 59$ MeV from lattice simulation [170], $m_a \lesssim 1.333 \times 10^{-18}$ eV and other parameters we obtain the upper bounds on f_a for which the axions can be sourced by Earth and Sun as $f_a \lesssim 1.91 \times 10^{13}$ GeV and $f_a \lesssim 10^{15}$ GeV respectively (using Eq.2.45). The mass of the axion is constrained by the distance between Earth and Sun.

In other words, Earth and Sun can be the sources of axions if the following two conditions are satisfied,

$$\rho_R \gtrsim m_a^2 f_a^2, \qquad \frac{1}{R} \lesssim \frac{\sqrt{\rho_R}}{f_a}, \tag{2.85}$$

where ρ_R is the mass density of the celestial body of radius R. We have checked that the m_a and f_a values that we obtain later in Section.2.4.4 satisfy Eq.(2.85). Hence, the Sun and the Earth are in fact the sources of axions. If q_1 and q_2 are the axion charges of Sun and Earth respectively, then the potential energy act between Sun and Earth is $V = \dfrac{q_1 q_2}{4\pi r} e^{-m_a r}$ which is long range Yukawa type. Hence, there is a long range axion mediated fifth force act between the Earth and the Sun. The two massive objects attract each other if $q_1 q_2 > 0$ and repel each other if $q_1 q_2 < 0$.

In Fig.2.8 we have shown the variation of axion field with the distance for the earth. For Earth $\frac{M}{R} \equiv \frac{GM}{R} = 1.04 \times 10^{-9}$ and for Sun $\frac{M}{R} \equiv \frac{GM}{R} = 2.84 \times 10^{-6}$ which are much smaller than unity. Hence, we use the axion charge for Earth and Sun as $q_a = 4\pi f_a R$ and the axion field outside of the compact object as $a(r > R) = \frac{q_a e^{-m_a r}}{r}$.

2.4.2 Light bending due to long range axionic Yukawa potential in the Schwarzschild background

The trajectory of light or photon follows null geodesic which is given by

$$g_{\mu\nu}V^{\mu}V^{\nu} = 0, \tag{2.86}$$

where $V^{\mu} = \frac{dx^{\mu}}{d\lambda}$ is the tangent vector of a curve which is a parametrized path through spacetime $x^{\mu}(\lambda)$, where λ is the affine parameter that varies smoothly and monotonically along the path and $x^{\mu} = (t, r, \theta, \phi)$ are the coordinates of the Schwarzschild spacetime which is defined by the metric $g_{\mu\nu}$ whose line element is

$$ds^2 = \Big(1 - \frac{2M}{r}\Big)dt^2 - \Big(1 - \frac{2M}{r}\Big)^{-1}dr^2 - r^2 d\Omega^2, \tag{2.87}$$

where we put Newton's universal gravitation constant $G = 1$ for convenience and $d\Omega^2 = d\theta^2 + \sin^2\theta d\phi^2$. M is the mass of the Sun outside of which Einstein's field solution is defined. For planar motion $\theta = \frac{\pi}{2}$ and the conserved quantities are $E = \Big(1 - \frac{2M}{r}\Big)\dot{t}$ and $L = r^2\dot{\phi}$. E and L are interpreted as the energy per unit mass and the angular momentum per unit mass of the system which are constants of motion.

Using Eq.(2.86) and Eq.(2.87) we can write for null geodesic

$$\Big(1 - \frac{2M}{r}\Big)\dot{t}^2 - \Big(1 - \frac{2M}{r}\Big)^{-1}\dot{r}^2 - r^2\dot{\phi}^2 = 0. \tag{2.88}$$

Expressions of L and E reduce Eq.(2.88) to

$$\begin{aligned} \frac{E^2}{2} &= \frac{\dot{r}^2}{2} + \frac{L^2}{2r^2}\Big(1 - \frac{2M}{r}\Big) \\ &= \frac{L^2}{2}\Big(\frac{du}{d\phi}\Big)^2 + \frac{L^2u^2}{2}(1 - 2Mu), \end{aligned} \tag{2.89}$$

where we use $\dot{r} = \frac{dr}{d\lambda} = \frac{L}{r^2}\frac{dr}{d\phi}$ and $u = \frac{1}{r}$ is the reciprocal coordinate. The right hand side of Eq.(2.89) is the effective potential of the system. As we have already discussed that the Sun and the Earth can be the sources of axions, the long range axion field mediates a Yukawa type fifth force (in addition to the gravitational force) between the Sun and the Earth which changes the effective potential per unit mass of the system as

$$V_{eff} = \frac{L^2}{2}\left(\frac{du}{d\phi}\right)^2 + \frac{L^2u^2}{2}(1-2Mu) - \frac{q_1q_2u}{4\pi M_p}e^{-\frac{m_a}{u}}, \tag{2.90}$$

where q_1 and q_2 are axion charges of the Sun and the Earth respectively, m_a is the mass of the axion and M_p is the mass of the Earth. Hence, from Eq.(2.89) and Eq.(2.90) we obtain

$$\frac{E^2}{2} = \frac{L^2}{2}\left(\frac{du}{d\phi}\right)^2 + \frac{L^2u^2}{2}(1-2Mu) - \frac{q_1q_2u}{4\pi M_p}e^{-\frac{m_a}{u}}. \tag{2.91}$$

Differentiating Eq.(2.91) with respect to ϕ, we get

$$0 = \frac{d^2u}{d\phi^2} + u - 3Mu^2 - \frac{q_1q_2}{4\pi M_pL^2}e^{-\frac{m_a}{u}} - \frac{q_1q_2m_a}{4\pi M_pL^2u}e^{-\frac{m_a}{u}}. \tag{2.92}$$

Expanding Eq.(2.92) up to the leading order of m_a, we obtain

$$\frac{d^2u}{d\phi^2} + u = 3Mu^2 + \frac{q_1q_2}{4\pi M_pL^2} - \frac{q_1q_2m_a^2}{8\pi M_pL^2u^2}, \tag{2.93}$$

where the first term in r.h.s of Eq.(2.93) arises in Einstein's standard GR calculation which causes the light bending and the last two terms contribution is within the experimental uncertainty in the measurement of light bending. This arises due to long range axion mediated Yukawa type fifth force between the celestial objects which change the effective potential.

Suppose the solution of the Eq.(2.93) is $u(\phi) = u_0(\phi) + \Delta u(\phi)$, where $u_0(\phi)$ is the solution for the homogeneous equation of Eq.(2.93) and $\Delta u(\phi)$ is the solution due to GR correction and the Yukawa contribution. Thus we can write

$$\frac{d^2u_0}{d\phi^2} + u_0 = 0. \tag{2.94}$$

The solution of Eq.(2.94) is $u_0 = \dfrac{\sin\phi}{b}$, where b denotes impact parameter and

$$\frac{d^2\Delta u}{d\phi^2} + \Delta u = 3M\frac{sin^2\phi}{b^2} + \frac{q_1q_2}{4\pi M_pL^2} - \frac{q_1q_2m_a^2b^2}{8\pi M_pL^2\sin^2\phi}. \tag{2.95}$$

The solution of Eq.(2.95) becomes

$$\Delta u(\phi) = \frac{3M}{2b^2}\left(1+\frac{1}{3}\cos 2\phi\right) + \frac{q_1q_2}{4\pi M_pL^2} - \frac{q_1q_2m_a^2b^2}{8\pi M_pL^2}[\cos\phi\ln|\text{cosec}\phi + \cot\phi| - 1]. \tag{2.96}$$

Therefore, the total solution of Eq.(2.93) is

$$u=\frac{\sin\phi}{b}+\frac{3M}{2b^2}\Big(1+\frac{1}{3}\cos 2\phi\Big)+\frac{q_1q_2}{4\pi M_pL^2}-\frac{q_1q_2m_a^2b^2}{8\pi M_pL^2}[\cos\phi\ln|\mathrm{cosec}\phi+\cot\phi|-1]. \tag{2.97}$$

Far from the Sun, $u\to 0$ as $\phi\to 0$. Hence, from Eq.(2.97) we can write the change in the angular coordinate ϕ is

$$\delta\phi=\frac{\frac{-2M}{b^2}-\frac{q_1q_2}{4\pi M_pL^2}(1-0.347m_a^2b^2)}{\frac{1}{b}+\frac{q_1q_2m_a^2b^2}{8\pi M_pL^2}}. \tag{2.98}$$

The contribution to $\delta\phi$ before and after the turning point are equal from symmetry. Hence the total light bending is

$$\Delta\phi=-2\delta\phi=\frac{\frac{4M}{b^2}+\frac{q_1q_2}{2\pi M_pL^2}(1-0.347m_a^2b^2)}{\frac{1}{b}+\frac{q_1q_2m_a^2b^2}{8\pi M_pL^2}}. \tag{2.99}$$

In absence of long range axion mediated Yukawa type of force ($q_1=q_2=0$), the deflection of light can be written from Eq.(2.99) as

$$\Delta\phi=\frac{4M}{b}=\frac{4GM}{R_\odot c^2}=1.75\ \ \text{arcsec}, \tag{2.100}$$

which is the standard GR result. We assume $b\sim R_\odot$ as the solar radius, c is the speed of light in vacuum. We replace $M\to GM$ and $b\to R_\odot c^2$ in the last step to write the deflection in SI system of units.

2.4.3 Shapiro time delay due to long range axionic Yukawa potential in the Schwarzschild background

To calculate the Shapiro time delay due to long range axion mediated Yukawa potential, we can write Eq.(2.91) as

$$\frac{E^2}{2}=\frac{\dot{r}^2}{2}+\frac{L^2}{2r^2}\Big(1-\frac{2M}{r}\Big)-\frac{q_1q_2}{4\pi M_pr}e^{-m_ar}, \tag{2.101}$$

where $\dot{r}=\frac{dr}{d\lambda}=\frac{dr}{dt}\frac{dt}{d\lambda}=\frac{E}{\Big(1-\frac{2M}{r}\Big)}\frac{dr}{dt}$. Thus, Eq.(2.101) becomes

$$\frac{E^2}{2}=\frac{E^2}{2\Big(1-\frac{2M}{r}\Big)^2}\Big(\frac{dr}{dt}\Big)^2+\frac{L^2}{2r^2}\Big(1-\frac{2M}{r}\Big)-\frac{q_1q_2}{4\pi M_pr}e^{-m_ar}. \tag{2.102}$$

For the closest approach of light, $\frac{dr}{dt} = 0$ at $r = r_0$. Hence, from Eq.(2.102) we can write

$$\frac{L^2}{E^2} = \left(1 + \frac{q_1 q_2 e^{-m_a r_0}}{2\pi M_p E^2 r_0}\right)\frac{r_0^2}{\left(1 - \frac{2M}{r_0}\right)}. \tag{2.103}$$

In absence of axion mediated Yukawa potential, Eq.(2.103) becomes $\frac{L^2}{E^2} = \frac{r_0^2}{\left(1 - \frac{2M}{r_0}\right)}$ which is the standard result in GR. Hence using Eq.(2.103), we can write Eq.(2.102) as

$$\frac{E^2}{2} = \frac{E^2}{2\left(1 - \frac{2M}{r}\right)^2}\left(\frac{dr}{dt}\right)^2 + \frac{1}{2r^2}\left(1 - \frac{2M}{r}\right)\frac{E^2 r_0^2}{\left(1 - \frac{2M}{r_0}\right)}\left(1 + \frac{q_1 q_2 e^{-m_a r_0}}{2\pi M_p E^2 r_0}\right) - \frac{q_1 q_2}{4\pi M_p r}e^{-m_a r}. \tag{2.104}$$

We can obtain the rate of change of r from Eq.(2.104) as

$$\frac{dr}{dt} = \left(1 - \frac{2M}{r}\right)\left[1 - \frac{1}{r^2}\left(1 - \frac{2M}{r}\right)\frac{r_0^2}{\left(1 - \frac{2M}{r_0}\right)}\left(1 + \frac{q_1 q_2 e^{-m_a r_0}}{2\pi M_p E^2 r_0}\right) - \frac{q_1 q_2}{2\pi M_p E^2 r}e^{-m_a r}\right]^{\frac{1}{2}}. \tag{2.105}$$

The time taken by the light to reach from r_0 to r is

$$t = \int_{r_0}^{r} \frac{dt}{dr} dr. \tag{2.106}$$

Hence, using Eq.(2.105) we obtain,

$$t = \int_{r_0}^{r} dr \frac{1}{\left(1 - \frac{2M}{r}\right)}\left[1 - \frac{r_0^2}{r^2}\frac{\left(1 - \frac{2M}{r}\right)}{\left(1 - \frac{2M}{r_0}\right)}\left(1 + \frac{q_1 q_2 e^{-m_a r_0}}{2\pi M_p E^2 r_0}\right) - \frac{q_1 q_2}{2\pi M_p E^2 r}e^{-m_a r}\right]^{-\frac{1}{2}}. \tag{2.107}$$

If there is no massive gravitating body between Earth and Venus, then we can put $M = 0$ in Eq.(2.107) and the required time becomes

$$\begin{aligned} t = t_1 = \sqrt{r^2 - r_0^2} - \frac{1}{2}\frac{a_0}{r}(-r_0^2 + 2r^2) - \frac{b_0 e^{-c_0 r} r_0^2}{48 r^4}[-36r^2(-1 + c_0 r) + \\ r_0^2(6 - 2c_0 r + c_0^2 r^2)] + \frac{b_0}{48}(48 + 36 c_0^2 r_0^2) Ei(-c_0 r) + \mathcal{O}(c_0^3), \end{aligned} \tag{2.108}$$

where $a_0 = \frac{q_1 q_2 e^{-m_a r_0}}{4\pi M_p E^2 r_0}$, $b_0 = \frac{q_1 q_2}{4\pi M_p E^2}$, and $c_0 = m_a$. $Ei(x)$ is the exponential integral function which is defined as $Ei(x) = -\int_{-x}^{\infty} \frac{e^{-t}}{t} dt$.

Now if there is a massive gravitating body- the Sun between Earth and Venus then $M \neq 0$ and from Eq.(2.107) we obtain the required time after expanding and linearising in M as

$$t = t_2 = \sqrt{r^2 - r_0^2} + 2M \ln \frac{\sqrt{r^2 - r_0^2} + r}{r_0} + M\left(\frac{r - r_0}{r + r_0}\right)^{\frac{1}{2}} - \frac{(2M + r_0)a_0 r_0}{\sqrt{r^2 - r_0^2}} + \frac{b_0}{2}\left[\sqrt{r^2 - r_0^2}\left\{2c_0(-1 + c_0 M) + \frac{c_0^2 r}{2} + \frac{2M}{r^2} + \frac{2}{r} - \frac{4c_0 M}{r}\right\}\right]. \tag{2.109}$$

Hence, if there is no massive gravitating body between Earth and Venus then the total time taken by the signal to go from Earth to Venus and then comes back to the Earth in $r \gg r_0$ limit is

$$T_1 = 2t_1 = 2\Big[\sqrt{r_e^2 - r_0^2} + \sqrt{r_v^2 - r_0^2} - a_0 r_e - a_0 r_v + \frac{b_0}{48}(48 + 36c_0^2 r_0^2)\{Ei(-c_0 r_e) + Ei(-c_0 r_v)\}\Big], \tag{2.110}$$

where r_e is the distance between Earth and Sun and r_v is the distance between Venus and Sun. Similarly the time taken by the signal to go from Earth to Venus and returns to Earth in presence of the Sun in $r \gg r_0$ limit is

$$T_2 = 2t_2 = 2\Big[\sqrt{r_e^2 - r_0^2} + \sqrt{r_v^2 - r_0^2} + 2M \ln\left(\frac{2r_e}{r_0}\right) + 2M \ln\left(\frac{2r_v}{r_0}\right) + 2M + b_0 c_0 r_e(-1 + c_0 M) + b_0 c_0 r_v(-1 + c_0 M) + b_0 - 2c_0 M b_0 + \frac{b_0 c_0^2}{4}(r_e^2 + r_v^2)\Big]. \tag{2.111}$$

Therefore, the excess time due to GR correction and the axion mediated fifth force is

$$\Delta T = T_2 - T_1 = 4M\Big[\ln\left(\frac{4r_e r_v}{r_0^2}\right) + 1\Big] + 2b_0 c_0(-1 + c_0 M)(r_e + r_v) + \frac{b_0 c_0^2}{2}(r_e^2 + r_v^2) + 2b_0 - 4c_0 M b_0 + 2a_0(r_e + r_v) + \frac{b_0}{24}(48 + 36c_0^2 r_0^2)[Ei(-c_0 r_e) + Ei(-c_0 r_v)]. \tag{2.112}$$

In absence of axion mediated fifth force, $a_0 = 0, b_0 = 0, c_0 = 0$ and from Eq.(2.112) we get back the standard GR result

$$\Delta T = \frac{4GM}{c^3}\Big[\ln\left(\frac{4r_e r_v}{r_0^2}\right) + 1\Big] = 2 \times 10^{-4}\text{sec}, \tag{2.113}$$

where we reinsert G and c.

2.4.4 Constraints on Axion Mass and Decay Constant from Light Bending and Shapiro Time Delay Measurements

The contribution of axions in the light bending must be within the excess of the GR prediction which implies $(\Delta\phi)_{obs} - \Delta\phi_{GR} \geq \Delta\phi_{axions}$. Hence, from Eq.(2.99) we can write

$$\Delta\phi_{axions} = \frac{\frac{4M}{b^2} + \frac{q_1 q_2}{2\pi M_p L^2}(1 - 0.347 m_a^2 b^2)}{\frac{1}{b} + \frac{q_1 q_2 m_a^2 b^2}{8\pi M_p L^2}} - \frac{4M}{b}, \tag{2.114}$$

where $q_1 = 4\pi f_a R_\odot$, $q_2 = 4\pi f_a R_\oplus$, $L^2 = MD(1 - e^2)$. The parameters $b \sim R_\odot$ and $R_\oplus$ are the solar radius and Earth radius respectively. D is the semi major axis of Earth's orbit and e is the orbital eccentricity. Now the uncertainty in the measurement of light bending from the GR prediction is 10^{-4} arcsec which puts upper bound on the axion decay constant f_a from Eq.(2.114) as

$$f_a \lesssim 1.58 \times 10^{10}\ \mathrm{GeV}. \tag{2.115}$$

Similarly, the contribution of axions in the Shapiro time delay must be within the excess of GR result which yields $(\Delta T)_{axions}$ from Eq.(2.112) as

$$\begin{aligned}\Delta T_{axions} = {} & 2b_0 c_0(-1 + c_0 M)(r_e + r_v) + \frac{b_0 c_0^2}{2}(r_e^2 + r_v^2) + 2b_0 - 4c_0 M b_0 + \\ & 2a_0(r_e + r_v) + \frac{b_0}{24}(48 + 36 c_0^2 r_0^2)[Ei(-c_0 r_e) + Ei(-c_0 r_v)].\end{aligned} \tag{2.116}$$

Now the uncertainty in the measurement of Shapiro time delay from the GR result is 2×10^{-5} s which puts upper bound on the axion decay constant by using Eq.(2.116) as

$$f_a \lesssim 9.85 \times 10^{6}\ \mathrm{GeV}. \tag{2.117}$$

Hence, Shapiro time delay gives the stronger bound on axion decay constant f_a. The mass of the axion is constrained by the distance between the Earth and Sun which gives $\frac{1}{D} = m_a \lesssim 1.33 \times 10^{-18}$ eV. Since, the separation between the massive objects is greater than the sizes of the individual objects, $m_a \lesssim \frac{1}{D}$ gives the stronger bound. In Fig.2.9 we numerically solve Eq.(2.92) and Eq.(2.107) and show the bounds on axion parameters obtained from light bending and Shapiro time delay. The red and blue curves denote the variation of f_a with m_a for light bending and Shapiro time delay measurements respectively. The regions above those curves are excluded. The

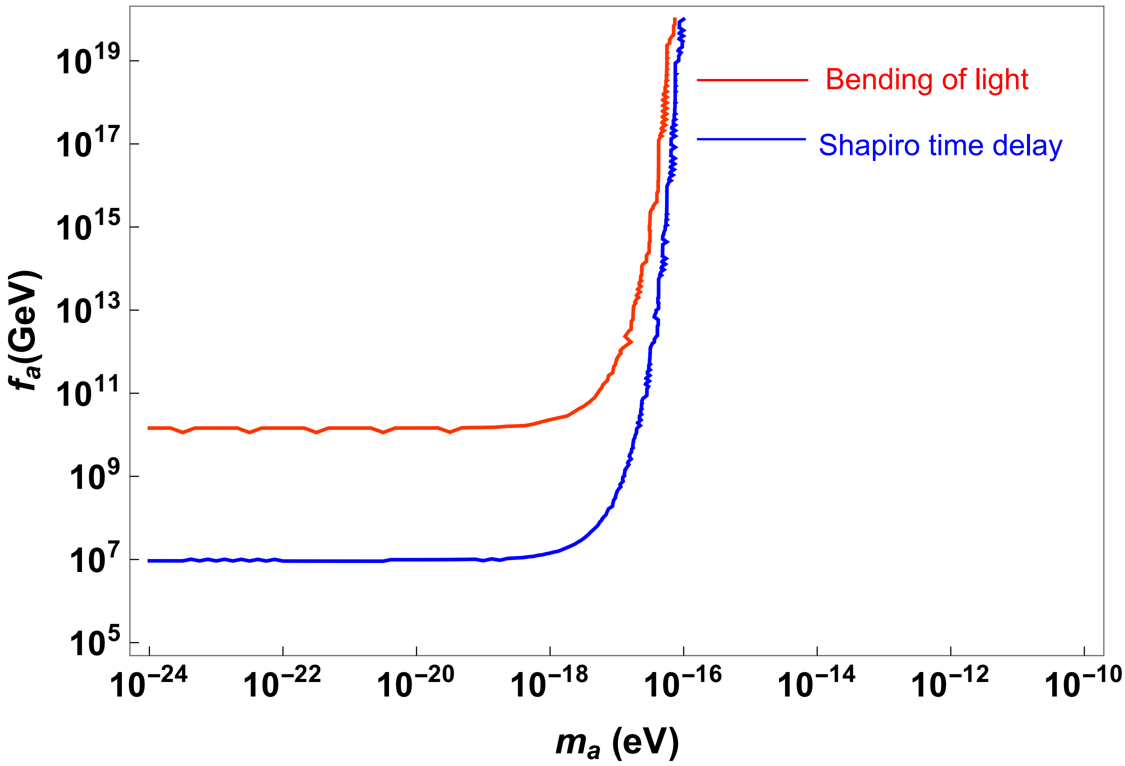

Figure 2.9: Exclusion plot in $m_a - f_a$ plane. The regions above these lines are excluded.

Shapiro time delay puts the stronger bound on f_a compared to the gravitational light bending and orbital period loss of compact binary systems. This bound is also stronger than SN1987A and other astrophysical bounds in the parameter space of interest, since we have obtained upper bound on f_a. Also, our bounds are consistent with Lyman-α constraints, disfavour ALPs as FDM candidates.

We obtain the upper bounds on the ratio of axionic fifth force to the gravitational force as $\alpha = \frac{q_1 q_2}{4\pi G m_1 m_2} \lesssim 10^{-2}$ from light bending and $\alpha = \frac{q_1 q_2}{4\pi G m_1 m_2} \lesssim 4.12 \times 10^{-9}$ from Shapiro time delay. The Shapiro time delay puts a stronger bound on α. Hence the axionic fifth force is weaker than the gravitational force by a factor of roughly 10^9. In Table 2.3 we summarize the bounds on f_a and m_a from light bending and Shapiro time delay [63].

In Fig.2.10 we plot Eq.(2.90) and show the variation of effective potential with distance. The nature of the effective potential does not change from its standard GR result in presence of long range axionic Yukawa potential. We have the circular unstable orbit at $r = 3M$.

Table 2.3: Summary of axion decay constant (f_a) and the ratio of axionic fifth force to gravity (α) obtained from light bending and Shapiro time delay for ALPs of mass $m_a \lesssim 1.33 \times 10^{-18}$ eV.

Experiments	axion decay constant (f_a)	α
Light bending	$\lesssim 1.58 \times 10^{10}$ GeV	$\lesssim 10^{-2}$
Shapiro time delay	$\lesssim 9.85 \times 10^{6}$ GeV	$\lesssim 4.12 \times 10^{-9}$

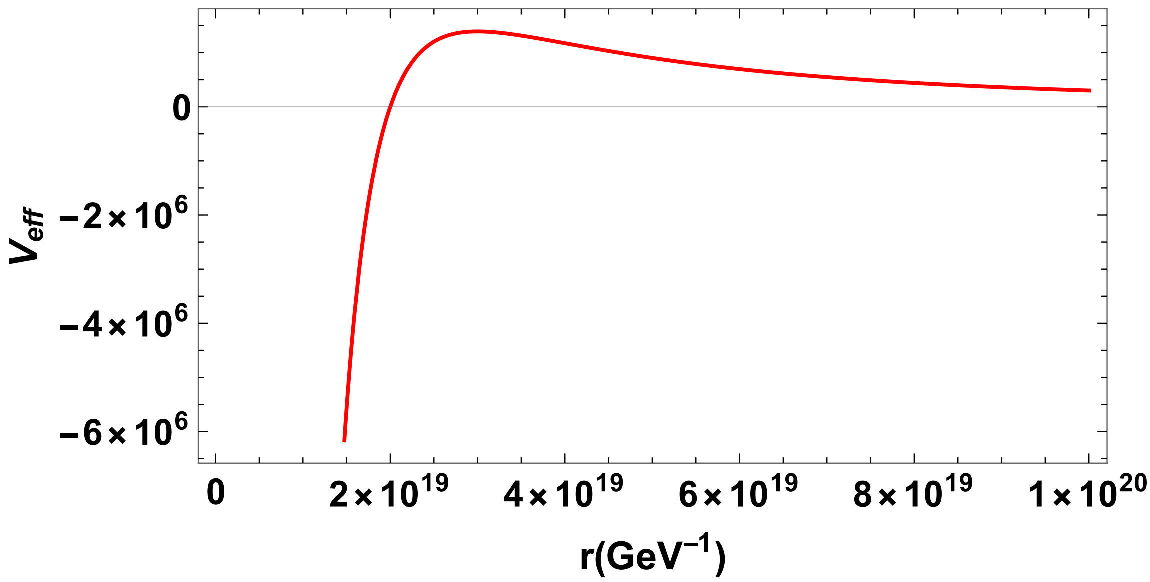

Figure 2.10: Variation of effective potential with distance.

The earth and Sun can behave as the sources of axions of mass $m_a \in (10^{-21}\text{ eV} - 10^{-22}\text{ eV})$ and they can be the candiates of FDM if f_a is $\mathcal{O}(10^{17}\text{ GeV})$ and $\theta_0 \sim \mathcal{O}(1)$. Any value of f_a other than 10^{17} GeV requires fine tuning of θ_0 which can take values $-\pi < \theta_0 < \pi$. The Shapiro time delay gives the stronger bound on f_a as $f_a \lesssim 9.85 \times 10^6$ GeV and Eq.(2.11) implies that if the ultralight ALPs have to satisfy FDM relic density, then the ALPs do not couple with quarks.

2.5 Discussions

In this chapter, we have discussed the prospects for light axion searches from the orbital period loss of compact binary systems, birefringent effect from the pulsars, gravitational light bending, and Shapiro time delay. We have discussed if ALPs are sourced by compact stars such as neutron stars and white dwarfs then the axionic field has a long range behaviour over a distance between the binary companions. Due to such axionic field, the binary system will emit scalar Larmor radiation. Although the gravitational quadrupole radiation mainly contributes to the decay of orbital period, the contribution of scalar radiation is not negligible. However, its contribution must be within the excess value of the observed decay in the orbital period. For the NS-NS and NS-WD binary systems, an additional axionic "fifth" force arises which is not relevant as much as the scalar radiation in our study. We have obtained the axionic profile for an isolated compact star assuming it to be a spherical object of uniform mass density. We have identified the form of effective axionic charge of the compact star [167] and its GR correction. We have also considered the eccentricity of the orbit of the binary system– a generalization of the previous results for axionic scalar radiation [167]. Using the updated formula for the total power radiated, we have studied four compact binary systems: PSR J0348+0432, PSR J0737-3039, PSR J1738+0333, and PSR B1913+16 (Hulse-Taylor binary pulsar). The upper bound on the axion decay constant f_a is found as $f_a \lesssim \mathcal{O}(10^{11}\text{ GeV})$. The bound $f_a \lesssim \mathcal{O}(10^{11}\text{ GeV})$ from NS-WD binaries do not favour ALPs as the FDM.

If the pulsar is immersed in a low mass axionic potential, then it can also develop a long range axion hair outside of the pulsar which can rotate the polarization of the electromagnetic radiation emitted from the same pulsar. Here we do not need any external magnetic field for the optical rotation. The birefringent angle that we have first derived is independent of the angular frequency of rotation, the radius of the pulsar, the mass of the axion, and the axion photon coupling constant. Our result is true for axions of mass $m_a < 10^{-11}$ eV and $f_a \lesssim \mathcal{O}(10^{17}$ GeV$)$. We obtain the birefringent angle as 0.42° if the pulsar has a long range axionic hair. The derived birefringent angle due to axion photon interaction may contribute to the systematic deviation of measuring the linear polarization angle of pulsar light which is $\leq 1.0^\circ$.

Like neutron stars, white dwarfs, and pulsars, celestial objects like planets and Sun can also be the source of axions. The Shapiro time delay gives the stronger bound on the axion decay constant as $f_a \lesssim 9.85 \times 10^6$ GeV. The sign change of the axion potential due to high nucleon density causes the Sun and the Earth to the possible sources of ALPs. The mass of axion is constrained by the distance between Earth and Sun which gives the upper bound on the mass of axion as $m_a \lesssim 1.33 \times 10^{-18}$ eV. The ultralight nature of axions results in a long range Yukawa behaviour of axion field over the distance between Earth and the Sun. The presence of long range Yukawa type axion mediated fifth force changes the effective gravitational potential between Earth and Sun and contributes to the time dilation along with the GR effect. The long range axionic fifth force is 10^9 times smaller than the gravitational force. The upper bounds on m_a and f_a disfavour ALPs as FDM candidates. Also, the FDM model is in strong tension from Lyman-α forest [84, 195]. Observation of the Milky Way substructure also puts a lower bound on the mass of FDM as $m_{FDM} \gtrsim 5.2 \times 10^{-21}$ eV [196] and the constraint is slightly weaker than the Lyman-α constraint. The Shapiro time delay puts the stronger bound on f_a compared to the gravitational light bending and orbital period loss of compact binary systems. This bound is also stronger than SN1987A and other astrophysical bounds in the parameter space of interest, since we have obtained upper bound on f_a. Also, our bounds are consistent with Lyman-α constraints, disfavour ALPs as FDM candidates. The ultralight ALPs can also be probed in the precision measurements of light bending and Shapiro time delay.

Chapter 3

Light Gauge Bosons (Spin 1): Long Range Force, Precision tests of Einstein's General Relativity Theory, and its Searches

3.1 Introduction

The standard model (SM) of particle physics is a gauge theory of $SU(3)_c \times SU(2)_L \times U(1)_Y$ that remains invariant under four global symmetries corresponding to the lepton numbers of the three lepton families and the baryon number. These symmetries are called the accidental symmetries. The conservation of baryon number implies that the proton is stable and the conservation of lepton number demands that the nature of neutrino is Dirac type. The SM is an effective field theory and these four global symmetries are approximate in a sense that they are expected to break by higher dimensional operators or high energy scales. One can construct three combinations of these four global symmetries in an anomaly free way and they can be gauged in the SM. These are $U(1)_{B-L}$, $U(1)_{L_e-L_\mu}$, and $U(1)_{L_\mu-L_\tau}$ ($U(1)_{L_e-L_\tau}$ is a linear combination of $U(1)_{L_e-L_\mu}$ and $U(1)_{L_\mu-L_\tau}$) [197–199]. The gauge bosons associated with these symmetries have interesting phenomenology and one can constrain the gauge boson mass and coupling from different experiments. Such U(1) gauge theories can explain several BSM physics such as neutrino mass, dark matter etc [200–204]. If the mass of the gauge boson is very small, then it can mediate long range force, where the range of the force is determined by the inverse of the gauge boson mass. The $L_i - L_j$ type of long range force can also act as a fifth force and the studies of fifth force can provide complementary checks of such particle physics models. The $L_e - L_\tau$ and $L_e - L_\mu$ long range forces from the electrons can be probed in neutrino oscillation experiments [205–208]. The $L_\mu - L_\tau$ gauge force cannot be generated in a macroscopic celestial bodies and cannot be probed in the neutrino oscillation experiments. However, if there is an inevitable $Z - Z'$ mixing then $L_\mu - L_\tau$ gauge force can be probed from the neutrino oscillation experiments [209].

The light gauge bosons can also serve as a background oscillating dark matter fields. The origin of vector gauge boson mass is model dependent where the mass can either be produced from the Stueckelberg mechanism or from the Higgs mechanism. Such small Z' mass ($< 10^{-19}$ eV) can be produced from the Fayet Ilioupoulous term in the SUSY theory or from the clockwork mechanism. The light vector dark matter is mainly produced through freeze-in, misalignment, and quantum fluctuations during inflation. As we have discussed in Chapter 2, the misalignment mechanism was first introduced for axions. Unlike axions, for vector particles, in the limit $H \gg M_{Z'}$, the energy density redshifts as $\rho_{Z'} \propto a^{-2}$. Thus the initial energy density dilutes during inflation and the misalignment mechanism for vector DM fails. This problem can be avoided by considering $\mathcal{O}(1)$ nonminimal coupling to gravity which makes the vector conformally invariant and is not affected by the expansion of the universe. In the $L_\mu - L_\tau$ model, the interaction Lagrangian describing the interaction of Z' gauge boson with the leptons in the weak basis can be written as

$$\mathcal{L} \supset g' Z'_\mu(\bar{\mu}\gamma^\mu\mu - \bar{\tau}\gamma^\mu\tau + \bar{\nu_\mu}\gamma^\mu L\nu_\mu - \bar{\nu_\tau}\gamma^\mu L\nu_\tau), \tag{3.1}$$

where $L = (1-\gamma_5)/2$. Similarly, for $L_e - L_\tau$ model, the interaction Lagrangian is

$$\mathcal{L} \supset g' Z'_\mu(\bar{e}\gamma^\mu e - \bar{\tau}\gamma^\mu\tau + \bar{\nu_e}\gamma^\mu L\nu_e - \bar{\nu_\tau}\gamma^\mu L\nu_\tau). \tag{3.2}$$

The other bounds on $L_i - L_j$ force are discussed in [210, 211]. $B - L$ symmetry can also be gauged in an anomaly free way and it can mediate long range force. The bounds on ultralight $B - L$ gauge bosons is discussed in [212]. Constraints on long and short range forces mediated by scalars and vectors are discussed in [213, 214].

In this chapter, we will discuss the phenomenology of ultralight vector gauge bosons of these symmetries in particular $U(1)_{L_\mu - L_\tau}$, $U(1)_{L_e - L_\tau}$, and $U(1)_{L_e - L_\mu}$ symmetries. We obtain bounds on the gauge bosons associated with these symmetries from the orbital period loss of compact binary systems and perihelion precession of planets. Particularly, we calculate the energy loss due to radiation of $U(1)_{L_\mu - L_\tau}$ type of gauge bosons for the orbital period loss of compact binary systems and obtain bound on the gauge coupling. We also calculate the contribution of $U(1)_{L_e - L_{\mu,\tau}}$ gauge bosons between the planets and Sun in the measurements of the perihelion precession of planets and obtain bounds on gauge coupling. We have also studied that these gauge bosons can also mediate Yukawa type fifth force between the compact/celestial objects.

The chapter is organized as follows. In Section 3.2, we discuss the constraints on ultralight $L_\mu - L_\tau$ type of vector gauge boson obtained from the orbital period loss of the compact binary systems. This section is based on [65]. In Section 3.3, we discuss the constraints on ultralight $L_e - L_{\mu,\tau}$ type of vector gauge bosons from the perihelion precession of planets which is based on the work done in [66]. Finally, in Section 3.4 we conclude the chapter with the important results.

3.2 Constraints on Vector Gauge Boson of $L_\mu - L_\tau$ type from Compact Binary Systems

In this section, we point out that neutron star (NS) can have a large number of muons and, therefore, the neutron star-neutron star (NS-NS) binaries and neutron star-white dwarf (NS-WD) binaries can radiate ultralight $L_\mu - L_\tau$ vector gauge bosons.

Besides muons, there are electrons, protons and neutrons inside a neutron star. There is around 10^{55} muons compared to about 10^{57} neutrons [215, 215–219] in a typical old neutron star.

For massive vector gauge boson radiation from the NS-NS, and NS-WD binaries, the orbital frequency of the binary orbit should be greater than the mass of the particle which restricts the mass spectrum of the massive gauge boson to $M_{Z'} < 10^{-19}$ eV. A

$L_\mu - L_\tau$ gauge boson (Z') exchange between muons of the neutron star gives rise to the Yukawa type potential $V(r) = \frac{g^2}{4\pi r}e^{-M_{Z'}r}$. The range λ of the force is determined by $\lambda = \frac{1}{M_{Z'}}$. For the emission of this ultra light vector gauge boson of mass $M_{Z'} < 10^{-19}$ eV from NS-NS and NS-WD binaries, the lower bound of the range of this force is $\lambda = 1/M_{Z'} > 10^{12}$ m. This ultra light mass or nearly massless gauge boson can mediate long range fifth force between the neutron stars of the binary system. Since there is no muon charge for white dwarf, the fifth force for NS-WD binaries are zero. In the following, we calculate the orbital energy loss due to radiation of proca vector boson and massive vector gauge boson of $L_\mu - L_\tau$ anomaly free gauge theory [197, 220–222] from the four compact binary (NS-NS, NS-WD) systems.

3.2.1 Calculation of the fraction of muons inside a compact star

The chemical potential of relativistic degenerate electrons in NS is

$$\mu_e = (m_e^2 + k_{fe}^2)^{\frac{1}{2}} = \left[m_e^2 + (3\pi^2\rho Y_e)^{\frac{2}{3}}\right]^{\frac{1}{2}}, \tag{3.3}$$

where m_e is the mass of the electron, k_f is the Fermi momentum, ρ is the nucleon number density and Y_e is the electron fraction. From the charge neutrality of the neutron star, $Y_p = Y_e + Y_\mu$ and $Y_n + Y_p = 1$. Above the nuclear matter density, when μ_e exceeds the mass of muon (~ 105 MeV, non-relativistic), electrons can convert into muons at the edge of the Fermi sphere. So $e^- \to \mu^- + \nu_e + \bar{\nu_\mu}$, $p + \mu^- \to n + \nu_\mu$, and $n \to p + \mu^- + \bar{\nu_\mu}$ maybe energetically favourable. Hence, both muons and electrons can stay in neutron star and stabilize through beta equilibrium. Thus the β stability condition becomes

$$\mu_n - \mu_p = \mu_e = \mu_\mu = \left[m_\mu^2 + (3\pi^2\rho Y_\mu)^{\frac{2}{3}}\right]^{\frac{1}{2}}, \tag{3.4}$$

where Y_μ is the muon fraction inside the neutron star [223]. Muon decay ($\mu^- \to e^- + \bar{\nu_e} + \nu_\mu$) inside the neutron star is prohibited by Fermi statistics. The Fermi energy of the electron is roughly 100 MeV (relativistic) whereas the Fermi energy of the muon is roughly 30 MeV (non relativistic). Hence the muon decay cannot take place as the energy levels of the electron are all filled up to the Fermi surface and the final state electron is Fermi blocked. For white dwarf, the Fermi energy of muon is very small (~ 1 eV) and Fermi suppression does not really apply. Thus muon decay is not obstructed in white dwarfs.

From the beta equilibrium condition the chemical potentials of muons and electrons inside the neutron star are equal which implies,

$$\rho_\mu = \frac{m_e^3}{3\pi^2}\Big[1 + \frac{(3\pi^2\rho Y_e)^{\frac{2}{3}}}{m_e^2} - \frac{m_\mu^2}{m_e^2}\Big]^{\frac{3}{2}}. \tag{3.5}$$

The electron fraction (Y_e) is given as [215]

$$Y_e = \frac{p_1 + p_2\rho + p_6\rho^{3/2} + p_3\rho^{p_7}}{1 + p_4\rho^{3/2} + p_5\rho^{p_7}}, \tag{3.6}$$

where p's are the parameters which can take different values for different QCD equation of states. Assuming there are 10^{57} nucleons, the nucleon number density is $\rho = 0.238\ \mathrm{fm}^{-3}$ and $Y_e = 0.052$ (here we put the values of p parameters for BSK24 [215] equation of state). From Eq. (3.5) we obtain the muon number density $\rho_\mu = 3.11 \times 10^4\ \mathrm{MeV}^3$. Hence, the total number of muons inside the neutron star is $\rho_\mu \times \frac{4}{3}\pi R^3 = 1.67 \times 10^{55}$, where we assume the radius of the neutron star is $R = 10$ km. In the following, we take the muon number as $N = 10^{55}$.

3.2.2 Energy loss due to massive proca vector field radiation

If there is a mismatch between the observed period loss of the binary system and its theoretical prediction from the gravitational quadrupole radiation, then other particles may also be radiated from the binaries which give hints for new physics. Neutron stars have a large number of muon charges ($N \approx 10^{55}$) and Z' massive proca vector boson can be emitted from the NS in addition to the gravitational radiation, contributing to the observed orbital period decay. Since, the Compton wavelength of radiation ($\lambda = 10^{12}$ m) is much larger than the size of NS (10 km), one can treat the NS as a point source. We will treat the radiation of massive Z' vector bosons from the NS classically. The classical current of muons J^μ in the NS is determined from the Kepler orbits and assuming the interaction vertex as $gZ'_\mu J^\mu$, where g is the coupling constant. Therefore, the rate of massive Z' boson radiation is given by

$$d\Gamma = g^2 \sum_{\lambda=1}^{3} [J^\mu(k')J^{\nu *}(k')\epsilon_\mu^\lambda(k)\epsilon_\nu^{\lambda *}(k)] 2\pi\delta(\omega - \omega')\frac{d^3k}{(2\pi)^3 2\omega}, \tag{3.7}$$

where the Fourier transform of $J^\mu(x)$ is $J^\mu(k')$ and $\epsilon_\mu^\lambda(k)$ denotes the polarization vector of massive vector gauge boson. The polarization sum is

$$\sum_{\lambda=1}^{3}\epsilon_\mu^\lambda(k)\epsilon_\nu^{\lambda*}(k)=-g_{\mu\nu}+\frac{k_\mu k_\nu}{M_{Z'}^2}. \tag{3.8}$$

Therefore, the emission rate is

$$\begin{aligned} d\Gamma =&\frac{g^2}{2(2\pi)^2}\int\Big[-|J^\mu(\omega')|^2+\frac{1}{M_{Z'}^2}\Big(|J^0(\omega')|^2\omega^2+J^i(\omega')J^{j*}(\omega')k_ik_j+\\ &2J^0(\omega')J^{i*}(\omega')k_0k_i\Big)\Big]\times\delta(\omega-\omega')\omega\Big(1-\frac{M_{Z'}^2}{\omega^2}\Big)^{\frac{1}{2}}d\omega d\Omega_k. \end{aligned} \tag{3.9}$$

The momentum four vector of the Z' boson is $k_\mu=(\omega,-\vec{k})$, $k_i=|\vec{k}|\hat{n}_i$ and $k_j=|\vec{k}|\hat{n}_j$. The third term in the first bracket will not contribute anything because

$$\int\hat{n}_i d\Omega_k=0,\qquad \int\hat{n}_i\hat{n}_j d\Omega_k=\frac{4\pi}{3}\delta_{ij}. \tag{3.10}$$

Therefore, the rate of energy loss due to massive Z' boson radiation is

$$\begin{aligned} \frac{dE}{dt}=&\frac{g^2}{2\pi}\int\Big[-|J^0(\omega')|^2+|J^i(\omega')|^2+\frac{\omega^2}{M_{Z'}^2}|J^0(\omega')|^2+\frac{\omega^2}{3M_{Z'}^2}|J^i(\omega')|^2\Big(1-\frac{M_{Z'}^2}{\omega^2}\Big)\Big]\\ &\times\delta(\omega-\omega')\omega^2\Big(1-\frac{M_{Z'}^2}{\omega^2}\Big)^{\frac{1}{2}}d\omega. \end{aligned} \tag{3.11}$$

The current density for the binary stars is written as

$$J^\mu(x)=\sum_{a=1,2}Q_a\delta^3(\mathbf{x}-\mathbf{x}_a(t))u_a^\mu, \tag{3.12}$$

where $a=1,2$ denotes labelling of the two stars in the binary system. Q_a denotes the total charge of the NS due to presence of muons and $\mathbf{x}_a(t)$ is the location of the NS. $u_a^\mu=(1,\dot{x}_a,\dot{y}_a,0)$ denotes the non relativistic four velocity of the Keplerian orbit in the x-y plane. In the parametric form, a Kepler orbit in the x-y plane can be written as

$$x=a(\cos\xi-e),\qquad y=a\sqrt{1-e^2}\sin\xi,\qquad \Omega t=\xi-e\sin\xi, \tag{3.13}$$

where e is the eccentricity, a is the semi major axis of the elliptic orbit, and the fundamental frequency is denoted as $\Omega=\Big[\frac{G(m_1+m_2)}{a^3}\Big]^{\frac{1}{2}}$. In an eccentric orbit, the angular velocity is not constant, that means the Fourier expansion must sum over the harmonics $n\Omega$ of the fundamental. The Fourier transform of Eq. (3.12) for the spatial part of $J^\mu(\omega')$ with $\omega' = n\Omega$ is

$$J^i(\omega') = \int \frac{1}{T}\int_0^T dte^{in\Omega t}\dot{x}_a^i(t)\sum_{a=1,2} Q_a d^3\mathbf{x}' e^{-i\mathbf{k}'.\mathbf{x}'}\delta^3(\mathbf{x}' - \mathbf{x}_a(t)). \tag{3.14}$$

We expand $e^{i\mathbf{k}'.\mathbf{x}'} = 1 + i\mathbf{k}'.\mathbf{x}' + ...$ and retain the leading order term as $\mathbf{k}'.\mathbf{x}' \sim \Omega a \ll 1$ for Keplerian orbits of compact binary systems. Hence, we can write Eq. (3.14) as

$$J^i(\omega') = \frac{Q_1}{T}\int_0^T dte^{in\Omega t}\dot{x}_1^i(t) + \frac{Q_2}{T}\int_0^T dte^{in\Omega t}\dot{x}_2^i(t). \tag{3.15}$$

In the centre of mass (c.o.m) coordinates we have $\mathbf{x}_1^i = \dfrac{m_2\mathbf{x}^i}{m_1+m_2} = \dfrac{M}{m_1}\mathbf{x}^i$ and $\mathbf{x}_2^i = -\dfrac{m_1\mathbf{x}^i}{m_1+m_2} = -\dfrac{M}{m_2}\mathbf{x}^i$. $M = m_1m_2/(m_1+m_2)$ denotes the reduced mass of the binary system. Hence, in terms of the reduced mass, the spatial part of the current density becomes

$$J^i(\omega') = \frac{1}{T}\Big(\frac{Q_1}{m_1} - \frac{Q_2}{m_2}\Big)M\int_0^T dte^{in\Omega t}\dot{x}^i(t). \tag{3.16}$$

The Fourier transform of the velocity is

$$\begin{aligned}\dot{x}_n &= \frac{1}{T}\int_0^T e^{i\Omega nt}\dot{x}dt \\ &= \frac{\Omega}{2\pi}\int_0^{2\pi} e^{in(\xi - e\sin\xi)}(-a\sin\xi)d\xi,\end{aligned} \tag{3.17}$$

where $T = 2\pi/\Omega$ and, from Eq. (3.13), we have used the fact that $\dot{x}dt = -a\sin\xi d\xi$. Similarly,

$$\dot{y}_n = \frac{1}{T}\int_0^T e^{i\Omega nt}\dot{y}dt. \tag{3.18}$$

From Eq. (3.13) we use the fact that $\dot{y}dt = a\sqrt{1-e^2}\cos\xi d\xi$ and we obtain

$$\begin{aligned}\dot{y}_n &= \frac{\Omega a\sqrt{1-e^2}}{2\pi}\int_0^{2\pi} e^{in(\xi - e\sin\xi)}\cos\xi d\xi \\ &= \frac{\Omega a\sqrt{1-e^2}}{2\pi e}\int_0^{2\pi} e^{in(\xi - e\sin\xi)}d\xi.\end{aligned} \tag{3.19}$$

Using the identity of the Bessel function

$$J_n(z) = \frac{1}{2\pi}\int_0^{2\pi} e^{i(n\xi - z\sin\xi)}d\xi, \tag{3.20}$$

in Eqs. (3.17) and (3.19), we obtain the velocities in Fourier space as

$$\dot{x}_n = -ia\Omega J_n'(ne), \qquad \dot{y}_n = \frac{a\sqrt{1-e^2}\Omega}{e}J_n(ne), \tag{3.21}$$

where the prime denotes the derivative of the Bessel function with respect to the argument. Hence, we have

$$\begin{aligned} J^x(\omega') &= \Omega\Big(\frac{Q_1}{m_1}-\frac{Q_2}{m_2}\Big)M\frac{1}{2\pi}\int_0^T dte^{in\Omega t}\dot{x}^i(t) \\ &= -ia\Omega\Big(\frac{Q_1}{m_1}-\frac{Q_2}{m_2}\Big)MJ'_n(ne). \end{aligned} \tag{3.22}$$

Similarly,

$$J^y(\omega') = \Omega\Big(\frac{Q_1}{m_1}-\frac{Q_2}{m_2}\Big)M\frac{a\sqrt{1-e^2}}{e}J_n(ne). \tag{3.23}$$

Hence, the square of the spatial part of $J^\mu(\omega')$ becomes

$$\begin{aligned} |J^i(\omega')|^2 &= |J^x(\omega')|^2+|J^y(\omega')|^2 \\ &= a^2\Omega^2M^2\Big(\frac{Q_1}{m_1}-\frac{Q_2}{m_2}\Big)^2\Big[J_n'^2(ne)+\frac{(1-e^2)}{e^2}J_n^2(ne)\Big]. \end{aligned} \tag{3.24}$$

From Eq. (3.12), we have the temporal component of $J^\mu(\omega')$ as

$$J^0(\omega) = \frac{1}{2\pi}\int e^{i\mathbf{k}'.\mathbf{x}'}e^{-i\omega t}\sum_{a=1,2}Q_a\delta^3(\mathbf{x}'-\mathbf{x}_a(t))d^3\mathbf{x}'dt. \tag{3.25}$$

In the centre of mass frame, the integral results in

$$J^0(\omega) = (Q_1+Q_2)\delta(\omega)+iM\left(\frac{Q_1}{m_1}-\frac{Q_2}{m_2}\right)(k_xx(\omega)+k_yy(\omega))+\mathcal{O}((\mathbf{k}.\mathbf{r})^2), \tag{3.26}$$

where the Fourier transforms of the orbital coordinates are $x(\omega) = aJ'_n(ne)/n$ and $y(\omega) = ia\sqrt{1-e^2}J_n(ne)/ne$. The first term in Eq. (3.26) is the delta function $\delta(\omega)$ and hence does not contribute. Hnece, the second term is the leading order term and we obtain

$$|J^0(\omega)|^2 = \frac{1}{3}a^2M^2\Omega^2\left(1-\frac{M_{Z'}^2}{n^2\Omega^2}\right)\left(\frac{Q_1}{m_1}-\frac{Q_2}{m_2}\right)^2\left(J_n'^2(ne)+\frac{1-e^2}{e^2}J_n^2(ne)\right), \tag{3.27}$$

where we have used $< k_x^2 >=< k_y^2 >= k^2/3$ and $\omega = n\Omega$. Using Eqs. (3.24) and (3.27) in Eq. (3.11), we obtain energy loss rate as

$$\begin{aligned} \frac{dE}{dt} &= \frac{g^2}{3\pi}a^2M^2\Big(\frac{Q_1}{m_1}-\frac{Q_2}{m_2}\Big)^2\Bigg[\frac{\Omega^6}{M_{Z'}^2}\sum_{n>n_0}n^4\Big[J_n'^2(ne)+\frac{(1-e^2)}{e^2}J_n^2(ne)\Big]\Big(1-\frac{n_0^2}{n^2}\Big)^{\frac{3}{2}} \\ &+\Omega^4\sum_{n>n_0}n^2\Big[J_n'^2(ne)+\frac{(1-e^2)}{e^2}J_n^2(ne)\Big]\Big(1-\frac{n_0^2}{n^2}\Big)^{\frac{1}{2}}\Big(1+\frac{1}{2}\frac{n_0^2}{n^2}\Big)\Bigg], \end{aligned} \tag{3.28}$$

where $n_0 = M_{Z'}/\Omega < 1$.

We define

$$K_1(n_0, e) = \sum_{n>n_0} n^4 \Big[J_n'^2(ne) + \frac{(1-e^2)}{e^2} J_n^2(ne) \Big] \Big(1 - \frac{n_0^2}{n^2}\Big)^{\frac{3}{2}}, \tag{3.29}$$

and

$$K_2(n_0, e) = \sum_{n>n_0} n^2 \Big[J_n'^2(ne) + \frac{(1-e^2)}{e^2} J_n^2(ne) \Big] \Big(1 - \frac{n_0^2}{n^2}\Big)^{\frac{1}{2}} \Big(1 + \frac{1}{2}\frac{n_0^2}{n^2}\Big), \tag{3.30}$$

and use these notations to rewrite Eq. (3.28) as

$$\frac{dE}{dt} = \frac{g^2}{3\pi} a^2 M^2 \Big(\frac{Q_1}{m_1} - \frac{Q_2}{m_2}\Big)^2 \Omega^4 \Big(\frac{\Omega^2}{M_{Z'}^2} K_1(n_0, e) + K_2(n_0, e)\Big). \tag{3.31}$$

This is the energy loss due to radiation of proca vector massive boson from NS-NS binaries. For NS-WD binaries, the energy loss is same as Eq. (3.31) with $Q_2 = 0$ because white dwarfs do not have any muon charges.

3.2.3 Energy loss due to massive $L_\mu - L_\tau$ gauge boson radiation

If the Z' is a gauge boson, then from the gauge invariance condition $k_\mu J^\mu = 0$. Consequently, the $k_\mu k_\nu$ term in the polarization sum of Eq. (3.8) will not contribute to the energy loss formula. Using the same procedure that has been described in the previous section, we derive the energy loss rate

$$\frac{dE}{dt} = \frac{g^2}{6\pi} a^2 M^2 \Big(\frac{Q_1}{m_1} - \frac{Q_2}{m_2}\Big)^2 \Omega^4 \sum_{n>n_0} 2n^2 \Big[J_n'^2(ne) + \frac{(1-e^2)}{e^2} J_n^2(ne) \Big] \Big(1 - \frac{n_0^2}{n^2}\Big)^{\frac{1}{2}} \times \Big(1 + \frac{1}{2}\frac{n_0^2}{n^2}\Big). \tag{3.32}$$

or

$$\frac{dE}{dt} = \frac{g^2}{3\pi} a^2 M^2 \Big(\frac{Q_1}{m_1} - \frac{Q_2}{m_2}\Big)^2 \Omega^4 K_2(n_0, e), \tag{3.33}$$

where $K_2(n_0, e)$ is defined earlier in Eq. (3.30). Since $K_2(n_0, e)_{n_0=0} \geq K_2(n_0, e)_{n_0\neq 0}$ the massless limit gives a stronger bound on the energy loss. This is the energy loss due to massive vector gauge boson radiation, which has a similar form to the one previously obtained in [166]. Our method in obtaining the formula is different, where we can differentiate between the radiation rate of massive vector gauge bosons from the massive Proca fields.

The orbital period loss and the enrgy loss are related by

$$\frac{dP_b}{dt} = -6\pi G^{-3/2}(m_1 m_2)^{-1}(m_1+m_2)^{-1/2}a^{5/2}\Big(\frac{dE}{dt}+\frac{dE_{GW}}{dt}\Big), \tag{3.34}$$

where $\frac{dE_{GW}}{dt}$ denotes the energy loss rate due to gravitational radiation and is given as [177]

$$\frac{dE_{GW}}{dt} = \frac{32}{5}G\Omega^6 M^2 a^4 (1-e^2)^{-7/2}\Big(1+\frac{73}{24}e^2+\frac{37}{96}e^4\Big). \tag{3.35}$$

In the massless limit of the vector gauge boson (i.e; $M_{Z'}=0$ implies $n_0=0$), the rate of energy loss from Eq. (3.32) becomes

$$\begin{aligned}\frac{dE}{dt} &= \frac{g^2}{3\pi}a^2M^2\Big(\frac{Q_1}{m_1}-\frac{Q_2}{m_2}\Big)^2\Omega^4\sum_{n=1}^{\infty}n^2\Big[J_n'^2(ne)+\frac{(1-e^2)}{e^2}J_n^2(ne)\Big]\\ &= \frac{g^2}{6\pi}a^2M^2\Big(\frac{Q_1}{m_1}-\frac{Q_2}{m_2}\Big)^2\Omega^4\frac{(1+\frac{e^2}{2})}{(1-e^2)^{\frac{5}{2}}}.\end{aligned} \tag{3.36}$$

If the orbit is circular then the angular velocity is a constant over the orbital period and the Fourier expansion of the orbit contains only one term for $\omega=\Omega$. In an eccentric orbit the angular velocity is not constant and that means the Fourier expansion must sum over the harmonics $n\Omega$ of the fundamental.

Next, we will put constraints on the mass of the vector gauge boson and on the $L_\mu - L_\tau$ coupling constant from the decay of the orbital period of four compact binary systems using Eq. (3.33), Eq. (3.34) and Eq. (3.35).

3.2.4 Constraints on gauge boson mass and its coupling for different compact binaries

Here we consider the same four compact binary systems, PSR B1913+16, PSR J0737-3039, PSR J0348+0432, and PSR J1738+0333 that we have taken in the earlier chapter. The ultralight $L_\mu - L_\tau$ gauge boson radiation is only possible if the stars of the binary contain different charge to mass ratios. For PSR B1913+16, Hulse-Taylor binary pulsar, $(Q_1/m_1 - Q_2/m_2) = 10^{-4}$ GeV^{-1} where $Q=N$, N is the number of muons which is roughly 10^{55} [219]. For PSR J0737-3039, $(Q_1/m_1 - Q_2/m_2) = 5.27\times10^{-4}$ GeV^{-1}. The white dwarfs do not contain any muon charge. Hence, for the pulsar-white dwarf binaries, PSR J0348+0432, and PSR J1738+0333, $Q_2=0$ and the charge to mass ratio are 4.97×10^{-3} GeV^{-1} and 6.85×10^{-3} GeV^{-1} respectively. The contribution from the radiation of some vector gauge boson particles must be within the excess of the decay of the orbital period, i.e $\dot{P}_{b(vector)} \leqslant |\dot{P}_{b(observed)} - \dot{P}_{b(gw)}|$. Since $K_2(n_0, e)_{n_0=0} > K_2(n_0, e)_{n_0 \neq 0}$, the massless limit gives the stronger bound.

In Table 3.1 we show the bounds on g from fifth force and orbital period decay for the four compact binary systems having gauge boson mass $M_Z' < 10^{-19}$ eV [65].

Table 3.1: Summary of the upper bounds on gauge boson-muon coupling g for PSR B1913+16, PSR J0737-3039, PSR J0348+0432, and PSR J1738+0333. We take the mass regime as $M_Z' < 10^{-19}$ eV.

Compact binary system	g(fifth force)	g(orbital period decay)
PSR B1913+16	$\leq 4.99 \times 10^{-17}$	$\leq 2.21 \times 10^{-18}$
PSR J0737-3039	$\leq 4.58 \times 10^{-17}$	$\leq 2.17 \times 10^{-19}$
PSR J0348+0432	–	$\leq 9.02 \times 10^{-20}$
PSR J1738+0333	–	$\leq 4.24 \times 10^{-20}$

In Fig.3.1 we show the exclusion plots to constrain the coupling g for the gauge field and the proca field using Eq. (3.31) in a gauged $L_\mu - L_\tau$ scenario for four compact binary systems. The regions above the coloured lines are excluded for the corresponding binary systems. Here, a larger parameter space of g is excluded for the proca field.

Fig.3.1(a) shows that for gauge boson, the coupling g is almost constant in the mass range $M_Z' < 10^{-19}$ eV. The coupling g will increase with $M_{Z'}$ in the mass range $M_{Z'} > 10^{-19}$ eV, as only higher modes $(n > n_0 > 1)$ contribute to $K_2(n_0, e)$. For low eccentric binary orbits, the rise in g with respect to $M_{Z'}$ is sharp. Note that for circular binary orbit only the $n = 1$ mode can contribute. As a result for $M_{Z'} > \Omega$, there is no constraint on g. In Fig.3.1(b), g varies linearly with respect to $M_{Z'} (< 10^{-19}$ eV) due to the contribution of $\Omega^2/M_{Z'}^2 K_1(n_0, e)$ term for the proca field. We obtain the upper bounds on $\dfrac{M_{Z'}}{g}$ for a proca field in the small $M_{Z'}$ limit. From the orbital period decay, for PSR B1913+16, we get $M_{Z'}/g \leq 0.306$ eV, for PSR J0737-3039, we get $M_{Z'}/g \leq 2.307$ eV, for PSR J0348+0432, the bound is $M_{Z'}/g \leq 5.13$ eV and for PSR J1738+0333, the bound is $M_{Z'}/g \leq 3.19$ eV.

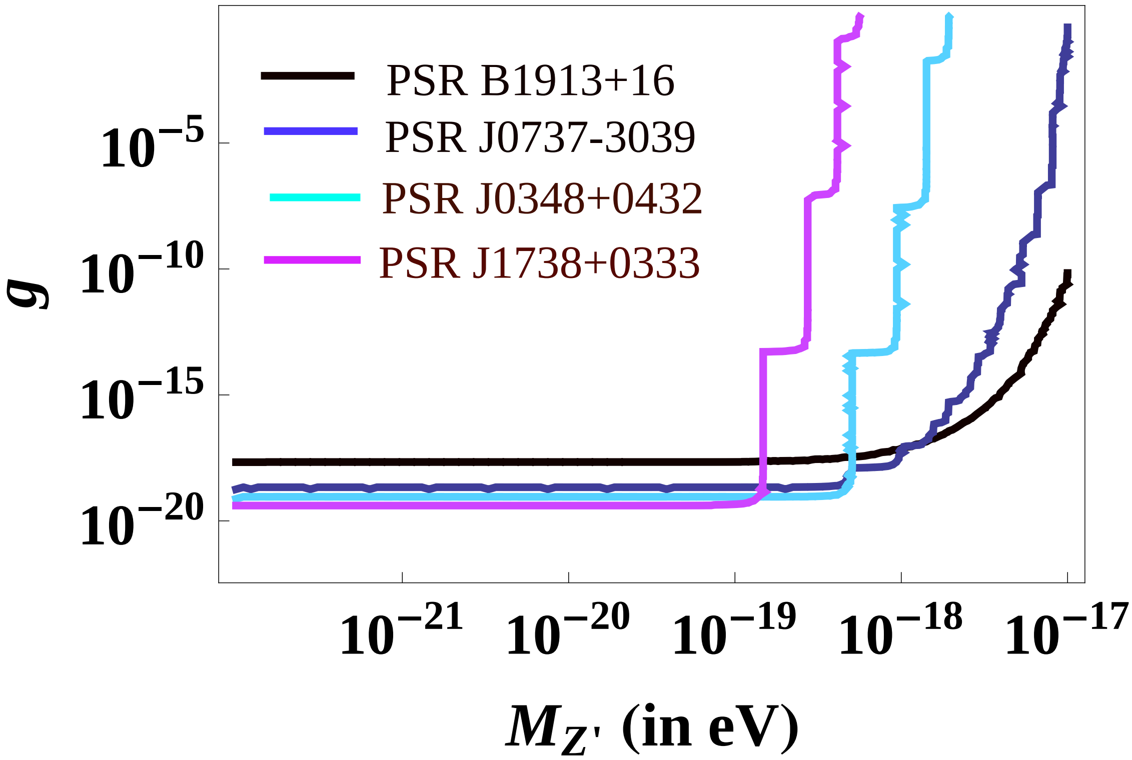

(a) g vs. $M_{Z'}$

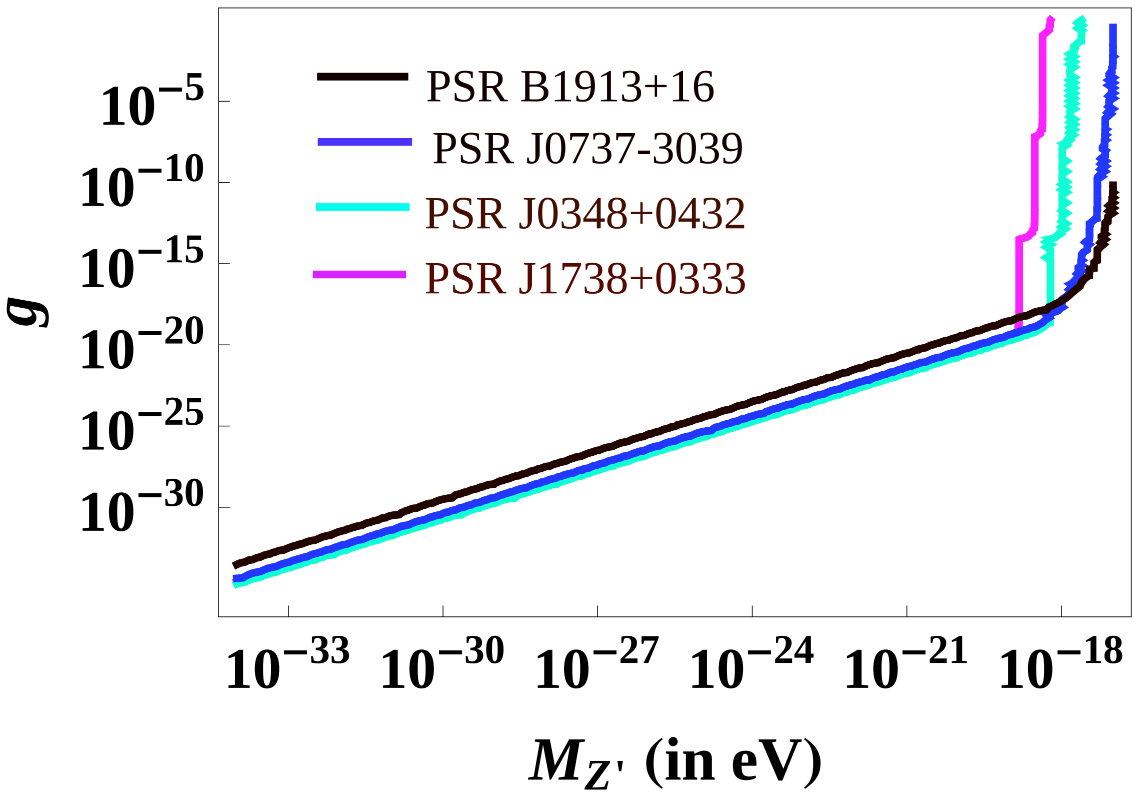

(b) g vs. $M_{Z'}$

Figure 3.1: (a) Exclusion plots to constrain the coupling of the gauge field and (b) the proca field in a gauged $L_\mu - L_\tau$ scenario for four compact binary systems. The regions above the coloured lines are excluded.

3.3 Constraints on Gauge Bosons of $L_e - L_{\mu,\tau}$ type from Perihelion Precession of Planets

It is well known that a deviation from the inverse square law force between the Sun and the planets results in the perihelion precession of the planetary orbits around the Sun. One of the most prominent example is the case of Einstein's general relativity (GR) which predicts a deviation from Newtonian $1/r^2$ gravity. In fact, one of the famous classical tests of GR was to explain the perihelion advancement of the Mercury. There was a mismatch of about 43 arc seconds per century from the observation [224] which could not be explained by Newtonian mechanics by considering all non-relativistic effects such as perturbations from the other Solar System bodies, oblateness of the Sun, etc. GR explains the discrepancy with a prediction of contribution of $42.9799''$/Julian century [9]. However, there is an uncertainty in the GR prediction which is about 10^{-3} arc seconds per century [8, 9, 224–226] for the Mercury orbit. The current most accurate detection of perihelion precession of Mercury is done by the MESSENGER mission [8]. In the near future, more accurate results will come from the BepiColombo mission [227]. Other planets also experience such perihelion shifts, although the shifts are small since they are at a larger distance from the Sun [228, 229]. The uncertainty in GR prediction opens up the possibility to explore the existence of Yukawa type potential between the Sun and the planets leading to the fifth force which is a deviation from the inverse-square law. Here, we consider the vector gauge boson mediated Yukawa type potential which arises in a gauged $L_e - L_{\mu,\tau}$ scenario and we calculate the perihelion shift of planets (Mercury, Venus, Earth, Mars, Jupiter, and Saturn) due to coupling of the ultralight vector gauge bosons with the electron current of the macroscopic objects along with the GR effect. As the Sun and the planets contain lots of electrons and the number of electrons is approximately equal to the number of baryons, we can probe $L_e - L_{\mu,\tau}$ long range force from the Solar System. The number of electrons in i'th macroscopic object (Sun or planet) is given by $N_i = M_i/m_n$, where M_i is the mass of the i'th object and m_n is the mass of nucleon which is roughly 1 GeV. $L_e - L_{\mu,\tau}$ gauge boson is mediated between the classical electron current sources: Sun and planet as shown in Fig.3.2. This causes a fifth force between the planet and the Sun along with the gravitational force and contributes to the perihelion shift of the planets. The Yukawa type of potential in such a scenario is $V(r) \simeq \frac{g^2}{4\pi r}e^{-M_{Z'}r}$, where g is the constant of coupling between the electron and the gauge boson and $M_{Z'}$ is the mass of the gauge boson. The distance between the Sun and the planets constrain the mass of the gauge boson and the strongest bound on the gauge boson mass is $M_{Z'} < 10^{-19}$ eV. Therefore, the lower bound of the range of this force is given by $\lambda = \frac{1}{M_{Z'}} > 10^9$ km. $L_e - L_{\mu,\tau}$ long range force can also be probed from MICROSCOPE experiment [230–232]. In this mass range the vector gauge boson can also be a candidate for fuzzy dark matter (FDM), although FDM is usually referred to as ultralight scalars [59, 64].

3.3.1 Perihelion precession of planets due to long range Yukawa type of potential in the Schwarzschild spacetime background

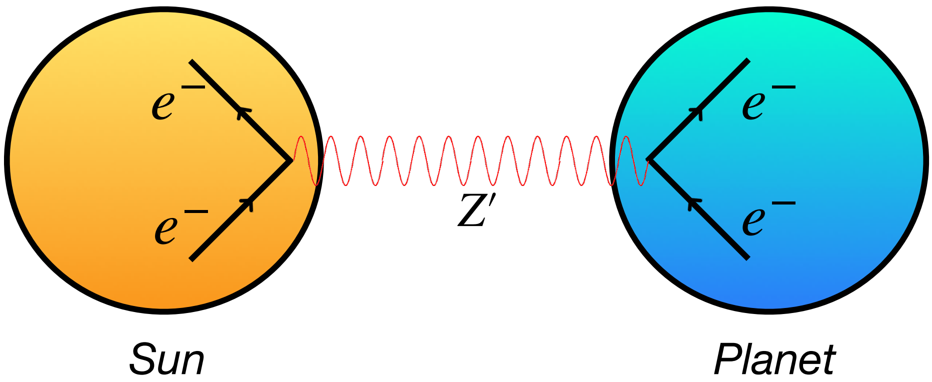

Figure 3.2: Mediation of $L_e - L_{\mu,\tau}$ vector gauge bosons between planet and Sun.

The dynamics of a Sun-planet system in presence of a Schwarzschild spacetime background and a non gravitational long range Yukawa type $L_e - L_{\mu,\tau}$ force is given by the following action:

$$S = -M_p \int \sqrt{-g_{\mu\nu}\dot{x}^\mu \dot{x}^\nu} d\tau - g \int A_\mu J^\mu d\tau, \tag{3.37}$$

where "˙" (overdot) denotes the derivative with respect to the proper time τ, $g_{\mu\nu}$ denotes the metric tensor for the background spacetime, M_p is the mass of the planet, g is the gauge coupling constant which couples the classical current $J^\mu = q\dot{x}^\mu$ of the planet with the $L_e - L_{\mu,\tau}$ gauge field A_μ due to the Sun, and q is the total charge due to the presence of electrons in the planet. We obtain the equation of motion of the planet by varying the action Eq. (3.37) as

$$\ddot{x}^{\alpha} + \Gamma^{\alpha}_{\mu\nu}\dot{x}^{\mu}\dot{x}^{\nu} = \frac{gq}{M_p}g^{\alpha\mu}(\partial_\mu A_\nu - \partial_\nu A_\mu)\dot{x}^{\nu}. \tag{3.38}$$

In Appendix B.1, we show the detailed calculation of Eq. (3.38). For the static case $A_\mu = \{V(r), 0, 0, 0\}$, where $V(r)$ is the potential leading to a long range $L_e - L_{\mu,\tau}$ Yukawa type force. $\Gamma^{\alpha}_{\mu\nu}$ denotes the Christoffel symbol for the background spacetime. For the Sun-Planet system, the background is a Schwarzschild spacetime outside the Sun and it is described by the line element

$$ds^2 = -\left(1 - \frac{2M}{r}\right)dt^2 + \left(1 - \frac{2M}{r}\right)^{-1}dr^2 + r^2 d\theta^2 + r^2\sin^2\theta d\phi^2, \tag{3.39}$$

where M denotes the solar mass. The Christoffel symbols for the metric Eq. (3.39) are given in Appendix B.2.

Hence, to obtain the solution for the temporal part of the Eq. (3.38), we write

$$\ddot{t} + \frac{2M}{r^2\left(1 - \frac{2M}{r}\right)}\dot{r}\dot{t} = \frac{gq}{M_p\left(1 - \frac{2M}{r}\right)}\frac{dV}{dr}\dot{r}. \tag{3.40}$$

Integrating Eq. (3.40) once, we get

$$\dot{t} = \frac{\left(E + \frac{gqV}{M_p}\right)}{\left(1 - \frac{2M}{r}\right)}, \tag{3.41}$$

where E is a constant of motion. E is interpreted as the total energy per unit rest mass for a timelike geodesic relative to a static observer at infinity.

Similarly, the ϕ part of Eq. (3.38) is

$$\ddot{\phi} + \frac{2}{r}\dot{r}\dot{\phi} = 0. \tag{3.42}$$

After integration, we get

$$\dot{\phi} = \frac{L}{r^2}, \tag{3.43}$$

where L is the angular momentum of the system per unit mass, which is also a constant of motion.

The radial part of Eq. (3.38) is

$$\ddot{r} - \frac{M\dot{r}^2}{r^2\left(1 - \frac{2M}{r}\right)} + \frac{M\left(1 - \frac{2M}{r}\right)}{r^2}\dot{t}^2 - r\left(1 - \frac{2M}{r}\right)\dot{\phi}^2 = \frac{gq}{M_p}\left(1 - \frac{2M}{r}\right)\frac{dV}{dr}\dot{t}. \tag{3.44}$$

Using Eqs. (3.41) and (3.43) in Eq. (3.44), we obtain

$$\ddot{r}+\frac{M}{r^2\left(1-\frac{2M}{r}\right)}\left(\left(E+\frac{gqV}{M_p}\right)^2-\dot{r}^2\right)-\frac{L^2}{r^3}\left(1-\frac{2M}{r}\right)=\frac{gq}{M_p}\left(E+\frac{gqV}{M_p}\right)\frac{dV}{dr}. \quad (3.45)$$

Again, for a timelike particle $g_{\mu\nu}\dot{x^\mu}\dot{x^\nu}=-1$ and this gives

$$\frac{\left(E+\frac{gqV}{M_p}\right)^2-1}{2}=\frac{\dot{r}^2}{2}+\frac{L^2}{2r^2}-\frac{ML^2}{r^3}-\frac{M}{r}. \quad (3.46)$$

Using Eq. (3.46) in Eq. (3.45), we get

$$\ddot{r}+\frac{3ML^2}{r^4}+\frac{M}{r^2}-\frac{L^2}{r^3}=\frac{gq}{M_p}\left(E+\frac{gqV}{M_p}\right)\frac{dV}{dr}. \quad (3.47)$$

We can also obtain Eq. (3.47) by directly differentiating Eq. (3.46).

The potential $V(r)$ is generated due to the presence of electrons in the Sun and it is given as $V(r)\simeq\frac{gQ}{4\pi r}e^{-M_{Z'}r}+\mathcal{O}\left(\frac{M}{R}\right)$, where R is the radius of the Sun. Note that we keep only the Yukawa term in the form of $V(r)$ as we are interested in the leading order contribution only (see Appendix B.3). Hence, from Eq. (3.46) we write

$$\frac{E^2-1}{2}=\frac{\dot{r}^2}{2}+\frac{L^2}{2r^2}-\frac{ML^2}{r^3}-\frac{M}{r}-\frac{g^2N_1N_2E}{4\pi M_p r}e^{-M_{Z'}r}, \quad (3.48)$$

where we have neglected $\mathcal{O}(g^4)$ term because the coupling is small and its contribution will be negligible. Here $Q=N_1$ is the number of electrons in the Sun and $q=N_2$ is the number of electrons in the planet. For planar motion, $L_x=L_y=0$, and $\theta=\pi/2$. The orbit of the planet is stable when $E<1$. In the presence of gravitational potential and fifth force, the total energy of the system per unit mass becomes $E\simeq 1-\frac{M}{2a}+\frac{g^2Qq}{4\pi M_p}\left(\frac{u_+u_-^2e^{-M_{Z'}/u_+}-u_+^2u_-e^{-M_{Z'}/u_-}}{u_+^2-u_-^2}\right)$, which is explained in Appendix B.4.

The first term on the right hand side of Eq. (3.48) represents the kinetic energy part, the second term is the centrifugal potential part, and the fourth term is the usual Newtonian potential. Due to the general relativistic $\frac{ML^2}{r^3}$ term, there is an advancement of the perihelion motion of a planet. The last term arises due to the exchange of a $U(1)_{L_e-L_{\mu,\tau}}$ gauge bosons between electrons of a planet and the Sun. Here, $M_{Z'}$ is the mass of the gauge boson. $M_{Z'}$ is constrained from the range of the potential which is basically the distance between the planet and the Sun. Using $\dot{r}=\frac{L}{r^2}\frac{dr}{d\phi}$, we write

Eq. (3.48) as

$$\left[\frac{d}{d\phi}\left(\frac{1}{r}\right)\right]^2 + \frac{1}{r^2} = \frac{E^2-1}{L^2} + \frac{2M}{r^3} + \frac{2M}{L^2 r} + \frac{g^2 N_1 N_2 E}{2\pi L^2 r M_p} e^{-M_{Z'} r}. \tag{3.49}$$

Applying $\frac{d}{d\phi}$ on both sides and using the reciprocal coordinate $u = \frac{1}{r}$ we obtain from Eq. (3.49)

$$\frac{d^2 u}{d\phi^2} + u = \frac{M}{L^2} + 3Mu^2 + \frac{g^2 N_1 N_2}{4\pi L^2 M_p} e^{-\frac{M_{Z'}}{u}} + \frac{g^2 N_1 N_2 E M_{Z'}}{4\pi L^2 M_p u} e^{-\frac{M_{Z'}}{u}}. \tag{3.50}$$

As E appears as a multiplication factor in Eq. (3.50), we take $E \approx 1$ as other terms are very small. Hence, expanding Eq. (3.50) up to the leading order of $M_{Z'}$, we get

$$\frac{d^2 u}{d\phi^2} + u = \frac{M}{L^2} + 3Mu^2 + \frac{g^2 N_1 N_2}{4\pi L^2 M_p} - \frac{g^2 N_1 N_2 M_{Z'}^2}{8\pi L^2 M_p u^2}, \tag{3.51}$$

where for non circular orbit $\frac{d}{d\phi}\left(\frac{1}{r}\right) \neq 0$. The first term on the right hand side of Eq. (3.51) is the usual term that comes in Newton's theory. The second term is the general relativistic term which is a perturbation of Newton's theory. The last two terms arise due to the presence of long range Yukawa type potential in the theory.

We write Eq. (3.51) as

$$\frac{d^2 u}{d\phi^2} + u = \frac{M'}{L^2} + 3Mu^2 - \frac{g^2 N_1 N_2 M_{Z'}^2}{8\pi L^2 M_p u^2}, \tag{3.52}$$

where $M' = M + g^2 N_1 N_2 / 4\pi M_p$.

We assume that $u = u_0(\phi) + \Delta u(\phi)$, where, $u_0(\phi)$ is the solution of Newton's theory with the effective mass M' and $\Delta u(\phi)$ is the solution due to general relativistic correction and Yukawa potential. Thus we write

$$\frac{d^2 u_0}{d\phi^2} + u_0 = \frac{M'}{L^2}. \tag{3.53}$$

The solution of Eq. (3.53) is

$$u_0 = \frac{M'}{L^2}(1 + e\cos\phi), \tag{3.54}$$

where e is the eccentricity of the planetary orbit. The equation of motion for $\Delta u(\phi)$ is

$$\begin{aligned} \frac{d^2 \Delta u}{d\phi^2} + \Delta u = {} & \frac{3MM'^2}{L^4}(1 + e^2\cos^2\phi + 2e\cos\phi) \\ & - \frac{g^2 N_1 N_2 M_{Z'}^2 L^4}{8\pi L^2 M_p M'^2 (1 + e^2\cos^2\phi + 2e\cos\phi)}. \end{aligned} \tag{3.55}$$

The solution of Eq. (3.55) is

$$\Delta u = \frac{3MM'^2}{L^4}\left[1+\frac{e^2}{2}-\frac{e^2}{6}\cos 2\phi + e\phi\sin\phi\right] - \frac{g^2N_1N_2M_{Z'}^2L^4}{8\pi L^2 M_p M'^2}\Big[-\frac{\cos\phi}{e(1+e\cos\phi)}+ \frac{\sin^2\phi}{(1-e^2)(1+e\cos\phi)} - \frac{e}{(1-e^2)^{3/2}}\sin\phi\cos^{-1}\left(\frac{e+\cos\phi}{1+e\cos\phi}\right)\Big]. \tag{3.56}$$

When Δu increases linearly with ϕ, it contributes to the perihelion precession of planets. Therefore, we identify only the related terms in Eq. (3.56), neglect all other terms, and rewrite Δu as

$$\Delta u = \frac{3MM'^2}{L^4}e\phi\sin\phi + \frac{g^2N_1N_2M_{Z'}^2L^2}{8\pi M_p M'^2}\frac{e}{(1-e^2)(1+e)}\phi\sin\phi, \tag{3.57}$$

where we have used $\cos^{-1}\left(\frac{e+\cos\phi}{1+e\cos\phi}\right) \simeq \frac{\sqrt{1-e^2}}{1+e}\phi + \mathcal{O}(\phi^2)$.

Using Eqs. (3.54) and (3.57), we get the total solution as

$$u = \frac{M'}{L^2}(1+e\cos\phi) + \frac{3MM'^2}{L^4}e\phi\sin\phi + \frac{g^2N_1N_2M_{Z'}^2L^2}{8\pi M_p M'^2}\frac{e}{(1-e^2)(1+e)}\phi\sin\phi, \tag{3.58}$$

or,

$$u = \frac{M'}{L^2}[1+e\cos\phi(1-\alpha)], \tag{3.59}$$

where,

$$\alpha = \frac{3MM'}{L^2} + \frac{g^2N_1N_2M_{Z'}^2L^4}{8\pi M_p M'^3}\frac{1}{(1-e^2)(1+e)}. \tag{3.60}$$

Under $\phi \to \phi + 2\pi$, u is not same. Hence, the planet does not follow the previous orbit. So the motion of the planet is not periodic. The change in azimuthal angle after one precession is

$$\Delta\phi = \frac{2\pi}{1-\alpha} - 2\pi \approx 2\pi\alpha. \tag{3.61}$$

The semi major axis and the orbital angular momentum are related by $a = \frac{L^2}{M'(1-e^2)}$. Using this expression in Eq. (3.61) we get

$$\Delta\phi = \frac{6\pi M}{a(1-e^2)} + \frac{g^2N_1N_2M_{Z'}^2a^2(1-e^2)}{4M_pM'(1+e)}. \tag{3.62}$$

In natural system of units Eq. (3.62) is

$$\Delta\phi = \frac{6\pi GM}{a(1-e^2)} + \frac{g^2N_1N_2M_{Z'}^2a^2(1-e^2)}{4M_p(GM+\frac{g^2N_1N_2}{4\pi M_p})(1+e)}. \tag{3.63}$$

The energy due to gravity is much larger than the energy due to long range Yukawa type force. The last term of Eq. (3.63) indicates that long range force, which arises due to $U(1)_{L_e-L_{\mu,\tau}}$ gauge boson exchange between the electrons of composite objects, contributes to the perihelion advance of planets within the permissible limit.

3.3.2 Constraints on $U(1)_{L_e-L_{\mu,\tau}}$ gauge coupling for planets in Solar system

The contribution of the gauge boson must be within the excess of perihelion advance from the GR prediction, i.e; $(\Delta\phi)_{obs} - (\Delta\phi)_{GR} \geq (\Delta\phi)_{L_e-L_{\mu,\tau}}$. The first term in the right hand side of Eq. (3.63) is $(\Delta\phi)_{GR}$ and the second term is $(\Delta\phi)_{L_e-L_{\mu,\tau}}$. Putting the observed and GR values for $(\Delta\phi)$, we can constrain the $U(1)_{L_e-L_{\mu,\tau}}$ gauge coupling constants for all the planets in our Solar System. For Mercury planet, we write

$$\frac{g^2 N_1 N_2 M_{Z'}^2 a^2(1-e^2)}{4M_p(GM + \frac{g^2 N_1 N_2}{4\pi M_p})(1+e)}\left(\frac{\text{century}}{T}\right) < 3.0 \times 10^{-3} \text{arcsecond/century}, \quad (3.64)$$

where 3×10^{-3} arcsecond/century is the uncertainty in the perihelion advancement from its GR prediction and put upper bound on the gauge coupling. $T = 88$ days is the orbital time period of Mercury. Similarly, we can put upper bounds on g for other planets. In this section, we constrain the $U(1)_{L_e-L_{\mu,\tau}}$ gauge coupling from the observed perihelion advancement of the planets in the Solar System. We consider six planets: Mercury, Venus, Earth, Mars, Jupiter, and Saturn. Here, we take the mass of the Sun as $M = 10^{57}$ GeV. Using Eq. (3.63), we put an upper bound on g from the uncertainty of their perihelion advance. In Table 3.2, we obtain the upper bound on masses of the gauge bosons which are mediated between the Sun and the planets and, in Table 3.3, we show the constraints on the gauge coupling constants from the uncertainties [233, 234] of perihelion advance.

We can write from the fifth force constraint

$$\frac{g^2 N_1 N_2}{4\pi G M M_p} < 1. \quad (3.65)$$

This gives the upper bound on g as $g < 3.54 \times 10^{-19}$ for all the planets. In Fig.3.3 we show the values of gauge coupling of the planets corresponding to the planet-Sun distance. For $U(1)_{L_e-L_{\mu,\tau}}$ vector gauge bosons exchange between the planet and the Sun,

Table 3.2: Summary of the masses, eccentricities (https://solarsystem.nasa.gov/planets/mercury/by-the-numbers/) of the orbits, perihelion distances from the Sun and upper bounds on gauge boson mass $M_{Z'}$ which are mediated between the planets and Sun in our Solar System.

Planet	Mass M_p(GeV)	Eccentricity (e)	Perihelion distance a (AU)	$M_{Z'}$(eV)
Mercury	1.84×10^{50}	0.206	0.31	$\leq 4.26 \times 10^{-18}$
Venus	2.73×10^{51}	0.007	0.72	$\leq 1.83 \times 10^{-18}$
Earth	3.35×10^{51}	0.017	0.98	$\leq 1.35 \times 10^{-18}$
Mars	3.59×10^{50}	0.093	1.38	$\leq 9.56 \times 10^{-19}$
Jupiter	1.07×10^{54}	0.048	4.95	$\leq 2.67 \times 10^{-19}$
Saturn	3.19×10^{53}	0.056	9.02	$\leq 1.46 \times 10^{-19}$

Table 3.3: Summary of the uncertainties in the perihelion advance in arcseconds per century and upper bounds on gauge boson-electron coupling g for the values of $M_{Z'}$ discussed in Table3.2 for planets in our Solar System.

Planet	Uncertainty in perihelion advance (as/cy)	g from perihelion advance
Mercury	3.0×10^{-3}	$\leq 1.055 \times 10^{-24}$
Venus	1.6×10^{-3}	$\leq 1.377 \times 10^{-24}$
Earth	1.9×10^{-4}	$\leq 6.021 \times 10^{-25}$
Mars	3.7×10^{-5}	$\leq 3.506 \times 10^{-25}$
Jupiter	2.8×10^{-2}	$\leq 2.477 \times 10^{-23}$
Saturn	4.7×10^{-4}	$\leq 5.040 \times 10^{-24}$

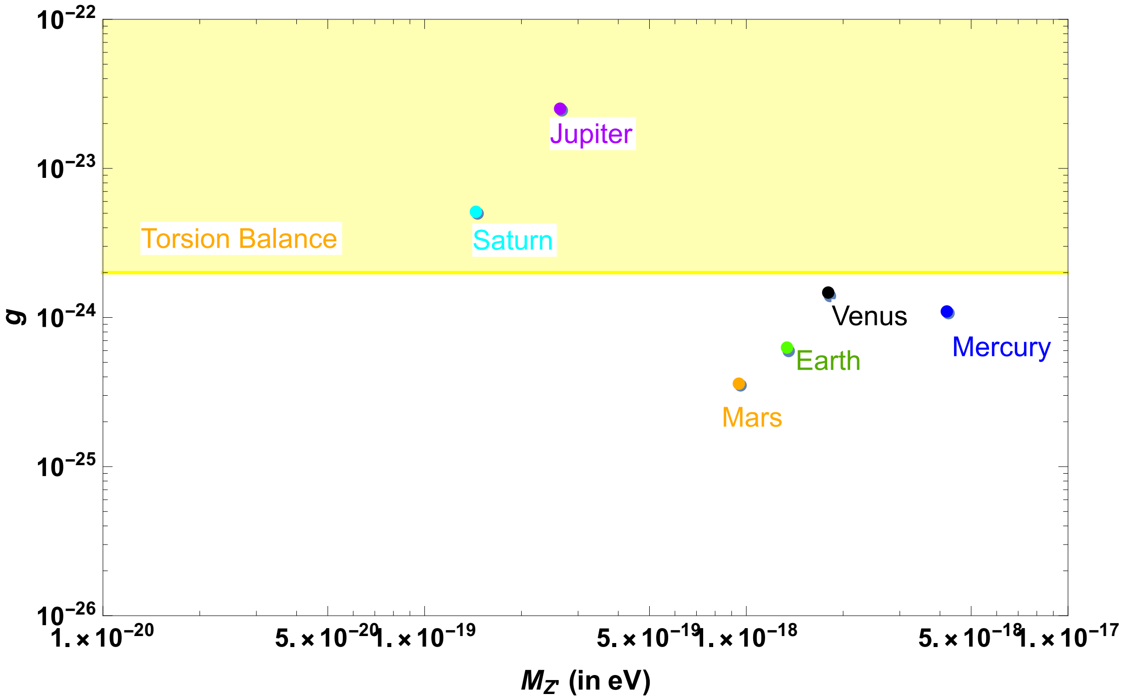

Figure 3.3: Values of the gauge coupling of each planets corresponding to the Sun-planet distance obtained from Table3.3. Violet dot is for Jupiter planet, blue dot is for Mercury planet, black dot is for Venus, cyan dot is for Saturn, green dot is for Earth and yellow dot is for Mars. The yellow shaded region is excluded from the torsion balance experiments.

the mass of the gauge boson is $M_{Z'} \leq \mathcal{O}(10^{-19})$ eV. In Fig.3.4, we obtain the exclusion plots of gauge boson electron coupling for the six planets by numerically solving Eq. (3.50). There is an extra multiplicative factor $\exp\left[\frac{-M'_Z L^2}{M'}\right]$ in the expression of α if we solve Eq. (3.50) numerically in order to incorporate the exponential suppresion due to higher values of $M_{Z'}$. The regions above the coloured lines corresponding

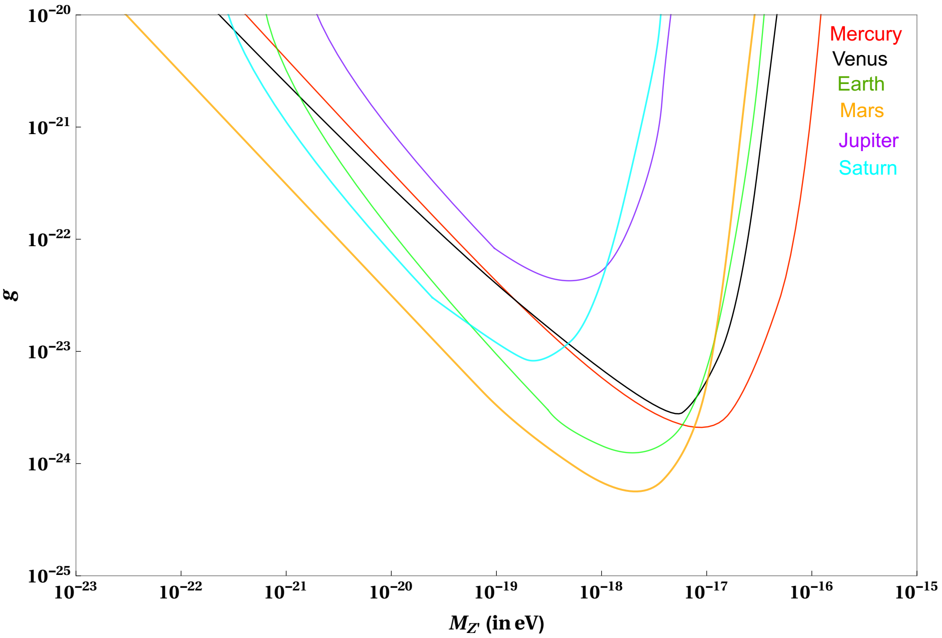

Figure 3.4: Plot of coupling constant g vs the mass of the gauge bosons M'_Z for all the planets. Violet line is for Jupiter planet, red line is for Mercury planet, black line is for Venus, cyan line is for Saturn, green line is for Earth and yellow line is for Mars.

to every planet are excluded. Eq. (3.63) suggests that the perihelion shift due to the mediation of $L_e - L_{\mu,\tau}$ gauge bosons is proportional to the square of the semi major axis. This is completely opposite to the standard GR result where the perihelion shift is inversely proportional to a for small $M_{Z'}$. However, for higher values of $M_{Z'}$, the exponential suppression starts dominating. So the contribution of the gauge boson mediation for perihelion shift is larger for outer planets. However, it also depends on the available uncertainties for perihelion precession of the planets and other parameters like orbital time period and eccentricity. From Table 3.3, we obtain the stronger bound on the gauge boson coupling as $g \leq \mathcal{O}(10^{-25})$. From Fig.3.4 it is clear that Mars gives the strongest bound among all the planets considered. As we go to the lower mass region, the exponential term in the potential will become less effective and the Yukawa potential effectively becomes Coulomb potential at $M_{Z'} \to 0$. Thus it will be degenerate with $1/r^2$-Newtonian force and will not contribute to the perihelion precession of planets at all [66]. So as we go to the lower mass ($< 10^{-19}$ eV) region, we get a weaker bound on g. On the other hand, for the higher mass region ($> 10^{-19}$ eV) the long range force theory breaks down and, thus we can not go arbitrarily for higher masses.

3.4 Discussions

In this chapter, we have discussed the constraints on ultralight vector gauge bosons of $L_i - L_j$ type obtained from the indirect evidence of GW, and the perihelion precession of planets. Due to the presence of a significant number of muons in the neutron stars, we can put bounds on the ultra light vector gauge boson mass in the gauged $L_\mu - L_\tau$ scenario and on the gauge coupling from the observations of the orbital period decay of the four compact binary systems. Mainly the gravitational quadrupole radiation contributes to the decay in the orbital period. The radiation by other ultra light particles also contribute to the orbital period decay to less than 1%. From the decay of orbital period, we obtain the $L_\mu - L_\tau$ gauge coupling for PSR B1913+16 as $g \leq 2.21 \times 10^{-18}$, for PSR J0737-3039, it is $g \leq 2.17 \times 10^{-19}$, for PSR J0348+0432, the coupling is $g < 9.02 \times 10^{-20}$ and, for PSR J1738+0333, the coupling is $g < 4.24 \times 10^{-20}$ in the massless limit and is true up to $M_Z' < 10^{-19}$ eV. Due to the fact of $K_2(n_0, e)_{n_0=0} \geq K_2(n_0, e)_{n_0 \neq 0}$, the massless limit gives the stronger bound for the radiation of massive vector gauge boson. The radiation of vector gauge boson particles is possible if the charge to mass ratio is different for two neutron stars. We have shown the exclusion plots of g vs $M_{Z'}$ for the radiation of massive vector gauge boson and proca field from the NS-NS and NS-WD binaries. The main uncertainty of the gauge coupling bound comes from the number of muons in the neutron star which depends on different QCD equation of states [219, 235, 236].

Since, the Sun and the planets contain a significant number of electrons, long range Yukawa type fifth force can be mediated between the electrons of the Sun and planet in a gauged $L_e - L_{\mu,\tau}$ scenario. Also, there can be the dipole radiation of the gauge boson for the planetary orbits. Following our previous work on compact binary systems in a gauged $L_\mu - L_\tau$ scenario, the energy loss due to dipole radiation is proportional to the fourth power of the orbital frequency. The orbital frequency of the Sun-Mercury binary system is $\Omega \sim 8.79 \times 10^{-31}$ GeV which is roughly three orders of magnitude smaller than the orbital frequency of neutron star-neutron star and neutron star-white dwarf binary systems ($\Omega \sim 10^{-28}$ GeV). The dipole radiation is also proportional to the square of the difference in the charge to mass ratio of the binary system. For the Sun-Planet binary system, the charge to mass ratio is negligibly small and hence, the dipole radiation is negligible.

Due to the presence of electrons in Earth and Moon, there can be a mediation of $L_e - L_{\mu,\tau}$ type of gauge bosons and the mass of the gauge boson is constrained by the distance between the Earth and the Moon which yields $M_{Z'} < 5.15 \times 10^{-16}$ eV. Due to this large gauge boson mass, we will have loose bound on the gauge coupling and it is subdominant since we are considering the mass range $M_{Z'} < 10^{-19}$ eV and probing the ultralight gauge boson from perihelion precession measurements. However, due to the presence of different electron number densities in the Earth and the Moon, there is a differential accelaration of the Earth-Moon system towards the Sun. The presence of electrons in the Sun at the solar distance causes a $L_e - L_{\mu,\tau}$ type of potential and it puts a bound on the gauge coupling $g < 6.4 \times 10^{-25}$ with the range $\sim 10^{13}$ cm (Earth-Sun distance)[206, 237, 238].

This ultralight vector gauge bosons mediated between the Sun and the planets can contribute to the perihelion shift in addition to the GR prediction. From the perihelion shift calculation in presence of a long range Yukawa type potential, we obtain an upper bound on the gauge coupling $g \leq \mathcal{O}(10^{-25})$ in a gauged $L_e - L_{\mu,\tau}$ scenario. The mass of the gauge bosons is constrained by the distance between the Sun and the planet which gives $M_{Z'} \leq \mathcal{O}(10^{-19})$eV. The electron-gauge boson coupling obtained from perihelion shift measurement is six orders of magnitude more stringent than our fifth force constraint Eq. (3.65). From Eq. (3.63) we conclude that, while the precession of perihelion due to GR is largely contributed by the planets close to Sun, the contribution of vector gauge bosons in perihelion precession is dominated by the outer planets.

The non-universal neutrino masses will explicitly break the $L_A - L_B$ where $A \neq$

$B = e, \mu, \tau$ as pointed out by [210]. For such light Z' the best bounds on the leptonic gauge couplings come from neutrino decays $\nu_i \to \nu_j Z'$. The decay of neutrino to the longitudinal component of Z' is equivalent to the decay into the Goldstone boson with coupling to the neutrinos $g_{ij} = g' m_\nu / M'_Z$. Such decays are suppressed by neutrino masses but enhanced by the small Z' mass and the best bounds on light Z' couplings come from constraints on neutrino decays.

The coupling constant of long range forces is constrained to be small (g' from fifth force and neutrino oscillation experiments). The Higgs field which gives mass to the Z' boson need not be the same as the fields whose vacuum expectation values give masses to neutrinos. There are several mechanisms for explaining the smallness of the long range gauge coupling g' compared to the other couplings of the standard model. For instance, the Z' mass may arise in a SUSY theory from the Fayet-Ilioupoulous (FI) term and the smallness of $M_{Z'}$ can then be related to the GUT scale vev of the FI term as motivated by inflation [231, 239]. Such a small value of coupling can also be generated by clockwork mechanism [240].

The bound on coupling g that we have obtained is not only as good as the torsion balance [241] or the neutrino oscillation experiment [206], but also our results possess additional importance for the following reasons:

(a) Our analysis of the perihelion precession is sensitive to the magnitude of the potential and the nature of the potential, i.e. the deviation from the inverse square law.

(b) In our analysis, we are probing a larger distance (up to the planet Saturn) compare to the Earth-Sun distance.

(c) Since the perihelion shift depends on the value of uncertainty in GR prediction, the future BepiColombo mission [227] can give more accurate results and the bound on coupling will become even stronger. The mission has an accuracy of measuring the perihelion shift at a few parts in 10^6[227] which will make our bound roughly one or two orders more stringent than our present bound in the mass range that we are considering (at $M_{Z'} \sim \mathcal{O}(10^{-18})$ eV, then the gauge coupling will be $g \sim \mathcal{O}(10^{-26})$) and the bound will be as good as neutrino decay[210]. Note that, in our analysis, the mass of the gauge boson cannot be very small, otherwise, it will be degenerate with the Coulomb potential. Also, the mass cannot be very large, otherwise the long range force theory breaks down.

Moreover, we emphasize the novel physics behind the work which suggests that we can study the gauge boson electron coupling in a gauged $L_e - L_{\mu,\tau}$ scenario by planetary observations and we can constrain the long range force from perihelion precession of planets. These gauge bosons ($M_{Z'} \leq 10^{-19}$ eV) can be a possible candidate for fuzzy dark matter and can be probed from the precision measurements of planetary orbits.

Chapter 4

Massive Graviton (Spin 2): A Simple extension of General Relativity, and its Searches

4.1 Introduction

Einstein's general relativity (GR), since its inception in 1916, has passed all experimental tests [242]. To move towards the correct quantum theory of gravity, it is important to test which variations of classical GR fail the experimental tests or have some theoretical inconsistencies. The two main motivations for studying the massive gravity theory are solving the cosmological constant problem and the dark matter. There are many types of massive gravity theory (modifying Einstein's GR theory). One such variation of GR which has been widely studied is the Fierz-Pauli (FP) theory of massive gravity [87]. In a scalar or vector field theory, an exchange of a massive particle of mass m_g gives rise to a $(1/r)e^{-m_g r}$ Yukawa potential which goes to the $1/r$ potential in the $m_g \to 0$ limits. The FP massive gravity theory has a peculiarity that in the zero graviton mass limit, the action of the theory goes to that of Einstein-Hilbert linearized theory however, due to the contribution of extra scalar mode, the propagator for the massive theory does not match with that of Einstein-Hilbert theory. Hence, in FP theory, the Newtonian potential becomes $4/3$ times larger in the zero graviton mass limit. This peculiarity of the FP theory where the action goes to the EH theory in the zero mass limit but the graviton propagator does not was first pointed out by van Dam and Veltman [243] and independently by Zakharov [244] and this feature which arises in most massive gravity theories [86, 245–247] is called the van Dam-Veltman-Zakharov (vDVZ) discontinuity (however, in the nonlinear FP theory, a proper decoupling limit will display the vDVZ discontinuity already in the action). Experimental constraints on the graviton mass are listed in [248]. However, there are few nonlinear ghost free massive gravity theories like dRGT, bimetric gravity, and multi gravity theory which are discussed in [89, 90, 245, 249, 250]. In some of the massive gravity theories, the massive graviton can serve as a dark matter and can also explain the accelerated expansion of the universe.

In the following, we have considered a one vertex graviton process like gravitational wave radiation for massive gravity theories instead of a graviton exchange diagram. It is interesting to check whether the prediction of gravitational wave radiation in standard GR theory matches that of massive gravity theories in $m_g \to 0$ limits and a manifestation of vDVZ discontinuity can be looked at such type of phenomenon.

In the weak field limit, GR can be treated as a quantum field theory of spin-2 fields in the Minkowski spacetime [251–255]. Any classical gravity interaction like Newtonian potential between massive bodies or bending of light by a massive body can be described by a tree level graviton exchange diagram. The result of the tree level diagrams should match the weak field classical GR results. The gravitational wave radiation from a compact binary system is equivalent to a tree level one graviton vertex process. The energy loss calculation for massless graviton radiation has been performed in [168, 256] using Feynman diagram techniques and the results match with the result of Peter and Mathews [177] who used the quadrupole formula of classical GR.

The first indirect evidence of Gravitational Wave (GW) was obtained from the orbital period loss of the Hulse -Taylor binary system [257–259]. The orbital period loss of the compact binary system confirms Einstein's GR [177] to $\sim 0.1\%$ accuracy [260]. Following the Hulse-Taylor binary, there have been other precision measurements from compact binary systems [179–181].

Compact binary systems can also radiate other ultra-light particles like axions and gauge bosons. The orbital frequency of binary systems is about $\Omega \sim 10^{-19}$ eV and particles with a mass lower than Ω can be radiated like the radiation of gravitational waves. The Feynman diagram method is pedagogically simpler to generalize the calculation of scalars and gauge bosons. Calculations of radiation of ultra-light scalars, axions, and gauge bosons have been discussed with this method in Chapter 2, and Chapter 3 and compared with experimental observations of compact binary systems (neutron star-neutron star, neutron star-white dwarf binaries). This enables us to probe the couplings of ultra-light dark matter [59, 64] which are predicted to be in the mass range $\sim 10^{-21} - 10^{-22}$ eV to be probed with orbital period loss measurements.

In this chapter, we study massive graviton theories with a single graviton vertex process namely graviton radiation from compact binary systems and we consider three models (1) the Fierz-Pauli ghost free theory which has a vDVZ discontinuity in the propagator, (2) a modification of Fierz-Pauli theory where there is a cancellation between the ghost and the scalar degrees so that there is no vDVZ discontinuity [261–264] and (3) the Dvali-Gabadadze-Porrati (DGP) theory [88, 265, 266] which is a ghost-free theory but the extra scalar degree of freedom gives rise to the vDVZ discontinuity. The mass term in DGP gravity is momentum dependent which serves the purpose of suppressing the long range interactions in a virtual graviton exchange process. For real gravitons the graviton mass is tachyonic. We compare our results with orbital period loss observations and put limits on the graviton mass allowed in each of these theories.

We also compare our results with the earlier classical field calculations in massive gravity theories [262, 267–271]. There are several existing bounds on graviton mass from the tests of Yukawa potential, modified dispersion relation, fifth force constraints, etc. (see [248] for review). The Vainshtein screening at the non-linear scales of the massive theories of gravity has already ruled out a range of m_g in various systems. For example, from the Lunar Laser Ranging experiments for the Earth-Moon system, the graviton mass range 10^{-32} eV $< m_g < 10^{-20}$ eV is ruled out [272]. For any theory containing the cubic Galileon in the decoupling limit (i.e. the Vainshtein screened regime), from the Hulse-Taylor binary system the mass range 10^{-27} eV $< m_g < 10^{-24}$ eV is ruled out [270]. In this chapter, we investigate the complementary regime, i.e.

the unscreened linear regime and, hence the mass ranges greater than the Vainshtein threshold value for the compact binary systems.

This chapter is based on [273] and is organized as follows. In Section 4.2 we discuss the Fierz-Pauli theory and derive the formula for energy loss by graviton radiation using the Feynman diagram method. In Section 4.3 we do the same study for the modified FP theory without the vDVZ discontinuity and in Section 4.4 we study the DGP theory. In Section 4.5, we compare the results with observations from the Hulse-Taylor binary (PSR B1913+16) and pulsar white dwarf binary (PSR J1738+0333) and put limits on the graviton mass for each of the massive gravity theories discussed. We also discuss the limits of applicability of the perturbation theory from the Vainshtein criterion and the corresponding limits on the range of graviton mass established from binary systems. In Section 4.6, we summarise the results and discuss future directions. In Appendix C.1, we derive the energy loss of massless graviton radiation for a one graviton vertex process using Feynman diagram technique in comparison with massive gravity theory results discussed in this chapter.

4.2 Fierz-Pauli theory

The action of the Fierz-Pauli theory [87] is

$$\begin{aligned} S &= \int d^4x \Big[-\frac{1}{2}(\partial_\mu h_{\nu\rho})^2 + \frac{1}{2}(\partial_\mu h)^2 - (\partial_\mu h)(\partial^\nu h^\mu_\nu) + (\partial_\mu h_{\nu\rho})(\partial^\nu h^{\mu\rho}) \\ &\qquad + \frac{1}{2}m_g^2\Big(h_{\mu\nu}h^{\mu\nu} - h^2\Big) + \frac{\kappa}{2}h_{\mu\nu}T^{\mu\nu}\Big] \\ &= \int d^4x \left[\frac{1}{2}h_{\mu\nu}\mathcal{E}^{\mu\nu\alpha\beta}h_{\alpha\beta} + \frac{1}{2}m_g^2 h_{\mu\nu}(\eta^{\mu(\alpha}\eta^{\beta)\nu} - \eta^{\mu\nu}\eta^{\alpha\beta})h_{\alpha\beta} + \frac{\kappa}{2}h_{\mu\nu}T^{\mu\nu}\right] \end{aligned} \tag{4.1}$$

where the operator $\mathcal{E}^{\mu\nu\alpha\beta}$ is given in Eq.C.4. The mass term breaks the gauge symmetry $h_{\mu\nu} \to h_{\mu\nu} - \partial_\mu\xi_\nu - \partial_\nu\xi_\mu$. We will assume that the energy-momentum is conserved, $\partial_\mu T^{\mu\nu} = 0$.

The equation of motion from Eq.4.1 is

$$\left(\Box + m_g^2\right) h_{\mu\nu} - \eta_{\mu\nu}\left(\Box + m_g^2\right) h - \partial_\mu\partial^\alpha h_{\alpha\nu} - \partial_\nu\partial^\alpha h_{\alpha\mu} + \eta_{\mu\nu}\partial^\alpha\partial^\beta h_{\alpha\beta} + \partial_\mu\partial_\nu h = -\kappa T_{\mu\nu}. \tag{4.2}$$

Taking the divergence of Eq.4.2 we have

$$m_g^2\left(\partial^\mu h_{\mu\nu} - \partial_\nu h\right) = 0. \tag{4.3}$$

These are 4 constraint equations that reduce the independent degrees of freedom of the graviton from 10 to 6.

Using Eq.4.3 in Eq.4.2 we obtain

$$\Box h_{\mu\nu} - \partial_\mu \partial_\nu h + m_g^2 \left(h_{\mu\nu} - \eta_{\mu\nu} h \right) = -\kappa T_{\mu\nu}. \tag{4.4}$$

Taking the trace of this equation we obtain the relation

$$h = \frac{\kappa}{3m_g^2} T. \tag{4.5}$$

Therefore trace h is not a propagating mode but is determined algebraically from the trace of the stress tensor. This is the ghost mode as the kinetic term for h in Eq.4.2 appears with the wrong sign. Therefore in the Fierz-Pauli theory, the ghost mode does not propagate. The number of independent propagating degrees of freedom of the Fierz Pauli theory is therefore 5. These are 2 tensor modes, 2 three-vector degrees of freedom that do not couple to the energy-momentum tensor and 1 scalar that couples to the trace of the energy-momentum tensor.

The propagator in the FP theory is given by

$$\left[\mathcal{E}^{\mu\nu\alpha\beta} + m_g^2 \left(\eta^{\mu(\alpha} \eta^{\beta)\nu} - \eta^{\mu\nu} \eta^{\alpha\beta} \right) \right] D^{(m)}_{\alpha\beta\rho\sigma}(x-y) = \delta^\mu_{(\rho} \delta^\nu_{\sigma)} \delta^4(x-y). \tag{4.6}$$

Using Eq.4.6, we can find $D^{(m)}_{\alpha\beta\rho\sigma}(k)$ by going to the momentum space ($\partial_\mu \to i k_\mu$). Hence, the Pauli-Fierz massive graviton propagator becomes

$$D^{(m)}_{\alpha\beta\rho\sigma}(k) = \frac{1}{-k^2 + m_g^2} \left(\frac{1}{2} (P_{\alpha\rho} P_{\beta\sigma} + P_{\alpha\sigma} P_{\beta\rho}) - \frac{1}{3} P_{\alpha\beta} P_{\rho\sigma} \right), \tag{4.7}$$

where

$$P_{\alpha\beta} \equiv \eta_{\alpha\beta} - \frac{k_\alpha k_\beta}{m_g^2}. \tag{4.8}$$

For a tree level graviton exchange process between two conserved currents, the amplitude is

$$\mathcal{A}_{FP} = \frac{\kappa^2}{4} T^{\alpha\beta} D^{(m)}_{\alpha\beta\mu\nu} T'^{\mu\nu}. \tag{4.9}$$

The propagator for the FP theory can be written as

$$D^{(m)}_{\mu\nu\alpha\beta}(k) = \frac{1}{-k^2 + m_g^2} \left(\frac{1}{2} (\eta_{\alpha\mu} \eta_{\beta\nu} + \eta_{\alpha\nu} \eta_{\beta\mu}) - \frac{1}{3} \eta_{\alpha\beta} \eta_{\mu\nu} + (k\text{--dependent terms}) \right). \tag{4.10}$$

When the graviton is treated as a quantum field, the Feynman propagator is defined as in the massless theory (Eq.C.16),

$$\begin{aligned} D^{(m)}_{\mu\nu\alpha\beta}(x-y) &= \langle 0|T(\hat{h}_{\mu\nu}(x)\hat{h}_{\alpha\beta}(y))|0\rangle \\ &= \int \frac{d^4k}{(2\pi)^4}\frac{1}{-k^2+m_g^2+i\epsilon}e^{ik(x-y)}\sum_{\lambda}\epsilon^{\lambda}_{\mu\nu}(k)\epsilon^{*\lambda}_{\alpha\beta}(k). \end{aligned} \tag{4.11}$$

Comparing Eq.4.10 and Eq.4.11 we can write the polarisation sum for the FP massive gravity theory as

$$\sum_{\lambda}\epsilon^{\lambda}_{\mu\nu}(k)\epsilon^{*\lambda}_{\alpha\beta}(k) = \frac{1}{2}(\eta_{\mu\alpha}\eta_{\nu\beta}+\eta_{\nu\alpha}\eta_{\mu\beta})-\frac{1}{3}\eta_{\alpha\beta}\eta_{\mu\nu}+(k\text{−dependent terms}). \tag{4.12}$$

Hence, for a single graviton vertex process, the amplitude square will have the form

$$|\mathcal{M}|^2 = \left(\frac{\kappa^2}{4}\right)\sum_{\lambda}|\epsilon^{\lambda}_{\mu\nu}(k)T^{\mu\nu}(k')|^2 = \left(\frac{\kappa^2}{4}\right)\sum_{\lambda}\epsilon^{\lambda}_{\mu\nu}(k)\epsilon^{*\lambda}_{\alpha\beta}(k)T^{\mu\nu}(k')T^{*\alpha\beta}(k'). \tag{4.13}$$

The conservation of the stress tensor demands $k_\mu T^{\mu\nu} = k_\nu T^{\mu\nu} = 0$. Hence, for tree level calculations one may drop the momentum dependent terms in Eq.4.10 and Eq.4.12 for the calculations of diagrams with graviton emission from external legs as we will do in this chapter.

We see that when the propagator (Eq.C.11) and polarisation sum (Eq.C.17) of the massless graviton theory are compared with the corresponding quantities Eq.4.6 and Eq.4.12, the massive theory differs from the massless theory even in the $m_g \to 0$ limits. There is an extra contribution of $(1/6)T^*T'$ to the amplitude (Eq.4.9) in the FP theory. This is the contribution of the scalar degree of freedom of $g_{\mu\nu}$ which does not decouple in the $m_g \to 0$ limits.

Consider the Newtonian potential between two massive bodies. The amplitude for the diagram with one graviton exchange in GR is

$$\mathcal{A}_{GR} = \frac{\kappa^2}{4}T^{\mu\nu}D^{(0)}_{\mu\nu\alpha\beta}(k)T'^{\alpha\beta}\,. \tag{4.14}$$

The stress tensor for massive bodies at rest in a given reference frame is of the form $T^{\mu\nu} = (M_1,0,0,0)$ and $T'^{\alpha\beta} = (M_2,0,0,0)$ and the massless graviton propagator in GR is Eq.C.11. The potential derived from Eq.4.14 has the usual Newtonian form

$$V_{GR} = \frac{\kappa^2}{4}\int\frac{d^3k}{(2\pi)^3}e^{ik\cdot r}\frac{1}{-k^2}\left(T_{\mu\nu}-\frac{1}{2}\eta_{\mu\nu}T^{\alpha}_{\alpha}\right)T'^{\mu\nu}$$

$$= \frac{GM_1M_2}{r}, \tag{4.15}$$

where $\kappa = \sqrt{32\pi G}$, and G stands for universal gravitational constant. On the other hand in the Fierz-Pauli theory, the one graviton exchange amplitude Eq.4.9 is

$$\mathcal{A}_{FP} = \frac{\kappa^2}{4}\frac{1}{-k^2+m_g^2}\left(T_{\mu\nu} - \frac{1}{3}\eta_{\mu\nu}T^{\alpha}_{\alpha}\right)T'^{\mu\nu}, \tag{4.16}$$

and the gravitational potential between two massive bodies in the FP theory is

$$\begin{aligned} V_{FP} = &= \frac{\kappa^2}{4}\int \frac{d^3k}{(2\pi)^3}e^{ik\cdot r}\frac{1}{-k^2+m_g^2}\left(T_{\mu\nu} - \frac{1}{3}\eta_{\mu\nu}T^{\alpha}_{\alpha}\right)T'^{\mu\nu} \\ &= \left(\frac{4}{3}\right)\frac{GM_1M_2}{r}e^{-m_g r}. \end{aligned} \tag{4.17}$$

The FP theory of massive gravity gives rise to a Yukawa type of potential. However, in $m_g \to 0$ limits of FP massive gravity theory, the gravitational potential between two massive bodies becomes $4/3$ times larger than the usual Newtonian potential arising from standard GR theory. This is ruled out from solar system tests of gravity [274] even in the $m_g \to 0$ limits. We note here that the bending of light by massive bodies is unaffected (in $m_g \to 0$ limits) as the stress tensor for photons $T^{\mu}_{\nu} = (\omega, 0, 0, -\omega)$ is traceless and the scattering amplitudes $\mathcal{A}_{FP}(m_g \to 0) = \mathcal{A}_{GR}$. Experimental observations [189] of the bending of radio waves by the Sun match GR to 1%. The two observations together imply that the extra factor of (4/3) in the Newtonian potential of FP theory cannot be absorbed by redefining G.

The fact that the FP theory action Eq.4.1 goes to the Einstein-Hilbert action Eq.C.3 in the $m_g \to 0$ limits while the propagator for the FP theory Eq.4.10 does not go to the Einstein-Hilbert propagator Eq.C.11 is called the vDVZ discontinuity which was pointed out by van Dam and Veltman [243] and independently by Zakharov [244].

It has been pointed out by Vainshtein [275, 276] that the linear FP theory breaks down at distances much larger than the Schwarzschild radius $R_s = 2GM$ below which the linearised GR is no longer valid ($\kappa h_{\mu\nu} \sim 1$ (below this distance)). The scalar mode in FP theory becomes strongly coupled with decreasing m_g and the minimum radius from a massive body at which the linearised FP theory is valid is called the Vainshtein radius and is given by $R_V = (R_s/m_g^4)^{1/5}$. In Section 4.5.1, we will discuss the Vainshtein radius of different massive gravity theories in this chapter and also obtain

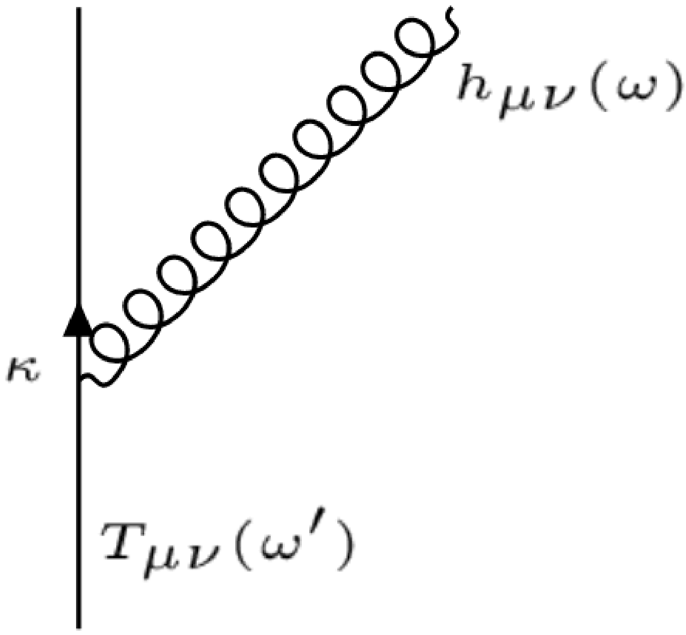

Figure 4.1: Emission of graviton from a classical source.

the theoretical bound on the mass of the graviton for these theories considering two compact binary systems.

4.2.1 Graviton radiation from compact binary systems in Fierz-Pauli theory

We derive the graviton radiation from the compact binary systems using Feynman diagram techniques. This is equivalent to a tree level one graviton vertex process. The pictorial representation of graviton emission from a classical source is shown in Fig.4.1. The classical graviton current $T^{\mu\nu}$ is determined from Kepler's orbit and the interaction vertex is $\frac{1}{2}\kappa h_{\mu\nu}T^{\mu\nu}$, where $h_{\mu\nu}$ is the graviton field and $\kappa = \sqrt{32\pi G}$. Here we use linearized gravity formulation with an extension of non zero graviton mass term Eq.4.1 to calculate the energy loss of a compact binary system due to graviton emission.

From the interaction Lagrangian between the gravity and source $\left(\frac{1}{2}\kappa h_{\mu\nu}T^{\mu\nu}\right)$, one can calculate the graviton emission rate as

$$d\Gamma = \frac{\kappa^2}{4}\sum_{\lambda}|T_{\mu\nu}(k')\epsilon_{\lambda}^{\mu\nu}(k)|^2 2\pi\delta(\omega-\omega')\frac{d^3k}{(2\pi)^3}\frac{1}{2\omega}, \tag{4.18}$$

where $T_{\mu\nu}(k')$ denotes the classical graviton current in the momentum space. We can write Eq.4.18 by expanding the modulus squared as

$$d\Gamma = \frac{\kappa^2}{8(2\pi)^2}\sum_{\lambda}\Big(T_{\mu\nu}(k')T^*_{\alpha\beta}(k')\epsilon^{\mu\nu}_{\lambda}(k)\epsilon^{*\alpha\beta}(k)\Big)\frac{d^3k}{\omega}\delta(\omega-\omega'). \tag{4.19}$$

Using the polarization sum of FP massive gravity theory Eq.4.12, the graviton emission rate becomes

$$d\Gamma = \frac{\kappa^2}{8(2\pi)^2}\int\Big[T_{\mu\nu}(k')T^*_{\alpha\beta}(k')\Big]\Big[\frac{1}{2}(\eta^{\mu\alpha}\eta^{\nu\beta}+\eta^{\mu\beta}\eta^{\nu\alpha}-\eta^{\mu\nu}\eta^{\alpha\beta})+\frac{1}{6}\eta^{\mu\nu}\eta^{\alpha\beta}\Big]\times \frac{d^3k}{\omega}\delta(\omega-\omega') \tag{4.20}$$

The extra $(1/6)\eta^{\mu\nu}\eta^{\alpha\beta}$ term compared to the standard GR case is the contribution of the scalar mode in FP theory. Simplifying we obtain

$$d\Gamma = \frac{\kappa^2}{8(2\pi)^2}\int\Big[|T_{\mu\nu}(k')|^2-\frac{1}{3}|T^{\mu}{}_{\mu}(k')|^2\Big]\delta(\omega-\omega')\omega\Big(1-\frac{m_g^2}{\omega^2}\Big)^{\frac{1}{2}}d\omega d\Omega_k, \tag{4.21}$$

where we have used $d^3k = k^2dkd\Omega$ and the dispersion relation $k^2 = (\omega^2 - m_g^2)$. Hence, using Eq.4.21 we can calculate the rate of energy loss due to massive graviton radiation as

$$\frac{dE}{dt} = \frac{\kappa^2}{8(2\pi)^2}\int\Big[|T_{\mu\nu}(k')|^2-\frac{1}{3}|T^{\mu}{}_{\mu}(k')|^2\Big]\delta(\omega-\omega')\omega^2\Big(1-\frac{m_g^2}{\omega^2}\Big)^{\frac{1}{2}}d\omega d\Omega_k. \tag{4.22}$$

The dispersion relation for the massive graviton is

$$|\mathbf{k}|^2 = \omega^2\Big(1-\frac{m_g^2}{\omega^2}\Big). \tag{4.23}$$

The direction of the massive graviton momentum is governed by the unit vector $\hat{k}^i = \dfrac{k^i}{\omega\sqrt{1-\frac{m_g^2}{\omega^2}}}$. Using the fact of the conservation of stress tensor $k_\mu T^{\mu\nu} = 0$ and Eq.4.23, we can write the T_{00} and T_{i0} components of the stress tensor in terms of T_{ij} as follows

$$T_{0j} = -\sqrt{1-\frac{m_g^2}{\omega^2}}\hat{k}^iT_{ij}, \quad T_{00} = \Big(1-\frac{m_g^2}{\omega^2}\Big)\hat{k}^i\hat{k}^jT_{ij}. \tag{4.24}$$

Therefore, we can write

$$\Big[|T_{\mu\nu}(k')|^2-\frac{1}{3}|T^{\mu}{}_{\mu}(k')|^2\Big] \equiv \Lambda_{ij,lm}T^{ij*}T^{lm}, \tag{4.25}$$

where,

$$\Lambda_{ij,lm} = \Big[\delta_{il}\delta_{jm} - 2\Big(1-\frac{m_g^2}{\omega^2}\Big)\hat{k_j}\hat{k_m}\delta_{il} + \frac{2}{3}\Big(1-\frac{m_g^2}{\omega^2}\Big)^2\hat{k_i}\hat{k_j}\hat{k_l}\hat{k_m} - \frac{1}{3}\delta_{ij}\delta_{lm} + \frac{1}{3}\Big(1-\frac{m_g^2}{\omega^2}\Big)\Big(\delta_{ij}\hat{k_l}\hat{k_m} + \delta_{lm}\hat{k_i}\hat{k_j}\Big)\Big]. \tag{4.26}$$

Hence, we can write Eq.4.22 as

$$\frac{dE}{dt} = \frac{\kappa^2}{8(2\pi)^2}\int \Lambda_{ij,lm}T^{ij*}T^{lm}\delta(\omega-\omega')\omega^2\Big(1-\frac{m_g^2}{\omega^2}\Big)^{\frac{1}{2}}d\omega d\Omega_k. \tag{4.27}$$

We can do the angular integrals using the relations C.26 and obtain

$$\int d\Omega_k\Lambda_{ij,lm}T^{ij*}(\omega')T^{lm}(\omega') = \frac{8\pi}{5}\left(\left[\frac{5}{2}-\frac{5}{3}\left(1-\frac{m_g^2}{\omega'^2}\right)+\frac{2}{9}\left(1-\frac{m_g^2}{\omega'^2}\right)^2\right]\times T^{ij}T^*_{ij} + \left[-\frac{5}{6}+\frac{5}{9}\left(1-\frac{m_g^2}{\omega'^2}\right)+\frac{1}{9}\left(1-\frac{m_g^2}{\omega'^2}\right)^2\right]|T^i{}_i|^2\right), \tag{4.28}$$

Hence, the rate of energy loss becomes

$$\frac{dE}{dt} = \frac{8G}{5}\int\Bigg[\Bigg\{\frac{5}{2}-\frac{5}{3}\left(1-\frac{m_g^2}{\omega'^2}\right)+\frac{2}{9}\left(1-\frac{m_g^2}{\omega'^2}\right)^2\Bigg\}T^{ij}T^*_{ij} + \Bigg\{-\frac{5}{6}+\frac{5}{9}\left(1-\frac{m_g^2}{\omega'^2}\right)+\frac{1}{9}\left(1-\frac{m_g^2}{\omega'^2}\right)^2\Bigg\}|T^i{}_i|^2\Bigg]\delta(\omega-\omega')\omega^2\Big(1-\frac{m_g^2}{\omega^2}\Big)^{\frac{1}{2}}d\omega. \tag{4.29}$$

In the massless gravity theory the prefactors of $T^{ij}T^*_{ij}$ and $|T^i{}_i|^2$ are 1 and $-1/3$ respectively. Note that the $m_g \to 0$ limits of Eq.4.29 gives different prefactors. In the massive graviton limit, all the five polarization components contribute to the energy loss instead of two as in the massless limit. Therefore, from Eq.4.29, we will not obtain the energy loss for massless limit by simply putting $m_g \to 0$. In AppendixC.1 we obtain the energy loss due to massless graviton radiation from compact binary systems. In massive gravity theories, the Newtonian gravitational potential takes a different form than GR. As a result, the Keplerian orbits are also affected. For, FP theory the potential energy for the binary system takes the form of Yukawa-type with 4/3 extra pre-factor as discussed in Eq. (4.17) when there is no screening. However, for GW emission we must have $n_0 = m_g/\Omega < 1$ which implies that $a < R_V$ and therefore the Newtonian potential for the orbital motion of the binary system is Vainshtein screened. There will be corrections in the Newtonian gravitational potential energy from the screened scalar mode.

Concretely, to see the effects of the scalar polarisation in this $a < R_V$ limit one can split the massive h into $\tilde{h} + \partial A/m_g + \partial\partial\phi/m_g^2$ such that $\tilde{h}_{\mu\nu}$ now enjoys a gauge invariance and carries only the two tensor modes, while ϕ carries the scalar mode (the vector mode A_μ can be consistently set to zero for this matter configuration). After $\tilde{h}_{\mu\nu}$ and ϕ, the action in the decoupling limit is [277],

$$S = \int d^4x \left[\frac{1}{2}\tilde{h}_{\mu\nu}\mathcal{E}^{\mu\nu\alpha\beta}\tilde{h}_{\alpha\beta} - \frac{1}{2}\phi\Box\phi + \frac{1}{2M_{pl}}\tilde{h}_{\mu\nu}T^{\mu\nu} + \frac{1}{2M_{pl}}\phi T + \mathcal{L}_{\text{int}}\right] \tag{4.30}$$

The precise interactions will depend on specific massive gravity theory. For FP theory, there will be non-linearities like,

$$\mathcal{L}_{\text{int}} \sim \left[\alpha(\Box\phi)^3 + \beta\Box\phi\phi_{,\mu\nu}\phi^{,\mu\nu}\right], \tag{4.31}$$

where α and β are model dependent coefficients. At $r = a << R_V$, deep inside the Vainshtein region, the equation of motion for ϕ gives,

$$\frac{\phi}{M_{pl}} \sim m_g^2\sqrt{R_s a^3} \sim n_0\frac{h}{M_{pl}}$$

from balancing $\mathcal{L}_{\text{int}} \sim \phi^3/(M_{pl}m_g^4 r^6)$ against $\phi T/M_{pl} \sim \phi M/(M_{pl}r^3)$. Here, a denotes the semi major axis of the binary orbit. So the scalar mediated fifth force is suppressed by n_0 relative to the Newtonian force.

However, we neglect the corrections as they are small and will not affect our order of magnitude results and, therefore, we only consider the GW stress-energy tensor. Thus our results are approximate and not valid for all orders of n_0.

From Eq.C.47 we get

$$\left[T_{ij}(\omega')T^*_{ji}(\omega') - \frac{1}{3}|T^i{}_i(\omega')|^2\right] = 4\mu^2\omega'^4 a^4 f(n,e). \tag{4.32}$$

where $n_0 = \dfrac{m_g}{\Omega}$, and

$$f(n,e) = \frac{1}{32n^2}\Big\{[J_{n-2}(ne) - 2eJ_{n-1}(ne) + 2eJ_{n+1}(ne) + \frac{2}{n}J_n(ne) - J_{n+2}(ne)]^2 + (1-e^2)[J_{n-2}(ne) - 2J_n(ne) + J_{n+2}(ne)]^2 + \frac{4}{3n^2}J_n^2(ne)\Big\}. \tag{4.33}$$

The final expression of dE/dt for massive theory can be written in the compact form as

$$\frac{dE}{dt} = \frac{32G}{5}\mu^2 a^4 \Omega^6 \sum_{n=1}^{\infty} n^6 \sqrt{1-\frac{n_0^2}{n^2}} \left[f(n,e)\left(\frac{19}{18}+\frac{11}{9}\frac{n_0^2}{n^2}+\frac{2}{9}\frac{n_0^4}{n^4}\right) + \frac{5J_n^2(ne)}{108n^4} \times \left(1-\frac{n_0^2}{n^2}\right)^2 \right]. \tag{4.34}$$

We can split Eq.4.34 as

$$\frac{dE}{dt} = \frac{32G}{5}\mu^2 a^4 \Omega^6 \sum_{n=1}^{\infty} n^6 \sqrt{1-\frac{n_0^2}{n^2}} \left[f(n,e)\left(1+\frac{4}{3}\frac{n_0^2}{n^2}+\frac{1}{6}\frac{n_0^4}{n^4}\right) - \frac{5J_n^2(ne)}{36n^4}\frac{n_0^2}{n^2} \times \left(1-\frac{n_0^2}{4n^2}\right)\right] + \frac{32G}{5}\mu^2 a^4 \Omega^6 \sum_{n=1}^{\infty} n^6 \sqrt{1-\frac{n_0^2}{n^2}} \left[\frac{1}{18} f(n,e)\left(1-\frac{n_0^2}{n^2}\right)^2 + \frac{5J_n^2(ne)}{108n^4} \times \left(1+\frac{n_0^2}{2n^2}\right)^2\right], \tag{4.35}$$

where the first term in Eq.4.35 denotes the energy loss in the massive gravity theory without vDVZ discontinuity (Eq.4.53) and the second term denotes the contribution due to the scalar mode associated with $\frac{1}{6}\eta_{\mu\nu}\eta_{\alpha\beta}$. We can also write Eq.4.35 to the leading order in n_0^2 as

$$\frac{dE}{dt} \simeq \frac{32G}{5}\mu^2 a^4 \Omega^6 \Big[\sum_{n=1}^{\infty} \left(\frac{19}{18} n^6 f(n,e) + \frac{5}{108} n^2 J_n^2(ne)\right) + n_0^2 \sum_{n=1}^{\infty} \left(\frac{25}{36} n^4 f(n,e) - \frac{25}{216} J_n^2(ne)\right)\Big] + \mathcal{O}(n_0^4). \tag{4.36}$$

The rate of energy loss in the Keplerian orbit gives rise to the decrease in the orbital period at a rate

$$\dot{P}_b = -6\pi G^{-\frac{3}{2}} (m_1 m_2)^{-1} (m_1+m_2)^{-\frac{1}{2}} a^{\frac{5}{2}} \left(\frac{dE}{dt}\right). \tag{4.37}$$

The energy loss or the power radiated from the binary system increases with increasing the eccentricity as it is clear from Fig.4.2, since the energy loss in the first term is proportional to $n^6 f(n,e)$. The radiation is dominated by the higher harmonics for $e \approx 1$. The radiation has a peak at some particular value of n for a given eccentric orbit.

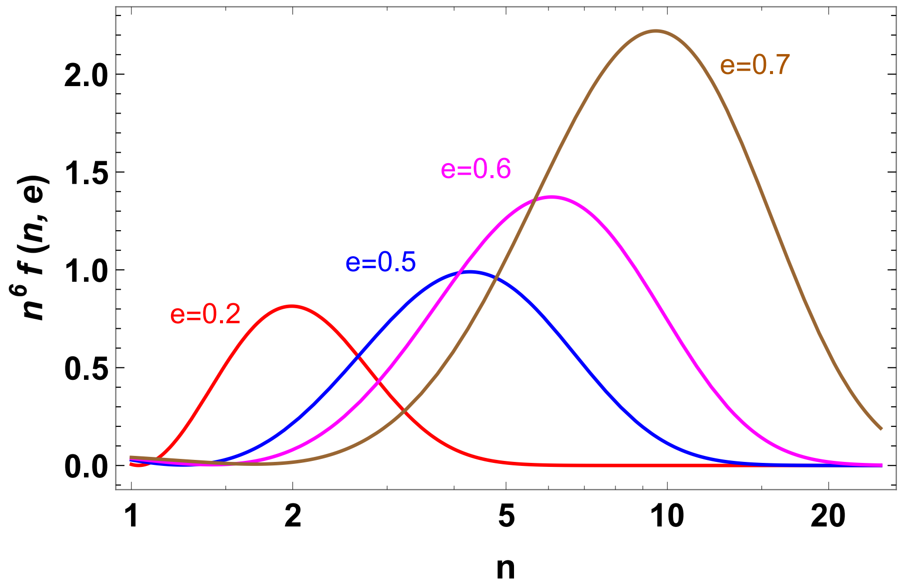

Figure 4.2: Variation of $n^6 f(n,e)$ with n for different orbital eccentricity.

4.3 Massive gravity theory without vDVZ discontinuity

In the action of the linearized massive gravity FP theory Eq.4.1, the relative coefficient between the terms h^2 and $h_{\mu\nu}h^{\mu\nu}$ is -1 which results in no ghosts in the theory. Generalising the theory beyond this point at which the relative coefficient between the terms h^2 and $h_{\mu\nu}h^{\mu\nu}$ are different from -1 leads to the appearance of ghosts. There is a special choice ($-1/2$) of the relative coefficient between the two terms for which the ghost mode cancels the scalar degree of freedom and there is no vDVZ discontinuity [263, 264]. Due to the modification of the FP action, the vDVZ discontinuity disappears from the theory. Phenomenologically this theory has the generalisation of spin-2 graviton with two polarizations and the theory obeys the massive graviton dispersion relation $k_0^2 = |\vec{k}|^2 + m_g^2$. Consider the one parameter generalisation of the FP theory

$$S = \int d^4x \left[\frac{1}{2}h_{\mu\nu}\mathcal{E}^{\mu\nu\alpha\beta}h_{\alpha\beta} + \frac{1}{2}m_g^2 h_{\mu\nu}\left(\eta^{\mu(\alpha}\eta^{\beta)\nu} - (1-a)\eta^{\mu\nu}\eta^{\alpha\beta}\right)h_{\alpha\beta} + \frac{\kappa}{2}h_{\mu\nu}T^{\mu\nu}\right], \tag{4.38}$$

where at $a = 0$ limits, the action Eq.4.38 reduces to that of FP theory Eq.4.1. In the following, we solve the action to get the equation of motion for a massive graviton field with $a \neq 0$. We will also see which values of a can solve the problem of vDVZ discontinuity which is generic in massive gravity theories.

The equation of motion from Eq.4.38 is

$$\left(\Box + m_g^2\right) h_{\mu\nu} - \eta_{\mu\nu}\left(\Box + m_g^2(1-a)\right) h - \partial_\mu\partial^\alpha h_{\alpha\nu} - \partial_\nu\partial^\alpha h_{\alpha\mu} + \eta_{\mu\nu}\partial^\alpha\partial^\beta h_{\alpha\beta} + \partial_\mu\partial_\nu h = -\kappa T_{\mu\nu}. \tag{4.39}$$

The divergence of Eq.4.39 yields

$$m_g^2\left(\partial^\mu h_{\mu\nu} - (1-a)\partial_\nu h\right) = 0. \tag{4.40}$$

These are 4 constraint equations that reduce the independent degrees of freedom of the graviton from 10 to 6.

Using Eq.4.40 in Eq.4.39 we obtain

$$(\Box + m_g^2)h_{\mu\nu} - a\eta_{\mu\nu}\Box h - (1-2a)\partial_\mu\partial_\nu h - m_g^2\eta_{\mu\nu}(1-a)h = -\kappa T_{\mu\nu}. \tag{4.41}$$

Taking the trace of this equation we get

$$-2a\Box h - (3m_g^2 - 4m_g^2 a)h = -\kappa T. \tag{4.42}$$

We see that the h is now a propagating field if $a \neq 0$. The kinetic term for h appears with a minus sign so h is a ghost field. The homogenous equation for h can be written as

$$\Box h - m_h^2 h = 0 \tag{4.43}$$

with the ghost mass given by

$$m_h^2 = \frac{m_g^2}{2}\left(1 + 3\left(1 - \frac{1}{a}\right)\right). \tag{4.44}$$

The propagator of the modified FP theory Eq.4.38 is given

$$\left[\mathcal{E}^{\mu\nu\alpha\beta} + m_g^2\left(\eta^{\mu(\alpha}\eta^{\beta)\nu} - \eta^{\mu\nu}\eta^{\alpha\beta}(1-a)\right)\right] D^{(a)}_{\alpha\beta\rho\sigma}(x-y) = \delta^\mu_{(\rho}\delta^\nu_{\sigma)}\delta^4(x-y). \tag{4.45}$$

Eq.4.45 can be inverted to obtain the propagator $D^{(a)}_{\alpha\beta\rho\sigma}(k)$ in momentum space as

$$D^{(a)}_{\alpha\beta\mu\nu}(k) = \frac{1}{-k^2 + m_g^2}\left(\frac{1}{2}(\eta_{\alpha\mu}\eta_{\beta\nu} + \eta_{\alpha\nu}\eta_{\beta\mu}) - \frac{1}{3}\eta_{\alpha\beta}\eta_{\mu\nu}\right) + \frac{i}{k^2 + m_h^2}\times \left(\frac{1}{6}\eta_{\alpha\beta}\eta_{\mu\nu}\right) + (k\text{−dependent terms}). \tag{4.46}$$

Hence, there are two types of contributions to the propagator, helicity-2 states of spin-2 massive gravitons (there are also helicity-1 and helicity-0 states) and a massive scalar with mass m_h. This part is identical to the propagator of the FP theory. In Eq.4.46 there is an additional contribution from the ghost mode with the kinetic operator k^2 with the wrong sign and mass m_h given in Eq.4.44. The remaining 3 vector degrees of freedom do not couple to the energy momentum tensor and we ignore their contribution here. Now for the choice of the parameter $a = 1/2$, the mass of the ghost mode Eq.4.44 becomes $m_h^2 = -m_g^2$. The ghost mode for $a = 1/2$ becomes tachyonic. Substituting $m_h^2 = -m_g^2$ in Eq.4.46 we see that the propagator becomes

$$D^{(1/2)}_{\alpha\beta\mu\nu}(k) = \frac{1}{-k^2 + m_g^2}\left(\frac{1}{2}(\eta_{\alpha\mu}\eta_{\beta\nu} + \eta_{\alpha\nu}\eta_{\beta\mu}) - \frac{1}{2}\eta_{\alpha\beta}\eta_{\mu\nu}\right) + (k\text{−dependent terms}). \tag{4.47}$$

The ghost term with the tachyonic mass cancels the contribution from the scalar degree of freedom. Hence, we are left with the same tensor structure of the propagator as in the case of massless graviton Eq.C.11 but the dispersion relation is the same as for massive graviton $k_0^2 = |\vec{k}|^2 + m_g^2$. In the massless graviton limit, the polarization sum Eq.4.47 for the modified FP theory takes the same form as for massless theory Eq.C.17 and there is no vDVZ discontinuity.

In modified FP theory with no vDVZ discontinuity, the gravitational potential between two massive bodies take the Yukawa behaviour

$$V^{(1/2)}(r) = \frac{GM_1M_2}{r}\, e^{-m_g r}. \tag{4.48}$$

The extra $4/3$ multiplicative factor which was there in the FP theory (Eq.4.17) is absent in modified FP theory where the scalar mode cancels the ghost contribution in the propagator. The Yukawa corrections to the $1/r$ potential will give rise to a perihelion precession in planetary orbits [66]. Constraints on the Yukawa potential between compact binary systems give bounds in the mass of the exchanged particle that has been discussed in [65, 66]. The long range Yukawa potential caused by axions can also affect the gravitational light bending and Shapiro time delay which is discussed in [63].

The modified FP theory with no vDVZ discontinuity is phenomenologically the most acceptable. The classical calculation of energy loss due to massive graviton radiation from the compact binary system in the modified FP theory was done by Finn and Sutton [262]. Here we calculate the gravitational radiation due to massive graviton from the Feynman diagram technique which is equivalent to a massive graviton emission from a one graviton vertex process. We find that our result matches the result of Finn and Sutton [262] at the leading order.

The direct detection of the gravitational wave was first confirmed from the gravitational wave event GW150914 by LIGO and Virgo which gives the upper bound on the mass of the graviton $m_g < 1.2 \times 10^{-22}$ eV.

4.3.1 Graviton radiation in massive gravity theory without vDVZ discontinuity

In the limit, $a < R_V$, the Keplerian orbits are also Vainshtein screened similar to FP theory as discussed before and there will be corrections at $\mathcal{O}(n_0)$ in Newtonian potential. Therefore, we consider GR stress-tensor in this case as well.

Following Appendix C.1, we calculate the rate of energy loss due to the massive graviton radiation as

$$\frac{dE}{dt} = \frac{\kappa^2}{8(2\pi)^2}\int \Big[|T_{\mu\nu}(k')|^2 - \frac{1}{2}|T^{\mu}{}_{\mu}(k')|^2\Big]\delta(\omega-\omega')\omega^2\Big(1-\frac{m_g^2}{\omega^2}\Big)^{\frac{1}{2}} d\omega d\Omega_k \tag{4.49}$$

$$= \frac{\kappa^2}{8(2\pi)^2}\int \tilde{\Lambda}_{ij,lm}T^{ij*}T^{lm}\delta(\omega-\omega')\omega^2\Big(1-\frac{m_g^2}{\omega^2}\Big)^{\frac{1}{2}} d\omega d\Omega_k, \tag{4.50}$$

where

$$\tilde{\Lambda}_{ij,lm} = \Bigg[\delta_{il}\delta_{jm} - 2\left(1-\frac{m_g^2}{\omega^2}\right)\hat{k_j}\hat{k_m}\delta_{il} + \frac{1}{2}\left(1-\frac{m_g^2}{\omega^2}\right)^2\hat{k_i}\hat{k_j}\hat{k_l}\hat{k_m} - \frac{1}{2}\delta_{ij}\delta_{lm} + \frac{1}{2}\left(1-\frac{m_g^2}{\omega^2}\right)\left(\delta_{ij}\hat{k_l}\hat{k_m} + \delta_{lm}\hat{k_i}\hat{k_j}\right)\Bigg]. \tag{4.51}$$

After computing the angular integration, we obtain the rate of energy loss as

$$\frac{dE}{dt} = \frac{8G}{5}\int\Bigg[\Bigg\{\frac{5}{2} - \frac{5}{3}\left(1-\frac{m_g^2}{\omega'^2}\right) + \frac{1}{6}\left(1-\frac{m_g^2}{\omega'^2}\right)^2\Bigg\} T^{ij}T^*_{ij} + \Bigg\{-\frac{5}{4} + \frac{5}{6}\left(1-\frac{m_g^2}{\omega'^2}\right) + \frac{1}{12}\left(1-\frac{m_g^2}{\omega'^2}\right)^2\Bigg\}|T^i{}_i|^2\Bigg]\delta(\omega-\omega')\omega^2\Big(1-\frac{m_g^2}{\omega^2}\Big)^{\frac{1}{2}} d\omega. \tag{4.52}$$

Simplifying Eq.4.52 we get

$$\frac{dE}{dt} = \frac{32G}{5}\mu^2 a^4 \Omega^6 \sum_{n=1}^{\infty} n^6 \sqrt{1-\frac{n_0^2}{n^2}} \left[f(n,e)\left(1+\frac{4}{3}\frac{n_0^2}{n^2}+\frac{1}{6}\frac{n_0^4}{n^4}\right) - \frac{5J_n^2(ne)}{36n^4}\frac{n_0^2}{n^2} \times \left(1-\frac{n_0^2}{4n^2}\right)\right]. \tag{4.53}$$

To the leading order in n_0^2, we can express Eq.4.53 as

$$\frac{dE}{dt} \simeq \frac{32G}{5}\mu^2 a^4 \Omega^6 \left[\sum_{n=1}^{\infty} n^6 f(n,e) + n_0^2 \sum_{n=1}^{\infty}\left(\frac{5}{6}n^4 f(n,e) - \frac{5}{36}J_n^2(ne)\right)\right] + \mathcal{O}(n_0^4). \tag{4.54}$$

We note that the expression reduces to that of GR in the limit $n_0 = 0$. Thus there is no vDVZ discontinuity. To the leading order in n_0^2 this agrees with the result of the classical calculation of Finn and Sutton [262].

4.4 Dvali-Gabadadze-Porrati (DGP) theory

The nonlinear GR theory obeys diffeomorphism invariance. However, in massive gravity theories, this symmetry is broken. In FP theory, if the graviton is expanded around curved spacetime, a ghost degree of freedom appears [278]. To get a consistent ghost free massive gravity theory, one can go to a higher dimension. One such massive gravity theory in higher dimensions using a braneworld model framework is the DGP theory [88, 265, 266, 279]. In the higher dimensions, the massless theory has a general covariance symmetry. The number of polarisation states of the massless graviton in 5-dimensions is 5. When the extra dimension compactifed, the number of degrees of freedom for a massive graviton in 4-d remains 5 and there is no (Boulware Deser) BD ghost. One advantage of the DGP theory is that it can account for the cosmological constant [280]. The mass of graviton is momentum dependent so that one can modify the infrared theory (at cosmological scales) while retaining Newtonian theory at solar system scales. However, the scalar degree of freedom still remains in the theory which contributes to the vDVZ discontinuity that creates problems for the phenomenological study of DGP theory [279]. In the following, we calculate the rate of energy loss due to massive graviton radiation in DGP theory.

4.4.1 Graviton radiation in DGP theory

In the five dimensional DGP theory, the matter field is localized in a four dimensional braneworld that leads to an induced curvature term on the brane. M_5 and M_{pl} denote the Planck scales of the five dimensional DGP theory and the four dimensional braneworld respectively. The five dimensional DGP massive gravity theory action [88, 265, 266] with the matter field localized in the four dimensional braneworld at $y = 0$ is

$$\mathcal{S} \supset \int d^4x dy \Big(\frac{M_5^3}{4} \sqrt{-^{(5)}g}^{(5)} R + \delta(y) \Big[\sqrt{-g} \frac{M_{pl}^2}{2} R[g] + \mathcal{L}_m(g, \psi_i) \Big] \Big), \tag{4.55}$$

where ψ_i denotes the matter field with the energy stress tensor $T_{\mu\nu}$ in the braneworld.

The modified linearized Einstein equation on the $y = 0$ brane is [86]

$$(\Box h_{\mu\nu} - \partial_\mu \partial_\nu h) - m_0 \sqrt{-\Box} (h_{\mu\nu} - h\eta_{\mu\nu}) = -\frac{\kappa}{2} T_{\mu\nu}(x), \tag{4.56}$$

where $m_0 = \dfrac{M_5^3}{M_{pl}^2}$, $M_{pl}^2 = 1/8\pi G = 4/\kappa^2$. Here, the Fierz-Pauli mass term $(h_{\mu\nu} - h\eta_{\mu\nu})$ appears naturally from the higher dimensional DGP theory. This corresponds to the linearized massive gravity with a scale-dependent effective mass $m_g^2(\Box) = m_0\sqrt{-\Box}$. The propagator is

$$D^{(5)}_{\alpha\beta\mu\nu}(k) = \frac{i}{(-\omega^2 + |\mathbf{k}|^2) + m_0(\omega^2 - |\mathbf{k}|^2)^{1/2}} \left(\frac{1}{2}(\eta_{\alpha\mu}\eta_{\beta\nu} + \eta_{\alpha\nu}\eta_{\beta\mu}) - \frac{1}{3}\eta_{\alpha\beta}\eta_{\mu\nu} \right). \tag{4.57}$$

The terms in the brackets represent the polarization sum which is identical to that of the FP theory (Eq.4.12). In the $m_0 \to 0$ limits, the DGP propagator does not go to the massless form (Eq.C.11) and the DGP theory also has the vDVZ discontinuity.

The dispersion relation corresponding to real gravitons in the DGP model is given by the pole of the propagator (Eq.4.57),

$$\omega^2 = |\mathbf{k}|^2 - m_0^2, \tag{4.58}$$

where $|\mathbf{k}|$ is the magnitude of the propagation vector. In the DGP model, the graviton has a tachyonic mass.

Following the same steps for FP theory, we write down the rate of energy loss in DGP theory due to massive graviton radiation. All the expressions in DGP theory differ from those of the FP theory by replacing $m_g^2 \to -m_0^2$ and $\tilde{n}_0^2 = m_0^2/\Omega^2 = -n_0^2$, i.e.

$$\frac{dE}{dt} = \frac{\kappa^2}{8(2\pi)^2} \int \left[|T_{\mu\nu}(k')|^2 - \frac{1}{3}|T^{\mu}{}_{\mu}(k')|^2\right] \delta(\omega - \omega')\omega^2 \left(1 + \frac{m_0^2}{\omega^2}\right)^{\frac{1}{2}} d\omega d\Omega_k. \quad (4.59)$$

The components of the stress tensor in $x - y$ plane is given in Eq.C.47. The direction of the massive graviton momnetum in the DGP theory is $\hat{k}^i = \dfrac{k^i}{\omega\sqrt{1+\frac{m_0^2}{\omega^2}}}$. The other components of $T_{\mu\nu}$ can be obtained by using $k_\mu T^{\mu\nu} = 0$ which yields,

$$T_{0j} = -\sqrt{1 + \frac{m_0^2}{\omega^2}}\hat{k}^i T_{ij}, \quad T_{00} = \left(1 + \frac{m_0^2}{\omega^2}\right)\hat{k}^i \hat{k}^j T_{ij}. \quad (4.60)$$

Hence, in terms of the projection operator $\tilde{\Lambda}_{ij,lm}$, the term in the third bracket of Eq.4.59 can be written as

$$\left[|T_{\mu\nu}(k')|^2 - \frac{1}{3}|T^{\mu}{}_{\mu}(k')|^2\right] = \tilde{\Lambda}_{ij,lm} T^{ij*} T^{lm}, \quad (4.61)$$

where

$$\begin{aligned}\tilde{\Lambda}_{ij,lm} = \Big[\delta_{il}\delta_{jm} - 2\left(1 + \frac{m_0^2}{\omega^2}\right)\hat{k_j}\hat{k_m}\delta_{il} + \frac{2}{3}\left(1 + \frac{m_0^2}{\omega^2}\right)^2 \hat{k_i}\hat{k_j}\hat{k_l}\hat{k_m} - \frac{1}{3}\delta_{ij}\delta_{lm} + \\ \frac{1}{3}\left(1 + \frac{m_0^2}{\omega^2}\right)\left(\delta_{ij}\hat{k_l}\hat{k_m} + \delta_{lm}\hat{k_i}\hat{k_j}\right)\Big].\end{aligned} \quad (4.62)$$

In DGP theory, there will be corrections to the Newtonian gravitational potential at $\mathcal{O}(n_0)$ in the $a < R_V$ region where Vainshtein screening is active. We can arrive at this fact by following the similar analysis as described in the FP theory. However, in the action Eq.4.30, there will be non-linearities like [270],

$$\mathcal{L}_{\text{int}} \sim \frac{1}{M_{pl} m_g^2}(\partial\phi)^2 \Box\phi. \quad (4.63)$$

At $r = a << R_V$, deep inside the Vainshtein region, the equation of motion for ϕ gives,

$$\frac{\phi}{M_{pl}} \sim m_g \sqrt{\frac{a^3}{R_s}} \frac{R_s}{a} \sim n_0 \frac{h}{M_{pl}} \quad (4.64)$$

from balancing $\mathcal{L}_{\text{int}} \sim \phi^3/(M_{pl} m_g^2 r^4)$ against $\phi T/M_{pl} \sim \phi M/(M_{pl} r^3)$, and so the fifth force mediated by the scalar polarisation is only suppressed by n_0 relative to the Newtonian force. As before we neglect the correction and consider the GR stress-energy tensor in the calculation of graviton emission rate.

Finally, we can write the rate of energy loss due to the massive graviton radiation in the DGP theory as

$$\frac{dE}{dt} = \frac{32G}{5}\mu^2 a^4 \Omega^6 \sum_{n=1}^{\infty} n^6 \sqrt{1+\frac{\tilde{n}_0^2}{n^2}}\Bigg[f(n,e)\left(\frac{19}{18}-\frac{11}{9}\frac{\tilde{n}_0^2}{n^2}+\frac{2}{9}\frac{\tilde{n}_0^4}{n^4}\right)+ \\ \frac{5J_n^2(ne)}{108n^4}\left(1+\frac{\tilde{n}_0^2}{n^2}\right)^2\Bigg]. \tag{4.65}$$

We can write Eq.4.65 to the leading order in n_0^2 as

$$\frac{dE}{dt} \simeq \frac{32G}{5}\mu^2 a^4 \Omega^6 \Bigg[\sum_{n=1}^{\infty}\left(\frac{19}{18}n^6 f(n,e)+\frac{5}{108}n^2 J_n^2(ne)\right) - \\ \tilde{n}_0^2 \sum_{n=1}^{\infty}\left(\frac{25}{36}n^4 f(n,e)-\frac{25}{216}J_n^2(ne)\right)\Bigg] + \mathcal{O}(\tilde{n}_0^4). \tag{4.66}$$

4.5 Constraints from observations

Table 4.1: Summary of the measured orbital parameters and the orbital period derivative values from observation and GR for PSR B1913+16 [260] and PSR J1738+0333 [181]. The uncertainties in the last digits are quoted in the parenthesis.

Parameters	PSR B1913+16	PSR J1738+0333
Pulsar mass m_1 (solar masses)	1.438 ± 0.001	$1.46^{+0.06}_{-0.05}$
Companion mass m_2 (solar masses)	1.390 ± 0.001	$0.181^{+0.008}_{-0.007}$
Eccentricity e	$0.6171340(4)$	$(3.4 \pm 1.1) \times 10^{-7}$
Orbital period P_b (d)	$0.322997448918(3)$	$0.3547907398724(13)$
Intrinsic $\dot{P}_b(10^{-12}\ \mathrm{ss}^{-1})$	-2.398 ± 0.004	$(-25.9 \pm 3.2) \times 10^{-3}$
GR $\dot{P}_b(10^{-12}\ \mathrm{ss}^{-1})$	-2.40263 ± 0.00005	$-27.7^{+1.5}_{-1.9} \times 10^{-3}$

In this section, we obtain bounds on the graviton mass for three above mentioned massive gravity theories from the orbital period loss of compact binary systems such as Hulse -Taylor binary system (PSR B1913+16) and a pulsar white-dwarf binary system (PSR J1738+0333). The orbital parameters and the orbital period derivative values from observation and GR for the two compact binary systems are given in Table 4.1. From the field theoretic approach of calculating the one graviton vertex process, we derive the rate of energy loss due to massless graviton radiation for a compact binary

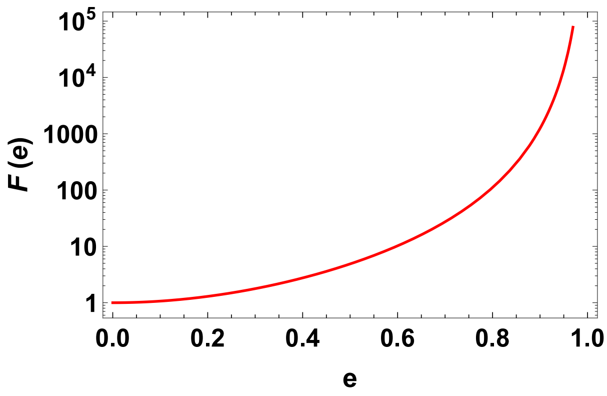

Figure 4.3: Variation of $F(e)$ with the eccentricity.

system Eq. C.51 that agrees with the Peters Mathews formula [177]. The variation of $F(e) = (1-e^2)^{-7/2}\left(1+\frac{73}{24}e^2+\frac{37}{96}e^4\right)$ with the eccentricity is shown in Fig.4.3. The energy loss due to the GR value is largely enhanced by the eccentricity enhancement factor $F(e)$. Its value is always greater than one for non zero eccentric orbits. Large eccentric Keplerian orbit has strong speed variation as it moves from periastron to apiastron which leads to produce a large amount of radiation in higher harmonics of orbital frequency. In the following, we compare three massive theories of gravity and find bounds on the graviton mass for PSR B1913+16 and PSR J1738+0333.

4.5.1 Vainshtein radius and limits of linear theory

For calculating the graviton emission, we have used the leading order perturbation of the metric. We can use the perturbation theory in linearised Einstein's gravity as long as $\kappa h_{\mu\nu} \ll 1$. This implies that perturbation theory breaks down at a radius smaller than the Schwarzschild radius $R_s = 2GM$ of the source. If the Fierz-Pauli and no-vDVZ theories are effective field theories describing gravity, with a non-linearly realised diffeomorphism symmetry, then there will inevitably be interactions below the scale $\Lambda_5 \sim (m_g^4 M_{pl})^{1/5}$ and that will set the Vainshtein limit of this linearised massive gravity theories [277]. Therefore, the smallest radius until which the perturbation theory can be applied is the Vainshtein radius [275] (R_V) and that is given by

$$R_V = \left(\frac{R_s}{m_g^4}\right)^{1/5} . \tag{4.67}$$

The Vainshtein radius is much larger than the Schwarzschild radius R_s and perturbative calculations of the Fierz-Pauli theory are valid in regions with $r > R_V$ away from the source. In our application of massive graviton radiation from compact binary systems, classically the gravitational field is evaluated at the radiation zone such that $R_V < \lambda$ (where $\lambda \sim \pi/\Omega$ is the wavelength of the gravitational waves radiated). Hence, in the FP theory, we must have

$$\lambda \sim \pi\Omega^{-1} > R_V = \left(\frac{R_s}{m_g^4}\right)^{1/5} . \tag{4.68}$$

We obtain a lower bound on the graviton mass from the Vainshtein limit above which the perturbative calculations are valid, given by

$$m_g > \frac{\Omega^{5/4}}{\pi^{5/4}}(2GM)^{1/4} \tag{4.69}$$

Hence, using the numbers as shown in Table.4.1 and Vainshtein limit for FP theory, we obtain theoretical lower bounds on the mass of the graviton as $m_g > 3.06 \times 10^{-22}$ eV for PSR B1913+16 and $m_g > 2.456 \times 10^{-22}$ eV for PSR J1738+0333.

The Vainshtein radius for DGP theory is given by [88, 276]

$$R_V = \left(\frac{R_s}{m_g^2}\right)^{1/3} . \tag{4.70}$$

Again we must have $\lambda \sim \pi\Omega^{-1} > R_V$ which yields a lower bound on the graviton mass in the DGP theory above which the perturbative calculation is valid, given by

$$m_g > \frac{\Omega^{3/2}}{\pi^{3/2}}(2GM)^{1/2} . \tag{4.71}$$

This number is 7.84×10^{-24} eV for PSR B1913+16 and 1.406×10^{-24} eV for PSR J1738+0333.

4.5.2 Constraints from observation for FP Theory

The massive graviton has five states of polarization and of these the scalar and the tensor modes couple to the energy momentum tensor. These modes contribute to the energy loss of the compact binary systems for massive theories. In the massless limit $m_g \to 0$ of the FP theory, the scalar mode contributes to the vDVZ discontinuity. In Fig.4.4(a) and Fig.4.4(b), we show the variation of the orbital period loss with the

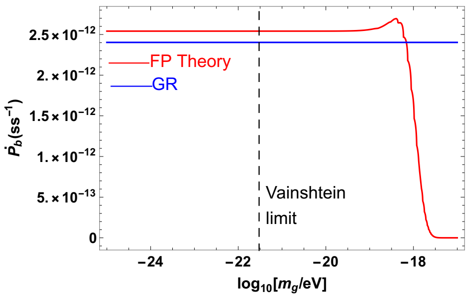

(a) Variation of orbital period loss with graviton mass for PSR B1913+16 in FP theory

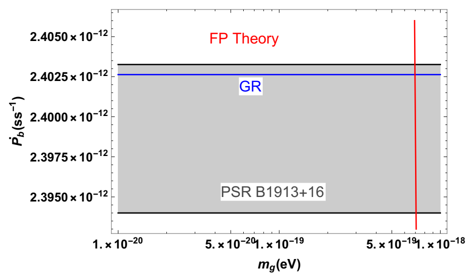

(b) Comparing the theoretical value for the orbital period loss with observation for PSR B1913+16 in FP theory in large m_g limit

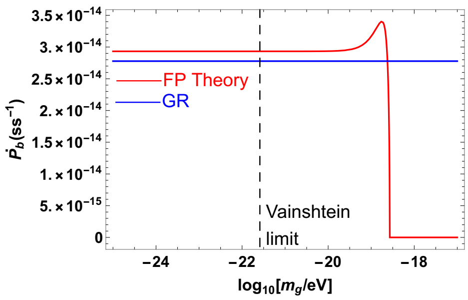

(c) Variation of orbital period loss with graviton mass for PSR J1738+0333 in FP theory

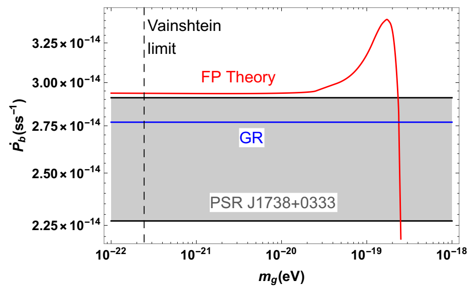

(d) Comparing the theoretical value for the orbital period loss with observation for PSR J1738+0333 in FP theory in large m_g limit

Figure 4.4: In the upper panel, we have shown (a) the Variation of orbital period loss with graviton mass and (b) comparing the theoretical value for the orbital period loss with observation for PSR B1913+16 in FP theory. In the lower panel (c) and (d) we have shown the same variation as above for PSR J1738+0333.

graviton mass for PSR B1913+16. Similarly, in Fig.4.4(c) and Fig.4.4(d) we obtain the same variation for PSR J1738+0333. The dotted lines denote the corresponding Vainshtein limit for the two binary systems. The red line denotes the analytical result of orbital period loss in FP theory as obtained above whereas the blue line denotes the corresponding GR value. The grey band denotes the allowed region of the orbital period loss from observation.

In the region $m_g \sim \Omega$, the phase space of graviton momentum shrinks and the energy loss falls with increasing m_g. There is a region where the theoretical red curve goes through the observational grey band as shown in Fig.4.4(b) and Fig.4.4(d) where the variation of the time derivative of the orbital period is shown with the observational uncertainty for the two compact binary systems.

The range of the graviton mass corresponds to $m_g \in (6.88 - 6.96) \times 10^{-19}$ eV (Fig.4.4(b)) for PSR B1913+16 and $m_g \in (2.31 - 2.48) \times 10^{-19}$ eV for PSR J1738+0333. There is no common mass range in the overlap region where the red line passes through the grey band for the two compact binary systems for any value of m_g.

Therefore, for the FP theory the limit on graviton mass comes from the theoretical Vainshtein limit $m_g > 3.06 \times 10^{-22}$ eV.

4.5.3 Constraints from observation for DGP Theory

In DGP theory, the massless limit $m_0 \to 0$ of the DGP theory does not simply give the massless result and here also one encounters vDVZ discontinuity due to the contribution of the scalar gravitons. In Fig.4.5(a) and Fig.4.5(b), we show the variation of the orbital period loss with m_0 for PSR B1913+16 and in Fig.4.5(c) and Fig.4.5(d) we obtain the same for PSR J1738+0333. The dotted lines denote the corresponding theoretical Vainshtein limit for the two binary systems which are $m_g > 7.84 \times 10^{-24}$ eV for PSR B1913+16 and $m_g > 1.406 \times 10^{-24}$ eV for PSR J1738+0333.

As in FP theory, the DGP theory also has some regions where the theoretical prediction crosses the observed band value which corresponds to the graviton mass $m_0 \in (2.45 - 2.47) \times 10^{-19}$ eV (Fig.4.4(b)) for PSR B1913+16 and $m_0 \in (0.31 - 1.41) \times 10^{-19}$ eV for PSR J1738+0333. Since for DGP theory, there is no common mass range in the overlap region for the two compact binary systems, we obtain the

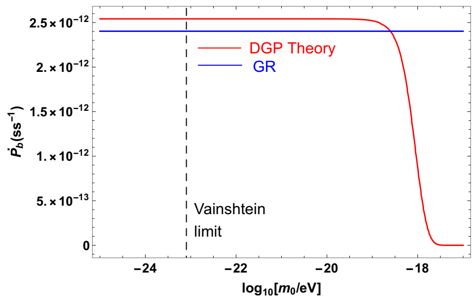

(a) Variation of orbital period loss with graviton mass for PSR B1913+16 in DGP theory

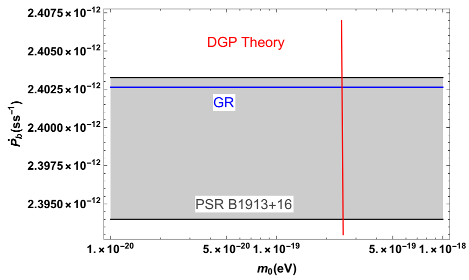

(b) Comparing the theoretical value for the orbital period loss with observation for PSR B1913+16 in DGP theory in large m_g limit

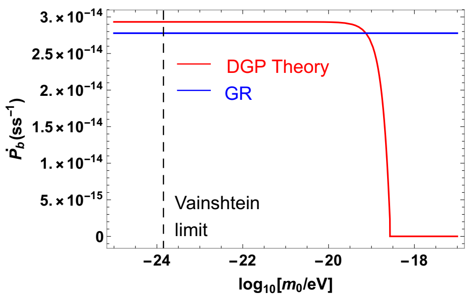

(c) Variation of orbital period loss with graviton mass for PSR J1738+0333 in DGP theory

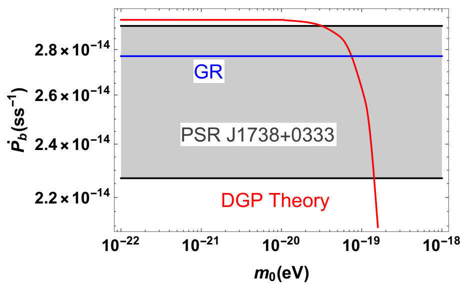

(d) Comparing the theoretical value for the orbital period loss with observation for PSR J1738+0333 in DGP theory in large m_g limit

Figure 4.5: In the upper panel, we have shown (a) the Variation of orbital period loss with graviton mass and (b) comparing the theoretical value for the orbital period loss with observation for PSR B1913+16 in DGP theory. In the lower panel (c) and (d) we have shown the same variation as above for PSR J1738+0333.

graviton mass bound from the Vainshtein limit as $m_0 > 7.84 \times 10^{-24}$ eV.

4.5.4 No vDVZ discontinuity theory

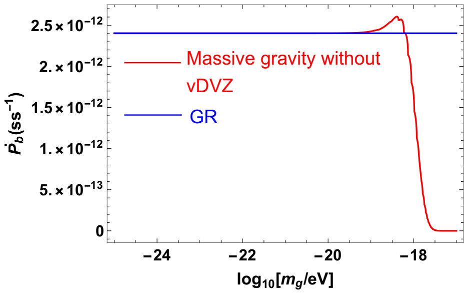

(a) Variation of orbital period loss with graviton mass for PSR B1913+16 in massive gravity theory without vDVZ discontinuity

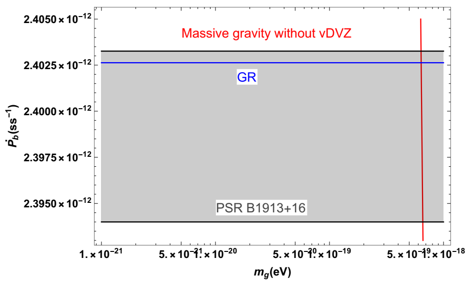

(b) Comparing the theoretical value for the orbital period loss with observation for PSR B1913+16 in massive gravity theory without vDVZ discontinuity for higher graviton mass

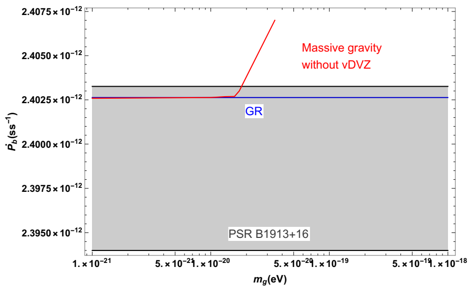

(c) Comparing the theoretical value for the orbital period loss with observation for PSR B1913+16 in massive gravity theory without vDVZ discontinuity for lower graviton mass

Figure 4.6: We have plotted the variation of orbital period loss with graviton mass for PSR B1913+16 in massive gravity theory without vDVZ discontinuity in (a). In (b) and (c) we have compared the theoretical value for the orbital period loss with observation for PSR B1913+16 in massive gravity theory without vDVZ discontinuity for higher graviton mass and lower graviton mass respectively.

Section 4.3 is the modified FP theory without vDVZ discontinuity at linear order. If one tunes the Fierz-Pauli term $(h_{\mu\nu}h^{\mu\nu} - h^2)$ to $(h_{\mu\nu}h^{\mu\nu} - \frac{1}{2}h^2)$ then at the linear order the ghost term with tachyonic mass cancels the scalar contribution to the propagator. Hence, we are left with the tensor structure of the propagator similar to the massless

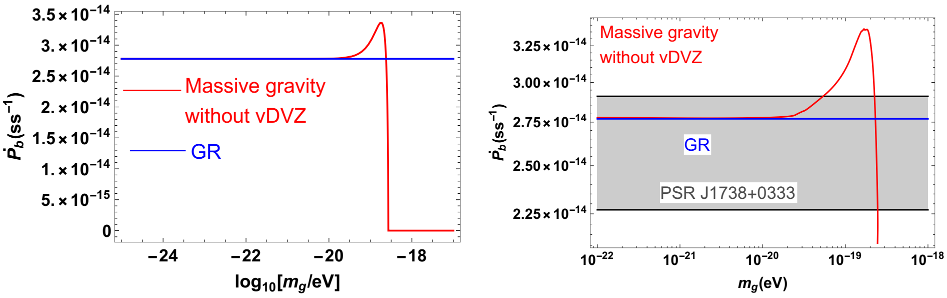

(a) Variation of orbital period loss with graviton mass for PSR J1738+0333 in massive gravity theory without vDVZ discontinuity

(b) Comparing the theoretical value for the orbital period loss with observation for PSR J1738+0333 in massive gravity theory without vDVZ discontinuity

Figure 4.7: We have plotted the variation of orbital period loss with graviton mass for PSR J1738+0333 in massive gravity theory without vDVZ discontinuity in (a). In (b) we have compared the theoretical value for the orbital period loss with observation for PSR J1738+0333 in massive gravity theory without vDVZ discontinuity.

graviton but having dispersion relation to that of a massive graviton. Due to the cancellation of scalar with the ghost, there is no vDVZ discontinuity in the $n_0 \to 0$ limits. All our calculations in this chapter are in linear order. However, if we include the non-linear terms in the action, there are interactions that will not eliminate the vDVZ discontinuity and the ghost will remain in the theory.

In modified FP theory without vDVZ discontinuity, the scalar mode is cancelled by the ghost mode. However, there will be a bound on graviton mass from Vainshtein limit in the theory similar to FP theory as mentioned in Eq. (4.67).

In Fig.4.6 and Fig.4.7, we show the variation of orbital period loss with the graviton mass for the two compact binary systems. It is clear that in the low graviton mass limit, the orbital period loss for this theory and massless theory become degenerate.

There exist two regions where the theoretical prediction agrees with the observational band. For PSR B1913+16 this corresponds to the graviton mass $m_g \in (6.32 - 6.50) \times 10^{-19}$ eV and $m_g < 1.81 \times 10^{-20}$ eV (Fig.4.6). For PSR J1738+0333, the corresponding graviton mass range are $m_g \in (2.18 - 2.34) \times 10^{-19}$ eV and $m_g < 5.29 \times 10^{-20}$ eV (Fig.4.7). Here, for the two compact binary systems, we find a common graviton mass region where there is an agreement with both observations and the bound on graviton mass is $m_g < 1.81 \times 10^{-20}$ eV.

All the bounds derived in this chapter are at 68% C.L.

4.6 Discussions

In this chapter, we obtain bounds on the graviton mass for three massive gravity theories from binary pulsar observations. We show that the bounds on graviton mass from binary observations are highly model dependent as the predictions for the gravitational luminosity for different graviton mass models have significant differences.

In massive gravity theories like FP and DGP with an extra propagating scalar, the contribution of the extra scalar to the energy loss is of the same order as that of the tensor gravitational waves and the region $m_g < \Omega$ is ruled out from orbital period loss observations. As the graviton mass approaches and becomes larger than Ω the energy radiated drops with increasing graviton mass. For each compact binary system, there is therefore a range of graviton mass where the theoretical predictions are within observational limits. We found that the allowed ranges of graviton mass from PSR B1913+16 and PSR J1738+0333 do not have any overlap. Therefore, combining observations from the two compact binary systems, we see that no range of graviton mass is consistent with both binary systems observations. In these theories, the linear order calculation breaks down below the Vainshtein radius.

The bound on graviton mass from the Vainshtein limit is a theoretical bound. Whereas, we describe an independent method of obtaining the graviton mass bound from the observation of orbital period loss of binary systems.

In this chapter, we have chosen two binary systems PSR B1913+16 and PSR J1738+0333 and computed the orbital period loss for the three massive gravity theories viz, FP theory, DGP theory and modified FP theory. Compared the observational data, we do not find any overlapping region of graviton mass for FP and DGP theory. For example, in DGP theory, the allowed ranges of mass are $(2.45 - 2.47) \times 10^{-19}$ eV for PSR B1913+16 and $(0.31 - 1.41) \times 10^{-19}$ eV for PSR J1738+0333. So, there is no common allowed mass range valid for both the compact binary systems and we can not give a universal graviton mass from the observation in DGP theory. Similarly, it is the case for FP theory as well. Therefore, we conclude that for FP and DGP theory, we obtain the stronger bound on the graviton mass from the Vainshtein limit.

Before comparing the observational data with our calculation, we cannot tell whether the Vainshtein limit puts a stronger limit on graviton mass or not. Although for modified FP theory with no vDVZ discontinuity, we found a common mass region for the two binary systems and obtain a bound on the graviton mass by comparing the observational data with our analytical calculations.

To summarise, observations from PSR B1913+16 and PSR J1738+0333 rule out all values of graviton mass and from the Vainshtein limit we can put the lower bounds $m_g > 3.06 \times 10^{-22}$ eV for the FP theory and $m_0 > 7.84 \times 10^{-24}$ eV for the DGP theory. For the No-vDVZ discontinuity theory, the upper bound from combined PSR B1913+16 and PSR J1738+0333 data is $m_g < 1.81 \times 10^{-20}$ eV. All bounds quoted in this chapter are with 68% C.L [273].

In [262] the authors used the method of a classical multipole expansion of the metric perturbation and kept the term in the expression of the energy loss up to $\mathcal{O}(m_g^2)$. However, in our chapter, we use the effective field theoretic approach where we treat the graviton as the quantum field and the binary stars as its classical source and we compute the graviton emission rate for a one graviton vertex process. The graviton emission is not possible for $\Omega < m_g$ and this is taken care of by the factor $(1 - m_g^2/\Omega^2)^{1/2}$ in the expression of the rate of energy loss.

In our study the hierarchy of scales is

$$\frac{a^2}{\lambda^2} \sim \frac{R_s}{a} << \frac{a^2}{R_V^2} << 1 << \frac{R_V}{R_S}, \tag{4.72}$$

where $R_s \sim 2M/M_{pl}^2$ and R_V are the usual Schwarzschild and Vainshtein radii around a compact object of mass M, a is the orbital separation of the binary, and λ is the wavelength of the emitted GW radiation. The condition for graviton emission $\Omega > m_g$ implies that $a < R_V$. This corresponds to a region of space screened by Vainshtein mechanism. Therefore, we can use the Keplerian orbit in GR in their evaluation of stress-energy tensor $T_{\mu\nu}$. Thus we neglect the corrections in the gravitational potential energy from the screened scalar mode, which are of $\mathcal{O}(n_0)$ for FP and DGP theories. Therefore, our results are approximate and not valid for all orders of n_0. These corrections in the Newtonian gravitational potential might change some order unity numerical factors but the order of magnitude of bounds on the graviton mass is expected to be the same as we have obtained.

In [270], the objective of the paper is different from ours. In this paper, the decoupling limit of the DGP theory has been considered, i.e. $M_{pl} \to \infty$ and $m_g \to 0$ keeping $m_g^2 M_{pl}$ fixed, where the helicity-2 modes are decoupled from the helicity-0 mode. However, we keep m_g finite. The key difference in our analysis is that we explore the complementary regime $\Omega R_V << 1$, so that the radiation is described by the linear theory whereas the paper [270] uses the opposite $\Omega R_V >> 1$ so that the radiation is Vainshtein screened. Also, there the authors used the classical multipole expansion method to obtain monopole, dipole, and quadrupole corrections at the leading and subleading orders. Therefore, our field theoretic method as mentioned earlier is quite different from theirs.

It should be noted that the upper bound on the graviton mass depends on the length scale of the observation. In fact, for DGP theory the mass of the graviton is scale dependent. Naturally, different observation will give different bound on the mass of the graviton. The bounds on the graviton mass mentioned in [248] and [271] are obtained for cubic galileon model which was originally derived from the decoupling limit of the DGP model. However, in our work, we have considered the actions for FP, DGP and modified FP theories from the first principle and calculate the energy loss from the binary system using Feynman diagram techniques at the tree level. The bounds on graviton mass that we have obtained are weaker than that for the cubic galileon models however our results are comparable with the LIGO bound for direct detection of gravitational waves.

Moreover, the calculations for energy loss that we have derived from Feynman diagram techniques are novel and provide interesting results.

There are other massive gravity theories like Lorentz violating gravitational mass [281–283] and more general Lorentz violating graviton bilinear terms [284, 285] which we have not covered in the Lorentz covariant calculation in this chapter. We will address these theories in future work.

This diagrammatic method can also be used for computing the wave-form of gravitational waves observed in direct detection experiments like LIGO and VIRGO [286, 287] for massive gravity theories. The gravitational wave from the extreme mass ratio mergers in massive graviton theories can also constrain the mass of the graviton [288]. It will be interesting to test massive gravity theory predictions [268, 269] with direct observations and in particular to constrain the scalar and vector modes of gravity from direct detection [289].

Chapter 5

Sterile Neutrino (Spin $1/2$): Dark Large Mixing Angle Solution and Neutrinoless Double Beta Decay

5.1 Introduction

The standard three flavour neutrino oscillation picture has been corroborated by the data from decades of experimentation on neutrinos. However some exceptions to this scenario have been reported over the years, calling for the necessity of transcending beyond the three neutrino paradigm. The first among these signatures came from the LSND $\bar{\nu_\mu} \to \bar{\nu_e}$ oscillation data [290], which could be explained by invoking additional neutrino states (sterile) that mix with active neutrinos [291–295]. This result was supported by the hints obtained : from the appearance data of $\bar{\nu_\mu} \to \bar{\nu_e}$ and $\nu_\mu \to \nu_e$ at MiniBooNE experiment [296–300], from the reactor neutrino anomaly [301, 302] where a deficit in the $\bar{\nu_e}$ reactor flux has been reported by short baseline(SBL) oscillation data and also from the missing neutrino flux at GALLEX [303–305] and SAGE [306] source experiments. However, accelerator experiments like KARMEN [307], ICARUS [308], NOMAD [309] have not found a positive signal. There are also disappearance experiments using reactors and accelerators as neutrino sources which have not reported any evidences of sterile neutrino [310]. The allowed region from the global analysis including all these data have been obtained in [311, 312]. Recently, analysis from MicrobooNE suggests no low energy excess of ν_e events [313–316]. However, their studies are model dependent and thus presence of light sterile neutrino is not completely ruled out [317, 318]. Several new experiments are planned to test the sterile neutrino hypothesis [319].

The basic question whether the neutrinos are Dirac particles or lepton number violating Majorana particles (for which particles and antiparticles are the same) remains as a major puzzle in neutrino physics. Since oscillation experiments do not help us to determine the nature of the neutrinos, one has to rely on studying the processes in which total lepton number is violated. In this regard, neutrino-less double beta decay ($0\nu\beta\beta$) process ($X_Z^A \rightarrow X_{Z+2}^A + 2e^-$) stands as a promising probe to establish the Majorana nature of neutrinos. $0\nu\beta\beta$ decay has not been observed so far and there are several ongoing and upcoming experiments that search for this signal. The best limit on the half life of $0\nu\beta\beta$ decay is $T_{1/2} > 1.07 \times 10^{26}$ years coming from the KamLAND-Zen experiment using ^{136}Xe [44]. This gives a bound on the effective Majorana mass ($m_{\beta\beta}$) as,

$$m_{\beta\beta} \leq 0.061 - 0.165 \,\text{eV}.$$

The range corresponds to the uncertainty in nuclear matrix elements (NME).

This process is suppressed by the proportionality of the transition amplitude to the effective Majorana mass $m_{\beta\beta}$, which in turn depends on the lowest neutrino mass, neutrino mass ordering, mixing angles and Majorana phases. However, the predictions for $m_{\beta\beta}$ are known to change substantially in a 3+1 mixing scenario when an additional sterile neutrino is introduced [320–329]. It is also well known that in the presence of non-standard interactions (NSI), solar neutrino data admits a new solution for $\theta_{12} > 45°$, known as the dark large mixing angle (DLMA) solution [32–34]. This is nearly a degenerate solution with $\Delta m^2_{21} \simeq 7.5 \times 10^{-5}$ eV^2 and $\sin^2\theta_{12} \simeq 0.7$. The DLMA parameter space was shown to be severely constrained from neutrino-nucleus scattering data from COHERENT experiment [35]. However the bound depends on the mass of the light mediator [36]. In this context, the effect of the DLMA solution on $0\nu\beta\beta$ for the standard three generation picture has been studied recently in ref. [330] where it was shown that the prediction for $m_{\beta\beta}$ remains unchanged for the inverted mass scheme whereas for normal hierarchy, it becomes higher for the Dark-LMA parameter space and shifts to the "desert region" between the two. This region can be tested in the next generation experiments.

In this chapter, we have studied the implications of the DLMA solution to the solar neutrino problem for $0\nu\beta\beta$ in the presence of a fourth sterile neutrino as introduced to explain the LSND/MiniBooNE results (see references [310, 331] for recent reviews on the status of eV scale sterile neutrinos.). In this case, the effective Majorana mass $m_{\beta\beta}$ governing $0\nu\beta\beta$ depends on the third mass-squared difference Δm^2_{LSND}, the mixing angle θ_{14} and an additional Majorana phase $\gamma/2$, in addition to the two mass squared differences Δm^2_{21} and Δm^2_{31}, two mixing angles θ_{12} (degenerate LMA or DLMA solutions) and θ_{13} and the Majorana phases $\alpha/2$ and $\beta/2$. Depending on the values of these parameters, there can be enhancement or cancellation of the $0\nu\beta\beta$ decay rate.

It has to be noted that the sum of masses of all the neutrino species is highly constrained from cosmology, which does not allow an eV scale sterile neutrino (see [331] for a recent review on the status of light sterile neutrinos and the cosmological bounds). To avoid the cosmological constraints, one can invoke "secret neutrino interactions" which can dynamically suppress the production of sterile neutrinos in the early universe by finite temperature effects [332]. One may also avoid the cosmological constraints by assuming a very low reheating temperature ($\sim MeV$) after inflation [333–335].

The rest of the chapter is organized as follows. In the next section, we discuss the DLMA solution and the MSW resonance condition in the presence of a fourth sterile neutrino. In section-5.3, we discuss the implications of the sterile neutrino and the DLMA solution for $0\nu\beta\beta$ process. The discovery sensitivity of $0\nu\beta\beta$ process in the the new allowed parameter space is discussed in section-5.4 in the context of ^{136}Xe based experiments. In Section- 5.5 we briefly discuss the cosmological constraints on eV scale sterile neutrino. Finally, we summarize our results in section-5.6. This chapter is based on [336]

5.2 DLMA solution in 3+1 neutrino framework

In the 3+1 neutrino framework, the neutrino mixing matrix U is a 4×4 unitary matrix which can be parametrized by three active neutrino mixing angles θ_{12}, θ_{13}, θ_{23}, three active-sterile mixing angles θ_{14}, θ_{24} and θ_{34} and the Dirac CP violating phases $\delta_{CP}, \delta_{14}, \delta_{24}$. Hence, the 4×4 unitary matrix is given by,

$$U = R_{34}\tilde{R_{24}}\tilde{R_{14}}R_{23}\tilde{R_{13}}R_{12}P, \tag{5.1}$$

where $P = diag(1, e^{i\alpha/2}, e^{i(\beta/2+\delta_{CP})}, e^{i(\gamma/2+\delta_{14})})$, and $\alpha/2,\ \beta/2,\ \gamma/2$ are the Majorana phases. The Dirac CP phases δ_{CP}, δ_{14} and δ_{24} are associated with $\tilde{R_{13}}$, $\tilde{R_{14}}$ and $\tilde{R_{24}}$ respectively. The Majorana phases can take values in the range $0 - \pi$. The rotation matrices R and $\tilde{R}$ are given in the Eq.(15) of reference [337]. The Majorana phase matrix comes into play while studying $0\nu\beta\beta$ process, but they are not relevant for oscillation studies. In Table 5.1, we have given the 3σ ranges of the mixing angles and mass squared differences in the three generation [338] as well as four generation schemes[311]. Similar analysis can also be found in references [339, 340] for three generation case and in [312] for the four generation case.

The neutral current Lagrangian for NSIs in matter is given by the effective dimension 6 four fermion operator as [341],

$$\mathcal{L}_{NSI} = -2\sqrt{2}G_F \sum_{f,P,\alpha,\beta} \epsilon^{fP}_{\alpha\beta}(\bar{\nu_\alpha}\gamma^\mu\nu_\beta)(\bar{f}\gamma_\mu P f), \tag{5.2}$$

where f is the charged fermion, P is the projection operator (left and right), and $\epsilon^{fP}_{\alpha\beta}$ are the parameters which govern the NSIs. The NSI affects the neutrino propagation in matter through vector coupling and we can write $\epsilon^{fP}_{\alpha\beta} = \epsilon^{fL}_{\alpha\beta} + \epsilon^{fR}_{\alpha\beta}$.

If we assume that the flavour structure of neutrino interaction is independent of charged fermion type, then one can write

$$\epsilon^{fP}_{\alpha\beta} = \epsilon^{\eta}_{\alpha\beta}\xi^{f,P}, \tag{5.3}$$

where $\epsilon^{\eta}_{\alpha\beta}$ denotes the coupling to the neutrino term and $\xi^{f,P}$ denotes the coupling to the charged fermion term. Hence, Eq. (5.2) can be written as

$$\mathcal{L}_{NSI} = -2\sqrt{2}G_F \sum_{\alpha,\beta} \epsilon^{\eta}_{\alpha\beta}(\bar{\nu_\alpha}\gamma^\mu\nu_\beta) \sum_{f,P} \xi^{f,P}(\bar{f}\gamma_\mu P f). \tag{5.4}$$

Parameter	NH	IH
$\Delta m^2_{sol}/10^{-5}eV^2$	$6.79 \rightarrow 8.01$	$6.79 \rightarrow 8.01$
$\Delta m^2_{atm}/10^{-3}eV^2$	$2.432 \rightarrow 2.618$	$2.416 \rightarrow 2.603$
$\sin^2\theta_{12}$	$0.275 \rightarrow 0.350$	$0.275 \rightarrow 0.350$
$\sin^2\theta_{23}$	$0.427 \rightarrow 0.609$	$0.430 \rightarrow 0.612$
$\sin^2\theta_{13}$	$0.02046 \rightarrow 0.02440$	$0.02066 \rightarrow 0.02461$
δ_{CP}	$0.783\pi \rightarrow 2.056\pi$	$1.139\pi \rightarrow 1.967\pi$
$\sin^2\theta_{14}$	$0.0098 \rightarrow 0.0310$	$0.0098 \rightarrow 0.0310$
$\sin^2\theta_{24}$	$0.0059 \rightarrow 0.0262$	$0.0059 \rightarrow 0.0262$
$\sin^2\theta_{34}$	$0 \rightarrow 0.0396$	$0 \rightarrow 0.0396$
δ_{14}	$0 \rightarrow 2\pi$	$0 \rightarrow 2\pi$
δ_{24}	$0 \rightarrow 2\pi$	$0 \rightarrow 2\pi$

Table 5.1: The oscillation parameters in their 3σ range, for NH and IH as given by the global analysis of neutrino oscillation data with three light active neutrinos [338] and one extra sterile neutrino [311].

it is convenient to write

$$\epsilon^f_{\alpha\beta} = \epsilon^\eta_{\alpha\beta}\xi^f \qquad \text{with,} \qquad \xi^{\rm f} = \xi^{\rm f,L} + \xi^{\rm f,R}. \tag{5.5}$$

We can parametrize the quark coupling in terms of η as

$$\xi^u = \frac{\sqrt{5}}{3}(2\cos\eta - \sin\eta), \qquad \xi^d = \frac{\sqrt{5}}{3}(2\sin\eta - \cos\eta). \tag{5.6}$$

The normalization constant is chosen in such a way that $\eta \approx 26.6^\circ$ corresponds to $\xi^u = 1$ and $\xi^d = 0$, which defines NSI with up quark and $\eta \approx 63.4^\circ$ corresponds to $\xi^u = 0$ and $\xi^d = 1$, which defines NSI with down quark. Under $\eta \rightarrow \eta + \pi$, ξ^u and ξ^d flip sign so it is sufficient to consider the parameter space $-\frac{\pi}{2} \leq \eta \leq \frac{\pi}{2}$. For $-38^\circ \leq \eta \leq 87^\circ$ the DLMA solution is allowed at 3σ [35]. In Table-5.2, we have chosen the parameter space for $\sin^2\theta_{12}$ corresponding to both LMA and DLMA solution obtained from global oscillation analysis data at 3σ [35]. In Table 5.1, all the neutrino oscillation parameters except $\sin^2\theta_{12}$ are robust in their 3σ range.

The total matter potential including standard and non-standard interactions is governed by the Hamiltonian,

$$H_{mat}^{sterile+NSI} = \sqrt{2}G_F N_e(r)\begin{bmatrix}1&0&0&0\\0&0&0&0\\0&0&0&0\\0&0&0&0\end{bmatrix} + \frac{G_F N_n}{\sqrt{2}}\begin{bmatrix}0&0&0&0\\0&0&0&0\\0&0&0&0\\0&0&0&1\end{bmatrix} + \sqrt{2}G_F\sum_{f=e,u,d} N_f(r)\begin{bmatrix}\epsilon^f_{ee}&\epsilon^f_{e\mu}&\epsilon^f_{e\tau}&0\\\epsilon^{f*}_{e\mu}&\epsilon^f_{\mu\mu}&\epsilon^f_{\mu\tau}&0\\\epsilon^{f*}_{e\tau}&\epsilon^{f*}_{\mu\tau}&\epsilon^f_{\tau\tau}&0\\0&0&0&0\end{bmatrix}, \tag{5.7}$$

where, N_e, N_n and N_f are the number densities of electron, neutron and the fermion f in the sun. Here, we have neglected non-standard interactions in the sterile sector [1]. Following the same approach as in [35] for three generation, we can now construct the Hamiltonian in an effective 2×2 model as $H^{eff} = H^{eff}_{vac} + H^{eff}_{mat}$ where,

$$H^{eff} = \frac{\Delta m^2_{21}}{4E}\begin{bmatrix}-\cos 2\theta_{12}&\sin 2\theta_{12}\\\sin 2\theta_{12}&\cos 2\theta_{12}\end{bmatrix} + A_i\begin{bmatrix}c^2_{13}c^2_{14}&0\\0&0\end{bmatrix} + A_j\begin{bmatrix}-k_1&k_2\\k^*_2&k_1\end{bmatrix} + A_i\sum_{f=e,u,d}\frac{N_f}{N_e}\begin{bmatrix}-\epsilon^f_D&\epsilon^f_N\\\epsilon^{f*}_N&\epsilon^f_D\end{bmatrix}. \tag{5.8}$$

Here, $A_i = \sqrt{2}G_F N_e$, $A_j = \dfrac{G_F N_n}{\sqrt{2}}$ and we have taken $\theta_{34} = 0$ (see Appendix D for detailed discussions). Now the new parameters $\epsilon^f_D, \epsilon^f_N$ are related to the old parameters $\epsilon^f_{\alpha\beta}$ through the following equations :

$$\begin{aligned}\epsilon^f_D &= c_{13}s_{13}Re[e^{i\delta_{CP}}(s_{23}c_{24}c_{14}\epsilon^f_{e\mu} + c_{14}c_{23}\epsilon^f_{e\tau})] - (1+s^2_{13})c_{23}s_{23}c_{24}Re(\epsilon^f_{\mu\tau})\\ &-\frac{c^2_{13}}{2}(\epsilon^f_{ee}c^2_{14} - \epsilon^f_{\mu\mu}c^2_{24}) + \frac{s^2_{23}-s^2_{13}c^2_{23}}{2}(\epsilon^f_{\tau\tau} - c^2_{24}\epsilon^f_{\mu\mu}) + c^2_{13}c_{14}s_{14}s_{24}Re(\epsilon^f_{e\mu}e^{i(\delta_{14}-\delta_{24})})\\ &-c_{13}c_{23}s_{14}s_{24}s_{13}Re(\epsilon^f_{\mu\tau}e^{i(\delta_{CP}-\delta_{14}+\delta_{24})}) - \epsilon^f_{\mu\mu}s_{13}c_{24}s_{23}c_{13}s_{14}s_{24}Re(e^{i(\delta_{CP}-\delta_{14}+\delta_{24})})\\ &-\frac{\epsilon^f_{\mu\mu}}{2}s^2_{14}s^2_{24}c^2_{13}\end{aligned} \tag{5.9}$$

and

$$\begin{aligned}\epsilon^f_N &= c_{13}[c_{14}c_{24}c_{23}\epsilon^f_{e\mu} - c_{14}s_{23}\epsilon^f_{e\tau}] + s_{13}e^{-i\delta_{CP}}[\epsilon^f_{\mu\tau}s^2_{23}c_{24} - c^2_{23}c_{24}\epsilon^{f*}_{\mu\tau}\\ &+c_{23}s_{23}(\epsilon^f_{\tau\tau} - \epsilon^f_{\mu\mu}c^2_{24})] + e^{-i(\delta_{14}-\delta_{24})}c_{13}s_{14}s_{24}(\epsilon^f_{\mu\tau}s_{23} - \epsilon^f_{\mu\mu}c_{23}c_{24})\end{aligned}. \tag{5.10}$$

[1]Studies including non-standard interactions of sterile neutrinos have been discussed in [342].

k_1 and k_2 are defined as,

$$k_1 = \frac{1}{2}(c_{23}^2 s_{24}^2 - c_{13}^2 c_{24}^2 s_{14}^2 - s_{13}^2 s_{23}^2 s_{24}^2) + s_{13}s_{23}s_{24}c_{13}c_{24}s_{14}Re(\delta_{14} - \delta_{CP} - \delta_{24}), \quad (5.11)$$

$$k_2 = e^{i(\delta_{24}-\delta_{14})}c_{23}s_{24}c_{13}c_{24}s_{14} - e^{-i\delta_{CP}}s_{13}s_{23}s_{24}^2 c_{23}. \quad (5.12)$$

In the absence of sterile neutrino ($\theta_{i4} = 0$ and $\delta_{i4} = 0$ where $i = 1, 2$)implying $k_1 = k_2 = 0$, we get back the expressions of ϵ_D^f and ϵ_N^f of [343].
Now we define $\delta = \dfrac{\Delta m_{21}^2}{2E}$, $\alpha_f = \dfrac{N_f}{N_e}$, and rewrite Eq. (5.8) as,

$$H^{eff} = \frac{\delta}{2}\begin{bmatrix} -\cos 2\theta_{12} & \sin 2\theta_{12} \\ \sin 2\theta_{12} & \cos 2\theta_{12} \end{bmatrix} + A_i \begin{bmatrix} c_{13}^2 c_{14}^2 & 0 \\ 0 & 0 \end{bmatrix} + A_j \begin{bmatrix} -k_1 & k_2 \\ k_2^* & k_1 \end{bmatrix} + A_i \sum_{f=e,u,d} \alpha_f \begin{bmatrix} -\epsilon_D^f & \epsilon_N^f \\ \epsilon_N^{f*} & \epsilon_D^f \end{bmatrix}. \quad (5.13)$$

Diagonalizing the above effective Hamiltonian gives the matter mixing angle θ_M as,

$$\tan 2\theta_M = \frac{\delta \sin 2\theta_{12} + 2A_i\alpha_f\epsilon_N^f + 2A_j k_2}{\delta \cos 2\theta_{12} + 2A_i\alpha_f\epsilon_D^f - A_i c_{13}^2 c_{14}^2 + 2A_j k_1}. \quad (5.14)$$

Hence, the resonance occurs when,

$$\delta \cos 2\theta_{12} + 2\alpha_f A_i \epsilon_D^f = A_i c_{13}^2 c_{14}^2 - 2A_j k_1, \quad (5.15)$$

i.e.,

$$\Delta m_{21}^2 \cos 2\theta_{12} + Bk_1 = A[c_{13}^2 c_{14}^2 - 2\alpha_f \epsilon_D^f]. \quad (5.16)$$

Here, $A = 2\sqrt{2}G_F N_e E$ and $B = 2\sqrt{2}G_F N_n E$.

It is crucial to ensure the occurrence of solar neutrino resonance with DLMA solution in a 3+1 neutrino scenario before we proceed to study the implications in $0\nu\beta\beta$ process. Keeping this in mind, we have used the resonance condition in Eq. (5.16) and obtained the neutrino energies at which the solar neutrino resonance occurs. For this study we have only considered ϵ_{ee}^u to be non-zero while setting other NSI parameters to be 0 for simplicity. In Fig.5.1, we have plotted the energy for which MSW resonance occurs for different values of ϵ_{ee} for both LMA (purple line) and the DLMA (green line) solutions. The figure shows that for $\sin^2\theta_{12}$ in the DLMA region, resonance condition can be obtained for different values of ϵ_{ee}^u, but for a lower energy. The chosen values of ϵ_{ee}^u are within the range allowed by the constraints from the COHERENT data as given in reference [344].

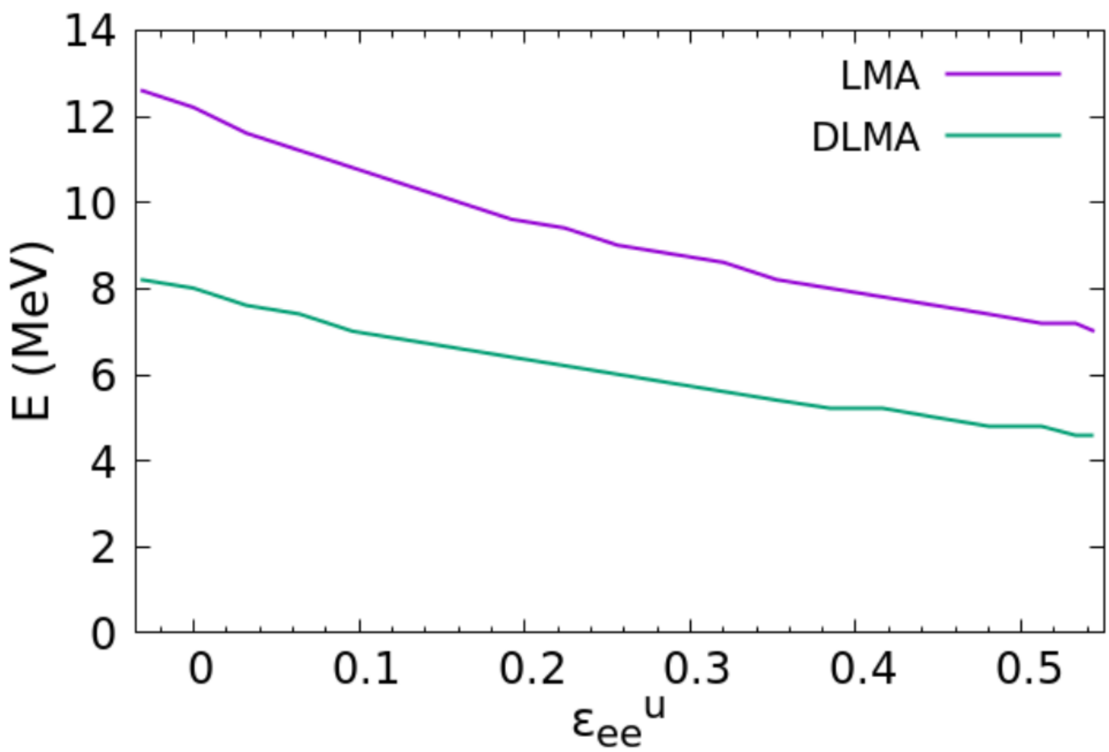

Figure 5.1: The energies corresponding to resonance for different values of ϵ_{ee}^u for LMA (purple line) and DLMA (green line) solutions.

5.3 $0\nu\beta\beta$ in 3+1 scenario

The half life for $0\nu\beta\beta$ in the standard scenario with light neutrino exchange is given by [345, 346],

$$(T_{1/2})^{-1} = G\left|\frac{M_\nu}{m_e}\right|^2 m_{\beta\beta}^2, \tag{5.17}$$

where G is the phase space factor, M_ν is the nuclear matrix element and m_e is the electron mass. The expression for the effective Majorana mass $m_{\beta\beta}$ is given by,

$$m_{\beta\beta} = |U_{ei}^2 m_i|, \tag{5.18}$$

where i runs from 1 to 3 (4) in the case of three (four) generations. m_i denotes the mass eigenstates and U is the unitary PMNS matrix as given in Eq. 5.1.

Thus, in 3+1 scheme,

$$m_{\beta\beta} = |m_1 c_{12}^2 c_{13}^2 c_{14}^2 + m_2 s_{12}^2 c_{13}^2 c_{14}^2 e^{i\alpha} + m_3 s_{13}^2 c_{14}^2 e^{i\beta} + m_4 s_{14}^2 e^{i\gamma}|, \tag{5.19}$$

where we have used the usual convention with $c_{ij} = \cos\theta_{ij}$ and $s_{ij} = \sin\theta_{ij}$. The above expression for $m_{\beta\beta}$ in the case of four generation is related to that in the case of three generation as,

$$m_{\beta\beta_{4gen}} = |c_{14}^2 \, m_{\beta\beta_{3gen}} + m_4 s_{14}^2 e^{i\gamma}|. \tag{5.20}$$

Thus, the $m_{\beta\beta}$ in the case of four generation depends on three extra parameters : the mixing angle θ_{14}, the third mass squared difference Δm^2_{LSND} ($m_4 = \sqrt{m_1^2 + \Delta m^2_{LSND}}$) and the Majorana phase $\gamma/2$. Depending on the values of these parameters, there can be additional enhancement or cancellation in the predictions of $m_{\beta\beta}$ compared to that in the three generation case.

In this chapter, we denote the standard LMA solution as θ_{12} and the DLMA solution as θ_{D12}. The 3σ ranges of these two parameters are shown in Table-5.2.

	$\sin^2\theta_{12}$	$\sin^2\theta_{D12}$	$\cos2\theta_{12}$	$\cos2\theta_{D12}$	$\sin^2\theta_{13}$
$Maximum$	0.356	0.745	0.57	-0.296	0.024
$Minimum$	0.214	0.648	0.29	-0.49	0.020

Table 5.2: The 3σ ranges of different combinations of oscillation parameters relevant for understanding the behavior of the effective mass in different limits.[35]

$m_{\beta\beta}$ is highly sensitive to the mass hierarchy of the light neutrinos, i.e; whether m_1 or m_3 is the lowest mass eigenstate.

For normal hierarchy (NH), m_1 is the lowest mass eigenstate $(m_1 < m_2 << m_3)$ and we can express the other mass eigenstates in terms of m_1 as

$$m_2 = \sqrt{m_1^2 + \Delta m^2_{sol}}\; m_3 = \sqrt{m_1^2 + \Delta m^2_{atm}}\; m_4 = \sqrt{m_1^2 + \Delta m^2_{LSND}}. \tag{5.21}$$

For inverted hierarchy (IH), m_3 is the lowest mass eigenstate $(m_3 << m_1 \approx m_2)$ and the other mass eigenstates in terms of m_3 are,

$$\begin{aligned} m_1 = \sqrt{m_3^2 + \Delta m^2_{atm}}\,, m_2 = \sqrt{m_3^2 + \Delta m^2_{sol} + \Delta m^2_{atm}}\,, \\ m_4 = \sqrt{m_3^2 + \Delta m^2_{atm} + \Delta m^2_{LSND}}. \end{aligned} \tag{5.22}$$

Here, $\Delta m^2_{sol} = m_2^2 - m_1^2$, $\Delta m^2_{atm} = m_3^2 - m_1^2 (m_1^2 - m_3^2)$ for NH (IH) and $\Delta m^2_{LSND} = m_4^2 - m_1^2$.

In Figs. 5.2 and 5.3 we have shown the predictions for $m_{\beta\beta}$ as a function of the lightest neutrino mass for two different values of the third mass squared difference,

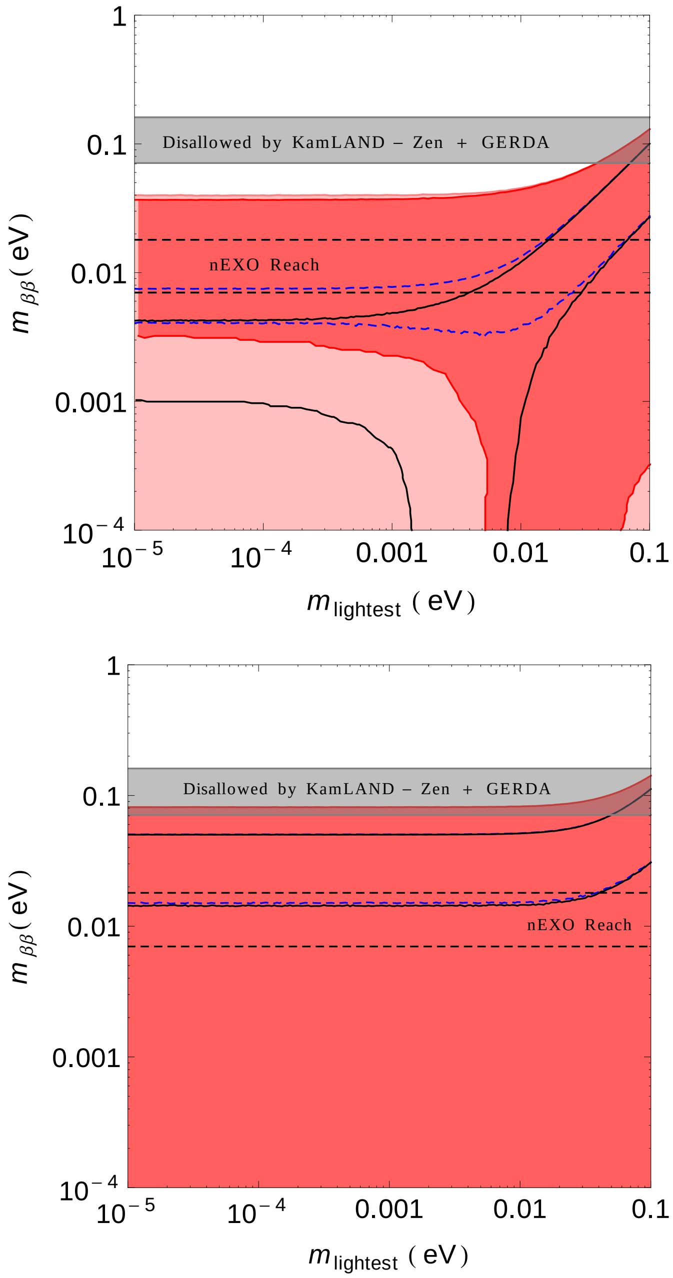

Figure 5.2: $m_{\beta\beta}$ vs $m_{lightest}$ for NH (left) and IH (right) for $\Delta m^2_{LSND} = 1.3$ eV^2. The pink and the red regions represent the predictions for the standard LMA as well as the DLMA solutions for θ_{12} respectively. The gray shaded region represents the current upper bound of $m_{\beta\beta}$ obtained from the combined results of KamLAND-Zen and GERDA experiments and the band defined by the two horizontal black dashed lines represents the future 3σ sensitivity of the nEXO experiment. The black solid lines and the blue dotted lines represent the predictions with the standard three neutrino case for the standard LMA and the DLMA solutions respectively.

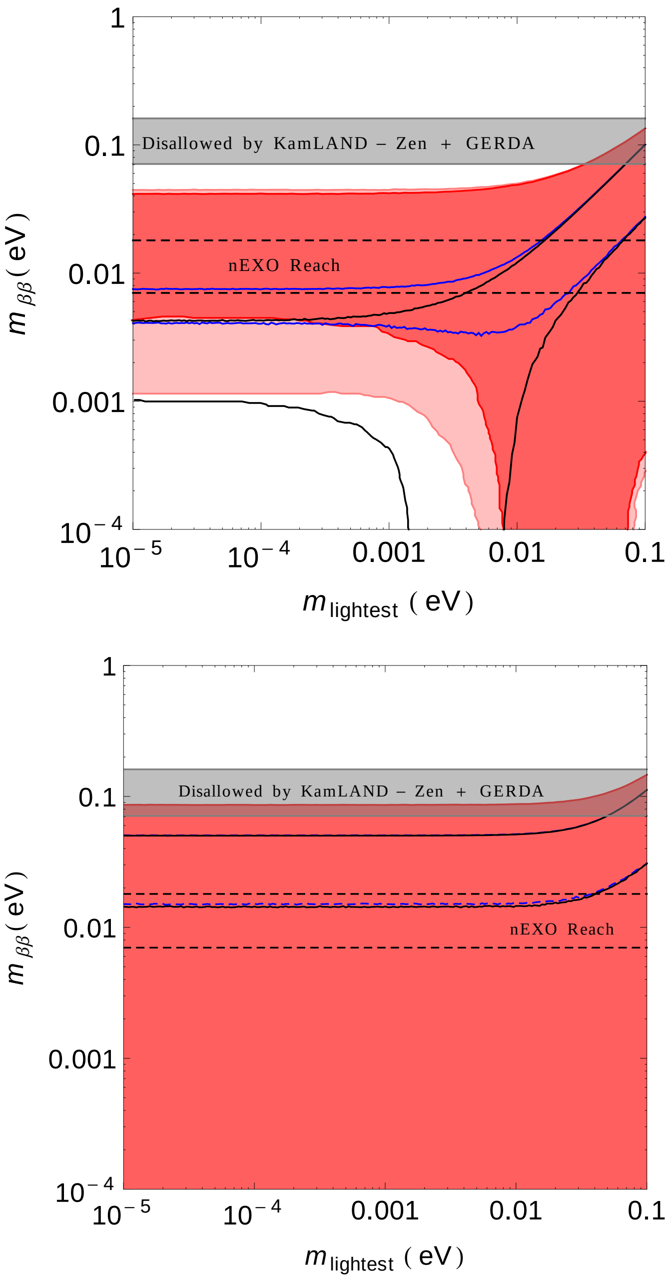

Figure 5.3: $m_{\beta\beta}$ vs $m_{lightest}$ for NH (left) and IH (right) for $\Delta m^2_{LSND} = 1.7$ eV^2. The pink and the red regions represent the predictions for the standard LMA as well as the DLMA solutions for θ_{12} respectively. The gray shaded region represents the current upper bound of $m_{\beta\beta}$ obtained from the combined results of KamLAND-Zen and GERDA experiments and the band defined by the two horizontal black dashed lines represents the future 3σ sensitivity of the nEXO experiment. The black solid lines and the blue dotted lines represent the predictions with the standard three neutrino case for the standard LMA and the DLMA solutions respectively.

i.e., $\Delta m^2_{LSND} = 1.3$ eV^2 and 1.7 eV^2. The left panels are for NH whereas the right panels are for IH. In plotting these figures, we have varied the oscillation parameters in their 3σ ranges [35, 338], the Majorana phases in the range $0 - \pi$ and the mixing angle θ_{14} in the range $\theta_{14} \sim 0.08 - 0.17$ radian.

In these plots, the pink and the red regions represent the predictions for the standard LMA as well as the DLMA solutions for θ_{12} respectively. The gray shaded region in the range between 0.071 eV and 0.161 eV represents the current upper bound of $m_{\beta\beta}$ obtained from the combined results of KamLAND-Zen and GERDA experiments [347]. This is a band due to the NME uncertainties [347–349]. The region above this band is disallowed. The band defined by the two horizontal black dashed lines represents the future 3σ sensitivity of the nEXO experiment : $T_{1/2} = 5.7 \times 10^{27}$ years [350], which, has been converted to $m_{\beta\beta} = 0.007 - 0.018$ eV using Eq. 5.17 by including the NME uncertainties. The black solid lines and the blue dotted lines represent the predictions for $m_{\beta\beta}$ with the standard three neutrino case for the standard LMA and the DLMA solutions respectively [330].

From Figs. 5.2 and 5.3, we can see that in the case of IH, the predictions of $m_{\beta\beta}$ remains same for both LMA and DLMA solutions and this is true for both the three generation as well as four generation cases. In addition, these predictions are independent of the values of Δm^2_{LSND} that we have considered. Also, complete cancellation of $m_{\beta\beta}$ can occur for the entire range of m_3 in the presence of the fourth sterile neutrino, unlike in the three generation case where there is no cancellation region for IH at all. In addition, the maximum predicted values for $m_{\beta\beta}$ are higher in the case of the four generation. Also, one can see that even though the non-observation of a positive signal for $0\nu\beta\beta$ in the future nEXO experiment will rule out the IH scenario in the case of three generation, it can still be allowed in the presence of the fourth sterile neutrino for both LMA and DLMA solution. In fact, the maximum value of $m_{\beta\beta}$ in this case is already in the region disallowed by the present results on $0\nu\beta\beta$, subject to the NME uncertainty. This can be used to constrain the θ_{14} mixing angle [337] .

In the case of NH, complete cancellation can occur for certain values of m_1 for both the standard LMA as well as the DLMA solutions in the four generation case, whereas for the three generation case, there is no cancellation region for the DLMA solution.

The values of $m_{lightest}$ for which complete cancellation of $m_{\beta\beta}$ occurs is larger for the DLMA solution. There is more cancellation region for $\Delta m^2_{LSND} = 1.3$ eV^2 compared to that for $\Delta m^2_{LSND} = 1.7$ eV^2. For $\Delta m^2_{LSND} = 1.3$ eV^2 with the standard LMA solution, cancellation is possible in the entire range of $m_{lightest}$ as in the case of IH. But for the DLMA solution cancellation is possible only for higher values of $m_{lightest}$. Another important point to be noted is that for the sterile neutrino scenario, there is no desert region between NH and IH unlike in the standard three generation picture [330]. This is true for both LMA and DLMA solutions. Also, the maximum allowed values of $m_{\beta\beta}$ is higher in the case of the four generation picture and is almost independent of whether one take the standard LMA or the DLMA solution. However, as compared to the three generation DLMA, the predictions for the maximum value of $m_{\beta\beta}$ are higher for the sterile neutrino case. The prediction of $m_{\beta\beta}$ for three neutrino DLMA picture is in the range (0.004-0.0075) eV while for the sterile DLMA (and LMA) this spans (0.004 - .04) eV (for $m_{lightest} \lesssim 0.005$ eV) for NH. The new allowed region of 0.0075-0.04 eV in the case of NH with four generation is in the complete reach of the future nEXO experiment.

The behavior of the effective Majorana mass $m_{\beta\beta}$ for the two different mass orderings can be understood by considering various limiting cases.

- Inverted Hierarchy: We discuss the following limiting cases:

  Case I : For $m_3 << \sqrt{\Delta m^2_{atm}}, m_1 \approx m_2 \approx \sqrt{\Delta m^2_{atm}}$ and $m_4 = \sqrt{\Delta m^2_{LSND}}$ the effective mass parameter from Eq. 5.19 becomes,

  $$m_{\beta\beta IO} \approx |\sqrt{\Delta m^2_{atm}} c^2_{13} c^2_{14} (c^2_{12} + s^2_{12} e^{i\alpha}) + \sqrt{\Delta m^2_{LSND}} s^2_{14} e^{i\gamma}|. \tag{5.23}$$

  Here we take the representative values of $\Delta m^2_{atm} = 2.5\times10^{-3}$ eV^2 and $\Delta m^2_{LSND} = 1.3$ eV^2. The above equation can lead to cancellation if we choose the following approximations $c^2_{13} \sim c^2_{14} \sim 1, s^2_{12} \sim 0.35, c^2_{12} \sim 0.65, \sqrt{\Delta m^2_{atm}} \sim 0.05, \sqrt{\Delta m^2_{LSND}} \sim \sqrt{1.3} \sim 1.140$. It implies,

  $$m_{\beta\beta} = 0.0322 + 0.0178 e^{i\alpha} + 1.14 s^2_{14} e^{i\gamma}. \tag{5.24}$$

  So the cancellation region corresponds to $\alpha \sim \pi$, $\gamma \sim \pi$ and $s^2_{14} \sim 0.0126$. The cancellation is achieved due to large value of $\sqrt{\Delta m^2_{LSND}}$. In three generation case, such cancellation is not there because of the absence of large valued term which can counter the first positive large term. In this region, the effective mass parameter is independent of the lightest neutrino mass eigenstate (Eq. 5.23) and is bounded from above and below by,

$$m_{\beta\beta IOmax} = |\sqrt{\Delta m^2_{atm}} c^2_{13} c^2_{14} + \sqrt{\Delta m^2_{LSND}} s^2_{14}|; (\alpha = 0, 2\pi; \gamma = 0, 2\pi), \tag{5.25}$$

$$m_{\beta\beta IOmin} = |\sqrt{\Delta m^2_{atm}} c^2_{13} c^2_{14} \cos 2\theta_{12} - \sqrt{\Delta m^2_{LSND}} s^2_{14}|; (\alpha = \pi; \gamma = \pi). \tag{5.26}$$

The maximum value of $m_{\beta\beta}$ is independent of θ_{12} whereas the minimum value of $m_{\beta\beta}$ depends on θ_{12}. But the minimum value of $m_{\beta\beta}$ is of the order of $\sim 10^{-4}$ and hence, this difference is not much pronounced.

Case II : As m_3 approaches to $\sqrt{\Delta m^2_{atm}}$, the other mass states are $m_1 \approx m_2 \approx \sqrt{2\Delta m^2_{atm}}$, $m_4 \approx \sqrt{\Delta m^2_{LSND}}$ and $m_{\beta\beta}$ from Eq. 5.19 becomes

$$m_{\beta\beta} = |\sqrt{2\Delta m^2_{atm}} c^2_{13} c^2_{14} (c^2_{12} + s^2_{12} e^{i\alpha}) + \sqrt{\Delta m^2_{atm}} s^2_{13} c^2_{14} e^{i\beta} + \sqrt{\Delta m^2_{LSND}} s^2_{14} e^{i\gamma}|. \tag{5.27}$$

Using the same values of those parameters as in case I and $s^2_{13} \sim 0.024$ we have,

$$m_{\beta\beta} = 0.0455 + 0.0252 e^{i\alpha} + 1.2 \times 10^{-3} e^{i\beta} + 1.14 s^2_{14} e^{i\gamma}. \tag{5.28}$$

Here the cancellation occurs for $\alpha \sim \beta \sim \gamma \sim \pi$ and $s^2_{14} \sim 0.017$. In three neutrino mixing the cancellation is not possible due to the absence of high m_4. Eq. 5.27 is maximum for $\alpha, \beta, \gamma = 0, 2\pi$ and is independent of θ_{12}. Since the value of s^2_{13} is small, the minimum value of $m_{\beta\beta}$ is independent of β. Hence the minimum value of $m_{\beta\beta}$ corresponds to $\alpha \sim \pi$ and $\gamma \sim \pi$. The minimum value of $m_{\beta\beta}$ becomes

$$m_{\beta\beta IOmin} = |\sqrt{2\Delta m^2_{atm}} c^2_{13} c^2_{14} \cos 2\theta_{12} - \sqrt{\Delta m^2_{LSND}} s^2_{14}|. \tag{5.29}$$

- Normal Hierarchy: We consider the following limiting cases:

  Case I: If $m_1 << m_2 \approx \sqrt{\Delta m^2_{sol}} << m_3 \approx \sqrt{\Delta m^2_{atm}}$, then $m_{\beta\beta}$ can be written from Eq. 5.19 as

$$m_{\beta\beta} = \sqrt{\Delta m^2_{atm}}\left|s^2_{13}c^2_{14}e^{i\beta} + \frac{\sqrt{\Delta m^2_{sol}}}{\sqrt{\Delta m^2_{atm}}}s^2_{12}c^2_{13}c^2_{14}e^{i\alpha} + \frac{\sqrt{\Delta m^2_{LSND}}}{\sqrt{\Delta m^2_{atm}}}s^2_{14}e^{i\gamma}\right|. \tag{5.30}$$

Taking the same representative values as we have used in IH discussion, we have

$$m_{\beta\beta} = \sqrt{\Delta m^2_{atm}}|s^2_{13}c^2_{14}e^{i\beta} + 0.172s^2_{12}c^2_{13}c^2_{14}e^{i\alpha} + 22.80s^2_{14}e^{i\gamma}|, \tag{5.31}$$

or,

$$m_{\beta\beta} = \sqrt{\Delta m^2_{atm}}|0.024e^{i\beta} + 0.059e^{i\alpha} + 22.80s^2_{14}e^{i\gamma}|. \tag{5.32}$$

We take the value of $\sin\theta_{14}$ in the range 0.08 to 0.17 which implies for small m_1 there is no cancellation as the value of m_4 is very large. The maximum value of $m_{\beta\beta}$ corresponds to $\alpha, \beta, \gamma = 0, 2\pi$ and the minimum value corresponds to $\gamma = 0$ and $\alpha, \beta = \pi$. $m_{\beta\beta}$ is higher for higher value of $\sin^2\theta_{12}$. This implies that $m_{\beta\beta}$ for the DLMA solution is higher in this region.

Case II: Now as $m_1 \sim \sqrt{\Delta m^2_{atm}}$, then Eq. 5.19 becomes

$$m_{\beta\beta} = |\sqrt{\Delta m^2_{atm}}c^2_{12}c^2_{13}c^2_{14} + \sqrt{\Delta m^2_{atm}}s^2_{12}c^2_{13}c^2_{14}e^{i\alpha} + \sqrt{2\Delta m^2_{atm}}s^2_{13}c^2_{14}e^{i\beta} + \sqrt{\Delta m^2_{LSND}}s^2_{14}e^{i\gamma}|. \tag{5.33}$$

Using the representative values as earlier, we obtain

$$m_{\beta\beta} = \sqrt{\Delta m^2_{atm}}\;|0.644 + 0.356e^{i\alpha} + 0.034e^{i\beta} + 22.80s^2_{14}e^{i\gamma}|. \tag{5.34}$$

So in this case the cancellation occurs since, $\sin\theta_{14}$ can take values in the range $0.08 - 0.17$.

5.4 Sensitivity in the future experiments

The future generation $0\nu\beta\beta$ experiments are intending to probe the region $m_{\beta\beta} \sim 10^{-2}$ eV. These experiments include LEGEND, SuperNEMO, CUPID, CUORE, SNO, KamLAND-Zen, nEXO, NEXT, PandaX etc. (See [351] for a review). A positive signal in these experiments could be due to IH (three generation or 3+1 generation) or due to NH (3+1 picture) for both LMA and DLMA solutions. If these experiments give a negative result, the next generation of experiments have to be designed with a sensitivity range of 10^{-3} eV [352, 353].

In this section, we calculate the sensitivity in the future ^{136}Xe experiments for which we have adopted the method discussed in reference [351]. The value of $T_{1/2}$ for which an experiment has a 50% probability of measuring a 3σ signal above the background is defined as the 3σ $T_{1/2}$ discovery sensitivity. It is given as,

$$T_{1/2} = \ln 2 \frac{N_A \epsilon}{m_a S_{3\sigma}(B)}. \tag{5.35}$$

In this equation, N_A is the Avogadro number, m_a is the atomic mass of the isotope, and $B = \beta\epsilon$ is the expected background where, ϵ is the sensitive exposure and β is the sensitive background. $S_{3\sigma}$ is the value for which half of the measurements would give a signal above B for a Poisson signal and this can be obtained from the equation,

$$1 - CDF_{Poisson}(C_{3\sigma}|S_{3\sigma} + B) = 50\%.$$

$C_{3\sigma}$ stands for the number of counts for which the cumulative Poisson distribution with mean as B obeys,

$$CDF_{Poisson}(C_{3\sigma}|B) = 3\sigma.$$

We use the normalized upper incomplete gamma function to define $CDF_{Poisson}$ as a continuous distribution in C as follows,

$$CDF_{Poisson}(C|\mu) = \frac{\Gamma(C+1, \mu)}{\Gamma(C+1)}.$$

This avoids the discrete variations that would arise in the discovery sensitivity if $C_{3\sigma}$ is restricted to be integer valued. Using the above equations, we have calculated the $T_{1/2}$ discovery sensitivities of $0\nu\beta\beta$ as a function of ϵ for various values of β for ^{136}Xe nucleus and the results are shown in Fig.5.4.

In this plot, the red shaded band corresponds to the new allowed region of $m_{\beta\beta} \sim 0.008 - 0.04$ eV for the DLMA solution for the NH case with a sterile neutrino. This band in $m_{\beta\beta}$ which is due to the variation of the parameters in the PMNS matrix, is converted to a band in $T_{1/2}$ using Eq. 5.17, by taking into account the NME uncertainty as given in Table 5.3. The dotted black line corresponds to the future 3σ sensitivity of nEXO, which is $T_{1/2} = 5.7 \times 10^{27}$ years [350]. The yellow, black, brown and blue lines

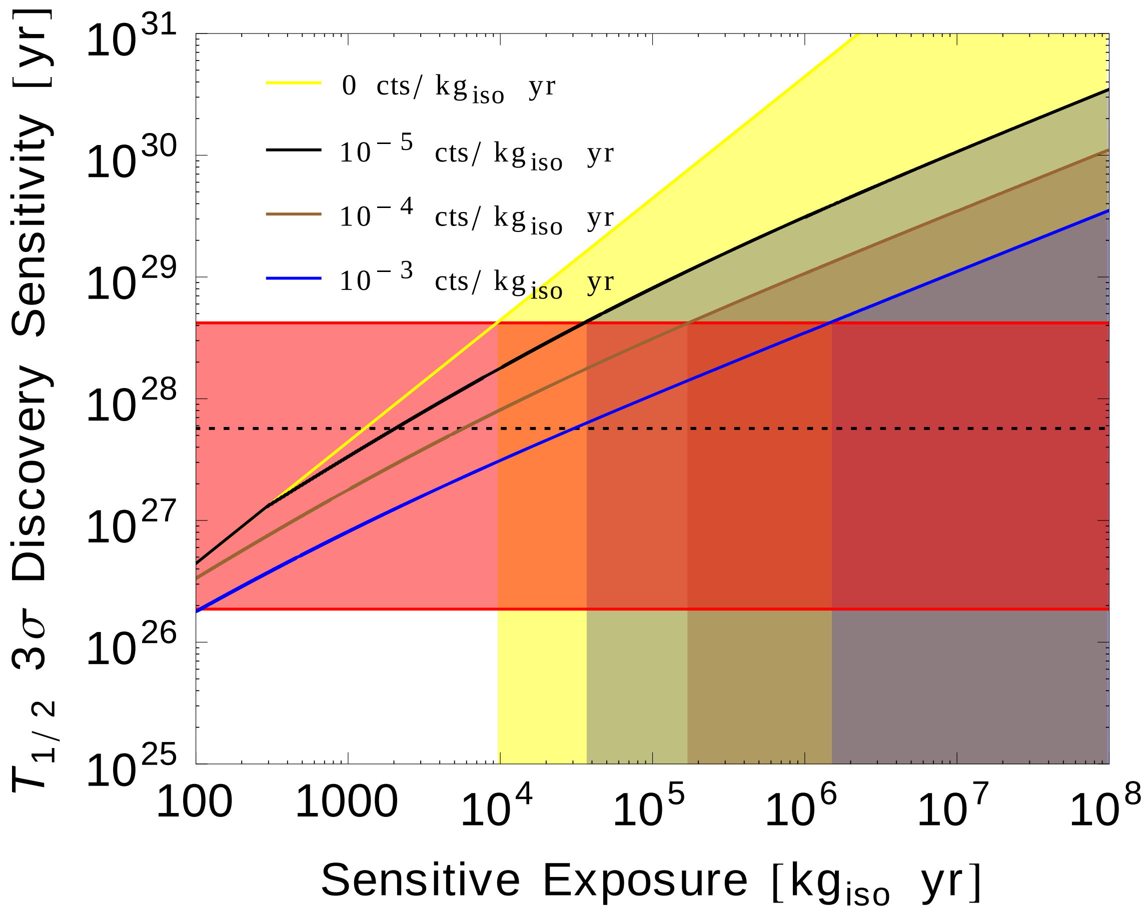

Figure 5.4: ^{136}Xe discovery sensitivity as a function of sensitive exposure for different sensitive background levels. The yellow, black, brown and blue lines correspond to four different values of the sensitive background levels as shown in the figure.

correspond to four different values of the sensitive background levels of 0, 10^{-5}, 10^{-4} and 10^{-3} $\text{cts}/(\text{kg}_{\text{iso}}\text{yr})$ respectively. From the figure, we can see that a large part of this newly allowed region for NH is in the reach of the nEXO experiment. With lower background levels and/or higher sensitive exposure, the next generation experiments can probe this entire region.

In Table 5.3, we have given the $T_{1/2}$ ranges corresponding to the new allowed region of $m_{\beta\beta}$ for the DLMA solution for the NH case with a sterile neutrino , i.e., $m_{\beta\beta} = 0.008 - 0.04$ eV for three different isotopes.

Note that even if one obtain a better limit on $T_{1/2}$ or even a measurement of $T_{1/2}$ from the future experiments, we have to convert this into $m_{\beta\beta}$ to get hints about the corresponding particle physics model and this will have uncertainties due to the NME elements. To calculate the matrix element, one can use different models like shell model, quasiparticle random-phase approximation (QRPA), interacting boson model (IBM), etc., and each model has their own advantages and disadvantages [348]. The inverse half life also depends on the fourth power of the weak axial vector (g_A). Hence a small uncertainty in g_A can lead to a large change in the value of $m_{\beta\beta}$. It depends on the mass number of the nucleus and the momentum transfer. The quenching of g_A from its free nucleon value arises due to nuclear medium effects and nuclear many body effects. The detail study of g_A and its possible uncertainties are discussed in [354]. In this chapter, we have used those values of M_ν for which g_A = 1.25 [347, 348].

Isotope	NME (M_ν)	$G(10^{-15}\text{year}^{-1})$	$T_{1/2}$ range (years)
^{136}Xe	$1.6 - 4.8$	14.58	$1.87 \times 10^{26} - 4.20 \times 10^{28}$
^{76}Ge	$2.8 - 6.1$	2.363	$7.13 \times 10^{26} - 8.47 \times 10^{28}$
^{130}Te	$1.4 - 6.4$	14.22	$1.08 \times 10^{26} - 5.63 \times 10^{28}$

Table 5.3: The $T_{1/2}$ ranges corresponding to the DLMA region $m_{\beta\beta} = 0.008 - 0.04$ eV, the new allowed region for the DLMA solution for the NH case with a sterile neutrino for different isotopes. The NME values [347, 348] and the phase space factors [349] used in the calculation are also given.

5.5 Cosmological constraints on eV scale sterile neutrino

The LSND-MiniBooNE collaborations have reported possible evidence for a light sterile neutrino of eV mass scale. However, such a state would be directly in conflict with Planck measurement of N_{eff} from BBN and standard cosmology. So if we include an eV scale sterile neutrino with the standard three flavours picture, the N_{eff} value will increase which is highly constrained by BBN ($N_{eff} \sim 3.046$) [355, 356]. So to account for an eV scale sterile neutrino, different models are proposed to evade the cosmological bound.

An eV scale sterile neutrino will require a reducing value of N_{eff}. One possibility is to allow for new interactions (secret interactions) of sterile neutrinos so that the active-sterile mixing becomes very less and eventually N_{eff} becomes less, evading the cosmological bounds. In the secret interaction picture, sterile state can interact with some other bosonic particles in the model [357] or they can have self interactions [358]. In $1+1$ flavour approximation, the active sterile mixing angle in a thermal ν_s background is given as [332]

$$\sin^2 2\theta_m = \frac{\sin^2 2\theta_0}{(\cos 2\theta_0 + \frac{2E}{\Delta m^2} V_{\text{eff}})^2 + \sin^2 2\theta_0}, \tag{5.36}$$

where the effective potential V_{eff} depends on the interaction between sterile neutrino and the new gauge boson in the model. One can parametrize $V_{\text{eff}} \sim T^n$ where n is a positive number ($\sim 2-4$). At very high temperature, the effective potential increases and the value of the active sterile mixing angle decreases. However, later in time, when the universe expands, the temperature decreases and active sterile mixing increases to the present constraints on mixing obtained from oscillation experiments ($U_{e4} \sim 0.1$). This mechanism generates a larger mass for ν_s in the high temperature phase of the scalar potential, precluding efficient ν_s production. After a late phase transition in the scalar sector, the sterile neutrino mass is reduced to the value observed today. In addition, if there are more number of sterile neutrinos in the picture, or if the sterile decays at late time, one can also evade the cosmological constraints [331].

The physical effects of non relativistic free streaming particles (after photon decoupling) on the cosmological background and perturbation evolution depend on the parameters ΔN_{eff}, ω_s, and $< v_s >$, defined below [359].

- **ΔN_{eff}:** The contribution of sterile neutrino to the relativistic density before the photon decoupling is parametrized by an effective neutrino number ΔN_{eff} which is defined as the relativistic density of neutrino species and one massless neutrino family in the instantaneous decoupling (id) limit,

$$\Delta N_{eff} = \frac{\rho_s^{\text{rel}}}{\rho_\nu}, \tag{5.37}$$

where ρ_ν denotes the energy density of neutrino and can be expressed as

$$\rho_\nu = \frac{7}{8}\frac{\pi^2}{30} g T_\nu^{id\,4}, \tag{5.38}$$

where g is the internal degree of freedom and $T_\nu^{id} = (4/11)^{1/3} T_\gamma$. The energy density of the sterile neutrino having momentum distribution $f(p)$ is given by

$$\rho_s = \frac{g}{(2\pi)^3} \int E(p) f(p) d^3p. \tag{5.39}$$

Hence, the effective neutrino number is

$$\Delta N_{\text{eff}} = \frac{\frac{1}{\pi^2}\int p^3 f(p) dp}{\frac{7}{8}\frac{\pi^2}{15} T_\nu^{id\,4}}, \tag{5.40}$$

since, for relativistic neutrinos, $E = p$.

- **ω_s:** The presence of extra massive free streaming particles can affect the current energy density budget of the universe and the amplitude in the small scale matter power spectrum. Its effect is parametrized by a dimensionless parameter ω_s defined as

$$\omega_s = \Omega_s h^2 = \frac{\rho_c^s}{\rho_c^0} h^2 = m \int \frac{g}{(2\pi)^3} f(p) d^3p \frac{h^2}{\rho_c^0}, \tag{5.41}$$

since, $\rho = mn$ and $n = \dfrac{g}{(2\pi)^3} \displaystyle\int f(p) d^3p$. Therefore, we can write,

$$\omega_s = \frac{m}{\pi^2} \int p^2 f(p) dp \times \frac{h^2}{\rho_c^0}, \tag{5.42}$$

where ρ_c^0 is the critical density today and h is the reduced Hubble parameter.

- **$< v_s >$:** The comoving free streaming length of sterile neutrino is related with the small scale matter power spectrum by its average velocity which in the non relativistic regime is given as

$$< v_s > = \frac{p^2 dp \frac{p}{m} f(p)}{\int p^2 dp f(p)}. \tag{5.43}$$

Hence, we can write,

$$< v_s > = \frac{7}{8}\frac{\pi^2}{15}\left(\frac{4}{11}\right)^{4/3}\frac{T_{CMB}^4 h^2}{\rho_c}\frac{\Delta N_{eff}}{\omega_s} = 5.618 \times 10^{-6}\frac{\Delta N_{eff}}{\omega_s}, \tag{5.44}$$

where we have taken $T_{\rm CMB} = 2.726\ K$. So the above three parameters satisfy the constraint Eq. 5.44. Hence, one needs to calculate ΔN_{eff}, ω_s and $< v_s >$ to see the effects of sterile neutrino on cosmology. For a light thermal relic sterile neutrino with Fermi-Dirac distribution and a different sterile temperature T_s, the three parameters are

$$\Delta N_{eff} = \left(\frac{T_s}{T_\nu^{id}}\right)^4, \ \omega_s = \frac{m_s}{94.05 \text{ eV}}\left(\frac{T_s}{T_\nu^{id}}\right)^3, \ < v_s > = \frac{0.5283 \text{ meV}}{m_s}\left(\frac{T_s}{T_\nu^{id}}\right). \tag{5.45}$$

The CMB analysis in $\Lambda_{CDM} + r_{0.05} + N_{\rm eff} + m_{eff}^s$ model using Planck data gives $N_{\rm eff} < 3.78$ and $m_{\rm eff}^s < 0.78\text{eV}$. $r_{0.05}$ denotes the tensor to scalar ratio at the pivot scale of $k_* = 0.05h\ \text{Mpc}^{-1}$. The effective neutrino mass $m_{\rm eff}^s$ is related with the physical mass m_s as $m_{\rm eff}^s = \Delta N_{\rm eff}^{3/4} m_s$, where $\Delta N_{\rm eff} = N_{\rm eff} - 3.046$ or in terms of temperature $\Delta N_{\rm eff} = \left(\frac{T_s}{T_\nu^{id}}\right)^4$ [360]. For our case, $\Delta m_{LSND}^2 = 1.3\ \text{eV}^2$, the physical mass is $m_4 = m_s = 1.14$ eV. Hence, to be consistent with cosmology, we must have $\frac{T_s}{T_\nu^{id}} < 0.88$, where we have chosen the lightest mass eigenstate $m_1 = 0$. Similarly, for $\Delta m_{LSND}^2 = 1.7\ \text{eV}^2$, $m_s = 1.30$ eV and $\frac{T_s}{T_\nu^{id}} < 0.84$.

5.6 Discussions

In this chapter, we have studied the implications of the DLMA solution to the solar neutrino problem for $0\nu\beta\beta$ in the 3+1 scenario, including an additional sterile neutrino. We have verified that even in the presence of sterile neutrino, the MSW resonance can take place in the DLMA region. Next, we have studied how for these values of θ_{12}, the predictions for $0\nu\beta\beta$ in 3+1 picture is changed as compared to the predictions for 3+1 scenario assuming ordinary LMA solution. We also compare with the predictions of $m_{\beta\beta}$ for the three generation picture.

We find that for IH, there is no change in $m_{\beta\beta}$ predictions as compared to the 3+1 case assuming θ_{12} to be in the standard LMA region. This is because in this case, the maximum value of $m_{\beta\beta}$ is independent of θ_{12} and the minimum value of $m_{\beta\beta}$ is of the order of $\sim 10^{-4}$ eV where the difference is not very evident. In particular, the cancellation region which was reported earlier for 3+1 sterile neutrino picture also continues to be present for the DLMA parameter space due to the contribution from the fourth mass eigenstate. This conclusion is similar to the conclusion obtained for the three generation case, for which also the LMA and DLMA solutions gave same predictions for $m_{\beta\beta}$ in the case of IH.

In the case of NH, cancellation can occur for certain values of $m_{lightest}$ and the values for which this happens is higher for the DLMA solution. Also, the maximum value of $m_{\beta\beta}$ is same for the standard LMA and DLMA solutions in the 3+1 scenario and unlike the three generation case there is no desert region between NH and IH. However, the maximum value is higher than that for the three generation DLMA case.

If future experiments with sensitivity reach of $\sim$ 0.015 eV observe a positive signal for $0\nu\beta\beta$ then it could be due to IH (three generation or 3+1 generation) or due to NH (3+1 picture) for both LMA and DLMA solutions. If however, no such signal is found then for three generation picture $0\nu\beta\beta$ experiments can disfavor IH and one moves to the next frontier of 0.001 eV [352, 353]. In this regime a demarcation between LMA and DLMA is possible for three generation picture if a signal is obtained for $m_{\beta\beta} \gtrsim 0.004$ eV [330]. However, if the sterile neutrino hypothesis is true then distinction between NH and IH is not possible from $0\nu\beta\beta$ experiments. This also spoils the sensitivity to demarcate between LMA and DLMA solutions. If however, the current indication of NH from accelerator experiments is confirmed by future data then the next generation of $0\nu\beta\beta$ experiments with sensitivity reach up to 10^{-3} eV can distinguish between LMA and DLMA solution in presence of a sterile neutrino for $m_{lightest} \lesssim 0.005$ eV.

Chapter 6

Summary and Conclusions

The standard model of particle physics and Einstein's theory of general relativity are very successful theories that can explain a wide range of experimental results with a high level of accuracy. However, there are both observational and theoretical motivations to go beyond these. In this thesis, we have considered light particles of different spins such as spin-0 axion, spin-1 vector gauge boson, spin-2 graviton, and spin-$1/2$ sterile neutrino to illuminate the universe unknown to us. We obtain bounds on the properties of these light particles from several astrophysical, and laboratory experiments such as orbital period loss of the binary systems which is the indirect evidence of gravitational waves, birefringence phenomena, perihelion precession of planets, gravitational light bending, Shapiro time delay, and $0\nu\beta\beta$ experiments.

After a brief introduction, in Chapter 2 we have focussed on spin-0 axions, and have obtained constraints on these particles from the orbital period loss of compact binary systems, birefringence from pulsars, gravitational light bending, and Shapiro time delay. The key findings of this chapter are as follows. We have derived bound on axion decay constant as $f_a \lesssim \mathcal{O}(10^{11})$ GeV for axion mass $m_a \lesssim 10^{-19}$ eV from the pulsar timing data which disfavors axion like particles as fuzzy dark matter candidate. Secondly, we have also obtained the parameter space $(f_a \lesssim \mathcal{O}(10^{17})\ \mathrm{GeV}, \mathrm{m_a} \lesssim 10^{-11}\ \mathrm{eV})$ for probing axions from birefringence effect of pulsars. Next, we have presented bounds on axion parameters from gravitational light bending ($f_a \lesssim 1.58 \times 10^{10}$ GeV, $\mathrm{m_a} \lesssim 10^{-18}$ eV) and Shapiro time delay ($f_a \lesssim 9.85 \times 10^6$ GeV, $\mathrm{m_a} \lesssim 1.33 \times 10^{-18}$ eV). The Shapiro time delay puts stronger bound than the gravitational light bending. The result from Shapiro time delay also disfavors axion like particles as fuzzy dark matter candidate. We have also delineated that these ultralight axions can mediate a long range fifth force between the compact/celestial objects.

Next in Chapter 3, we have discussed spin-1 ultralight gauge bosons and have obtained bounds on the parameters of these particles from pulsar timing data, and perihelion precession of planets. Through these astrophysical observations, we have also constrained $U(1)_{L_i-L_j}$ models. The key findings of this chapter are as follows. We constrain gauged $U(1)_{L_\mu-L_\tau}$ model from orbital period loss of binary systems and obtain bound on gauge coupling $g \lesssim 4.24 \times 10^{-20}$ for the gauge boson of mass $M_{Z'} \lesssim 10^{-19}$ eV. We have also constrained gauged $U(1)_{L_e-L_{\mu,\tau}}$ model from perihelion precession of planets and have gleaned bound on the gauge coupling as $g \lesssim 3.506 \times 10^{-25}$ for the gauge boson of mass $M_{Z'} \lesssim 10^{-19}$ eV. These ultralight gauge bosons can also mediate long range fifth force.

In Chapter 4, we have discussed massive spin-2 graviton in several massive gravity theories, such as Fierz-Pauli (FP) theory, Dvali-Gabadadze-Porrati (DGP) theory, modified Fierz-Pauli theory and obtained bounds on the graviton mass from the pulsar timing data. The key findings of this chapter are as follows. We have calculated the obital period loss due to massive graviton radiation for these three massive gravity theories. We have followed the Feynman diagram technique-a field theoretic approach to calculate the energy loss. The orbital period loss of compact binary systems cannot give a universal graviton mass bound for the FP and DGP theories. Hence, we have derived bounds on those two theories from Vainshtein radius. From the Vainshtein limit, we have given the graviton mass bound $m_g > 3.06 \times 10^{-22}$ eV for FP theory, and $m_g > 7.84 \times 10^{-24}$ eV for DGP theory. However, for modified FP theory, we have obtained the universal graviton mass bound $m_g < 1.81 \times 10^{-20}$ eV from the orbital period loss of binary systems.

Lastly in chapter 5, we have studied the spin-1/2 sterile neutrino and its implications in $0\nu\beta\beta$ for the Dark Large Mixing Angle (DLMA) solution which is present if there is Non Standard Interaction (NSI) leading to an extra solution for the solar mixing angle as $\theta_{12} > 45^\circ$. The key findings of this chapter are as follows. In the case of IH, the prediction of $m_{\beta\beta}$ remains same for both LMA and DLMA solutions and this is true for both the three as well as four generations. The predictons are independent of the values of $\Delta m^2_{\rm LSND} = m_4^2 - m_1^2$. The complete cancellation of the effective majorana mass can occur for the entire range of m_3 in the presence of fourth sterile neutrino, unlike in the three generation case where there is no cancellation region for IH at all. The maximum values for $m_{\beta\beta}$ are higher in the case of four generations. For the $3+1$ scenario, there is no desert region between NH and IH unlike in the standard three generation picture. This is true for both LMA and DLMA solutions. Even the non observation of a positive signal for $0\nu\beta\beta$ in the future nEXO experiment will rule out the IH scenario in the case of three generation, it can still be allowed in the presence of the fourth sterile neutrino for both LMA, and DLMA. The prediction of $m_{\beta\beta}$ for three neutrino DLMA picture is in the range $(0.004 - 0.0075)$ eV while for the sterile DLMA, this spans $(0.004 - 0.04)$ eV (for $m_{\rm lightest} \lesssim 0.005$ eV) for NH. The new allowed region of $0.0075 - 0.04$ eV in the case of NH with four generations is in the complete reach of the future nEXO experiment.

As a general summary of the thesis, we have tried to explore the dark universe through light particles, such as axions (splin-0), gauge bosons (spin-1), massive graviton (spin-2) and sterile neutrinos (spin-$1/2$). We obtain constraints on the properties of these light particles from several observations and experiments such as pulsar timing data, perihelion precession of planets through the MESSENGER mission, Shapiro time delay, and gravitational light bending from Cassini spacecraft, VLBA, and results from several $0\nu\beta\beta$ experiments. Some of these light particles are good candidates of dark matter. The axions, ultralight gauge bosons, massive gravitons can put imprints on the gravitational waveforms, and from the future LIGO-Virgo data, we can obtain improved bounds on those light particles. Moreover future spacecraft missions can play important roles in obtaining better results to constrain the properties of ultralight particles.

Also several future generation $0\nu\beta\beta$ experiments are trying to find the nature of neutrino. More precise data from future experiments and observations will improve the perspectives to probe the dark universe using the light particle sector.

Appendix A

Long Range Axion Hair

A.1 Equation of Motion of Long Range Axion Hair

The equation of motion of long range axion hair is $\nabla_\mu \nabla^\mu a = m_a^2 a$. Hence,

$$\begin{aligned}
\nabla_\mu \nabla^\mu a &= g^{\mu\nu} \nabla_\mu \nabla_\nu a \\
&= g^{\mu\nu} [\partial_\mu (\partial_\nu a) - \Gamma^\rho_{\mu\nu} \partial_\rho a] \\
&= g^{\mu\nu} \partial_\mu \partial_\nu a - g^{\mu\nu} \Gamma^\rho_{\mu\nu} \partial_\rho a \\
&= g^{rr} \frac{d^2 a}{dr^2} - g^{\mu\nu} \Gamma^r_{\mu\nu} \frac{da}{dr} \\
&= \Big(1 - \frac{2M}{r}\Big) \frac{d^2 a}{dr^2} - (g^{rr} \Gamma^r_{rr} + g^{tt} \Gamma^r_{tt} + g^{\theta\theta} \Gamma^r_{\theta\theta} + g^{\phi\phi} \Gamma^r_{\phi\phi}) \frac{da}{dr}.
\end{aligned}$$

Putting the Christoffel symbols for the Schwarzschild metric and the components of $g_{\mu\nu}$ we obtain

$$\nabla_\mu \nabla^\mu a = \Big(1 - \frac{2M}{r}\Big) \frac{d^2 a}{dr^2} - \Big[\Big(1 - \frac{2M}{r}\Big) \frac{M}{2Mr - r^2} + \frac{r}{2M - r} \frac{M(r - 2M)}{r^3} + \frac{1}{r^2}(2M - r) + \frac{1}{r^2 \sin^2\theta}(2M - r)\sin^2\theta\Big] \frac{da}{dr}.$$

Hence,

$$\nabla_\mu \nabla^\mu a = \Big(1 - \frac{2M}{r}\Big) \frac{d^2 a}{dr^2} + \frac{2}{r}\Big(1 - \frac{M}{r}\Big) \frac{da}{dr}.$$

Therefore, the equation of motion of long range axion hair becomes

$$\Big(1 - \frac{2M}{r}\Big) \frac{d^2 a}{dr^2} + \frac{2}{r}\Big(1 - \frac{M}{r}\Big) \frac{da}{dr} = m_a^2 a. \tag{A.1}$$

A.2 Relation Between the Orbital Period Loss and Energy Loss

If we denote the orbital frequency of a binary system as Ω, consisting of two masses m_1 and m_2 then $\Omega^2 = \dfrac{G(m_1+m_2)}{a^3}$ and $P_b^2 = \dfrac{4\pi^2}{\Omega^2} = \dfrac{4\pi^2 a^3}{G(m_1+m_2)}$. Taking time deriative of P_b^2, we obtain

$$\dot{a} = \frac{G(m_1+m_2)}{6\pi^2 a^2} P_b \dot{P}_b.$$

The total energy of the binary system is $E = T + V = -\frac{1}{2}V + V = \frac{1}{2}V = -\frac{Gm_1 m_2}{2a}$, where we have used the virial theorem $< T >= -\frac{1}{2} < V >$. The time derivative of the total energy yields,

$$\frac{dE}{dt} = \frac{Gm_1 m_2}{2a^2}\dot{a} = \frac{G^{3/2}}{6\pi} a^{-5/2}(m_1 m_2)(m_1+m_2)^{1/2}\dot{P}_b.$$

Hence, the orbital period loss related with the energy loss as

$$\dot{P}_b = 6\pi G^{-3/2}(m_1 m_2)^{-1}(m_1+m_2)^{-1/2} a^{5/2}\frac{dE}{dt}. \tag{A.2}$$

Appendix B

Planet in Presence of a Yukawa Potential

B.1 Equation of motion of a planet in presence of a Schwarzschild background and a non gravitational Yukawa type of potential

The action which describes the motion of a planet in Schwarzschild background and a non gravitational long range Yukawa type of potential is given by Eq. (3.37). Suppose $S_1 = M_p \int \sqrt{-g_{\mu\nu}\dot{x}^\mu \dot{x}^\nu} d\tau$. For this action, the Lagrangian is

$$\mathcal{L} = M_p \sqrt{g_{\mu\nu}\frac{dx^\mu}{d\tau}\frac{dx^\nu}{d\tau}}. \tag{B.1}$$

Hence, the equation of motion is

$$\frac{d}{d\tau}\Big(\frac{\partial \mathcal{L}}{\partial\big(\frac{\partial x^\sigma}{\partial \tau}\big)}\Big) - \frac{\partial \mathcal{L}}{\partial x^\sigma} = 0, \tag{B.2}$$

or,

$$\frac{1}{\mathcal{L}}\frac{d\mathcal{L}}{d\tau}g_{\mu\sigma}\frac{dx^\mu}{d\tau} = g_{\mu\sigma}\frac{d^2x^\mu}{d\tau^2} + \partial_\alpha g_{\mu\sigma}\frac{dx^\alpha}{d\tau}\frac{dx^\mu}{d\tau} - \frac{1}{2}\partial_\sigma g_{\mu\nu}\frac{dx^\mu}{d\tau}\frac{dx^\nu}{d\tau}. \tag{B.3}$$

Multiplying $g^{\rho\sigma}$ we have,

$$\frac{d^2x^\rho}{d\tau^2} + g^{\rho\sigma}\partial_\nu g_{\mu\sigma}\frac{dx^\nu}{d\tau}\frac{dx^\mu}{d\tau} - g^{\rho\sigma}\frac{1}{2}\partial_\sigma g_{\mu\nu}\frac{dx^\mu}{d\tau}\frac{dx^\nu}{d\tau} = \frac{1}{\mathcal{L}}\frac{d\mathcal{L}}{d\tau}\frac{dx^\rho}{d\tau}, \tag{B.4}$$

or,

$$\frac{d^2x^\rho}{d\tau^2} + \frac{1}{2}g^{\rho\sigma}(\partial_\nu g_{\mu\sigma} + \partial_\mu g_{\nu\sigma} - \partial_\sigma g_{\mu\nu})\frac{dx^\mu}{d\tau}\frac{dx^\nu}{d\tau} = \frac{1}{\mathcal{L}}\Big(\frac{d\mathcal{L}}{d\tau}\Big)\frac{dx^\rho}{d\tau}, \tag{B.5}$$

or,

$$\frac{d^2x^\rho}{d\tau^2} + \Gamma^\rho_{\mu\nu}\frac{dx^\mu}{d\tau}\frac{dx^\nu}{d\tau} = \frac{1}{\mathcal{L}}\frac{d\mathcal{L}}{d\tau}\frac{dx^\rho}{d\tau}, \tag{B.6}$$

where, $\Gamma^\rho_{\mu\nu} = \frac{1}{2}g^{\rho\sigma}(\partial_\nu g_{\mu\sigma} + \partial_\mu g_{\nu\sigma} - \partial_\sigma g_{\mu\nu})$ is called the Christoffel symbol. We can choose τ in such a way that $\frac{d\mathcal{L}}{d\tau} = 0$. This is called affine parametrization. So,

$$\frac{d^2x^\rho}{d\tau^2} + \Gamma^\rho_{\mu\nu}\frac{dx^\mu}{d\tau}\frac{dx^\nu}{d\tau} = 0. \tag{B.7}$$

Suppose $S_2 = gq\int A_\mu \frac{dx^\mu}{d\tau}d\tau = gq\int A_\mu dx^\mu$. Hence,

$$\delta S_2 = gq\int \delta A_\mu dx^\mu + gq\int A_\mu \delta(dx^\mu), \tag{B.8}$$

or,

$$\delta S_2 = gq\int \frac{\partial A_\mu}{\partial x^\nu}\delta x^\nu dx^\mu + gq\int A_\mu d(\delta x^\mu). \tag{B.9}$$

Using integration by parts and using the fact that the total derivative term will not contribute to the integration, we can write

$$\delta S_2 = gq\int \frac{\partial A_\mu}{\partial x^\nu}\delta x^\nu dx^\mu - gq\int dA_\mu \delta x^\mu. \tag{B.10}$$

or,

$$\delta S_2 = gq\int \frac{\partial A_\mu}{\partial x^\nu}\delta x^\nu dx^\mu - gq\int \frac{\partial A_\mu}{\partial x^\nu}dx^\nu \delta x^\mu. \tag{B.11}$$

Since μ and ν are dummy indices, we interchange μ and ν in the first term. Hence, we can write

$$\begin{aligned} \delta S_2 &= gq\int (\partial_\mu A_\nu - \partial_\nu A_\mu)dx^\nu \delta x^\mu \\ &= gq\int (\partial_\mu A_\nu - \partial_\nu A_\mu)\frac{dx^\nu}{d\tau}\delta x^\mu d\tau. \end{aligned} \tag{B.12}$$

Imposing the fact $\delta S_1 + \delta S_2 = 0$ and using Eq. (3.37), Eq. (B.7) and Eq. (B.12) we can write

$$\ddot{x}^\rho + \Gamma^\rho_{\mu\nu}\dot{x}^\mu\dot{x}^\nu = \frac{gq}{M_p}g^{\rho\mu}(\partial_\mu A_\nu - \partial_\nu A_\mu)\dot{x}^\nu, \tag{B.13}$$

which matches with Eq. (3.38).

B.2 Christoffel symbols for the Schwarzschild metric

The christoffel symbols for the Schwarzschild metric defined in Eq. (3.39) are

$$\Gamma^t_{rt} = \frac{M}{r^2\left(1-\frac{2M}{r}\right)}, \quad \Gamma^r_{tt} = \frac{M}{r^2}\left(1-\frac{2M}{r}\right), \quad \Gamma^r_{rr} = -\frac{M}{r^2\left(1-\frac{2M}{r}\right)}, \quad \Gamma^r_{\theta\theta} = -r\left(1-\frac{2M}{r}\right),$$
$$\Gamma^r_{\phi\phi} = -r\sin^2\theta\left(1-\frac{2M}{r}\right), \quad \Gamma^\theta_{r\theta} = \frac{1}{r}, \quad \Gamma^\theta_{\phi\phi} = -\sin\theta\cos\theta, \quad \Gamma^\phi_{\phi r} = \frac{1}{r}, \quad \Gamma^\phi_{\theta\phi} = \cot\theta. \tag{B.14}$$

B.3 Equation of motion for the vector field A_μ

The vector field A_μ satisfies the Klein-Gordon equation

$$\Box A_\mu = M^2_{Z'} A_\mu. \tag{B.15}$$

Now, for the static case, $A_\mu = \{V(r), 0, 0, 0\}$. Hence,

$$\Box V(r) = M^2_{Z'} V(r). \tag{B.16}$$

In the background of the Schwarzschild spacetime, Equation (B.16) becomes

$$\left(1-\frac{2M}{r}\right)\frac{d^2V}{dr^2} + \frac{2}{r}\left(1-\frac{M}{r}\right)\frac{dV}{dr} = M^2_{Z'}V(r). \tag{B.17}$$

So, in the Schwarzschild background, $V(r)$ will not satisfy the Klein-Gordon equation. So we expand $V(r)$ in a perturbation series where the perturbation parameter is $\frac{M}{R}$, and the leading order term is the Yukawa term. Let,

$$V(r) = V_0(r) + \frac{M}{R}V_1(r) + \mathcal{O}\left(\frac{M}{R}\right)^2, \tag{B.18}$$

where

$$V_0(r) = c\frac{e^{-M'_Z r}}{r}, \qquad c = \frac{g^2 N_1 N_2}{4\pi}, \tag{B.19}$$

such that

$$\frac{d^2V_0}{dr^2} + \frac{2}{r}\frac{dV_0}{dr} = M^2_{Z'}V_0. \tag{B.20}$$

Inserting Eq. (B.18) in Eq. (B.17), we get the equation for $V_1(r)$

$$\frac{1}{R}\frac{d^2V_1}{dr^2} + \frac{2}{rR}\frac{dV_1}{dr} = \frac{M^2_{Z'}V_1}{R} + \frac{2}{r}\frac{d^2V_0}{dr^2} + \frac{2}{r^2}\frac{dV_0}{dr}. \tag{B.21}$$

Let,

$$V_1(r) = \chi(r)\frac{e^{-M'_Z r}}{r}. \tag{B.22}$$

Now, Eq. (B.21) becomes

$$\frac{1}{R}\frac{d^2\chi}{dr^2} - \frac{1}{R}2M'_Z\frac{d\chi}{dr} = 2c\Big(\frac{M^2_{Z'}}{r} + \frac{1}{r^3} + \frac{M'_Z}{r^2}\Big). \tag{B.23}$$

Integrating Eq. (B.23) once we get

$$\frac{d\chi}{dr} - 2M'_Z\chi = 2cR\Big[M^2_{Z'}\ln(M'_Z r) - \frac{1}{2r^2} - \frac{M'_Z}{r}\Big] + k_1 R, \tag{B.24}$$

where k_1 is the integration constant. Eq. (B.24) can be written as

$$\frac{d}{dr}\Big(e^{-2M'_Z r}\chi\Big) = 2cRe^{-2M'_Z r}\Big[M^2_{Z'}\ln(M'_Z r) - \frac{1}{2r^2} - \frac{M'_Z}{r}\Big] + k_1 R e^{-2M'_Z r}. \tag{B.25}$$

From Eq. (B.25), we can write

$$e^{-2M'_Z r}\chi(r) = 2cR\Big[M^2_{Z'}\int_\infty^r e^{-2M'_Z x}\ln(M'_Z x)dx - \int_\infty^r \frac{e^{-2M'_Z x}}{2x^2}dx - \int_\infty^r \frac{M'_Z e^{-2M'_Z x}}{x}dx\Big] - \frac{k_1 R}{2M'_Z}e^{-2M'_Z r} + k_2, \tag{B.26}$$

where k_2 is an integration constant. Doing integration by parts, Eq. (B.26) becomes

$$\chi(r) = cR\Big[-M'_Z\ln(M'_Z r) + \frac{1}{r} + M'_Z e^{2M'_Z r}E_i(-2M'_Z r)\Big] - \frac{k_1 R}{2M'_Z} + k_2 e^{2M'_Z r}, \tag{B.27}$$

where $E_i(x)$ is a special function called the exponential integral function which is defined as

$$E_i(x) = -\int_{-x}^{\infty}\frac{e^{-t}}{t}dt. \tag{B.28}$$

We chose $k_2 = 0$ as $e^{2M'_Z r}$ diverges. We also chose $k_1 = 0$ as we are looking for particular integral. Hence, from Eq. (B.27) we get

$$V_1(r) = \frac{cRe^{-M'_Z r}}{r}\Big[\frac{1}{r} - M'_Z\ln(M'_Z r) + M'_Z e^{2M'_Z r}E_i(-2M'_Z r)\Big]. \tag{B.29}$$

So the total solution of the potential is

$$V(r) = \frac{ce^{-M'_Z r}}{r}\Big[1+\frac{M}{r}\{1-M'_Z r\ln(M'_Z r)+M'_Z r e^{2M'_Z r}E_i(-2M'_Z r)\}\Big]+\mathcal{O}\Big(\frac{M^2}{R^2}\Big). \tag{B.30}$$

We take the leading order term which is the Yukawa term in our calculation. The higher order terms are comparatively small.

B.4 Total energy of the binary system due to gravity and long range Yukawa type potential

For Newtonian gravity, we can write

$$\frac{E^2-1}{L^2} = -\frac{1}{a^2(1-e^2)}, \quad \frac{2M}{L^2} = \frac{2}{a(1-e^2)}. \tag{B.31}$$

Dividing the above two expression, we obtain

$$\frac{E^2-1}{M} = -\frac{1}{a}, \tag{B.32}$$

or,

$$E \simeq \sqrt{1-\frac{M}{a}} \approx 1 - \frac{M}{2a}. \tag{B.33}$$

In presence of long range Yukawa potential, we obtain E from the condition $\frac{du}{d\phi} = 0$ at $u = u_+ = 1/a(1+e)$ (aphelion) and $u = u_- = 1/a(1-e)$ (perihelion),

$$E \simeq 1 - \frac{M}{2a} + \frac{g^2 Qq}{4\pi M_p}\left(\frac{u_+ u_-^2 e^{-M_{Z'}/u_+} - u_+^2 u_- e^{-M_{Z'}/u_-}}{u_+^2 - u_-^2}\right) \tag{B.34}$$

where 1 in the right hand side is the rest energy per unit mass in the Minkowski background. The second term is $\approx 10^{-8}$ and the third Yukawa term is smaller than the Newtonian term.

Appendix C

Energy Loss from a Binary system Due to Massless Graviton Radiation

C.1 ENERGY LOSS BY MASSLESS GRAVITON RADIATION FROM BINARIES

The action for the graviton field $h_{\mu\nu}$ is obtained by starting with the Einstein-Hilbert action for gravity and matter fields

$$S_{EH} = \int d^4x\sqrt{-g}\left[-\frac{1}{16\pi G}R + \mathcal{L}_m\right], \tag{C.1}$$

and expanding the metric $g_{\mu\nu} = \eta_{\mu\nu} + \kappa h_{\mu\nu}$ to the linear order in $h_{\mu\nu}$, where $\kappa = \sqrt{32\pi G}$ is the gravitational coupling. For consistency the inverse metric $g^{\mu\nu}$ and square root of determinant $\sqrt{-g}$ should be expanded to quadratic order

$$\begin{aligned}
g_{\mu\nu} &= \eta_{\mu\nu} + \kappa h_{\mu\nu}\,, \\
g^{\mu\nu} &= \eta^{\mu\nu} - \kappa h^{\mu\nu} + \kappa^2 h^{\mu\lambda}h^{\nu}_{\lambda} + \mathcal{O}(\kappa^3)\,, \\
\sqrt{-g} &= 1 + \frac{\kappa}{2}h + \frac{\kappa^2}{8}h^2 - \frac{\kappa^2}{4}h^{\mu\nu}h_{\mu\nu} + \mathcal{O}(\kappa^3),
\end{aligned} \tag{C.2}$$

where $\eta_{\mu\nu} = \mathrm{diag}(1,-1,-1,-1)$ is the background Minkowski metric and $h = h^{\mu}_{\mu}$. Indices are raised and lowered by $\eta^{\mu\nu}$ and $\eta_{\mu\nu}$ respectively.

The linearised Einstein-Hilbert action for the graviton field $h_{\mu\nu}$ is then given by

$$S_{EH} = \int d^4x\left[-\frac{1}{2}(\partial_\mu h_{\nu\rho})^2 + \frac{1}{2}(\partial_\mu h)^2 - (\partial_\mu h)(\partial^\nu h^{\mu}_{\nu}) + (\partial_\mu h_{\nu\rho})(\partial^\nu h^{\mu\rho}) + \frac{\kappa}{2}h_{\mu\nu}T^{\mu\nu}\right]$$

$$= \int d^4x \left[\frac{1}{2} h_{\mu\nu} \mathcal{E}^{\mu\nu\alpha\beta} h_{\alpha\beta} + \frac{\kappa}{2} h_{\mu\nu} T^{\mu\nu}\right], \tag{C.3}$$

where the kinetic operator $\mathcal{E}^{\mu\nu\alpha\beta}$ has the form

$$\mathcal{E}^{\mu\nu\alpha\beta} = \left(\eta^{\mu(\alpha}\eta^{\beta)\nu} - \eta^{\mu\nu}\eta^{\alpha\beta}\right)\Box - \eta^{\mu(\alpha}\partial^{\beta)}\partial^{\nu} - \eta^{\nu(\alpha}\partial^{\beta)}\partial^{\mu} + \eta^{\alpha\beta}\partial^{\mu}\partial^{\nu} + \eta^{\mu\nu}\partial^{\alpha}\partial^{\beta}, \tag{C.4}$$

and indices enclosed by brackets denote symmetrisation, $A^{(\mu}B^{\nu)} = \frac{1}{2}(A^{\mu}B^{\nu} + A^{\nu}B^{\mu})$. The massless graviton propagator $D^{(0)}_{\mu\nu\alpha\beta}$ is the inverse of the kinetic operator $\mathcal{E}^{\mu\nu\alpha\beta}$

$$\mathcal{E}^{\mu\nu\alpha\beta} D^{(0)}_{\alpha\beta\rho\sigma}(x-y) = \delta^{\mu}_{(\rho}\delta^{\mu}_{\sigma)}\delta^4(x-y)\,. \tag{C.5}$$

The massless graviton action Eq.C.3 has the gauge symmetry $h_{\mu\nu} \to h_{\mu\nu} - \partial_{\mu}\xi_{\nu} - \partial_{\nu}\xi_{\mu}$ due to which the operator $\mathcal{E}^{\mu\nu\alpha\beta}$ cannot be inverted so the propagator cannot be determined from the relation Eq.C.5. To invert the kinetic operator we need to choose a gauge. The gauge choice for which the propagator has the simplest form is the de-Dhonder gauge choice in which,

$$\partial^{\mu} h_{\mu\nu} - \frac{1}{2}\partial_{\nu} h = 0, \tag{C.6}$$

where $h = h^{\alpha}{}_{\alpha}$. We can incorporate this gauge choice by adding the following gauge fixing term to the Lagrangian Eq.C.3,

$$S_{gf} = -\int d^4x \left(\partial^{\mu} h_{\mu\nu} - \frac{1}{2}\partial_{\nu} h\right)^2. \tag{C.7}$$

The total action with the gauge fixing term turns out to be of the form

$$\begin{aligned} S_{EH} + S_{gf} &= \int d^4x \left(\frac{1}{2} h_{\mu\nu}\Box h^{\mu\nu} - \frac{1}{4} h\Box h + \frac{\kappa}{2} h_{\mu\nu} T^{\mu\nu}\right) \\ &= \int d^4x \left(\frac{1}{2} h_{\mu\nu}\mathcal{K}^{\mu\nu\alpha\beta} h_{\alpha\beta} + \frac{\kappa}{2} h_{\mu\nu} T^{\mu\nu}\right), \end{aligned} \tag{C.8}$$

where $\mathcal{K}^{\mu\nu\alpha\beta}$ is the kinetic operator in the de Donder gauge given by

$$\mathcal{K}^{\mu\nu\alpha\beta} = \left(\frac{1}{2}(\eta^{\mu\alpha}\eta^{\nu\beta} + \eta^{\mu\beta}\eta^{\nu\alpha}) - \frac{1}{2}\eta^{\mu\nu}\eta^{\alpha\beta}\right)\Box\,. \tag{C.9}$$

The propagator in the de Donder gauge is the inverse of the kinetic operator Eq.C.9 and is given by

$$\mathcal{K}^{\mu\nu\alpha\beta} D^{(0)}_{\alpha\beta\rho\sigma}(x-y) = \delta^{\mu}_{(\rho}\delta^{\mu}_{\sigma)}\delta^4(x-y)\,. \tag{C.10}$$

This relation can be used to solve for $D^{(0)}_{\alpha\beta\rho\sigma}$ which in the momentum space ($\partial_\mu = ik_\mu$) is then given

$$D^{(0)}_{\mu\nu\alpha\beta}(k) = \frac{1}{-k^2}\left(\frac{1}{2}(\eta_{\mu\alpha}\eta_{\nu\beta} + \eta_{\mu\beta}\eta_{\nu\alpha}) - \frac{1}{2}\eta_{\mu\nu}\eta_{\alpha\beta}\right) . \tag{C.11}$$

We treat the graviton as a quantum field by expanding it in terms of creation and annihilation operators,

$$\hat{h}_{\mu\nu}(x) = \sum_\lambda \int \frac{d^3k}{(2\pi)^3}\frac{1}{\sqrt{2\omega_k}}\left[\epsilon^\lambda_{\mu\nu}(k)a_\lambda(k)e^{-ik\cdot x} + \epsilon^{*\lambda}_{\mu\nu}(k)a^\dagger_\lambda(k)e^{ik\cdot x}\right] . \tag{C.12}$$

Here $\epsilon^\lambda_{\mu\nu}(k)$ are the polarization tensors which obey the orthogonality relation

$$\epsilon^\lambda_{\mu\nu}(k)\epsilon^{*\lambda'\mu\nu}(k) = \delta_{\lambda\lambda'}, \tag{C.13}$$

while $a_\lambda(k)$ and $a^\dagger_\lambda(k)$ are graviton annihilation and creation operators which obey the canonical commutation relations

$$\left[a_\lambda(k), a^\dagger_{\lambda'}(k')\right] = \delta^4(k-k')\delta_{\lambda\lambda'} . \tag{C.14}$$

The Feynman propagator of gravitons is defined as the time ordered two point function

$$D^{(0)}_{\mu\nu\alpha\beta}(x-y) \equiv \langle 0|T(\hat{h}_{\mu\nu}(x)\hat{h}_{\alpha\beta}(y))|0\rangle, \tag{C.15}$$

which may be evaluated using Eq.C.12 to give

$$D^{(0)}_{\mu\nu\alpha\beta}(x-y) = \int \frac{d^4k}{(2\pi)^4}\frac{1}{-k^2+i\epsilon}e^{ik(x-y)}\sum_\lambda \epsilon^\lambda_{\mu\nu}(k)\epsilon^{*\lambda}_{\alpha\beta}(k). \tag{C.16}$$

Comparing Eq.C.11 and Eq.C.16 we have the expression for the polarization sum of massless spin-2 gravitons

$$\sum_{\lambda=1}^{2}\epsilon^\lambda_{\mu\nu}(k)\epsilon^{*\lambda}_{\alpha\beta}(k) = \frac{1}{2}(\eta_{\mu\alpha}\eta_{\nu\beta} + \eta_{\mu\beta}\eta_{\nu\alpha}) - \frac{1}{2}\eta_{\mu\nu}\eta_{\alpha\beta}. \tag{C.17}$$

This will be used in the computation of massless graviton radiation from classical sources.

We now calculate the energy loss due to the radiation of massless graviton from compact binary systems [168, 256] by evaluating the Feynman diagram shown in Fig.4.1. We treat the current $T_{\mu\nu}$ of the binary stars as classical source and the gravitons as quantum fields. From the interaction Lagrangian Eq.C.8 we see that the interaction vertex is $\frac{1}{2}\kappa h^{\mu\nu}T_{\mu\nu}$, therefore we can write the emission rate of massless gravitons with polarisation tensor $\epsilon_\lambda^{\mu\nu}(k')$ from the classical source $T_{\mu\nu}(k)$ as

$$d\Gamma = \frac{\kappa^2}{4}\sum_{\lambda=1}^{2}|T_{\mu\nu}(k')\epsilon_\lambda^{\mu\nu}(k)|^2 2\pi\delta(\omega-\omega')\frac{d^3k}{(2\pi)^3}\frac{1}{2\omega}. \tag{C.18}$$

Expanding the modulus squared in Eq.C.18, we can write

$$d\Gamma = \frac{\kappa^2}{8(2\pi)^2}\sum_{\lambda=1}^{2}\Big(T_{\mu\nu}(k')T^*_{\alpha\beta}(k')\epsilon_\lambda^{\mu\nu}(k)\epsilon_\lambda^{*\alpha\beta}(k)\Big)\frac{d^3k}{\omega}\delta(\omega-\omega'). \tag{C.19}$$

Using the polarization sum of massless spin-2 gravitons from Eq.C.17, we can write the emission rate as

$$\begin{aligned} d\Gamma &= \frac{\kappa^2}{8(2\pi)^2}\int\Big[T_{\mu\nu}(k')T^*_{\alpha\beta}(k')\Big]\Big[\frac{1}{2}(\eta^{\mu\alpha}\eta^{\nu\beta}+\eta^{\mu\beta}\eta^{\nu\alpha}-\eta^{\mu\nu}\eta^{\alpha\beta})\Big]\frac{d^3k}{\omega}\delta(\omega-\omega')\,. \\ &= \frac{\kappa^2}{8(2\pi)^2}\int\Big[|T_{\mu\nu}(k')|^2-\frac{1}{2}|T^\mu{}_\mu(k')|^2\Big]\delta(\omega-\omega')\omega d\omega d\Omega_k, \end{aligned} \tag{C.20}$$

where we use $d^3k = k^2dkd\Omega$. Thus, the rate of energy loss due to massless graviton radiation becomes

$$\frac{dE}{dt} = \frac{\kappa^2}{8(2\pi)^2}\int\Big[|T_{\mu\nu}(k')|^2-\frac{1}{2}|T^\mu{}_\mu(k')|^2\Big]\delta(\omega-\omega')\omega^2 d\omega d\Omega_k. \tag{C.21}$$

Using the conserved current relation $k_\mu T^{\mu\nu}=0$, we can write the T^{00} and T^{i0} components of the stress tensor in terms of the T^{ij} components,

$$T_{0j} = -\hat{k}^i T_{ij}, \quad T_{00} = \hat{k}^i\hat{k}^j T_{ij}. \tag{C.22}$$

Therefore, we can write

$$\Big[|T_{\mu\nu}(k')|^2-\frac{1}{2}|T^\mu{}_\mu(k')|^2\Big] = \Lambda^0_{ij,lm}T^{ij*}T^{lm}, \tag{C.23}$$

where,

$$\Lambda^0_{ij,lm} = \Big[\delta_{il}\delta_{jm}-2\hat{k}_j\hat{k}_m\delta_{il}+\frac{1}{2}\hat{k}_i\hat{k}_j\hat{k}_l\hat{k}_m-\frac{1}{2}\delta_{ij}\delta_{lm}+\frac{1}{2}\Big(\delta_{ij}\hat{k}_l\hat{k}_m+\delta_{lm}\hat{k}_i\hat{k}_j\Big)\Big]. \tag{C.24}$$

We do the angular integrals

$$\int d\Omega_k\Lambda^0_{ij,lm}T^{ij*}(\omega')T^{lm}(\omega') = \frac{8\pi}{5}\Big(T_{ij}(\omega')T^*_{ji}(\omega')-\frac{1}{3}|T^i{}_i(\omega')|^2\Big), \tag{C.25}$$

using the relations

$$\int d\Omega \hat{k^i}\hat{k^j} = \frac{4\pi}{3}\delta_{ij}, \qquad \int d\Omega \hat{k^i}\hat{k^j}\hat{k^l}\hat{k^m} = \frac{4\pi}{15}(\delta_{ij}\delta_{lm}+\delta_{il}\delta_{jm}+\delta_{im}\delta_{jl}). \quad \text{(C.26)}$$

The stress tensor or the current density for this compact binary system is

$$T_{\mu\nu}(x') = \mu\delta^3(\mathbf{x}' - \mathbf{x}(t))U_\mu U_\nu, \quad \text{(C.27)}$$

where $\mu = \dfrac{m_1 m_2}{m_1 + m_2}$ is the reduced mass of the binary system and m_1 and m_2 are the masses of the two stars in the binary system. $U_\mu = (1, \dot{x}, \dot{y}, 0)$ is the non relativistic four velocity of the reduced mass of the binary system in the $x - y$ plane of the Keplerian orbit.

This stress energy tensor only corresponds to the matter fields but not the effective stress-energy tensor which, in general, is $T_{\mu\nu} = T_{\mu\nu}^{matter} + T_{\mu\nu}^{GW}$, $T_{\mu\nu}^{matter}$ is the usual stress-energy tensor for matter fields and $T_{\mu\nu}^{GW}$ corresponds to the energy content of the gravitational waves. The expression for the $T_{\mu\nu}^{GW}$ is

$$T_{\mu\nu}^{GW} = \langle h_{\alpha\beta,\mu}h^{\alpha\beta}{}_{,\nu} - \frac{1}{2}h_{,\mu}h_{,\nu}\rangle. \quad \text{(C.28)}$$

Now at the tree-level, from the equation of motion for $h_{\alpha\beta}$, we can write

$$h_{\alpha\beta} \sim \frac{1}{M_{pl}}(\Box - m_g^2)^{-1}T_{\alpha\beta}^{matter}. \quad \text{(C.29)}$$

Therefore,

$$T_{\mu\nu}^{GW}(k_\alpha) \sim \frac{1}{M_{pl}^2}\left((T_{\alpha\beta}^{matter})^2 - \frac{(T^{matter})^2}{2}\right)\left(\frac{k_\mu k_\nu}{(k^\alpha k_\alpha - m_g^2)^2}\right). \quad \text{(C.30)}$$

Thus in the radiation zone, i.e. far from the source, $T_{\mu\nu}^{GW}$ is suppressed by the factor of $1/M_{pl}^2$ in comparison with the part ($T_{\mu\nu}^{matter}$) from the matter field. Therefore, for gravitational radiation from compact binaries, $T_{\mu\nu} \simeq T_{\mu\nu}^{matter}$.

We can write the Keplerian orbit in the parametric form as

$$x = a(\cos\xi - e), \quad y = a\sqrt{(1-e^2)}\sin\xi, \quad \Omega t = \xi - e\sin\xi, \quad \text{(C.31)}$$

where a and e are the semi-major axis and eccentricity of the elliptic orbit respectively. Since the angular velocity of an eccentric orbit is not constant, we can write the Fourier transform of the current density in terms of the n harmonics of the fundamental frequency $\Omega = \left[G\frac{(m_1+m_2)}{a^3}\right]^{\frac{1}{2}}$. Using Eq.C.31, we can write the Fourier transforms of the velocity components in the Kepler orbit as

$$\dot{x}_n = \frac{1}{T}\int_0^T e^{in\Omega t}\dot{x}dt = -ia\Omega J_n'(ne), \tag{C.32}$$

and

$$\dot{y}_n = \frac{1}{T}\int_0^T e^{in\Omega t}\dot{y}dt = \frac{a\sqrt{(1-e^2)}}{e}\Omega J_n(ne), \tag{C.33}$$

where we use $T = 2\pi/\Omega$, and the Bessel identity $J_n(z) = \frac{1}{2\pi}\int_0^{2\pi} e^{i(n\xi - z\sin\xi)}d\xi$. The prime over the Bessel function denotes the derivative with respect to the argument. Hence the Fourier transforms of the orbital coordinates become

$$x_n = \frac{\dot{x}_n}{-i\Omega n} = \frac{a}{n}J_n'(ne), \quad y_n = \frac{\dot{y}_n}{-i\Omega n} = \frac{ia\sqrt{1-e^2}}{ne}J_n(ne). \tag{C.34}$$

Now we will calculate the Fourier transforms of different components of the stress tensor with $\omega' = n\Omega$ as below. Thus,

$$\begin{aligned} T_{ij}(\mathbf{k}',\omega') &= \frac{1}{T}\int_0^T\int T_{ij}(\mathbf{x},t)e^{-i(\mathbf{k}'\cdot\mathbf{x}-\omega' t)}d^3x dt \\ &= \int T_{ij}(\mathbf{x},\omega')e^{-i\mathbf{k}'\cdot\mathbf{x}}d^3x. \end{aligned} \tag{C.35}$$

Expanding $e^{-i\mathbf{k}'.\mathbf{x}} \approx 1 - i\mathbf{k}'.\mathbf{x} - \cdots$ and retaining the leading order term $\mathbf{k}'.\mathbf{x} \sim \Omega a \ll 1$ for binary orbit, we can write Eq.C.35 as

$$T_{ij}(\mathbf{k}',\omega') \simeq T_{ij}(\omega') = \int T_{ij}(\mathbf{x},\omega')d^3x. \tag{C.36}$$

From conservation of the stress-energy tensor, i.e. $\partial_\mu T^{\mu\nu}(\mathbf{x},t) = 0$, we get

$$\partial^i\partial^j T_{ij}(\mathbf{x},\omega') = -\omega'^2 T_{00}(\mathbf{x},\omega'). \tag{C.37}$$

Multiplying both side of the Eq.C.37 by $x_k x_l$ and integrating over all $\mathbf{x}$ we get

$$T_{kl}(\omega') = -\frac{\omega'^2}{2}\int T_{00}(\mathbf{x},\omega')x_k x_l d^3x \tag{C.38}$$

$$= -\frac{\mu\omega'^2}{2T}\int_0^T\int \delta^3(\mathbf{x}'-\mathbf{x}(t))e^{i\omega' t}x_k x_l d^3x dt \tag{C.39}$$

$$= -\frac{\mu\omega'^2}{2T}\int_0^T x_k'(t)x_l'(t)e^{i\omega' t}dt, \tag{C.40}$$

where in the Eq.C.39 we have used the Eq.C.27. Doing integration by parts of Eq.C.40 and using the Bessel function identities[1], we can write the different components of stress tensor in the $x - y$ plane. The xx-component of stress tensor in the Fourier space is

$$\begin{aligned} T_{xx}(\omega') &= -\frac{\mu\omega'^2}{2T}\int_0^T x^2(t)e^{i\omega' t}dt \\ &= -\frac{\mu\omega'^2}{4\pi}\int_0^{2\pi} a^2(\cos\xi - e)^2 e^{in\beta}d\beta, \end{aligned} \tag{C.41}$$

where we used Eq.C.31 and $\omega' = n\Omega$, $\beta = \Omega t$, and $T = 2\pi/\Omega$. Doing integration by parts of Eq.C.41 we get

$$\begin{aligned} T_{xx}(\omega') &= \frac{\mu\omega'^2}{4\pi in}\int_0^{2\pi} e^{in\beta}\frac{d}{d\beta}(\cos\xi - e)^2\, d\beta \\ &= \frac{\mu\omega'^2}{2\pi in}\int_0^{2\pi} \sin\xi(\cos\xi - e)e^{in\beta}d\xi \\ &= -\frac{\mu\omega'^2}{8\pi n}\int_0^{2\pi} \left[(e^{2i\xi} - e^{-2i\xi}) - 2e(e^{i\xi} - e^{-i\xi})\right] e^{in\beta}d\xi \\ &= -\frac{\mu\omega'^2}{4n}\left[J_{n-2}(ne) - 2eJ_{n-1}(ne) + 2eJ_{n+1}(ne) - J_{n+2}(ne)\right], \end{aligned} \tag{C.42}$$

where in the last step we used the definition of the Bessel function and $\beta = \Omega t = \xi - e\sin\xi$.

Similarly,

$$\begin{aligned} T_{yy}(\omega') &= -\frac{\mu\omega'^2}{2T}\int_0^T y^2(t)e^{i\omega' t}dt \\ &= -\frac{\mu\omega'^2(1-e^2)}{4\pi}\int_0^{2\pi} a^2\sin^2\xi\, e^{in\beta}d\beta. \end{aligned} \tag{C.43}$$

Adding Eq.C.41 and Eq.C.43 we get

$$\begin{aligned} T_{yy}(\omega') + T_{xx}(\omega') &= -\frac{\mu\omega'^2 a^2}{4\pi}\int_0^{2\pi} (1 - e\cos\xi)^2 e^{in\beta}d\beta \\ &= \frac{\mu\omega'^2 a^2 e}{2\pi in}\int_0^{2\pi} \sin\xi\, e^{in\beta}d\beta, \\ &= \frac{\mu\omega'^2 a^2}{2\pi n^2}\int_0^{2\pi} e\cos\xi\, e^{in\beta}d\xi, \\ &= \frac{\mu\omega'^2 a^2}{2\pi n^2}\int_0^{2\pi} e^{in\beta}d\xi = \frac{\mu\omega'^2 a^2}{n^2}J_n^2(ne). \end{aligned} \tag{C.44}$$

[1] $J_{n-1}(z) - J_{n+1}(z) = 2J'_n(z), \qquad J_{n-1}(z) + J_{n+1}(z) = \frac{2n}{z}J_n(z)$

Therefore

$$\begin{aligned}
T_{yy}(\omega') &= -T_{xx}(\omega') + \frac{\mu\omega'^2 a^2}{n^2} J_n^2(ne) \\
&= \frac{\mu\omega'^2 a^2}{4n}\Big[J_{n-2}(ne) - 2eJ_{n-1}(ne) + \frac{4}{n}J_n(ne) + 2eJ_{n+1}(ne) - \\
&\quad J_{n+2}(ne)\Big]. \qquad \text{(C.45)}
\end{aligned}$$

The xy-component of the stress tensor in the Fourier space is

$$\begin{aligned}
T_{xy}(\omega') &= -\frac{\mu\omega'^2}{2T}\int_0^T x(t)y(t)e^{i\omega' t}dt \\
&= -\frac{\mu\omega'^2\sqrt{1-e^2}}{4\pi}\int_0^{2\pi} a^2(\cos\xi - e)\sin\xi\, e^{in\beta}d\beta \\
&= \frac{\mu\omega'^2 a^2\sqrt{1-e^2}}{4\pi i n}\int_0^{2\pi} (\cos(2\xi) - e\cos\xi)\, e^{in\beta}d\xi, \\
&= -i\frac{\mu\omega'^2 a^2\sqrt{1-e^2}}{4\pi n}\int_0^{2\pi} (\cos(2\xi) - 1)\, e^{in\beta}d\xi \\
&= -i\frac{\mu\omega'^2 a^2\sqrt{1-e^2}}{4n}\left[J_{n+2}(ne) - 2J_n(ne) + J_{n-2}(ne)\right] \qquad \text{(C.46)}
\end{aligned}$$

For convenience we summarize the final expressions of $T_{ij}(\omega')$ as

$$\begin{aligned}
T_{xx}(\omega') &= -\frac{\mu\omega'^2 a^2}{4n}\Big[J_{n-2}(ne) - 2eJ_{n-1}(ne) + 2eJ_{n+1}(ne) - J_{n+2}(ne)\Big], \\
T_{yy}(\omega') &= \frac{\mu\omega'^2 a^2}{4n}\Big[J_{n-2}(ne) - 2eJ_{n-1}(ne) + \frac{4}{n}J_n(ne) + 2eJ_{n+1}(ne) - J_{n+2}(ne)\Big], \\
T_{xy}(\omega') &= \frac{-i\mu\omega'^2 a^2}{4n}(1-e^2)^{\frac{1}{2}}\Big[J_{n-2}(ne) - 2J_n(ne) + J_{n+2}(ne)\Big]. \qquad \text{(C.47)}
\end{aligned}$$

Using Eq.C.47, we get two useful results

$$\begin{aligned}
T_{ij}(\omega')T^{ij*}(\omega') &= \frac{\mu^2\omega'^4 a^4}{8n^2}\Big\{[J_{n-2}(ne) - 2eJ_{n-1}(ne) + 2eJ_{n+1}(ne) + \frac{2}{n}J_n(ne) - \\
&\quad J_{n+2}(ne)]^2 + (1-e^2)[J_{n-2}(ne) - 2J_n(ne) + J_{n+2}(ne)]^2 + \frac{4}{n^2}J_n^2(ne)\Big\} \\
&= 4\mu^2\omega'^4 a^4\left(f(n,e) + \frac{J_n^2(ne)}{12n^4}\right), \qquad \text{(C.48)}
\end{aligned}$$

where

$$\begin{aligned}
f(n,e) = \frac{1}{32n^2}\Big\{&[J_{n-2}(ne) - 2eJ_{n-1}(ne) + 2eJ_{n+1}(ne) + \frac{2}{n}J_n(ne) - J_{n+2}(ne)]^2 + \\
&(1-e^2)[J_{n-2}(ne) - 2J_n(ne) + J_{n+2}(ne)]^2 + \frac{4}{3n^2}J_n^2(ne)\Big\}
\end{aligned} \qquad \text{(C.49)}$$

and

$$|T^i{}_i|^2 = \frac{\mu^2 \omega'^4 a^4}{n^4} J_n^2(ne). \tag{C.50}$$

Thus the energy loss due to massless graviton radiation becomes

$$\begin{aligned}
\frac{dE}{dt} &= \frac{\kappa^2}{8(2\pi)^2} \int \frac{8\pi}{5} \Big[T_{ij}(\omega') T^*_{ji}(\omega') - \frac{1}{3} |T^i{}_i(\omega')|^2 \Big] \delta(\omega - \omega') \omega^2 d\omega, \\
&= \frac{32G}{5} \sum_{n=1}^{\infty} (n\Omega)^2 \mu^2 a^4 (n\Omega)^4 f(n,e) \\
&= \frac{32G}{5} \Omega^6 \Big(\frac{m_1 m_2}{m_1 + m_2} \Big)^2 a^4 (1 - e^2)^{-7/2} \Big(1 + \frac{73}{24} e^2 + \frac{37}{96} e^4 \Big). \quad \text{(C.51)}
\end{aligned}$$

This expression is called Einstein's quadrupole gravitational radiation which matches with the Peters-Mathews result [177]. From the energy loss formula we can calculate the change in time period ($P_b = 2\pi/\Omega$). From Kepler's law $\Omega^2 a^3 = G(M_1 + M_2)$ we have $\dot{a}/a = (2/3)(\dot{P}_b/P_b)$. The gravitational energy is $E = -GM_1M_2/2a$ which implies $\dot{a}/a = -(\dot{E}/E)$. Using these two relations we get $\dot{P}_b/P_b = -(3/2)(\dot{E}/E)$.

Appendix D

Hamiltonian of neutrino evolution equation in presence of Non Standard Interaction (NSI) and a sterile state

D.1 Two flavours neutrino evolution in vacuum and matter

The three neutrino flavour eigenstates $(\nu_e, \nu_\mu, \nu_\tau)$ can be expressed as a quantum superposition of three mass eigenstates (ν_1, ν_2, ν_3) with masses m_i. The evolution equation of neutrinos in vacuum in the mass eigenstate basis can be written as

$$i \begin{pmatrix} \dot{\nu_1} \\ \dot{\nu_2} \end{pmatrix} = \begin{pmatrix} E_1 & 0 \\ 0 & E_2 \end{pmatrix} \begin{pmatrix} \nu_1 \\ \nu_2 \end{pmatrix}, \tag{D.1}$$

where we consider the two flavour case and the Hamiltonian is diagonalized in the mass eigenstate basis. We can also write

$$iU \begin{pmatrix} \dot{\nu_1} \\ \dot{\nu_2} \end{pmatrix} = U \begin{pmatrix} E_1 & 0 \\ 0 & E_2 \end{pmatrix} U^T U \begin{pmatrix} \nu_1 \\ \nu_2 \end{pmatrix}, \tag{D.2}$$

where U is called the transformation matrix or the lepton mixing matrix which transforms a mass state of neutrino to its flavour state. Hence, we can write Eq.D.2 as

$$i\begin{pmatrix}\dot{\nu}_e \\ \dot{\nu}_\mu\end{pmatrix} = U\begin{pmatrix}E_1 & 0 \\ 0 & E_2\end{pmatrix}U^T\begin{pmatrix}\nu_e \\ \nu_\mu\end{pmatrix}, \tag{D.3}$$

where we choose the orthogonal mixing matrix U as

$$U = \begin{pmatrix}\cos\theta & \sin\theta \\ -\sin\theta & \cos\theta\end{pmatrix}. \tag{D.4}$$

Now, we can write

$$\begin{aligned} U\begin{pmatrix}E_1 & 0 \\ 0 & E_2\end{pmatrix}U^T &= U\begin{pmatrix}p+\frac{m_1^2}{2E} & 0 \\ 0 & p+\frac{m_2^2}{2E}\end{pmatrix}U^T \\ &= U\begin{pmatrix}\frac{m_1^2}{2E} & 0 \\ 0 & \frac{m_2^2}{2E}\end{pmatrix}U^T \\ &= U\begin{pmatrix}\delta_1 & 0 \\ 0 & \delta_2\end{pmatrix}U^T, \end{aligned} \tag{D.5}$$

where we use the dispersion relation $E = p + \frac{m^2}{2p} \approx p + \frac{m^2}{2E}$, in the ultra relativistic limit. We extract the constant phase as it does not contribute to the transition probability, $\delta_i = \frac{m_i^2}{2E}$ and $\delta = \delta_2 - \delta_1 = \frac{\Delta m_{21}^2}{2E}$. Inserting D.4 in Eq.D.5 we obtain

$$\begin{pmatrix}\cos\theta & \sin\theta \\ -\sin\theta & \cos\theta\end{pmatrix}\begin{pmatrix}\delta_1 & 0 \\ 0 & \delta_2\end{pmatrix}\begin{pmatrix}\cos\theta & -\sin\theta \\ \sin\theta & \cos\theta\end{pmatrix} = \frac{(\delta_1+\delta_2)I}{2}+\frac{\delta}{2}\begin{pmatrix}-\cos 2\theta & \sin 2\theta \\ \sin 2\theta & \cos 2\theta\end{pmatrix}, \tag{D.6}$$

where the first term with the identity matrix I is again the cosntant phase part and has no contribution in the transition probability. So the evolution equation becomes

$$i\begin{pmatrix}\dot{\nu}_e \\ \dot{\nu}_\mu\end{pmatrix} = \frac{\delta}{2}\begin{pmatrix}-\cos 2\theta & \sin 2\theta \\ \sin 2\theta & \cos 2\theta\end{pmatrix}\begin{pmatrix}\nu_e \\ \nu_\mu\end{pmatrix}. \tag{D.7}$$

Hence, the two flavour Hamiltonian in vacuum becomes

$$H_{\text{vac}} = \frac{\Delta m_{21}^2}{4E}\begin{pmatrix}-\cos 2\theta_{12} & \sin 2\theta_{12} \\ \sin 2\theta_{12} & \cos 2\theta_{12}\end{pmatrix}. \tag{D.8}$$

In presence of matter, the corresponding Hamiltonian becomes

$$H_{\text{vac+matt}} = \begin{pmatrix} -\frac{\Delta m^2_{21}}{4E}\cos 2\theta_{12} + \sqrt{2}G_F N_e - \frac{G_F N_n}{\sqrt{2}} & \frac{\Delta m^2_{21}}{4E}\sin 2\theta_{12} \\ \frac{\Delta m^2_{21}}{4E}\sin 2\theta_{12} & \frac{\Delta m^2_{21}}{4E}\cos 2\theta_{12} - \frac{G_F N_n}{\sqrt{2}} \end{pmatrix}, \tag{D.9}$$

since the electron neutrino has both charge and neutral current interactions whereas the muon neutrino has only the neutral current interaction. The total matter potential of electron neutrino is $V_{\nu_e} = \sqrt{2}G_F N_e - \frac{G_F N_n}{\sqrt{2}}$, and the matter potential for muon neutrino is $V_{\nu_\mu} = -\frac{G_F N_n}{\sqrt{2}}$. Hence, the term $\frac{G_F N_n}{\sqrt{2}}$ behaves as the constant phase part in the evolution equation and has no contribution in the transition probability. Hence, the two flavour neutrino evolution equation becomes

$$i\begin{pmatrix} \dot{\nu}_e \\ \dot{\nu}_\mu \end{pmatrix} = \begin{pmatrix} -\frac{\Delta m^2_{21}}{4E}\cos 2\theta_{12} + \sqrt{2}G_F N_e & \frac{\Delta m^2_{21}}{4E}\sin 2\theta_{12} \\ \frac{\Delta m^2_{21}}{4E}\sin 2\theta_{12} & \frac{\Delta m^2_{21}}{4E}\cos 2\theta_{12} \end{pmatrix}\begin{pmatrix} \nu_e \\ \nu_\mu \end{pmatrix}. \tag{D.10}$$

D.2 Three flavours neutrino evolution in presence of non standard interaction (NSI)

In the three flavour scenario, the Hamiltonians for neutrino and anti neutrino flavour states are given as

$$H^\nu = H_{\text{vac}} + H_{\text{matt}}, \tag{D.11}$$

and

$$H^{\bar{\nu}} = (H_{\text{vac}} - H_{\text{matt}})^*, \tag{D.12}$$

where the Hamiltonian in vacuum is given as

$$H_{\text{vac}} = U_{\text{vac}} D_{\text{vac}} U^\dagger_{\text{vac}}, \tag{D.13}$$

with

$$D_{\text{vac}} = \frac{1}{2E} diag(0, \Delta m^2_{21}, \Delta m^2_{31}), \tag{D.14}$$

where $\Delta m^2_{ij} = m^2_i - m^2_j$, and U is the 3×3 orthogonal mixing matrix.

Including the Non Standard Interaction (NSI), the total potential can be parametrized as

$$H_{\rm m} = H_{\rm matt}+H_{\rm NSI} = \sqrt{2}G_F N_e(r)\begin{pmatrix}1 & 0 & 0\\ 0 & 0 & 0\\ 0 & 0 & 0\end{pmatrix}+\sqrt{2}G_F\sum_{f=e,u,d} N_f(r)\begin{pmatrix}\epsilon^f_{ee} & \epsilon^f_{e\mu} & \epsilon^f_{e\tau}\\ \epsilon^{f*}_{e\mu} & \epsilon^f_{\mu\mu} & \epsilon^f_{\mu\tau}\\ \epsilon^{f*}_{e\tau} & \epsilon^{f*}_{\mu\tau} & \epsilon^f_{\tau\tau}\end{pmatrix}, \tag{D.15}$$

where the first term in the right hand side corresponds to the matter Hamiltonian and the second term denotes the Hamiltonian for NSI.

The neutral current Lagrangian for the NSI in matter which affects the neutrino propagation is given by the effective four fermion operator

$$\mathcal{L}^{NC}_{\rm NSI} = -2\sqrt{2}G_F\epsilon^{fP}_{\alpha\beta}(\bar{\nu_\alpha}\gamma^\mu\nu_\beta)(\bar{f}\gamma_\mu Pf), \tag{D.16}$$

where f is the charged fermion, P is the projection operator (left and right), and $\epsilon^{fP}_{\alpha\beta}$ are the NSI parameters which governs the deviation from the standard interactions. NSI affects the neutrino propagation in matter through vector coupling and we can write the NSI parameters as $\epsilon^f_{\alpha\beta} = \epsilon^{fL}_{\alpha\beta} + \epsilon^{fR}_{\alpha\beta}$.

D.2.1 Effective Hamiltonian for atmospheric and Long baseline (LBL) neutrinos

For different charged fermions, we have different NSI parameters in the generalized potential. However, for the propagation of atmospheric and LBL neutrinos, the neutrino to electron ratio (Y_n) is almost constant all over the earth. This implies that those oscillations are only sensitive to the sum of these interactions weighted with the relative abundance of each particle. Hence, we can define

$$\epsilon_{\alpha\beta} = \sum_{f=e,u,d}\Big\langle\frac{Y_f}{Y_e}\Big\rangle\epsilon^f_{\alpha\beta} = \epsilon^e_{\alpha\beta} + Y_u\epsilon^u_{\alpha\beta} + Y_d\epsilon^d_{\alpha\beta}. \tag{D.17}$$

From the PREM model we can write the values of $Y_n = 1.012$ in the mantle and $Y_n = 1.137$ in the core, with an average value $Y_n = 1.051$ all over the earth. A proton has two up quarks and one down quark, a neutron has one up quark and two down quarks, and neutral matter obviuosly has the same number of protons and electrons ($Y_p = 1$). So we have $Y_u = 2 + Y_n = 3.051$ and $Y_d = 1 + 2Y_n = 3.102$ in the earth. So the total Hamiltonian including the matter and NSI effects can be expressed as

$$H_m = \sqrt{2}G_F N_e(r) \begin{pmatrix} 1+\epsilon_{ee} & \epsilon_{e\mu} & \epsilon_{e\tau} \\ \epsilon^*_{e\mu} & \epsilon_{\mu\mu} & \epsilon_{\mu\tau} \\ \epsilon^*_{e\tau} & \epsilon^*_{\mu\tau} & \epsilon_{\tau\tau}, \end{pmatrix} \tag{D.18}$$

where the "1+" term in the ee entry is due to for the standard interaction term. Since, H_m is Hermitian and its trace is irrelevant for oscillation, so we are left with eight parameters.

D.2.2 Effective Hamiltonian for solar and KamLAND neutrinos

For these types of neutrino propagation, we work in the limit $\Delta m^2_{31} \to \infty$ which effectively means $G_F \sum_f N_f(r)\epsilon^f_{\alpha\beta} \ll \frac{\Delta m^2_{31}}{E}$. In this approximation, the survival probability can be written as

$$P_{ee} = c^4_{13} P_{\text{eff}} + s^4_{13}. \tag{D.19}$$

Hence, the total Hamiltonian (vacuum+matter) including the NSI effect is

$$H_\nu = R_{23}\tilde{R_{13}}R_{12}D_{\text{vac}}R^\dagger_{12}\tilde{R}^\dagger_{13}R^\dagger_{23} + H_m, \tag{D.20}$$

where $U_{\text{vac}} = R_{23}\tilde{R}_{13}R_{12}$ and,

$$R_{12} = \begin{pmatrix} c_{12} & s_{12} & 0 \\ -s_{12} & c_{12} & 0 \\ 0 & 0 & 1 \end{pmatrix}, \tag{D.21}$$

$$\tilde{R}_{13} = \begin{pmatrix} c_{13} & 0 & s_{13}e^{-i\delta_{CP}} \\ 0 & 1 & 0 \\ -s_{13}e^{i\delta_{CP}} & 0 & c_{13} \end{pmatrix}, \tag{D.22}$$

$$R_{23} = \begin{pmatrix} 1 & 0 & 0 \\ 0 & c_{23} & s_{23} \\ 0 & -s_{23} & c_{23} \end{pmatrix}, \tag{D.23}$$

and

$$D_{\text{vac}} = \frac{1}{2E}\begin{pmatrix} 0 & 0 & 0 \\ 0 & \Delta m^2_{21} & 0 \\ 0 & 0 & \Delta m^2_{31} \end{pmatrix}. \tag{D.24}$$

Hence, from Eq.D.20 we can write

$$H'_\nu = R_{12} D_{\text{vac}} R^\dagger_{12} + \tilde{R}^\dagger_{13} R^\dagger_{23} H_m R_{23} \tilde{R}_{13}. \tag{D.25}$$

The first term of Eq.D.25 becomes

$$R_{12} D_{\text{vac}} R^\dagger_{12} = \frac{1}{2E}\begin{pmatrix} \frac{\Delta m^2_{21}}{2}(1-\cos 2\theta_{12}) & \frac{\Delta m^2_{21}}{2}\sin 2\theta_{12} & 0 \\ \frac{\Delta m^2_{21}}{2}\sin 2\theta_{12} & \frac{\Delta m^2_{21}}{2}(1+\cos 2\theta_{12}) & 0 \\ 0 & 0 & \Delta m^2_{31} \end{pmatrix}. \tag{D.26}$$

We are looking for solar resonance in $1-2$ plane and from Eq.D.26, we can see that the third component is decoupled and we are left with effective 2×2 traceless matrix. After removing the constant phse part, we can write Eq.D.26 as

$$H^{\text{eff}}_{\text{vac}} = \frac{\Delta m^2_{21}}{4E}\begin{pmatrix} -\cos 2\theta_{12} & \sin 2\theta_{12} \\ \sin 2\theta_{12} & \cos 2\theta_{12} \end{pmatrix}. \tag{D.27}$$

Similarly, in the effective 2×2 model, we can write the matter+NSI Hamiltonian as

$$H^{\text{eff}}_{\text{m}} = \sqrt{2} G_F N_e(r)\begin{pmatrix} c^2_{13} & 0 \\ 0 & 0 \end{pmatrix} + \sqrt{2} G_F \sum_f N_f(r)\begin{pmatrix} -\epsilon^f_D & \epsilon^f_N \\ \epsilon^{f*}_N & \epsilon^f_D \end{pmatrix}. \tag{D.28}$$

The new parameters ϵ^f_D and ϵ^f_N are related to the original parameters $\epsilon^f_{\alpha\beta}$ by the following relations

$$\epsilon^f_D = c_{13}s_{13}Re[e^{i\delta_{CP}}(s_{23}\epsilon^f_{e\mu} + c_{23}\epsilon^f_{e\tau})] - (1+s^2_{13})c_{23}s_{23}Re(\epsilon^f_{\mu\tau}) - \frac{c^2_{13}}{2}(\epsilon^f_{ee} - \epsilon^f_{\mu\mu}) + \frac{s^2_{23} - s^2_{13}c^2_{23}}{2}(\epsilon^f_{\tau\tau} - \epsilon^f_{\mu\mu}), \tag{D.29}$$

and

$$\epsilon^f_N = c_{13}(c_{23}\epsilon^f_{e\mu} - s_{23}\epsilon^f_{e\tau}) + s_{13}e^{-i\delta_{CP}}[s^2_{23}\epsilon^f_{\mu\tau} - c^2_{23}\epsilon^{f*}_{\mu\tau} + c_{23}s_{23}(\epsilon^f_{\tau\tau} - \epsilon^f_{\mu\mu})]. \tag{D.30}$$

Hence, effectively the oscillation probabilities depend on the following real parameters $\Delta m_{21}^2, \theta_{12}, \theta_{13}$, one real matter parameter ϵ_D^f and one complex matter parameter ϵ_N^f for each f. The matter chemical composition of the Sun varies substabtially along the neutrino production region. The values of Y_n in the centre is $1/2$ and $1/6$ at the border of the solar core. So like earth, it is not possible to introduce a common set of parameters for all the different f. Hence, in the analysis of solar data, one should consider only one particular choice of $f = e, f = u, f = d$ at a time.

D.3 Incorporating the effect of sterile neutrino

Now if we add an extra sterile neutrino state, then the Hamiltonian becomes

$$H_\nu = R_{34}\tilde{R}_{24}\tilde{R}_{14}R_{23}\tilde{R}_{13}R_{12}D_{vac}R_{12}^\dagger\tilde{R}_{13}^\dagger R_{23}^\dagger\tilde{R}_{14}^\dagger\tilde{R}_{24}^\dagger R_{34}^\dagger + H_m, \tag{D.31}$$

Hence,

$$H'_\nu = R_{12}D_{\text{vac}}R_{12}^\dagger + \tilde{R}_{13}^\dagger R_{23}^\dagger\tilde{R}_{14}^\dagger\tilde{R}_{24}^\dagger R_{34}^\dagger H_{mat}R_{34}\tilde{R}_{24}\tilde{R}_{14}R_{23}\tilde{R}_{13}, \tag{D.32}$$

where

$$D_{\text{vac}} = \frac{1}{2E}\begin{pmatrix} 0 & 0 & 0 & 0 \\ 0 & \Delta m_{21}^2 & 0 & 0 \\ 0 & 0 & \Delta m_{31}^2 & 0 \\ 0 & 0 & 0 & \Delta m_{41}^2. \end{pmatrix} \tag{D.33}$$

The total matter potential including standard and non-standard interactions is governed by the Hamiltonian,

$$H_{mat}^{sterile+NSI} = \sqrt{2}G_F N_e(r)\begin{pmatrix}1 & 0 & 0 & 0\\ 0 & 0 & 0 & 0\\ 0 & 0 & 0 & 0\\ 0 & 0 & 0 & 0\end{pmatrix} + \frac{G_F N_n}{\sqrt{2}}\begin{pmatrix}0 & 0 & 0 & 0\\ 0 & 0 & 0 & 0\\ 0 & 0 & 0 & 0\\ 0 & 0 & 0 & 1\end{pmatrix} + \\ \sqrt{2}G_F \sum_{f=e,u,d} N_f(r)\begin{pmatrix}\epsilon^f_{ee} & \epsilon^f_{e\mu} & \epsilon^f_{e\tau} & 0\\ \epsilon^{f*}_{e\mu} & \epsilon^f_{\mu\mu} & \epsilon^f_{\mu\tau} & 0\\ \epsilon^{f*}_{e\tau} & \epsilon^{f*}_{\mu\tau} & \epsilon^f_{\tau\tau} & 0\\ 0 & 0 & 0 & 0\end{pmatrix}, \tag{D.34}$$

where we assume that there is no NSI parameters for sterile neutrinos. Following the same procedure for three flavours, we can construct the effective 2×2 model and the corresponding Hamiltonian $H^{\text{eff}} = H^{\text{eff}}_{\text{vac}} + H^{eff}_m$ is given as

$$H^{\text{eff}} = \frac{\Delta m^2_{21}}{4E}\begin{pmatrix}-\cos 2\theta_{12} & \sin 2\theta_{12}\\ \sin 2\theta_{12} & \cos 2\theta_{12}\end{pmatrix} + \begin{pmatrix}A_i c^2_{13}c^2_{14} & 0\\ 0 & 0\end{pmatrix} + A_j\begin{pmatrix}-k_1 & k_2\\ k_2^* & k_1\end{pmatrix} + \\ A_i \sum_{f=e,u,d}\frac{N_f}{N_e}\begin{pmatrix}-\epsilon^f_D & \epsilon^f_N\\ \epsilon^{f*}_N & \epsilon^f_D\end{pmatrix}, \tag{D.35}$$

where the parameters $A_i, A_j, k_1, k_2, \epsilon^f_D, \epsilon^f_N$ are defined in Chapter 5.

Bibliography

[1] G. Aad *et al.*, *Observation of a new particle in the search for the Standard Model Higgs boson with the ATLAS detector at the LHC,* Phys. Lett. B **716**, 1–29 (2012).

[2] S. Chatrchyan *et al.*, *Observation of a New Boson at a Mass of 125 GeV with the CMS Experiment at the LHC,* Phys. Lett. B **716**, 30–61 (2012).

[3] N. Aghanim *et al.*, *Planck 2018 results. VI. Cosmological parameters,* Astron. Astrophys. **641**, A6 (2020). [Erratum: Astron.Astrophys. 652, C4 (2021)].

[4] B. P. Abbott *et al.*, *Observation of Gravitational Waves from a Binary Black Hole Merger,* Phys. Rev. Lett. **116**, 061102 (2016).

[5] B. P. Abbott *et al.*, *Multi-messenger Observations of a Binary Neutron Star Merger,* Astrophys. J. Lett. **848**, L12 (2017).

[6] J. H. Taylor, *Pulsar timing and relativistic gravity,* Class. Quant. Grav. **10**, S167–S174 (1993).

[7] D. Krause, H. T. Kloor, and E. Fischbach, *Multipole radiation from massive fields: Application to binary pulsar systems,* Phys. Rev. D **49**, 6892–6906 (1994).

[8] A. Genova, E. Mazarico, S. Goossens, F. G. Lemoine, G. A. Neumann, D. E. Smith, and M. T. Zuber, *Solar system expansion and strong equivalence principle as seen by the NASA MESSENGER mission,* Nature Communications **9**, 289 (2018).

[9] R. S. Park, W. M. Folkner, A. S. Konopliv, J. G. Williams, D. E. Smith, and M. T. Zuber, *Precession of Mercury's Perihelion from Ranging to the MESSENGER Spacecraft,* **153**, 121 (2017).

[10] C. Wu, E. Ambler, R. Hayward, D. Hoppes, and R. Hudson, *EXPERIMENTAL TEST OF PARITY CONSERVATION IN BETA DECAY,* Phys.Rev. **105**, 1413–1414 (1957).

[11] M. Goldhaber, L. Grodzins, and A. Sunyar, *HELICITY OF NEUTRINOS,* Phys.Rev. **109**, 1015–1017 (1958).

[12] B. T. Cleveland, T. Daily, R. Davis, Jr., J. R. Distel, K. Lande, C. K. Lee, P. S. Wildenhain, and J. Ullman, *Measurement of the solar electron neutrino flux with the Homestake chlorine detector,* Astrophys. J. **496**, 505–526 (1998).

[13] Y. Fukuda *et al.*, *Solar neutrino data covering solar cycle 22,* Phys. Rev. Lett. **77**, 1683–1686 (1996).

[14] J. N. Abdurashitov *et al.*, *Measurement of the solar neutrino capture rate with gallium metal. III: Results for the 2002–2007 data-taking period,* Phys. Rev. **C80**, 015807 (2009).

[15] P. Anselmann *et al.*, *Solar neutrinos observed by GALLEX at Gran Sasso.* Phys. Lett. **B285**, 376–389 (1992).

[16] W. Hampel *et al.*, *GALLEX solar neutrino observations: Results for GALLEX IV,* Phys. Lett. **B447**, 127–133 (1999).

[17] M. Altmann *et al.*, *Complete results for five years of GNO solar neutrino observations,* Phys. Lett. **B616**, 174–190 (2005).

[18] S. Fukuda *et al.*, *Determination of solar neutrino oscillation parameters using 1496 days of Super-Kamiokande I data,* Phys. Lett. **B539**, 179–187 (2002).

[19] Q. R. Ahmad *et al.*, *Measurement of the rate of* $\nu_e + d \to p + p + e^-$ *interactions produced by* ^8B *solar neutrinos at the Sudbury Neutrino Observatory,* Phys. Rev. Lett. **87**, 071301 (2001).

[20] Q. Ahmad *et al.*, *Direct evidence for neutrino flavor transformation from neutral current interactions in the Sudbury Neutrino Observatory,* Phys.Rev.Lett. **89**, 011301 (2002).

[21] Y. Ashie *et al.*, *Evidence for an oscillatory signature in atmospheric neutrino oscillation,* Phys.Rev.Lett. **93**, 101801 (2004).

[22] K. Eguchi *et al.*, *First results from KamLAND: Evidence for reactor antineutrino disappearance,* Phys.Rev.Lett. **90**, 021802 (2003).

[23] T. Araki *et al.*, *Measurement of neutrino oscillation with KamLAND: Evidence of spectral distortion,* Phys. Rev. Lett. **94**, 081801 (2005).

[24] D. Michael *et al.*, *Observation of muon neutrino disappearance with the MINOS detectors and the NuMI neutrino beam,* Phys.Rev.Lett. **97**, 191801 (2006).

[25] P. Adamson *et al.*, *Measurement of Neutrino Oscillations with the MINOS Detectors in the NuMI Beam,* Phys.Rev.Lett. **101**, 131802 (2008).

[26] S. Abe *et al.*, *Precision Measurement of Neutrino Oscillation Parameters with KamLAND,* Phys.Rev.Lett. **100**, 221803 (2008).

[27] K. Abe *et al.*, *Solar neutrino results in Super-Kamiokande-III,* Phys.Rev. **D83**, 052010 (2011).

[28] P. Adamson *et al.*, *Improved search for muon-neutrino to electron-neutrino oscillations in MINOS,* Phys.Rev.Lett. **107**, 181802 (2011).

[29] K. Abe *et al.*, *Measurement of Neutrino Oscillation Parameters from Muon Neutrino Disappearance with an Off-axis Beam,* Phys. Rev. Lett. **111**, 211803 (2013).

[30] K. Abe *et al.*, *First Muon-Neutrino Disappearance Study with an Off-Axis Beam,* Phys.Rev. **D85**, 031103 (2012).

[31] K. Abe *et al.*, *Evidence for the Appearance of Atmospheric Tau Neutrinos in Super-Kamiokande,* Phys. Rev. Lett. **110**, 181802 (2013).

[32] O. G. Miranda, M. A. Tortola, and J. W. F. Valle, *Are solar neutrino oscillations robust?* JHEP **10**, 008 (2006).

[33] F. J. Escrihuela, O. G. Miranda, M. A. Tortola, and J. W. F. Valle, *Constraining nonstandard neutrino-quark interactions with solar, reactor and accelerator data,* Phys. Rev. **D80**, 105009 (2009). [Erratum: Phys. Rev.D80,129908(2009)].

[34] Y. Farzan and M. Tortola, *Neutrino oscillations and Non-Standard Interactions,* Front.in Phys. **6**, 10 (2018).

[35] I. Esteban, M. C. Gonzalez-Garcia, M. Maltoni, I. Martinez-Soler, and J. Salvado, *Updated Constraints on Non-Standard Interactions from Global Analysis of Oscillation Data,* JHEP **08**, 180 (2018).

[36] P. B. Denton, Y. Farzan, and I. M. Shoemaker, *Testing large non-standard neutrino interactions with arbitrary mediator mass after COHERENT data,* JHEP **07**, 037 (2018).

[37] Y. Farzan, *A model for large non-standard interactions of neutrinos leading to the LMA-Dark solution,* Phys. Lett. B **748**, 311–315 (2015).

[38] V. N. Aseev *et al.*, *An upper limit on electron antineutrino mass from Troitsk experiment,* Phys. Rev. **D84**, 112003 (2011).

[39] C. Kraus *et al.*, *Final results from phase II of the Mainz neutrino mass search in tritium beta decay,* Eur. Phys. J. **C40**, 447–468 (2005).

[40] A. Osipowicz *et al.*, *KATRIN: A Next generation tritium beta decay experiment with sub-eV sensitivity for the electron neutrino mass. Letter of intent,* (2001).

[41] F. Frankle, *KATRIN: An experiment to determine the neutrino mass,* PoS **EPS-HEP2009**, 271 (2009).

[42] W. Furry, *On transition probabilities in double beta-disintegration,* Phys.Rev. **56**, 1184–1193 (1939).

[43] J. Schechter and J. Valle, *Neutrino Masses in SU(2) x U(1) Theories,* Phys.Rev. **D22**, 2227 (1980).

[44] A. Gando *et al.*, *Search for Majorana Neutrinos near the Inverted Mass Hierarchy Region with KamLAND-Zen,* Phys. Rev. Lett. **117**, 082503 (2016). [Addendum: Phys. Rev. Lett.117,no.10,109903(2016)].

[45] V. C. Rubin, N. Thonnard, and W. K. Ford, Jr., *Rotational properties of 21 SC galaxies with a large range of luminosities and radii, from NGC 4605 /R = 4kpc/ to UGC 2885 /R = 122 kpc/,* Astrophys. J. **238**, 471 (1980).

[46] M. Persic, P. Salucci, and F. Stel, *The Universal rotation curve of spiral galaxies: 1. The Dark matter connection,* Mon. Not. Roy. Astron. Soc. **281**, 27 (1996).

[47] D. Clowe, A. Gonzalez, and M. Markevitch, *Weak lensing mass reconstruction of the interacting cluster 1E0657-558: Direct evidence for the existence of dark matter,* Astrophys. J. **604**, 596–603 (2004).

[48] G. Jungman, M. Kamionkowski, and K. Griest, *Supersymmetric dark matter,* Phys. Rept. **267**, 195–373 (1996).

[49] Z. Ahmed *et al.*, *Search for Weakly Interacting Massive Particles with the First Five-Tower Data from the Cryogenic Dark Matter Search at the Soudan Underground Laboratory,* Phys. Rev. Lett. **102**, 011301 (2009).

[50] D. S. Akerib *et al.*, *First results from the LUX dark matter experiment at the Sanford Underground Research Facility,* Phys. Rev. Lett. **112**, 091303 (2014).

[51] E. Aprile *et al.*, *Dark Matter Search Results from a One Ton-Year Exposure of XENON1T,* Phys. Rev. Lett. **121**, 111302 (2018).

[52] O. Adriani *et al.*, *An anomalous positron abundance in cosmic rays with energies 1.5-100 GeV,* Nature **458**, 607–609 (2009).

[53] D. Grasso *et al.*, *On possible interpretations of the high energy electron-positron spectrum measured by the Fermi Large Area Telescope,* Astropart. Phys. **32**, 140–151 (2009).

[54] L. Bergstrom, T. Bringmann, I. Cholis, D. Hooper, and C. Weniger, *New Limits on Dark Matter Annihilation from AMS Cosmic Ray Positron Data,* Phys. Rev. Lett. **111**, 171101 (2013).

[55] X. Cui *et al.*, *Dark Matter Results From 54-Ton-Day Exposure of PandaX-II Experiment,* Phys. Rev. Lett. **119**, 181302 (2017).

[56] J. Cooley, *Overview of Non-Liquid Noble Direct Detection Dark Matter Experiments,* Phys. Dark Univ. **4**, 92–97 (2014).

[57] L. J. Hall, K. Jedamzik, J. March-Russell, and S. M. West, *Freeze-In Production of FIMP Dark Matter,* JHEP **03**, 080 (2010).

[58] Y. Hochberg, E. Kuflik, T. Volansky, and J. G. Wacker, *Mechanism for Thermal Relic Dark Matter of Strongly Interacting Massive Particles,* Phys. Rev. Lett. **113**, 171301 (2014).

[59] W. Hu, R. Barkana, and A. Gruzinov, *Cold and fuzzy dark matter,* Phys. Rev. Lett. **85**, 1158–1161 (2000).

[60] A. Boyarsky, M. Drewes, T. Lasserre, S. Mertens, and O. Ruchayskiy, *Sterile neutrino Dark Matter,* Prog. Part. Nucl. Phys. **104**, 1–45 (2019).

[61] L. D. Duffy and K. van Bibber, *Axions as Dark Matter Particles,* New J. Phys. **11**, 105008 (2009).

[62] T. Kumar Poddar, S. Mohanty, and S. Jana, *Constraints on ultralight axions from compact binary systems,* Phys. Rev. D **101**, 083007 (2020).

[63] T. K. Poddar, *Constraints on axionic fuzzy dark matter from light bending and Shapiro time delay,* JCAP **09**, 041 (2021).

[64] L. Hui, J. P. Ostriker, S. Tremaine, and E. Witten, *Ultralight scalars as cosmological dark matter,* Phys. Rev. D **95**, 043541 (2017).

[65] T. Kumar Poddar, S. Mohanty, and S. Jana, *Vector gauge boson radiation from compact binary systems in a gauged* $L_\mu - L_\tau$ *scenario,* Phys. Rev. D **100**, 123023 (2019).

[66] T. Kumar Poddar, S. Mohanty, and S. Jana, *Constraints on long range force from perihelion precession of planets in a gauged* $L_e - L_{\mu,\tau}$ *scenario,* Eur. Phys. J. C **81**, 286 (2021).

[67] P. Salucci, *The distribution of dark matter in galaxies,* Astron. Astrophys. Rev. **27**, 2 (2019).

[68] B. Carr, F. Kuhnel, and M. Sandstad, *Primordial Black Holes as Dark Matter,* Phys. Rev. D **94**, 083504 (2016).

[69] B. C. Lacki and J. F. Beacom, *Primordial Black Holes as Dark Matter: Almost All or Almost Nothing,* Astrophys. J. Lett. **720**, L67–L71 (2010).

[70] M. Khlopov, B. A. Malomed, and I. B. Zeldovich, *Gravitational instability of scalar fields and formation of primordial black holes,* Mon. Not. Roy. Astron. Soc. **215**, 575–589 (1985).

[71] M. Milgrom, *A Modification of the Newtonian dynamics as a possible alternative to the hidden mass hypothesis,* Astrophys. J. **270**, 365–370 (1983).

[72] P. van Dokkum *et al.*, *A galaxy lacking dark matter,* Nature **555**, 629–632 (2018).

[73] B. Moore, *Evidence against dissipationless dark matter from observations of galaxy haloes,* Nature **370**, 629 (1994).

[74] S.-H. Oh *et al.*, *High-resolution mass models of dwarf galaxies from LITTLE THINGS,* Astron. J. **149**, 180 (2015).

[75] J. S. Bullock and M. Boylan-Kolchin, *Small-Scale Challenges to the ΛCDM Paradigm,* Ann. Rev. Astron. Astrophys. **55**, 343–387 (2017).

[76] S.-H. Oh, W. J. G. de Blok, E. Brinks, F. Walter, and R. C. Kennicutt, Jr, *Dark and luminous matter in THINGS dwarf galaxies,* Astron. J. **141**, 193 (2011).

[77] S. Tulin and H.-B. Yu, *Dark Matter Self-interactions and Small Scale Structure,* Phys. Rept. **730**, 1–57 (2018).

[78] S. Garrison-Kimmel, M. Boylan-Kolchin, J. Bullock, and K. Lee, *ELVIS: Exploring the Local Volume in Simulations,* Mon. Not. Roy. Astron. Soc. **438**, 2578–2596 (2014).

[79] S. Y. Kim, A. H. G. Peter, and J. R. Hargis, *Missing Satellites Problem: Completeness Corrections to the Number of Satellite Galaxies in the Milky Way are Consistent with Cold Dark Matter Predictions,* Phys. Rev. Lett. **121**, 211302 (2018).

[80] M. Viel, G. D. Becker, J. S. Bolton, and M. G. Haehnelt, *Warm dark matter as a solution to the small scale crisis: New constraints from high redshift Lyman-α forest data,* Phys. Rev. D **88**, 043502 (2013).

[81] P. Svrcek and E. Witten, *Axions In String Theory,* JHEP **06**, 051 (2006).

[82] R. Hlozek, D. Grin, D. J. E. Marsh, and P. G. Ferreira, *A search for ultra-light axions using precision cosmological data,* Phys. Rev. D **91**, 103512 (2015).

[83] P. Mocz, L. Lancaster, A. Fialkov, F. Becerra, and P.-H. Chavanis, *Schrödinger-Poisson–Vlasov-Poisson correspondence,* Phys. Rev. D **97**, 083519 (2018).

[84] T. Kobayashi, R. Murgia, A. De Simone, V. Iršič, and M. Viel, *Lyman-α constraints on ultralight scalar dark matter: Implications for the early and late universe,* Phys. Rev. D **96**, 123514 (2017).

[85] J. Martin, *Everything You Always Wanted To Know About The Cosmological Constant Problem (But Were Afraid To Ask),* Comptes Rendus Physique **13**, 566–665 (2012).

[86] C. de Rham, *Massive Gravity,* Living Rev. Rel. **17**, 7 (2014).

[87] M. Fierz and W. Pauli, *On relativistic wave equations for particles of arbitrary spin in an electromagnetic field,* Proc. Roy. Soc. Lond. A **173**, 211–232 (1939).

[88] G. R. Dvali, G. Gabadadze, and M. Porrati, *4-D gravity on a brane in 5-D Minkowski space,* Phys. Lett. B **485**, 208–214 (2000).

[89] C. de Rham, G. Gabadadze, and A. J. Tolley, *Resummation of Massive Gravity,* Phys. Rev. Lett. **106**, 231101 (2011).

[90] S. F. Hassan and R. A. Rosen, *Bimetric Gravity from Ghost-free Massive Gravity,* JHEP **02**, 126 (2012).

[91] B. P. Abbott *et al.*, *GW170104: Observation of a 50-Solar-Mass Binary Black Hole Coalescence at Redshift 0.2,* Phys. Rev. Lett. **118**, 221101 (2017). [Erratum: Phys.Rev.Lett. 121, 129901 (2018)].

[92] E. Fischbach, D. Sudarsky, A. Szafer, C. Talmadge, and S. H. Aronson, *Reanalysis of the Eotvos Experiment,* Phys. Rev. Lett. **56**, 3 (1986). [Erratum: Phys.Rev.Lett. 56, 1427 (1986)].

[93] A. J. Krasznahorkay, M. Csatlós, L. Csige, Z. Gácsi, J. Gulyás, M. Hunyadi, I. Kuti, B. M. Nyakó, L. Stuhl, J. Timár, T. G. Tornyi, Z. Vajta, T. J. Ketel, and A. Krasznahorkay, *Observation of Anomalous Internal Pair Creation in ^{8}Be: A Possible Indication of a Light, Neutral Boson,* **116**, 042501 (2016).

[94] B. Abi *et al.*, *Measurement of the Positive Muon Anomalous Magnetic Moment to 0.46 ppm,* Phys. Rev. Lett. **126**, 141801 (2021).

[95] R. D. Peccei and H. R. Quinn, *CP Conservation in the Presence of Instantons,* Phys. Rev. Lett. **38**, 1440–1443 (1977).

[96] S. Weinberg, *A New Light Boson?* Phys. Rev. Lett. **40**, 223–226 (1978).

[97] F. Wilczek, *Problem of Strong P and T Invariance in the Presence of Instantons,* Phys. Rev. Lett. **40**, 279–282 (1978).

[98] R. D. Peccei and H. R. Quinn, *Constraints Imposed by CP Conservation in the Presence of Instantons,* Phys. Rev. D **16**, 1791–1797 (1977).

[99] S. L. Adler, *Axial vector vertex in spinor electrodynamics,* Phys. Rev. **177**, 2426–2438 (1969).

[100] C. A. Baker, D. D. Doyle, P. Geltenbort, K. Green, M. G. D. van der Grinten, P. G. Harris, P. Iaydjiev, S. N. Ivanov, D. J. R. May, J. M. Pendlebury, J. D. Richardson, D. Shiers, and K. F. Smith, *Improved experimental limit on the electric dipole moment of the neutron,* Phys. Rev. Lett. **97**, 131801 (2006).

[101] S. A. Clough, Y. Beers, G. P. Klein, and L. S. Rothman, *Dipole moment of water from stark measurements of h2o, hdo, and d2o,* Journal of Chemical Physics **59**, 2254–2259 (1973).

[102] A. Hook, *TASI Lectures on the Strong CP Problem and Axions,* PoS **TASI2018**, 004 (2019).

[103] C. A. Baker *et al.*, *An Improved experimental limit on the electric dipole moment of the neutron,* Phys. Rev. Lett. **97**, 131801 (2006).

[104] J. M. Pendlebury *et al.*, *Revised experimental upper limit on the electric dipole moment of the neutron,* Phys. Rev. D **92**, 092003 (2015).

[105] B. Graner, Y. Chen, E. G. Lindahl, and B. R. Heckel, *Reduced Limit on the Permanent Electric Dipole Moment of Hg199,* Phys. Rev. Lett. **116**, 161601 (2016). [Erratum: Phys.Rev.Lett. 119, 119901 (2017)].

[106] G. Grilli di Cortona, E. Hardy, J. Pardo Vega, and G. Villadoro, *The QCD axion, precisely,* JHEP **01**, 034 (2016).

[107] S. Profumo, *An Introduction to Particle Dark Matter* (World Scientific, 2017).

[108] J. E. Moody and F. Wilczek, *NEW MACROSCOPIC FORCES?* Phys. Rev. D **30**, 130 (1984).

[109] G. Raffelt, *Limits on a CP-violating scalar axion-nucleon interaction,* Phys. Rev. D **86**, 015001 (2012).

[110] M. Kamionkowski, J. Pradler, and D. G. E. Walker, *Dark energy from the string axiverse,* Phys. Rev. Lett. **113**, 251302 (2014).

[111] D. Baumann, H. S. Chia, and R. A. Porto, *Probing Ultralight Bosons with Binary Black Holes,* Phys. Rev. D **99**, 044001 (2019).

[112] F. V. Day and J. I. McDonald, *Axion superradiance in rotating neutron stars,* JCAP **10**, 051 (2019).

[113] S. Nakagawa, F. Takahashi, and W. Yin, *Stochastic Axion Dark Matter in Axion Landscape,* JCAP **05**, 004 (2020).

[114] R. Kitano and W. Yin, *Strong CP problem and axion dark matter with small instantons,* JHEP **07**, 078 (2021).

[115] A. Arvanitaki, S. Dimopoulos, M. Galanis, L. Lehner, J. O. Thompson, and K. Van Tilburg, *Large-misalignment mechanism for the formation of compact axion structures: Signatures from the QCD axion to fuzzy dark matter,* Phys. Rev. D **101**, 083014 (2020).

[116] T. W. B. Kibble, *Topology of Cosmic Domains and Strings,* J. Phys. A **9**, 1387–1398 (1976).

[117] T. W. B. Kibble, *Some Implications of a Cosmological Phase Transition,* Phys. Rept. **67**, 183 (1980).

[118] F. Takahashi and W. Yin, *Kilobyte Cosmic Birefringence from ALP Domain Walls,* JCAP **04**, 007 (2021).

[119] M. Cicoli, J. P. Conlon, and F. Quevedo, *Dark radiation in LARGE volume models,* Phys. Rev. D **87**, 043520 (2013).

[120] T. Higaki and F. Takahashi, *Dark Radiation and Dark Matter in Large Volume Compactifications,* JHEP **11**, 125 (2012).

[121] J. P. Conlon and M. C. D. Marsh, *The Cosmophenomenology of Axionic Dark Radiation,* JHEP **10**, 214 (2013).

[122] A. Hebecker, P. Mangat, F. Rompineve, and L. T. Witkowski, *Dark Radiation predictions from general Large Volume Scenarios,* JHEP **09**, 140 (2014).

[123] J. A. Dror, H. Murayama, and N. L. Rodd, *Cosmic axion background,* Phys. Rev. D **103**, 115004 (2021).

[124] J. Jaeckel and W. Yin, *Using the spectrum of dark radiation as a probe of reheating,* Phys. Rev. D **103**, 115019 (2021).

[125] S. Mohanty and S. N. Nayak, *Determination of pseudo-goldstone-boson–photon coupling by the differential time delay of pulsar signals,* Phys. Rev. Lett. **70**, 4038–4041 (1993).

[126] T. Liu, G. Smoot, and Y. Zhao, *Detecting axionlike dark matter with linearly polarized pulsar light,* Phys. Rev. D **101**, 063012 (2020).

[127] G. Sigl and P. Trivedi, *Axion-like Dark Matter Constraints from CMB Birefringence,* (2018).

[128] S. Mohanty, J. F. Nieves, and P. B. Pal, *Optical activity of a neutrino gas,* Phys. Rev. D **58**, 093007 (1998).

[129] A. D. Plascencia and A. Urbano, *Black hole superradiance and polarization-dependent bending of light,* JCAP **04**, 059 (2018).

[130] Y. Chen, J. Shu, X. Xue, Q. Yuan, and Y. Zhao, *Probing axions with event horizon telescope polarimetric measurements,* Phys. Rev. Lett. **124**, 061102 (2020).

[131] T. Fujita, R. Tazaki, and K. Toma, *Hunting axion dark matter with protoplanetary disk polarimetry,* Phys. Rev. Lett. **122**, 191101 (2019).

[132] D. Horns, L. Maccione, A. Mirizzi, and M. Roncadelli, *Probing axion-like particles with the ultraviolet photon polarization from active galactic nuclei in radio galaxies,* Phys. Rev. D **85**, 085021 (2012).

[133] A. Payez, J. R. Cudell, and D. Hutsemekers, *New polarimetric constraints on axion-like particles,* JCAP **07**, 041 (2012).

[134] Y. Inoue, Y. Akimoto, R. Ohta, T. Mizumoto, A. Yamamoto, and M. Minowa, *Search for solar axions with mass around 1 eV using coherent conversion of axions into photons,* Phys. Lett. B **668**, 93–97 (2008).

[135] E. Arik *et al.*, *Probing eV-scale axions with CAST,* JCAP **02**, 008 (2009).

[136] S. Hannestad, A. Mirizzi, and G. Raffelt, *New cosmological mass limit on thermal relic axions,* JCAP **07**, 002 (2005).

[137] A. Melchiorri, O. Mena, and A. c. v. Slosar, *Improved cosmological bound on the thermal axion mass,* Phys. Rev. D **76**, 041303 (2007).

[138] S. Hannestad, A. Mirizzi, G. G. Raffelt, and Y. Y. Y. Wong, *Cosmological constraints on neutrino plus axion hot dark matter: Update after WMAP-5,* JCAP **04**, 019 (2008).

[139] J. Hamann, S. Hannestad, G. G. Raffelt, and Y. Y. Y. Wong, *Isocurvature forecast in the anthropic axion window,* JCAP **06**, 022 (2009).

[140] Y. Semertzidis, R. Cameron, G. Cantatore, A. C. Melissinos, J. Rogers, H. Halama, A. Prodell, F. Nezrick, C. Rizzo, and E. Zavattini, *Limits on the Production of Light Scalar and Pseudoscalar Particles,* Phys. Rev. Lett. **64**, 2988–2991 (1990).

[141] R. Cameron *et al.*, *Search for nearly massless, weakly coupled particles by optical techniques,* Phys. Rev. D **47**, 3707–3725 (1993).

[142] C. Robilliard, R. Battesti, M. Fouche, J. Mauchain, A.-M. Sautivet, F. Amiranoff, and C. Rizzo, *No light shining through a wall,* Phys. Rev. Lett. **99**, 190403 (2007).

[143] A. S. Chou, W. C. Wester, III, A. Baumbaugh, H. R. Gustafson, Y. Irizarry-Valle, P. O. Mazur, J. H. Steffen, R. Tomlin, X. Yang, and J. Yoo, *Search for axion-like particles using a variable baseline photon regeneration technique,* Phys. Rev. Lett. **100**, 080402 (2008).

[144] P. Sikivie, D. B. Tanner, and K. van Bibber, *Resonantly enhanced axion-photon regeneration,* Phys. Rev. Lett. **98**, 172002 (2007).

[145] J. E. Kim, *Light Pseudoscalars, Particle Physics and Cosmology,* Phys. Rept. **150**, 1–177 (1987).

[146] H.-Y. Cheng, *The Strong CP Problem Revisited,* Phys. Rept. **158**, 1 (1988).

[147] L. J. Rosenberg and K. A. van Bibber, *Searches for invisible axions,* Phys. Rept. **325**, 1–39 (2000).

[148] M. P. Hertzberg, M. Tegmark, and F. Wilczek, *Axion Cosmology and the Energy Scale of Inflation,* Phys. Rev. D **78**, 083507 (2008).

[149] L. Visinelli and P. Gondolo, *Dark Matter Axions Revisited,* Phys. Rev. D **80**, 035024 (2009).

[150] R. A. Battye and E. P. S. Shellard, *Axion string constraints,* Phys. Rev. Lett. **73**, 2954–2957 (1994). [Erratum: Phys.Rev.Lett. 76, 2203–2204 (1996)].

[151] M. Yamaguchi, M. Kawasaki, and J. Yokoyama, *Evolution of axionic strings and spectrum of axions radiated from them,* Phys. Rev. Lett. **82**, 4578–4581 (1999).

[152] C. Hagmann, S. Chang, and P. Sikivie, *Axion radiation from strings,* Phys. Rev. D **63**, 125018 (2001).

[153] Y. Kahn, B. R. Safdi, and J. Thaler, *Broadband and Resonant Approaches to Axion Dark Matter Detection,* Phys. Rev. Lett. **117**, 141801 (2016).

[154] J. L. Ouellet *et al.*, *First Results from ABRACADABRA-10 cm: A Search for Sub-μeV Axion Dark Matter,* Phys. Rev. Lett. **122**, 121802 (2019).

[155] P. W. Graham and S. Rajendran, *New Observables for Direct Detection of Axion Dark Matter,* Phys. Rev. D **88**, 035023 (2013).

[156] D. Budker, P. W. Graham, M. Ledbetter, S. Rajendran, and A. Sushkov, *Proposal for a Cosmic Axion Spin Precession Experiment (CASPEr),* Phys. Rev. X **4**, 021030 (2014).

[157] D. F. Jackson Kimball *et al.*, *Overview of the Cosmic Axion Spin Precession Experiment (CASPEr),* Springer Proc. Phys. **245**, 105–121 (2020).

[158] A. Garcon *et al.*, *The Cosmic Axion Spin Precession Experiment (CASPEr): a dark-matter search with nuclear magnetic resonance,* (2017).

[159] S. Pustelny *et al.*, *The Global Network of Optical Magnetometers for Exotic physics (GNOME): A novel scheme to search for physics beyond the Standard Model,* Annalen Phys. **525**, 659 (2013).

[160] S. Afach *et al.*, *Characterization of the Global Network of Optical Magnetometers to search for Exotic Physics (GNOME),* Phys. Dark Univ. **22**, 162–180 (2018).

[161] S. Afach *et al.*, *Search for topological defect dark matter using the global network of optical magnetometers for exotic physics searches (GNOME),* (2021).

[162] D. Kim, Y. Kim, Y. K. Semertzidis, Y. C. Shin, and W. Yin, *Cosmic Axion Force,* (2021).

[163] P. W. Graham, S. Hacıömeroğlu, D. E. Kaplan, Z. Omarov, S. Rajendran, and Y. K. Semertzidis, *Storage ring probes of dark matter and dark energy,* Phys. Rev. D **103**, 055010 (2021).

[164] S. A. Hoedl, F. Fleischer, E. G. Adelberger, and B. R. Heckel, *Improved Constraints on an Axion-Mediated Force,* Phys. Rev. Lett. **106**, 041801 (2011).

[165] T. K. Poddar and S. Mohanty, *Probing the angle of birefringence due to long range axion hair from pulsars,* Phys. Rev. D **102**, 083029 (2020).

[166] D. E. Krause, H. T. Kloor, and E. Fischbach, *Multipole radiation from massive fields: Application to binary pulsar systems,* Phys. Rev. D **49**, 6892–6906 (1994).

[167] A. Hook and J. Huang, *Probing axions with neutron star inspirals and other stellar processes,* JHEP **06**, 036 (2018).

[168] S. Mohanty and P. Kumar Panda, *Particle physics bounds from the Hulse-Taylor binary,* Phys. Rev. D **53**, 5723–5726 (1996).

[169] T. D. Cohen, R. J. Furnstahl, and D. K. Griegel, *Quark and gluon condensates in nuclear matter,* Phys. Rev. C **45**, 1881–1893 (1992).

[170] J. M. Alarcon, J. Martin Camalich, and J. A. Oller, *The chiral representation of the πN scattering amplitude and the pion-nucleon sigma term,* Phys. Rev. D **85**, 051503 (2012).

[171] M. Kamionkowski and J. March-Russell, *Planck scale physics and the Peccei-Quinn mechanism,* Phys. Lett. B **282**, 137–141 (1992).

[172] S. Jana and S. Mohanty, *Constraints on $f(R)$ theories of gravity from GW170817,* Phys. Rev. D **99**, 044056 (2019).

[173] T. Liu, X. Zhang, and W. Zhao, *Constraining $f(R)$ gravity in solar system, cosmology and binary pulsar systems,* Phys. Lett. B **777**, 286–293 (2018).

[174] S. Alexander, E. McDonough, R. Sims, and N. Yunes, *Hidden-Sector Modifications to Gravitational Waves From Binary Inspirals,* Class. Quant. Grav. **35**, 235012 (2018).

[175] D. Croon, A. E. Nelson, C. Sun, D. G. E. Walker, and Z.-Z. Xianyu, *Hidden-Sector Spectroscopy with Gravitational Waves from Binary Neutron Stars,* Astrophys. J. Lett. **858**, L2 (2018).

[176] J. Kopp, R. Laha, T. Opferkuch, and W. Shepherd, *Cuckoo's eggs in neutron stars: can LIGO hear chirps from the dark sector?* JHEP **11**, 096 (2018).

[177] P. C. Peters and J. Mathews, *Gravitational radiation from point masses in a Keplerian orbit,* Phys. Rev. **131**, 435–439 (1963).

[178] J. Huang, M. C. Johnson, L. Sagunski, M. Sakellariadou, and J. Zhang, *Prospects for axion searches with Advanced LIGO through binary mergers,* Phys. Rev. D **99**, 063013 (2019).

[179] J. Antoniadis *et al.*, *A Massive Pulsar in a Compact Relativistic Binary,* Science **340**, 6131 (2013).

[180] M. Kramer *et al.*, *Tests of general relativity from timing the double pulsar,* Science **314**, 97–102 (2006).

[181] P. C. C. Freire, N. Wex, G. Esposito-Farese, J. P. W. Verbiest, M. Bailes, B. A. Jacoby, M. Kramer, I. H. Stairs, J. Antoniadis, and G. H. Janssen, *The relativistic pulsar-white dwarf binary PSR J1738+0333 II. The most stringent test of scalar-tensor gravity,* Mon. Not. Roy. Astron. Soc. **423**, 3328 (2012).

[182] P. Moran, A. Shearer, R. Mignani, A. Słowikowska, A. De Luca, C. Gouiffès, and P. Laurent, *Optical Polarimetry of the Inner Crab Nebula and Pulsar,* Mon. Not. Roy. Astron. Soc. **433**, 2564 (2013).

[183] A. Arvanitaki, M. Baryakhtar, and X. Huang, *Discovering the QCD Axion with Black Holes and Gravitational Waves,* Phys. Rev. D **91**, 084011 (2015).

[184] A. Arvanitaki and S. Dubovsky, *Exploring the string axiverse with precision black hole physics,* Phys. Rev. D **83**, 044026 (2011).

[185] K. Blum, R. T. D'Agnolo, M. Lisanti, and B. R. Safdi, *Constraining Axion Dark Matter with Big Bang Nucleosynthesis,* Phys. Lett. B **737**, 30–33 (2014).

[186] C. M. Will, *The Confrontation between General Relativity and Experiment,* Living Rev. Rel. **17**, 4 (2014).

[187] C. M. Will, *The 1919 measurement of the deflection of light,* Class. Quant. Grav. **32**, 124001 (2015).

[188] A. Einstein, *The Foundation of the General Theory of Relativity,* Annalen Phys. **49**, 769–822 (1916).

[189] E. Fomalont, S. Kopeikin, G. Lanyi, and J. Benson, *Progress in Measurements of the Gravitational Bending of Radio Waves Using the VLBA,* Astrophys. J. **699**, 1395–1402 (2009).

[190] I. I. Shapiro, *Fourth Test of General Relativity,* Phys. Rev. Lett. **13**, 789–791 (1964).

[191] I. I. Shapiro, G. H. Pettengill, M. E. Ash, M. L. Stone, W. B. Smith, R. P. Ingalls, and R. A. Brockelman, *Fourth Test of General Relativity: Preliminary Results,* Phys. Rev. Lett. **20**, 1265–1269 (1968).

[192] B. Bertotti, L. Iess, and P. Tortora, *A test of general relativity using radio links with the Cassini spacecraft,* Nature **425**, 374–376 (2003).

[193] E. O. Kahya and S. Desai, *Constraints on frequency-dependent violations of Shapiro delay from GW150914,* Phys. Lett. B **756**, 265–267 (2016).

[194] S. Boran, S. Desai, and E. O. Kahya, *Constraints on differential Shapiro delay between neutrinos and photons from IceCube-170922A,* Eur. Phys. J. C **79**, 185 (2019).

[195] V. Iršič, M. Viel, M. G. Haehnelt, J. S. Bolton, and G. D. Becker, *First constraints on fuzzy dark matter from Lyman-α forest data and hydrodynamical simulations,* Phys. Rev. Lett. **119**, 031302 (2017).

[196] M. Benito, J. C. Criado, G. Hütsi, M. Raidal, and H. Veermäe, *Implications of Milky Way substructures for the nature of dark matter,* Phys. Rev. D **101**, 103023 (2020).

[197] R. Foot, *New Physics From Electric Charge Quantization?* Mod. Phys. Lett. A **6**, 527–530 (1991).

[198] R. Foot, X. G. He, H. Lew, and R. R. Volkas, *Model for a light Z-prime boson,* Phys. Rev. D **50**, 4571–4580 (1994).

[199] X.-G. He, G. C. Joshi, H. Lew, and R. R. Volkas, *Simplest Z-prime model,* Phys. Rev. D **44**, 2118–2132 (1991).

[200] S. Baek, N. G. Deshpande, X. G. He, and P. Ko, *Muon anomalous g-2 and gauged L(muon) - L(tau) models,* Phys. Rev. D **64**, 055006 (2001).

[201] S. Baek and P. Ko, *Phenomenology of U(1)(L(mu)-L(tau)) charged dark matter at PAMELA and colliders,* JCAP **10**, 011 (2009).

[202] J. Heeck and W. Rodejohann, *Gauged $L_\mu - L_\tau$ Symmetry at the Electroweak Scale,* Phys. Rev. D **84**, 075007 (2011).

[203] W. Altmannshofer, S. Gori, S. Profumo, and F. S. Queiroz, *Explaining dark matter and B decay anomalies with an $L_\mu - L_\tau$ model,* JHEP **12**, 106 (2016).

[204] S. N. Gninenko and N. V. Krasnikov, *Probing the muon g_μ - 2 anomaly, $L_\mu - L_\tau$ gauge boson and Dark Matter in dark photon experiments,* Phys. Lett. B **783**, 24–28 (2018).

[205] J. A. Grifols and E. Masso, *Neutrino oscillations in the sun probe long range leptonic forces,* Phys. Lett. B **579**, 123–126 (2004).

[206] A. S. Joshipura and S. Mohanty, *Constraints on flavor dependent long range forces from atmospheric neutrino observations at super-Kamiokande,* Phys. Lett. B **584**, 103–108 (2004).

[207] A. Bandyopadhyay, A. Dighe, and A. S. Joshipura, *Constraints on flavor-dependent long range forces from solar neutrinos and kamland,* Phys. Rev. D **75**, 093005 (2007).

[208] M. Bustamante and S. K. Agarwalla, *Universe's worth of electrons to probe long-range interactions of high-energy astrophysical neutrinos,* Phys. Rev. Lett. **122**, 061103 (2019).

[209] J. Heeck and W. Rodejohann, *Gauged $L_\mu - L_\tau$ and different Muon Neutrino and Anti-Neutrino Oscillations: MINOS and beyond,* J. Phys. G **38**, 085005 (2011).

[210] J. A. Dror, *Discovering leptonic forces using nonconserved currents,* Phys. Rev. D **101**, 095013 (2020).

[211] P. Coloma, M. C. Gonzalez-Garcia, and M. Maltoni, *Neutrino oscillation constraints on U(1)' models: from non-standard interactions to long-range forces,* JHEP **01**, 114 (2021).

[212] D. López Nacir and F. R. Urban, *Vector Fuzzy Dark Matter, Fifth Forces, and Binary Pulsars,* JCAP **10**, 044 (2018).

[213] G. Vasilakis, J. M. Brown, T. W. Kornack, and M. V. Romalis, *Limits on new long range nuclear spin-dependent forces set with a K - He-3 comagnetometer,* Phys. Rev. Lett. **103**, 261801 (2009).

[214] H. Yan, G. A. Sun, J. Gong, B. B. Pang, Y. Wang, Y. W. Yang, J. Zhang, and Y. Zhang, *Probing the short range spin dependent interactions by polarized ^{3}He atom beams,* Eur. Phys. J. C **74**, 3088 (2014).

[215] J. M. Pearson, N. Chamel, A. Y. Potekhin, A. F. Fantina, C. Ducoin, A. K. Dutta, and S. Goriely, *Unified equations of state for cold non-accreting neutron stars with Brussels–Montreal functionals – I. Role of symmetry energy,* Mon. Not. Roy. Astron. Soc. **481**, 2994–3026 (2018). [Erratum: Mon.Not.Roy.Astron.Soc. 486, 768 (2019)].

[216] A. Y. Potekhin, A. F. Fantina, N. Chamel, J. M. Pearson, and S. Goriely, *Analytical representations of unified equations of state for neutron-star matter,* Astron. Astrophys. **560**, A48 (2013).

[217] S. Goriely, N. Chamel, and J. M. Pearson, *Further explorations of Skyrme-Hartree-Fock-Bogoliubov mass formulas. 13. The 2012 atomic mass evaluation and the symmetry coefficient,* Phys. Rev. C **88**, 024308 (2013).

[218] S. Goriely, N. Chamel, and J. M. Pearson, *Further explorations of Skyrme-Hartree-Fock-Bogoliubov mass formulas. XII: Stiffness and stability of neutron-star matter,* Phys. Rev. C **82**, 035804 (2010).

[219] R. Garani and J. Heeck, *Dark matter interactions with muons in neutron stars,* Phys. Rev. D **100**, 035039 (2019).

[220] X.-G. He, G. C. Joshi, H. Lew, and R. R. Volkas, *Simplest $Z^{'}$ model,* Phys. Rev. D **44**, 2118–2132 (1991).

[221] R. Foot, X.-G. He, H. Lew, and R. R. Volkas, *Model for a light z' boson,* Phys. Rev. D **50**, 4571–4580 (1994).

[222] J. Heeck and W. Rodejohann, *Gauged $L_\mu - L_\tau$ symmetry at the electroweak scale,* Phys. Rev. D **84**, 075007 (2011).

[223] F. Zhang and L. Chen, *Proton fraction in neutron stars,* Chin. Phys. Lett. **18**, 142 (2001).

[224] I. I. Shapiro, *Solar system tests of general relativity: recent results and present plans,* in “General Relativity and Gravitation, 1989,” , N. Ashby, D. F. Bartlett, and W. Wyss, eds. (1990), p. 313.

[225] L. Iorio, *First evidence of the general relativistic gravitomagnetic field of the Sun and new constraints on a Yukawa-like fifth force,* Planet. Space Sci. **55**, 1290–1298 (2007).

[226] B. Sun, Z. Cao, and L. Shao, *Constraints on fifth forces through perihelion precession of planets,* Phys. Rev. D **100**, 084030 (2019).

[227] C. M. Will, *New General Relativistic Contribution to Mercury's Perihelion Advance,* Phys. Rev. Lett. **120**, 191101 (2018).

[228] A. Biswas and K. R. S. Mani, *Relativistic Perihelion Precession of Orbits of Venus and the Earth,* Central Eur. J. Phys. **6**, 754 (2008).

[229] L. Iorio, *On the recently determined anomalous perihelion precession of Saturn,* Astron. J. **137**, 3615 (2009).

[230] P. Touboul *et al.*, *MICROSCOPE Mission: First Results of a Space Test of the Equivalence Principle,* Phys. Rev. Lett. **119**, 231101 (2017).

[231] P. Fayet, *MICROSCOPE limits for new long-range forces and implications for unified theories,* Phys. Rev. D **97**, 055039 (2018).

[232] P. Fayet, *MICROSCOPE limits on the strength of a new force, with comparisons to gravity and electromagnetism,* Phys. Rev. D **99**, 055043 (2019).

[233] C. M. Will, *Solar system versus gravitational-wave bounds on the graviton mass,* Class. Quant. Grav. **35**, 17LT01 (2018).

[234] E. V. Pitjeva and N. P. Pitjev, *Relativistic effects and dark matter in the Solar system from observations of planets and spacecraft,* Mon. Not. Roy. Astron. Soc. **432**, 3431 (2013).

[235] R. Garani, Y. Genolini, and T. Hambye, *New Analysis of Neutron Star Constraints on Asymmetric Dark Matter,* JCAP **05**, 035 (2019).

[236] N. F. Bell, G. Busoni, and S. Robles, *Capture of Leptophilic Dark Matter in Neutron Stars,* JCAP **06**, 054 (2019).

[237] E. G. Adelberger, B. R. Heckel, and A. E. Nelson, *Tests of the gravitational inverse square law,* Ann. Rev. Nucl. Part. Sci. **53**, 77–121 (2003).

[238] J. G. Williams, X. X. Newhall, and J. O. Dickey, *Relativity parameters determined from lunar laser ranging,* Phys. Rev. D **53**, 6730–6739 (1996).

[239] P. Fayet and J. Iliopoulos, *Spontaneously Broken Supergauge Symmetries and Goldstone Spinors,* Phys. Lett. B **51**, 461–464 (1974).

[240] A. S. Joshipura, S. Mohanty, and K. M. Patel, *Inflation and long-range force from a clockwork D term,* Phys. Rev. D **103**, 035008 (2021).

[241] T. A. Wagner, S. Schlamminger, J. H. Gundlach, and E. G. Adelberger, *Torsion-balance tests of the weak equivalence principle,* Class. Quant. Grav. **29**, 184002 (2012).

[242] S. Weinberg, *Gravitation and Cosmology: Principles and Applications of the General Theory of Relativity* (John Wiley and Sons, New York, 1972).

[243] H. van Dam and M. J. G. Veltman, *Massive and massless Yang-Mills and gravitational fields,* Nucl. Phys. B **22**, 397–411 (1970).

[244] V. I. Zakharov, *Linearized gravitation theory and the graviton mass,* JETP Lett. **12**, 312 (1970).

[245] K. Hinterbichler, *Theoretical Aspects of Massive Gravity,* Rev. Mod. Phys. **84**, 671–710 (2012).

[246] E. Mitsou, *Aspects of Infrared Non-local Modifications of General Relativity,* Ph.D. thesis, Geneva U. (2015).

[247] A. Joyce, B. Jain, J. Khoury, and M. Trodden, *Beyond the Cosmological Standard Model,* Phys. Rept. **568**, 1–98 (2015).

[248] C. de Rham, J. T. Deskins, A. J. Tolley, and S.-Y. Zhou, *Graviton Mass Bounds,* Rev. Mod. Phys. **89**, 025004 (2017).

[249] C. de Rham and G. Gabadadze, *Generalization of the Fierz-Pauli Action,* Phys. Rev. D **82**, 044020 (2010).

[250] K. Hinterbichler and R. A. Rosen, *Interacting Spin-2 Fields,* JHEP **07**, 047 (2012).

[251] R. P. Feynman, *Feynman lectures on gravitation* (1996).

[252] S. Weinberg, *Photons and Gravitons in S-Matrix Theory: Derivation of Charge Conservation and Equality of Gravitational and Inertial Mass,* Phys. Rev. **135**, B1049–B1056 (1964).

[253] M. J. G. Veltman, *Quantum Theory of Gravitation,* Conf. Proc. C **7507281**, 265–327 (1975).

[254] J. F. Donoghue, M. M. Ivanov, and A. Shkerin, *EPFL Lectures on General Relativity as a Quantum Field Theory,* (2017).

[255] A. Kuntz, F. Piazza, and F. Vernizzi, *Effective field theory for gravitational radiation in scalar-tensor gravity,* JCAP **05**, 052 (2019).

[256] S. Mohanty, *Astroparticle Physics and Cosmology: Perspectives in the Multimessenger Era*, vol. 975 (2020).

[257] R. A. Hulse and J. H. Taylor, *Discovery of a pulsar in a binary system,* Astrophys. J. Lett. **195**, L51–L53 (1975).

[258] J. H. Taylor and J. M. Weisberg, *A new test of general relativity: Gravitational radiation and the binary pulsar PS R 1913+16,* Astrophys. J. **253**, 908–920 (1982).

[259] J. M. Weisberg and J. H. Taylor, *Observations of Post-Newtonian Timing Effects in the Binary Pulsar PSR 1913+16,* Phys. Rev. Lett. **52**, 1348–1350 (1984).

[260] J. M. Weisberg and Y. Huang, *Relativistic Measurements from Timing the Binary Pulsar PSR B1913+16,* Astrophys. J. **829**, 55 (2016).

[261] M. Visser, *Mass for the graviton,* Gen. Rel. Grav. **30**, 1717–1728 (1998).

[262] L. S. Finn and P. J. Sutton, *Bounding the mass of the graviton using binary pulsar observations,* Phys. Rev. D **65**, 044022 (2002).

[263] G. Gambuti and N. Maggiore, *A note on harmonic gauge(s) in massive gravity,* Phys. Lett. B **807**, 135530 (2020).

[264] G. Gambuti and N. Maggiore, *Fierz–Pauli theory reloaded: from a theory of a symmetric tensor field to linearized massive gravity,* Eur. Phys. J. C **81**, 171 (2021).

[265] G. R. Dvali, G. Gabadadze, and M. Porrati, *Metastable gravitons and infinite volume extra dimensions,* Phys. Lett. B **484**, 112–118 (2000).

[266] G. R. Dvali and G. Gabadadze, *Gravity on a brane in infinite volume extra space,* Phys. Rev. D **63**, 065007 (2001).

[267] P. Van Nieuwenhuizen, *Radiation of massive gravitation,* Phys. Rev. D **7**, 2300–2308 (1973).

[268] C. M. Will, *Bounding the mass of the graviton using gravitational wave observations of inspiralling compact binaries,* Phys. Rev. D **57**, 2061–2068 (1998).

[269] S. L. Larson and W. A. Hiscock, *Using binary stars to bound the mass of the graviton,* Phys. Rev. D **61**, 104008 (2000).

[270] C. de Rham, A. J. Tolley, and D. H. Wesley, *Vainshtein Mechanism in Binary Pulsars,* Phys. Rev. D **87**, 044025 (2013).

[271] L. Shao, N. Wex, and S.-Y. Zhou, *New Graviton Mass Bound from Binary Pulsars,* Phys. Rev. D **102**, 024069 (2020).

[272] G. Dvali, A. Gruzinov, and M. Zaldarriaga, *The Accelerated universe and the moon,* Phys. Rev. D **68**, 024012 (2003).

[273] T. K. Poddar, S. Mohanty, and S. Jana, *Gravitational radiation from binary systems in massive graviton theories,* (2021).

[274] C. Talmadge, J. P. Berthias, R. W. Hellings, and E. M. Standish, *Model Independent Constraints on Possible Modifications of Newtonian Gravity,* Phys. Rev. Lett. **61**, 1159–1162 (1988).

[275] A. I. Vainshtein, *To the problem of nonvanishing gravitation mass,* Phys. Lett. B **39**, 393–394 (1972).

[276] E. Babichev and C. Deffayet, *An introduction to the Vainshtein mechanism,* Class. Quant. Grav. **30**, 184001 (2013).

[277] N. Arkani-Hamed, H. Georgi, and M. D. Schwartz, *Effective field theory for massive gravitons and gravity in theory space,* Annals Phys. **305**, 96–118 (2003).

[278] D. G. Boulware and S. Deser, *Can gravitation have a finite range?* Phys. Rev. D **6**, 3368–3382 (1972).

[279] G. Dvali, *Predictive Power of Strong Coupling in Theories with Large Distance Modified Gravity,* New J. Phys. **8**, 326 (2006).

[280] C. Deffayet, G. R. Dvali, and G. Gabadadze, *Accelerated universe from gravity leaking to extra dimensions,* Phys. Rev. D **65**, 044023 (2002).

[281] V. A. Rubakov, *Lorentz-violating graviton masses: Getting around ghosts, low strong coupling scale and VDVZ discontinuity,* (2004).

[282] S. L. Dubovsky, *Phases of massive gravity,* JHEP **10**, 076 (2004).

[283] V. A. Rubakov and P. G. Tinyakov, *Infrared-modified gravities and massive gravitons,* Phys. Usp. **51**, 759–792 (2008).

[284] V. A. Kostelecký and M. Mewes, *Testing local Lorentz invariance with gravitational waves,* Phys. Lett. B **757**, 510–514 (2016).

[285] V. A. Kostelecký and M. Mewes, *Testing local Lorentz invariance with short-range gravity,* Phys. Lett. B **766**, 137–143 (2017).

[286] J. Aasi *et al.*, *Advanced LIGO,* Class. Quant. Grav. **32**, 074001 (2015).

[287] F. Acernese *et al.*, *Advanced Virgo: a second-generation interferometric gravitational wave detector,* Class. Quant. Grav. **32**, 024001 (2015).

[288] V. Cardoso, G. Castro, and A. Maselli, *Gravitational waves in massive gravity theories: waveforms, fluxes and constraints from extreme-mass-ratio mergers,* Phys. Rev. Lett. **121**, 251103 (2018).

[289] B. P. Abbott *et al.*, *Tests of general relativity with GW150914,* Phys. Rev. Lett. **116**, 221101 (2016). [Erratum: Phys.Rev.Lett. 121, 129902 (2018)].

[290] A. Aguilar-Arevalo *et al.*, *Evidence for neutrino oscillations from the observation of anti-neutrino(electron) appearance in a anti-neutrino(muon) beam,* Phys. Rev. **D64**, 112007 (2001).

[291] S. Goswami, *Accelerator, reactor, solar and atmospheric neutrino oscillation: Beyond three generations,* Phys. Rev. **D55**, 2931–2949 (1997).

[292] N. Okada and O. Yasuda, *A Sterile neutrino scenario constrained by experiments and cosmology,* Int. J. Mod. Phys. **A12**, 3669–3694 (1997).

[293] S. M. Bilenky, C. Giunti, and W. Grimus, *Neutrino mass spectrum from the results of neutrino oscillation experiments,* Eur. Phys. J. **C1**, 247–253 (1998).

[294] S. M. Bilenky, C. Giunti, W. Grimus, and T. Schwetz, *Four neutrino mass spectra and the Super-Kamiokande atmospheric up - down asymmetry,* Phys. Rev. **D60**, 073007 (1999).

[295] M. Maltoni, T. Schwetz, M. A. Tortola, and J. W. F. Valle, *Status of global fits to neutrino oscillations,* New J. Phys. **6**, 122 (2004).

[296] A. A. Aguilar-Arevalo *et al.*, *A Search for Electron Neutrino Appearance at the $\Delta m^2 \sim 1eV^2$ Scale,* Phys. Rev. Lett. **98**, 231801 (2007).

[297] A. A. Aguilar-Arevalo *et al.*, *Unexplained Excess of Electron-Like Events From a 1-GeV Neutrino Beam,* Phys. Rev. Lett. **102**, 101802 (2009).

[298] A. A. Aguilar-Arevalo *et al.*, *Event Excess in the MiniBooNE Search for $\bar{\nu}_\mu \to \bar{\nu}_e$ Oscillations,* Phys. Rev. Lett. **105**, 181801 (2010).

[299] A. A. Aguilar-Arevalo *et al.*, *Improved Search for $\bar{\nu}_\mu \to \bar{\nu}_e$ Oscillations in the MiniBooNE Experiment,* Phys. Rev. Lett. **110**, 161801 (2013).

[300] A. A. Aguilar-Arevalo *et al.*, *Significant Excess of ElectronLike Events in the MiniBooNE Short-Baseline Neutrino Experiment,* Phys. Rev. Lett. **121**, 221801 (2018).

[301] Y. Declais *et al.*, *Search for neutrino oscillations at 15-meters, 40-meters, and 95-meters from a nuclear power reactor at Bugey,* Nucl. Phys. **B434**, 503–534 (1995).

[302] G. Mention, M. Fechner, T. Lasserre, T. A. Mueller, D. Lhuillier, M. Cribier, and A. Letourneau, *The Reactor Antineutrino Anomaly,* Phys. Rev. **D83**, 073006 (2011).

[303] P. Anselmann *et al.*, *First results from the Cr-51 neutrino source experiment with the GALLEX detector,* Phys. Lett. **B342**, 440–450 (1995).

[304] W. Hampel *et al.*, *Final results of the Cr-51 neutrino source experiments in GALLEX,* Phys. Lett. **B420**, 114–126 (1998).

[305] C. Giunti and M. Laveder, *Statistical Significance of the Gallium Anomaly,* Phys. Rev. **C83**, 065504 (2011).

[306] D. Abdurashitov *et al.*, *The Russian-American gallium experiment (SAGE) Cr neutrino source measurement,* Phys. Rev. Lett. **77**, 4708–4711 (1996).

[307] B. Armbruster *et al.*, *Upper limits for neutrino oscillations muon-anti-neutrino $\to$ electron-anti-neutrino from muon decay at rest,* Phys. Rev. **D65**, 112001 (2002).

[308] M. Antonello *et al.*, *Search for anomalies in the ν_e appearance from a ν_μ beam,* Eur. Phys. J. **C73**, 2599 (2013).

[309] P. Astier *et al.*, *Search for nu(mu) $\to$ nu(e) oscillations in the NOMAD experiment,* Phys. Lett. **B570**, 19–31 (2003).

[310] C. Giunti and T. Lasserre, *eV-scale Sterile Neutrinos,* (2019).

[311] S. Gariazzo, C. Giunti, M. Laveder, and Y. F. Li, *Updated Global 3+1 Analysis of Short-BaseLine Neutrino Oscillations,* JHEP **06**, 135 (2017).

[312] M. Dentler, Hernández-Cabezudo, J. Kopp, P. A. N. Machado, M. Maltoni, I. Martinez-Soler, and T. Schwetz, *Updated Global Analysis of Neutrino Oscillations in the Presence of eV-Scale Sterile Neutrinos,* JHEP **08**, 010 (2018).

[313] P. Abratenko *et al.*, *Search for an anomalous excess of inclusive charged-current ν_e interactions in the MicroBooNE experiment using Wire-Cell reconstruction,* (2021).

[314] P. Abratenko *et al.*, *Search for an Excess of Electron Neutrino Interactions in MicroBooNE Using Multiple Final State Topologies,* (2021).

[315] P. Abratenko *et al.*, *Search for an anomalous excess of charged-current ν_e interactions without pions in the final state with the MicroBooNE experiment,* (2021).

[316] P. Abratenko *et al.*, *Search for an anomalous excess of charged-current quasi-elastic ν_e interactions with the MicroBooNE experiment using Deep-Learning-based reconstruction,* (2021).

[317] P. B. Denton, *Sterile Neutrino Searches with MicroBooNE: Electron Neutrino Disappearance,* (2021).

[318] A. A. Aguilar-Arevalo *et al.*, *MiniBooNE and MicroBooNE Joint Fit to a 3+1 Sterile Neutrino Scenario,* (2022).

[319] J. M. Conrad and M. H. Shaevitz, *Sterile Neutrinos: An Introduction to Experiments,* Adv. Ser. Direct. High Energy Phys. **28**, 391–442 (2018).

[320] S. M. Bilenky, S. Pascoli, and S. T. Petcov, *Majorana neutrinos, neutrino mass spectrum, CP violation and neutrinoless double beta decay. 2. Mixing of four neutrinos,* Phys. Rev. **D64**, 113003 (2001).

[321] P. Benes, A. Faessler, F. Simkovic, and S. Kovalenko, *Sterile neutrinos in neutrinoless double beta decay,* Phys. Rev. **D71**, 077901 (2005).

[322] S. Goswami and W. Rodejohann, *Constraining mass spectra with sterile neutrinos from neutrinoless double beta decay, tritium beta decay and cosmology,* Phys. Rev. **D73**, 113003 (2006).

[323] J. Barry, W. Rodejohann, and H. Zhang, *Light Sterile Neutrinos: Models and Phenomenology,* JHEP **07**, 091 (2011).

[324] Y. F. Li and S.-s. Liu, *Vanishing effective mass of the neutrinoless double beta decay including light sterile neutrinos,* Phys. Lett. **B706**, 406–411 (2012).

[325] W. Rodejohann, *Neutrinoless double beta decay and neutrino physics,* J.Phys. **G39**, 124008 (2012).

[326] I. Girardi, A. Meroni, and S. T. Petcov, *Neutrinoless Double Beta Decay in the Presence of Light Sterile Neutrinos,* JHEP **11**, 146 (2013).

[327] C. Giunti and E. M. Zavanin, *Predictions for Neutrinoless Double-Beta Decay in the 3+1 Sterile Neutrino Scenario,* JHEP **07**, 171 (2015).

[328] C. H. Jang, B. J. Kim, Y. J. Ko, and K. Siyeon, *Neutrinoless Double Beta Decay and Light Sterile Neutrino,* J. Korean Phys. Soc. **73**, 1625–1630 (2018).

[329] G.-Y. Huang and S. Zhou, *Impact of an eV-mass sterile neutrino on the neutrinoless double-beta decays: a Bayesian analysis,* (2019).

[330] K. N. Vishnudath, S. Choubey, and S. Goswami, *New sensitivity goal for neutrinoless double beta decay experiments,* Phys. Rev. **D99**, 095038 (2019).

[331] S. Böser, C. Buck, C. Giunti, J. Lesgourgues, L. Ludhova, S. Mertens, A. Schukraft, and M. Wurm, *Status of Light Sterile Neutrino Searches,* (2019).

[332] X. Chu, B. Dasgupta, M. Dentler, J. Kopp, and N. Saviano, *Sterile neutrinos with secret interactions—cosmological discord?* JCAP **11**, 049 (2018).

[333] G. Gelmini, S. Palomares-Ruiz, and S. Pascoli, *Low reheating temperature and the visible sterile neutrino,* Phys. Rev. Lett. **93**, 081302 (2004).

[334] C. E. Yaguna, *Sterile neutrino production in models with low reheating temperatures,* JHEP **06**, 002 (2007).

[335] P. F. de Salas, M. Lattanzi, G. Mangano, G. Miele, S. Pastor, and O. Pisanti, *Bounds on very low reheating scenarios after Planck,* Phys. Rev. **D92**, 123534 (2015).

[336] K. N. Deepthi, S. Goswami, V. K. N., and T. Kumar Poddar, *Implications of the Dark LMA solution and Fourth Sterile Neutrino for Neutrino-less Double Beta Decay,* Phys. Rev. **D102**, 015020 (2020).

[337] K. Chakraborty, S. Goswami, and B. Karmakar, *Consequences of μ-τ reflection symmetry for $3+1$ neutrino mixing,* (2019).

[338] I. Esteban, M. C. Gonzalez-Garcia, A. Hernandez-Cabezudo, M. Maltoni, and T. Schwetz, *Global analysis of three-flavour neutrino oscillations: synergies and tensions in the determination of $\theta_2 3, \delta_C P$, and the mass ordering,* JHEP **01**, 106 (2019).

[339] P. F. de Salas, D. V. Forero, C. A. Ternes, M. Tortola, and J. W. F. Valle, *Status of neutrino oscillations 2018: 3σ hint for normal mass ordering and improved CP sensitivity,* Phys. Lett. **B782**, 633–640 (2018).

[340] F. Capozzi, E. Di Valentino, E. Lisi, A. Marrone, A. Melchiorri, and A. Palazzo, *Global constraints on absolute neutrino masses and their ordering,* Phys. Rev. **D95**, 096014 (2017).

[341] L. Wolfenstein, *Neutrino Oscillations in Matter,* Phys. Rev. **D17**, 2369–2374 (1978). [,294(1977)].

[342] A. Esmaili and H. Nunokawa, *On the robustness of IceCube's bound on sterile neutrinos in the presence of non-standard interactions,* Eur. Phys. J. **C79**, 70 (2019).

[343] M. C. Gonzalez-Garcia and M. Maltoni, *Determination of matter potential from global analysis of neutrino oscillation data,* JHEP **09**, 152 (2013).

[344] P. Coloma, I. Esteban, M. C. Gonzalez-Garcia, and M. Maltoni, *Improved global fit to Non-Standard neutrino Interactions using COHERENT energy and timing data,* JHEP **02**, 023 (2020).

[345] M. Doi, T. Kotani, and E. Takasugi, *Double beta Decay and Majorana Neutrino,* Prog. Theor. Phys. Suppl. **83**, 1 (1985).

[346] W. C. Haxton and G. J. Stephenson, *Double beta Decay,* Prog. Part. Nucl. Phys. **12**, 409–479 (1984).

[347] M. Agostini *et al.*, *Improved Limit on Neutrinoless Double-β Decay of ^{76}Ge from GERDA Phase II,* Phys. Rev. Lett. **120**, 132503 (2018).

[348] J. Engel and J. Menéndez, *Status and Future of Nuclear Matrix Elements for Neutrinoless Double-Beta Decay: A Review,* Rept. Prog. Phys. **80**, 046301 (2017).

[349] J. Kotila and F. Iachello, *Phase space factors for double-β decay,* Phys. Rev. **C85**, 034316 (2012).

[350] S. A. Kharusi *et al.*, *nEXO Pre-Conceptual Design Report,* (2018).

[351] M. Agostini, G. Benato, and J. Detwiler, *Discovery probability of next-generation neutrinoless double- decay experiments,* Phys. Rev. **D96**, 053001 (2017).

[352] S. Pascoli and S. Petcov, *Majorana Neutrinos, Neutrino Mass Spectrum and the —lt;mgt;— $10-^{3}$ eV Frontier in Neutrinoless Double Beta Decay,* Phys.Rev. **D77**, 113003 (2008).

[353] J. T. Penedo and S. T. Petcov, *The 10^{3} eV frontier in neutrinoless double beta decay,* Phys. Lett. **B786**, 410–417 (2018).

[354] J. T. Suhonen, *Value of the Axial-Vector Coupling Strength in and Decays: A Review,* Front.in Phys. **5**, 55 (2017).

[355] G. Mangano, G. Miele, S. Pastor, T. Pinto, O. Pisanti, and P. D. Serpico, *Relic neutrino decoupling including flavor oscillations,* Nucl. Phys. B **729**, 221–234 (2005).

[356] E. Grohs, G. M. Fuller, C. T. Kishimoto, M. W. Paris, and A. Vlasenko, *Neutrino energy transport in weak decoupling and big bang nucleosynthesis,* Phys. Rev. D **93**, 083522 (2016).

[357] M. Archidiacono, S. Hannestad, R. S. Hansen, and T. Tram, *Cosmology with self-interacting sterile neutrinos and dark matter - A pseudoscalar model,* Phys. Rev. D **91**, 065021 (2015).

[358] N. Song, M. C. Gonzalez-Garcia, and J. Salvado, *Cosmological constraints with self-interacting sterile neutrinos,* JCAP **10**, 055 (2018).

[359] M. A. Acero and J. Lesgourgues, *Cosmological constraints on a light non-thermal sterile neutrino,* Phys. Rev. D **79**, 045026 (2009).

[360] S. Roy Choudhury and S. Choubey, *Constraining light sterile neutrino mass with the BICEP2/Keck Array 2014 B-mode polarization data,* Eur. Phys. J. C **79**, 557 (2019).

List of Publications

Thesis related Publications

1. **Tanmay Kumar Poddar**, Subhendra Mohanty, and Soumya Jana,
   Constraints on ultralight axions from compact binary systems
   Phys. Rev. D **101**, 8, 083007 (2020). arXiv: 1906.00666
2. **Tanmay Kumar Poddar**, and Subhendra Mohanty
   Probing the angle of birefringence due to long range axion hair from pulsars
   Phys. Rev. D **102**, 8, 083029 (2020). arXiv: 2003.11015
3. **Tanmay Kumar Poddar**
   Constraints on axionic fuzzy dark matter from light bending and Shapiro time delay
   JCAP 09 (2021) 041. arXiv: 2104.09772
4. **Tanmay Kumar Poddar**, Subhendra Mohanty and Soumya Jana,
   Vector gauge boson radiation from compact binary systems in a gauged $L_\mu - L_\tau$ scenario
   Phys. Rev. D **100**, 12, 123023 (2019). arXiv: 1908.09732
5. **Tanmay Kumar Poddar**, Subhendra Mohanty, and Soumya Jana,
   Constraints on long range force from perihelion precession of planets in a gauged $L_e - L_{\mu,\tau}$ scenario
   Eur. Phys. J. C **81**, 4, 286 (2021). arXiv: 2002.02935
6. **Tanmay Kumar Poddar**, Subhendra Mohanty, and Soumya Jana,
   Gravitational radiation from binary systems in massive graviton theories
   JCAP 03 (2022) 019. arXiv: 2105.13335

7. K. N. Deepthi, Srubabati Goswami, Vishnudath K. N., and **Tanmay Kumar Poddar**,
Implications of the dark large mixing angle solution and a fourth sterile neutrino for neutrinoless double beta decay
Phys.Rev.D **102**, 1, 015020 (2020). arXiv: 1909.09434

Publication not attached with thesis

1. **Tanmay Kumar Poddar**, Jonathan L. Feng et al,
   The Forward Physics Facility at the High-Luminosity LHC
   arXiv: 2203.05090 (white paper)

2. **Tanmay Kumar Poddar**,
   Constraints on ultralight axions, vector gauge bosons, and unparticles from geodetic and frame-dragging effects
   arXiv: 2111.05632 (under review)

3. Arindam Das, Srubabati Goswami, Vishnudath K. N., and **Tanmay Kumar Poddar**,
   Freeze-in sterile neutrino dark matter in a class of $U(1)'$ models with inverse seesaw
   arXiv:2104.13986 (under review)

4. **Tanmay Kumar Poddar**, Subhendra Mohanty, and Soumya Jana
   Constraints on Ultra Light Dark Matter from Compact Binary Systems
   Springer Proc.Phys. 248 (2020) 317-320.

5. Subhendra Mohanty, and **Tanmay Kumar Poddar**
   Astronomical Probes of Ultra Light Dark Matter
   Springer Proc.Phys. 248 (2020) 221-227.

6. **Tanmay Kumar Poddar**
   Probing Ultralight dark matter: constraints from gravitational waves and other astrophysical observations
   arXiv:2110.09880, J.Phys.Conf.Ser. 2156 (2021) 1, 012052.

7. **Tanmay Kumar Poddar**

Probing light dark matter particles with astrophysical experiments
arXiv:2110.03365, PoS 398 (2022).